Springer Series in Materials Science 244

Pablo D. Esquinazi *Editor*

Basic Physics of Functionalized Graphite

Springer

Springer Series in Materials Science

Volume 244

The Springer Series in Materials Science covers the complete spectrum of materials physics, including fundamental principles, physical properties, materials theory and design. Recognizing the increasing importance of materials science in future device technologies, the book titles in this series reflect the state-of-the-art in understanding and controlling the structure and properties of all important classes of materials.

More information about this series at http://www.springer.com/series/856

Pablo D. Esquinazi
Editor

Basic Physics of Functionalized Graphite

Springer

Editor
Pablo D. Esquinazi
Institute for Experimental Physics II
University of Leipzig
Leipzig
Germany

ISSN 0933-033X ISSN 2196-2812 (electronic)
Springer Series in Materials Science
ISBN 978-3-319-39353-7 ISBN 978-3-319-39355-1 (eBook)
DOI 10.1007/978-3-319-39355-1

Library of Congress Control Number: 2016942908

Printed on acid-free paper

This Springer imprint is published by Springer Nature
The registered company is Springer International Publishing AG Switzerland

Preface

What can still be written about graphite, the multi-graphene layer material that has not yet been experimentally and theoretically throughout studied and discussed in the last, let us say, 60 years? The study of this carbon-based material has provided us not only with interesting, non-simple basic physics (and chemistry), but also with several industrial applications—as bulk materials (nowadays commercially available and known as highly oriented pyrolytic graphite (HOPG)), polycrystalline pressed powder (pencil mine, for example), or just as highly pure powder—described in a very rich and exhaustive literature. However, the experimental and theoretical work done in the last ~ 15 years points to the existence of phenomena in graphite that were either unknown or not seriously considered by the community in the time before. On the other hand, the rise of the single-layer two-dimensional material graphene in the last 10 years, with all its interesting physics and applications, pushed a reconsideration of graphite and its properties. Therefore, we believe that to publish a book that reviews the new, and to some extent, rediscovered phenomena of graphite is timely.

The aim of this book is to provide the reader with three important and new aspects of the physics of graphite that triggered the interest of the community the last years. The three basic phenomena this book considers are as follows: magnetic order, superconductivity, and high magnetic field-induced phase transitions. We consider them as unavoidable parts of the basic physics of functionalized graphite. Firstly, the possibility of having magnetic order at high temperatures in graphite without the need of any magnetic ions, only through lattice defects or with the help of, e.g., protons. This magnetic order phenomenon, nowadays called defect-induced magnetism (DIM), has actually been discovered and confirmed first in graphite, before its existence was recognized later in a large number of other materials, mainly non-magnetic and nonmetallic materials such as several oxides. The first three chapters of this book deal with the theoretical basis of this phenomenon and the experimental evidence for its existence in graphite.

In Chap. 1 of this book, Oleg Yazyev provides an overview of the theory of magnetism and magnetic order in graphitic materials. This chapter starts considering first the electronic band structure within tight-binding and mean-field Hubbard models of a single graphene layer. It discusses the so-called counting rule theorems, useful to understand the physical mechanism of magnetic ordering in graphene-based systems, and as alternative approach, the magnetic states at armchair and zigzag nanoribbon edges are also considered. Although the influence of temperature fluctuations and the necessary small size a graphene-based device needs, restrict severally its realization and possible applicability at room temperature, the high spin stiffness and a further functionalization of the edges of graphene-based systems suggest a less pessimistic realization of magnetic order on nano-, two-dimensional devices in the future. It continues discussing magnetic order triggered by defects within the atomic lattice (DIM) in graphene and graphite, providing the main concepts to understand its realization above room temperature.

Chapters 2 and 3 deal with the experimental evidence for the existence of magnetic order at temperatures above room temperature in graphite with defects and/or hydrogen (protons). In Chap. 2, Hendrik Ohldag discusses the results of X-ray magnetic circular dichroism (XMCD) obtained in magnetic graphite, whereas its magnetic order is triggered by carbon vacancies or the influence of hydrogen. The XMCD method is of importance because it is element specific, can rule out the influence of magnetic impurities, and provides a hint for the origin of the magnetic order. Chapter 2 describes in detail all the necessary concepts to interpret XMCD results in graphite and why those results can be taken as the "smoking gun" experiment to prove the intrinsic character of the magnetic order induced by lattice defects or non-magnetic ions in a (pure) carbon material.

In Chap. 3 Daniel Spemann and the editor review the experimental evidence from magnetization and transport measurements that support the existence of magnetic order triggered by defects and/or non-magnetic ions in graphite. It provides the reader the key experimental facts and characterization methods, including trace element analysis to obtain the magnetic and non-magnetic impurity concentration, necessary to arrive at such conclusion. Chapter 3 provides also an overview of the literature that supports the existence of magnetic order at high temperatures in graphitic materials, without the need of magnetic elements.

Chapter 4 deals with the quantum limit of a three-dimensional metal, which is attained at a sufficiently strong magnetic field with only a few occupied Landau levels. Benoît Fauqué and Kamran Behnia argue that the small Fermi surface found in graphite samples is an ideal candidate to explore this limit. For example, a magnetic field of 7.5 T confines already the carriers to their lowest Zeeman split Landau level. The chapter discusses results obtained in the early 1980s for the in-plane magnetoresistance of graphite at magnetic fields above 20 T as well as recent transport measurements up to 80 T that reveal a rich and complex field phase diagram of graphite as a function of temperature and magnetic field. Whether part of the observed phenomena is related to the existence of internal interfaces in the measured samples remains a subject to be clarified in the near future.

The phenomenon of superconductivity in (non-intercalated) graphite is the subject of the last three chapters (Chaps. 5–7) of the book. In the first chapter of these three, Eduardo Marino and Lizardo Nunes describe theoretically the possible superconducting properties of layered systems of Dirac electrons under the assumption that some pairing mechanism exists. The phase diagram, quantum critical points, the effects of temperature, magnetic field, chemical potential (through doping), number of layers, as well as the interplay between superconductivity and excitonic interaction are discussed. According to the results presented by the authors, a novel mechanism, other than the traditional BCS, is required to explain superconductivity of Dirac electrons.

In Chap. 6, Tero Heikkilä and Grigori Volovik stress the importance of a dispersionless (flat) energy dispersion relation as a possible route to increase substantially the critical temperature for superconductivity, assuming that a finite Cooper pair coupling exists, whatever its strength. According to the authors, these flat bands might be generated only on surfaces or interfaces and indicate that graphite is a good candidate where high-temperature flat-band interface superconductivity could be found. Related to this prediction, in Chap. 7, Yury Lysogorskiy and the editor review the experimental evidence that speaks for the existence of embedded interfaces between crystalline regions with Bernal and rhombohedral stacking or between twisted Bernal stacking ordered regions in usual graphite samples, and their relationship with the observed metallic and superconducting behavior.

Acknowledgments

The enterprize of editing a book takes a long, longtime, longer than the time responsible for the publication of the book thought at the very beginning. I have to acknowledge our colleague Yakov Kopelevich, for convincing me about the necessity of the publication of a book on graphite. Although he could not contribute with a chapter, his work on the graphite issue is recognized in the literature and cited all over the chapters of this book. I thank all the contributors of this book for their patience and their efforts to get it done in a reasonable timescale. Certainly, several open questions about the physics of graphite remain, especially now where it became more clear the large influence of lattice defects, like interfaces, and adatoms, like hydrogen, on several properties of graphite.

Leipzig, Germany Pablo D. Esquinazi

Contents

Contributors

Kamran Behnia ESPCI ParisTech, PSL Research University, CNRS, Sorbonne Universities, UPMC Univ, Paris Cedex 5, France

Pablo D. Esquinazi Division of Superconductivity and Magnetism, Institute for Experimental Physics II, University of Leipzig, Leipzig, Germany

Benoît Fauqué ESPCI ParisTech, PSL Research University, CNRS, Sorbonne Universities, UPMC Univ, Paris Cedex 5, France

Tero T. Heikkilä Department of Physics and Nanoscience Center, University of Jyväskylä, Jyvaskyla, Finland

Yury V. Lysogorskiy Institute of Physics, Kazan Federal University, Kazan, Russia

Eduardo C. Marino Instituto de Física, UFRJ, Rio de Janeiro, RJ, Brazil

Lizardo H.C.M. Nunes Departamento de Ciências Naturais, UFSJ, São João Del-rei, MG, Brazil

Hendrik Ohldag Stanford Synchotron Radiation Lightsource, Menlo Park, CA, USA

Daniel Spemann Physical Department, Leibniz Institute for Surface Modification (IOM), Leipzig, Germany

Grigory E. Volovik Low Temperature Laboratory, Department of Applied Physics, Aalto University, Aalto, Finland; L. D. Landau Institute for Theoretical Physics, Moscow, Russia

Oleg V. Yazyev Institute of Physics, Ecole Polytechnique Fédérale de Lausanne (EPFL), Lausanne, Switzerland

Acronyms

BCS	Bardeen–Cooper–Schrieffer
CDW	Charge density waves
CNT	Carbon nanotubes
DIM	Defect-induced magnetism
DOS	Density of states
DW	Density wave
FS	Fermi surface
HOPG	Highly oriented pyrolytic graphite
LL	Landau level
MIT	Metal–insulator transition
NEXAFS	Near edge X-ray absorption fine structure
QHE	Quantum Hall effect
SdH	Schubnikow–de Haas
SDW	Spin density wave
SEM	Scanning electron microscope
STM	Scanning tunneling microscope
TBG	Twisted bilayer graphene
TEM	Transmission electron microscope
vHs	Van Hove singularity

Chapter 1
Theory of Magnetism in Graphitic Materials

Oleg V. Yazyev

Abstract This chapter provides a pedagogical introduction into the theoretical models of magnetism in graphene nanostructures and graphite. The onset of magnetism in the considered systems is mostly discussed at the level of very simple models, namely, the tight-binding model and the Hubbard model in the mean-field approximation. The simplicity of these models further allows to introduce two counting-rule theorems that establish basic intuition behind the emergence of ferromagnetic and antiferromagnetic correlations in graphene systems. The chapter covers different models of magnetic graphene systems categorized according to their dimensionality. First, several examples of magnetic graphene molecules are discussed for the purpose of illustrating the application of counting-rule theorems. Next, the physical mechanism behind the magnetic ordering at one-dimensional edges of graphene is extensively covered. It will be shown how the presence of localized edge states results in the onset of magnetism in zigzag and chiral graphene nanoribbons. Finally, we will discuss common defects in graphene and graphite created as a result of irradiation by high-energy particles and the physical mechanism of defect-induced magnetism in these materials. The theoretical developments of this chapter are presented along with the latest achievements in studying the electronic structure and magnetic properties of graphene-based systems using experimental methods, notable a range of scanning probe microscopy techniques.

1.1 Electronic Structure Models

1.1.1 Tight-Binding and Mean-Field Hubbard Models

The simplest model Hamiltonian that one can use for studying magnetic systems based on graphene is the one-orbital mean-field Hubbard model. This model includes only the electronic states formed by unhybridized p_z atomic orbitals of carbon atoms.

O.V. Yazyev (✉)
Institute of Physics, Ecole Polytechnique Fédérale de Lausanne (EPFL),
1015 Lausanne, Switzerland
e-mail: oleg.yazyev@epfl.ch

P.D. Esquinazi (ed.), *Basic Physics of Functionalized Graphite*,
Springer Series in Materials Science 244, DOI 10.1007/978-3-319-39355-1_1

These electronic states constitute the leading contribution to low-energy properties of graphene, including most of magnetic effects discussed in this chapter. The Hamiltonian for the Hubbard model can be written as

$$\mathscr{H} = \mathscr{H}_0 + \mathscr{H}'. \tag{1.1}$$

In this expression, the first term represents the nearest-neighbor tight-binding Hamiltonian [1]

$$\mathscr{H}_0 = -t \sum_{\langle i,j\rangle,\sigma} [c^\dagger_{i\sigma} c_{j\sigma} + \text{h.c.}]. \tag{1.2}$$

The operators $c_{i\sigma}$ and $c^\dagger_{i\sigma}$ annihilate and create, respectively, an electron with spin σ at site i; $\langle \cdot, \cdot \rangle$ denotes the pairs of nearest-neighbor atoms. It is important to point out that the honeycomb lattice of graphene represents a bipartite lattice, that is carbon atoms belong to either sublattice A or sublattice B, and each atom has its nearest neighbors only in the complementary sublattice (see Fig. 1.1a). Since we restrict ourselves to only the interactions between nearest-neighbor atoms located at 1.42 Å distance away from each other, the only empirical parameter is the hopping integral t that defines the energy scale. The often-quoted value of t is 2.7 eV, although the hopping integral can also be related to the Fermi velocity ν_F at the Dirac point as $t = 2\nu_\text{F}/(\sqrt{3}a)$ ($a = 0.246$ nm is the lattice constant of graphene). The experimental values $\nu_\text{F} \approx 10^6$ m/s results in a larger $t = 3.09$ eV [2]. This simple one-parameter tight-binding model is sufficient for describing the vast majority of low-energy electronic properties of graphene such as the linear dispersion of electronic bands at the K and K' points of the Brillouin zone (see Fig. 1.1b–d). This model can be systematically improved by including farther nearest-neighbor hopping parameters, although their magnitudes are much smaller than the one of parameter t [3]. Finally, interlayer hopping terms can be included in order to reproduce the differences between monolayer graphene and multilayer systems such as bilayer graphene and graphite [4, 5]. The leading effect corresponds to the hopping between two carbon atoms in different layers located directly on top of each other at a distance of 3.35 Å. The magnitude of the corresponding hopping parameter t' is an order of magnitude smaller than that of t. In below, we will be considering only the simplest tight-binding model based on intralayer nearest-neighbor hopping.

From computational point of view, the Hamiltonian matrix of the nearest-neighbor tight-binding model is the sparse $N \times N$ matrix for a system with N carbon atoms in sp^2 hybridization. The off-diagonal matrix elements (i, j) and (j, i) are equal to $-t$ if atoms i and j participate in a covalent bond, and to 0 otherwise. In a neutral graphene system each atom contributes one p_z orbital and one π electron, hence the system is half-filled. Under realistic conditions the discussed graphene-based systems are at half-filling or sufficiently close to it. One important property of the nearest-neighbor tight-binding model is electron-hole symmetry, that is the energy spectrum is symmetric with respect to zero energy (Fermi level at half-filling). For

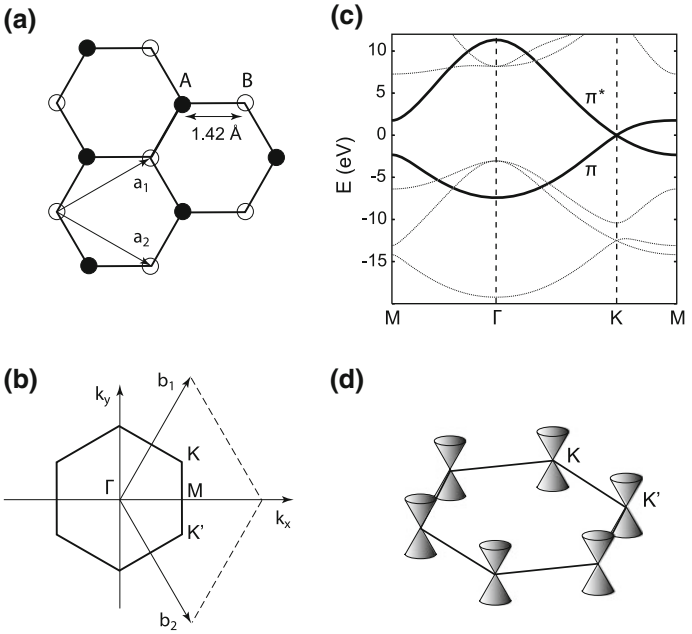

Fig. 1.1 **a** Honeycomb crystalline lattice of graphene with lattice vectors a_1 and a_2 indicated. The atoms belonging to sublattices A and B of the bipartite lattice of graphene are distinguished. **b** Brillouin zone of graphene with reciprocal lattice vectors b_1 and b_2 and high-symmetry points Γ, M and K indicated. **c** Band structure of graphene calculated from first-principles. The π-symmetry bands forming a linear intersection at the K point are highlighted. **d** Schematic illustration of the low-energy region of the band structure of graphene showing Dirac cones at the inequivalent points K and K' of the two-dimensional Brillouin zone of graphene

each eigenvalue $\epsilon < 0$ corresponding to a bonding state, there is an anti-bonding state with $\epsilon^\star = -\epsilon$. The states with $\epsilon = 0$ are refereed to as non-bonding or zero-energy states.

Investigating the electronic structure and properties of magnetic systems based on graphene demands for explicit treatment of electron–electron interactions. Within the Hubbard model electron–electron interactions are described by the on-site Coulomb repulsion term

$$\mathscr{H}' = U \sum_i n_{i\uparrow} n_{i\downarrow}, \tag{1.3}$$

where $n_{i\sigma} = c^\dagger_{i\sigma} c_{i\sigma}$ is the spin-resolved electron density at site i while parameter $U > 0$ defines the magnitude of the on-site Coulomb repulsion. This model considers only the short-range Coulomb interaction, i.e. two electrons interact with each other only if they occupy the p_z atomic orbital belonging to the same atom. Straightforward application of the Hubbard model to realistic systems is no longer trivial in most cases and requires further simplification. This is achieved by the mean-field approximation

$$\mathscr{H}'_{\mathrm{mf}} = U \sum_i \left(n_{i\uparrow} \langle n_{i\downarrow} \rangle + \langle n_{i\uparrow} \rangle n_{i\downarrow} - \langle n_{i\uparrow} \rangle \langle n_{i\downarrow} \rangle \right), \tag{1.4}$$

which allows for considerable reduction of the computational demand. In this approximation, a spin-up electron at site i interacts with the mean population of spin-down electron $\langle n_{i\downarrow} \rangle$ at the same site, and vice versa. This model is a lattice equivalent of the unrestricted Hartree–Fock method. Several works employing exact diagonalization, quantum Monte-Carlo and functional renormalization group techniques [6–8] confirmed the validity of the mean-field approximation up to $U/t \sim 1$, which corresponds to the strength of electron–electron interaction in graphene-based systems discussed in more details below. This conclusion implies that magnetic graphitic materials are not strongly-correlated electronic systems in most situations.

From the point of view of practical computations, the mean-field Hubbard model term concerns only the diagonal elements of the Hamiltonian matrix. These matrix elements in the spin-up and spin-down blocks depend on the unknown expectation values of spin-resolved electron densities $\langle n_{i\downarrow} \rangle$ and $\langle n_{i\uparrow} \rangle$, respectively. The problem thus has to be solved in a self-consistent way starting from some initial values of $\langle n_{i\downarrow} \rangle$ and $\langle n_{i\uparrow} \rangle$, which can in principle be chosen randomly. One important point to keep in mind is that in certain cases the broken-symmetry (antiferromagnetic) solutions can be found only if the initial guess of spin-resolved electron densities breaks the spin-spatial symmetry [9]. The iterative process involving (1) calculating the Hamiltonian matrix elements, (2) diagonalization of the Hamiltonian, and (3) the computation of updated spin densities is then repeated until all values of $\langle n_{i\downarrow} \rangle$ and $\langle n_{i\uparrow} \rangle$ are converged. The final solution provides the spin densities

$$M_i = \frac{\langle n_{i\uparrow} \rangle - \langle n_{i\downarrow} \rangle}{2} \tag{1.5}$$

on each atom i as well as the total spin of the system $S = \sum_i M_i$. One can notice that for a given graphene system described within the mean-field Hubbard model both the local magnetic moments and the total spin depend exclusively on the dimensionless ratio U/t.

We shall now discuss the magnitude of the U/t ratio. Its straightforward experimental determination in graphene-based systems appears to be difficult. The closest material extensively investigated in this context already long time ago is *trans*-polyacetylene. This one-dimensional polymer is formed by sp^2 carbon atoms and can be considered as the smallest possible width zigzag graphene nanoribbon. Magnetic resonance studies of neutral solitons hosting unpaired electrons in this material concluded on the approximate values $U \approx 3.0\,\mathrm{eV}$ [10, 11]. It has also been shown that the results of calculations performed using the mean-field Hubbard model are very close to those obtained using first-principles methods based on density functional theory for certain values of U/t [12–14]. In particular, the results of the local-spin-density (LDA) approximation calculations correspond to $U/t \approx 0.9$, while the generalized-gradient-approximation (GGA) density functionals match $U/t \approx 1.3$ results. Hybrid functional calculations explicitly including exact exchange were shown to corre-

spond to larger values of U/t [13]. A more recent work addressed the magnitude of U/t using the constrained random phase approximation (cRPA) [15], resulting in a considerably large value $U/t \approx 3$. However, one has to bear in mind that these calculations are based on a model that goes beyond the on-site Coulomb interactions. It was later pointed the range of effective on-site Coulomb interaction parameter in graphene is $U^{\star}/t = 1.6 \pm 0.2$ [16].

Overall, $U/t = 1$ can be considered as a reasonable choice for modeling the onset of magnetism in graphene systems. Increasing U/t inevitably results in the enhancement of local magnetic moments, and at $U/t \approx 2.23$ within the mean-field Hubbard model pristine graphene undergoes a Mott–Hubbard transition into an antiferromagnetic insulating phase [17]. One should also keep in mind that U/t is an effective parameter, hence its magnitude is affected by a range of external conditions. For example, a reduced value of U/t would be appropriate for graphene systems deposited on metallic substrates due to the enhanced screening of electron–electron interactions.

1.1.2 Counting-Rule Theorems

One important advantage of electronic structure models introduced in the previous section, as compared to more accurate first-principles techniques, is their simplicity. This allows for the formulation of mathematically rigorous theorems that can be used for making important conclusion regarding the electronic structure of graphene systems without performing straightforward numerical calculations. Two such 'counting rule' theorems that are very useful for understanding the physical mechanism of magnetic ordering in graphene-based systems will be discussed and illustrated in this section. We first define the benzenoid system as a fragment of honeycomb lattice with all faces being hexagons, and hence all carbon atoms being either 2- or 3-fold coordinated. The spectrum of eigenvalues of the nearest-neighbor tight-binding Hamiltonian of such a system can be addressed using the so-called benzenoid graph theory [18]. In particular, the benzenoid graph theory allows determining the number of zero-energy states in a very simple way. The number of zero-energy states is equal to the nullity of benzenoid graph

$$\eta = 2\alpha - N, \tag{1.6}$$

where N is the total number of sites, α is the maximum number of non-adjacent sites, that is the sites that are not nearest neighbors to each other. The onset of magnetism in a system is determined by the Stoner criterion that refers to the competition between negative exchange energy and positive kinetic energy as the system undergoes spin-polarization. The gain in exchange energy as a result of exchange splitting of the electronic states due to spin polarization [19]

$$\Delta_S = \epsilon_{\uparrow} - \epsilon_{\downarrow} = \frac{U}{2} \sum_i n_i^2, \tag{1.7}$$

where $\sum_i n_i^2$ is the inverse participation ratio which quantifies the degree of localization of the electronic state under consideration. The kinetic energy penalty, on the other hand, is proportional to the energy of this state. This implies that the zero-energy states become spin-polarized at any $U > 0$ irrespective of their degree of localization. Spin-polarization is thus one of the mechanisms allowing to relieve the instability associated with the presence of large density of low-energy electronic states in the system. Other possible mechanisms, e.g. the Peierls distortion, were demonstrated to be inefficient for neutral graphene system [13].

The benzenoid graph theory is useful for predicting the occurrence of zero-energy states that undergo spin polarization, but it does not provide any information on how the electron spins align in these states. The complementary knowledge is contributed by Lieb's theorem [20] that determines the total spin of any bipartite system of any dimensionality described by the Hubbard model with repulsive ($U > 0$) on-site Coulomb interactions. This theorem states that the ground state of such a bipartite system at half-filling is characterized by the total spin

$$S = \frac{1}{2}|N_A - N_B|, \tag{1.8}$$

where N_A and N_B are the numbers of sites in the two sublattices A and B.

The application of these two theorems can be demonstrated with the help of three scenarios of magnetic ordering realized in small finite size graphene fragments described below. These simple examples reproduced from [21] help understanding the physical mechanism underlying the onset of magnetic ordering in more complex graphitic systems that will be considered later. Below, we compare the results obtained with the help of counting-rule theorems to the ones resulted from explicit model Hamiltonian calculations. The π-bonding networks of these graphene fragments shown in Fig. 1.2 can be realized in the polycyclic aromatic hydrocarbon (PAH) molecules with the edge carbon atoms assumed to be passivated by hydrogen atoms.

The first molecular fragment of hexagonal shape shown in Fig. 1.2a corresponds to what is called coronene in chemistry. In this molecule, the number of sites in the two sublattices is equal, that is $N_A = N_B = 12$, due to the presence of inversion symmetry. The number of non-adjacent sites α is maximized if all atoms in one of the sublattices are selected (shown as circles in Fig. 1.2a), i.e. $\alpha = 12$. Hence, the benzenoid graph theory and the Lieb theorem conclude that the number of zero-energy states η and the total spin S should be zero. Explicit tight-binding model calculation predicts a relatively wide band gap of $1.08t \approx 3.0\,\mathrm{eV}$ for this system (bottom panel of Fig. 1.2a). The mean-field Hubbard model calculations do not reveal any local magnetic moments, which agree with what is known for this molecule from experiments.

The second model system of triangular shape is shown in Fig. 1.2b. This graphene fragment corresponds to the hypothetical molecule triangulane, derivatives of which have been synthesized. In this system the two sublattices are no longer equivalent, thus $N_A = 12$ and $N_B = 10$. The choice of non-adjacent sites maximizing α is unique and corresponds to atoms belonging to sublattice A (circles in Fig. 1.2b), hence

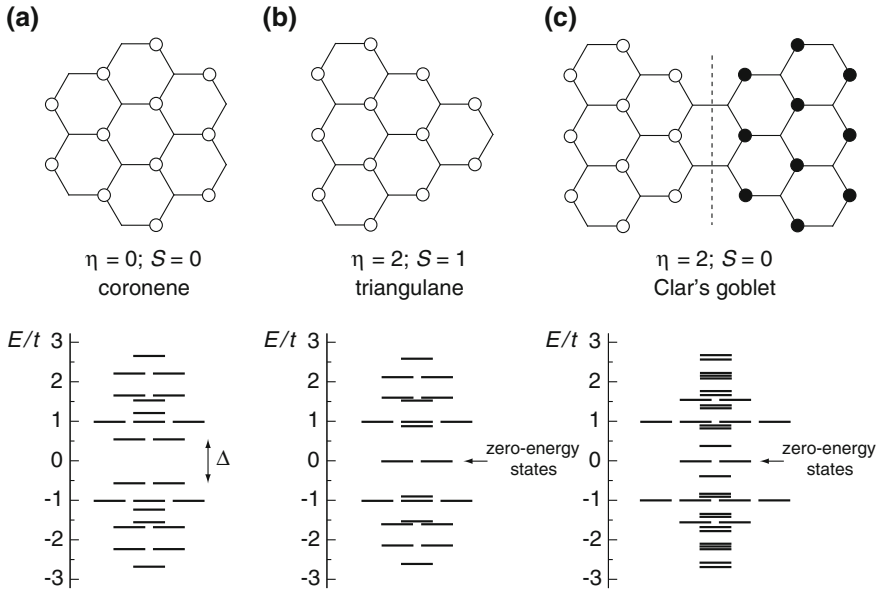

Fig. 1.2 Atomic structures of three small-size graphene fragments: **a** coronene, **b** triangulane, and **c** a bowtie-shaped molecule. The *circles* show the selections of sites that correspond to the maximum number of non-adjacent sites α. For clarity, *empty* and *filled circles* correspond to sublattice A and sublattice B, respectively. The *bottom panels* show the respective tight-binding model spectra with *arrows* indicating the presence of zero-energy states. Adapted with permission from [21]

$\alpha = N_A = 12$. Therefore, the benzenoid graph theory predicts the presence of doubly degenerate zero-energy state on sublattice A, while according to Lieb's theorem triangulane has spin-triplet ($S = 1$) ground state (that is 2 μ_B). This can be viewed as two electrons populating the doubly degenerate zero-energy state according to Hund's rule or, in other words, the electron spins are ferromagnetically correlated. The results of explicit mean-field Hubbard model calculation performed at $U/t = 1.2$ are shown in Fig. 1.3a. The degeneracy of zero-energy states is lifted due to spin-polarization opening a gap of $\Delta_S = 0.30t \approx 0.8\,\text{eV}$. The spin-up density (shaded circles in Fig. 1.3a) localized on sublattice A originates from the two electrons populating the zero-energy states. However, a sizable spin-down electron density can also be observed on sublattice B. This is a manifestation of the so-called spin-polarization effect related to exchange interaction between the half-occupied zero-energy states and the fully occupied states at lower energies.

The third example is represented by a bowtie-shaped fragment composed of two triangulane parts joined together by one common hexagon (Fig. 1.2c). This molecule is inversion symmetric, hence $N_A = N_B = 19$ and its ground state is spin-singlet following the arguments of Lieb's theorem. Unlike in the other two cases discussed

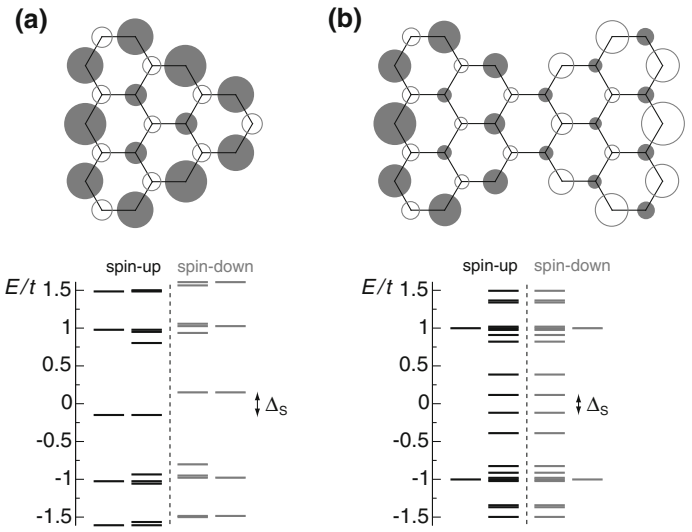

Fig. 1.3 Results of mean-field Hubbard model calculations performed at $U/t = 1.2$ for **a** triangulane and **b** the bowtie-shaped molecule. Local magnetic moments, visualized by *circles*, and spin-resolved one-electron energies are shown. Area of each circle indicates the magnitude of local magnetic moment. *Shaded* and *empty circles* correspond to spin-up and spin-down electron densities, respectively. The corresponding mean-field Hubbard model spectra are shown for spin-up and spin-down states separately. Adapted with permission from [21]

above, the set of atoms maximizing the number non-adjacent sites α is less trivial for this system. Figure 1.2c illustrates such a selection resulting in $\alpha = 20$, which involves atoms pertaining to sublattice A in the left and to sublattice B in the right part of the fragment (delimited by dashed line in Fig. 1.2c). Therefore, there are $\eta = 2 \times 20 - 38 = 2$ zero-energy states as confirmed by the tight-binding model calculations (Fig. 1.2c). These states are spatially separated in the left and right parts of the molecule. In order to obtain the $S = 0$ ground state, the doubly degenerate zero-energy states has to be populated by two electrons with oppositely oriented (that is antiferromagnetically correlated) spins. This result is also easily verified by means of the mean-field approximation Hubbard model calculations presented in Fig. 1.3b. The molecule corresponding to such bowtie-shaped graphene system was hypothesized by Eric Clar and called "Clar's goblet" [22].

The examples discussed above illustrate how three different scenarios—nonmagnetic, ferromagnetic and antiferromagnetic—can be realized in very simple systems owing to the bipartite symmetry of graphene lattice. Next sections of this chapter will explain how magnetism emerges in extended graphene systems.

1.2 Magnetic Edge States in Graphene-Based Systems

A viewpoint alternative to the one presented in the previous section considers only the boundaries of graphene systems. The edges of graphene are defined by their crystallographic orientation and the atomic structure details of their termination [23]. The commonly used model for studying the effects of edges are graphene nanoribbons, one-dimensional periodic strips of graphene. In this case, the additional degree of freedom is the nanoribbon width. At the very basic level, one can consider two high-symmetry crystallographic orientations, the zigzag and the armchair directions, which correspond to the $(1, 0)$ and $(1, 1)$ translational vectors on graphene lattice. Figure 1.4 shows the structures of armchair and zigzag nanoribbons of $\approx$1.5 nm width assuming the simplest edge termination.

The most striking point is that armchair and zigzag nanoribbons reveal remarkably different electronic properties. Figure 1.4a shows the tight-binding band structure of an armchair nanoribbon. This particular configuration of armchair graphene nanoribbon has an electronic band gap of $0.27t$. The density of states shows a series of Van Hove singularities that are characteristic of quantum confinement in one dimension. These Van Hove singularities are located symmetrically with respect to $E = 0$

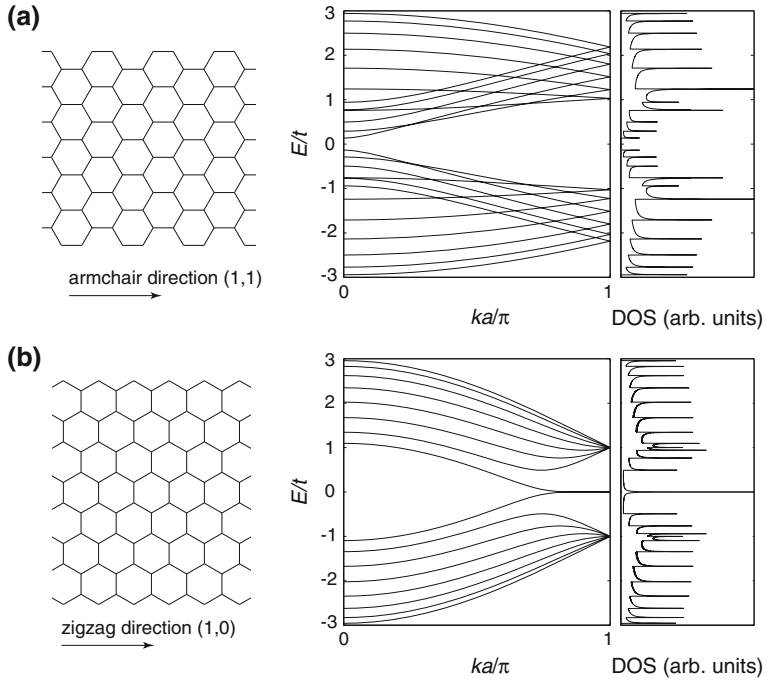

Fig. 1.4 Atomic structures of **a** armchair and **b** zigzag graphene nanoribbons. *Right panels* show the corresponding tight-binding band structures and density of states plots

since electron-hole symmetry is guaranteed within the nearest-neighbor tight-binding model. Generally speaking, the tight-binding model predicts either metallic or semiconducting band structures for armchair nanoribbons [24–28], with these two types alternating upon the increase of nanoribbon width. The band gap of semiconducting armchair nanoribbons decreases monotonically upon the width increase. In the band structures of metallic armchair nanoribbons two bands cross the Fermi level $E = 0$ at the Γ point.

Within the nearest-neighbor tight-binding model all zigzag graphene nanoribbons are found to be metallic irrespective of their width. The band structures exhibit the presence of a flat band spanning one-third of the one-dimensional Brillouin zone length at $k \in (2\pi/3a; \pi/a)$ (here, $a = 0.25\,\text{nm}$ is the unit cell of the zigzag edge, which is equal to the lattice constant of graphene) as shown in Fig. 1.4b [29]. The electronic states that correspond to this flat band are localized at the edges. The lack of dispersion of this band results in high density of low-energy electronic states, thus suggesting a possibility of the onset of magnetic ordering close to the half-filling after including electron–electron interactions. Indeed, the mean-field Hubbard model calculations performed for the zigzag graphene nanoribbon show the presence of magnetic moments localized at the edges (Fig. 1.5a) [30]. The ground state configuration exhibits ferromagnetic arrangement of local magnetic moments along the edge, while the relative orientation of local magnetic moments at the opposite edges is antiparallel. Therefore, the total magnetic moment of a zigzag nanoribbon is zero, which is fully consistent with the expectation of Lieb's theorem as in this case the balance between the two sublattices is preserved ($N_A = N_B$). Figure 1.4b compares the band structures and the density of states plots for the mean-field Hubbard model and the tight-binding model. The introduction of the Hubbard term splits the entire flat-band segment opening a band gap of $\Delta_z^0 = 0.16t$ (at $U/t = 1$). The single peak at $E = 0$ in the tight-binding density of states splits into two pairs of Van Hove singularities. One pair of Van Hove singularities characterized by splitting Δ_z^0 corresponds to the band extrema at $k \approx 2\pi/3a$ that define the band gap. The other pair of peaks with a larger splitting $\Delta_z^1 = 0.27t$ is due to the band extrema at the Brillouin zone boundary $k = \pi/a$. Spin-polarization affects only the low-energy flat band and has practically no effect on the electronic states at higher energies. All Van Hove singularities at higher energies result from the quantum confinement in one dimension, as verified by their presence in the tight-binding density of states plot. The band structures for the spin-up and spin-down channels are identical, although spin-spatial symmetry of electronic states is broken.

The dependence of splittings Δ_z^0 and Δ_z^1 on the nanoribbon width investigated in [25] by means of first-principles calculations is reproduced in Fig. 1.6. The states at the Brillouin zone boundary $k = \pi/a$ are strongly localized states at the edges. Hence, the corresponding splitting Δ_z^1 is practically independent on width beyond $w = 1\,\text{nm}$. On the contrary, the states at $k = 2\pi/3a$ penetrate deep into the bulk region and the corresponding Δ_z^0 splitting shows a w^{-1}-dependence on the nanoribbon width. These slowly decaying states are responsible for the antiferromagnetic correlation between magnetic moments localized at the opposite edges. The magnitude of this exchange interaction was shown theoretically to have a w^{-2}-dependence on the nanoribbon

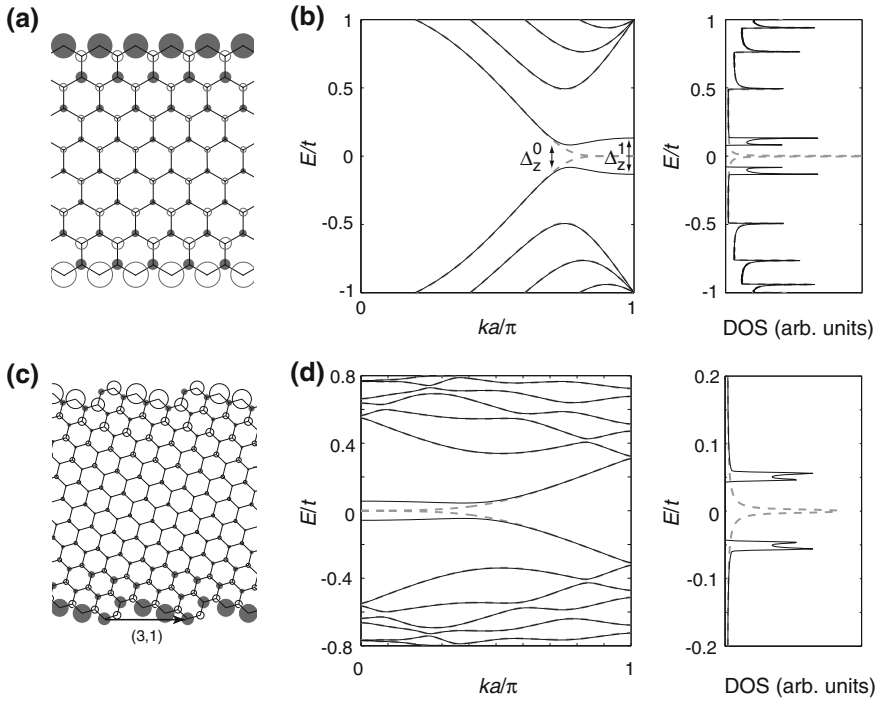

Fig. 1.5 **a** Atomic structure of a zigzag graphene nanoribbon with local magnetic moments calculated using the mean-field Hubbard model. Area of each circle is proportional to the magnitude of the local magnetic moment. *Filled* and *empty circles* indicate spin-up and spin-down moments, respectively. **b** Mean-field Hubbard model ($U/t = 1$) band structure and the corresponding density of states plot (*solid lines*) compared to the results of the tight-binding model calculations (*dashed lines*). The band structures for spin-up and spin-down electrons are equivalent. **c** Atomic structure of a chiral graphene nanoribbon defined by periodicity vector (3, 1) and chirality angle $\theta = 13.9°$. Area of each circle is proportional to the magnitude of the local magnetic moment. *Filled* and *empty circles* indicate spin-up and spin-down moments, respectively. **d** Mean-field Hubbard model ($U/t = 1$) band structure and the corresponding density of states plot (*solid lines*) compared to the results of the tight-binding model calculations (*dashed lines*)

width w [31]. First principles calculations predict coupling strength of ∼25 meV per unit cell for a zigzag nanoribbon of ∼1.5 nm width [13]. Unlike the insulating antiferromagnetic ground state, a zigzag graphene nanoribbon with ferromagnetic orientation of edge-localized magnetic moments is metallic with a pair of bands crossing the Fermi level at $k \approx 2\pi/3a$. The possibility of switching between these two states was proposed theoretically as a basis for graphene-based magnetic sensor [32]. Exchange coupling between magnetic edges can also be controlled by means of either electron or hole doping of the nanoribbons [33, 34]. High levels of doping are expected to suppress magnetism since the flat band moves away from the Fermi level, thus eliminating the instability associated with the high density of low-energy electronic states [34].

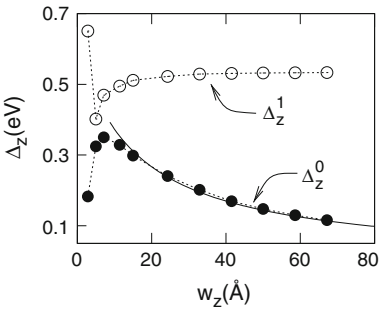

Fig. 1.6 Bands splitting Δ_z^0 and Δ_z^1 calculated from first-principles as a function of width w_z for zigzag graphene nanoribbons. Reproduced with permission from [25]

In fact, the presence of zero-energy states is a general property of low-symmetry edges irrespective of their crystallographic orientation, not only of the high-symmetry zigzag edges. This was pointed out already in the pioneering work by Nakada et al. [29] and supported by the tight-binding calculations. The edge direction of low-symmetry edges can be characterized by the so-called chirality angle

$$\theta = \arcsin\sqrt{\frac{3}{4}\left(\frac{m^2}{n^2+nm+m^2}\right)}, \tag{1.9}$$

where the pair of integers n and m defines the translational vector (n, m) oriented along the edge. Thus, chirality angles of $\theta = 0°$ and $\theta = 30°$ correspond to zigzag and armchair edges, respectively. Chirality angles of low-symmetry edges, below referred to as chiral, span the range of values between these two values of θ. It was later demonstrated analytically that the density of localized zero-energy states per edge unit length depends on chirality angle θ as [35]

$$\rho(\theta) = \frac{2}{3a_0}\cos\left(\theta + \frac{\pi}{3}\right). \tag{1.10}$$

The maximum value of $\rho = 1/(3a)$ achieved for the case of zigzag edges directly corresponds to the flat band spanning one-third of the one dimensional Brillouin zone. Importantly, only strictly armchair edges are characterized by zero density of edge states as in this case the presence of the edge does not break the sublattice compensation. An example of chiral graphene nanoribbon characterized by $\theta = 13.9°$ is shown in Fig. 1.5c. The chirality angle of this edge corresponds to the (3, 1) translational vector, and the edge can be viewed as composed of one armchair and two zigzag units. Similar to the case of zigzag nanoribbons, their chiral counterparts are expected to undergo the onset of spin polarization upon including electron–electron interactions. This is illustrated by the mean-field Hubbard model calculations of the above-mentioned (3, 1) chiral graphene nanoribbon as shown in Fig. 1.5d. The results look qualitatively similar to the case of zigzag graphene nanoribbon, although the energy splittings, in particular Δ^1, are reduced compared to the corresponding

values for zigzag graphene nanoribbon of equivalent width. More generally, the magnetic moments per edge length follow closely the density of edge states provided by expression (1.10) [36]. It is worth stressing once again, only graphene nanoribbons with edges oriented along armchair direction or close to it have non-magnetic ground state.

Beyond the structures of ordered edge terminations considered above it is worth highlighting the results of a tight-binding investigation carried out for a model of large graphene quantum dot [37]. The local density of states revealed the presence of localized edge states along the entire perimeter of the considered irregularly shaped graphene quantum dot. However, it is reduced in the regions with edge orientation close to the armchair direction. The effects of random atomic-scale disorder at the edge were also studied in this paper. It was found that at rough edges the density of zero-energy states decreases, but do not vanish. Thus, one can expect that the edge magnetism in graphene is robust with respect to disorder. On the other hand, Wassmann et al. have shown that certain types of ordered terminations of zigzag edges lack localized edge states as a result of recovered sublattice compensation [38].

It was immediately recognized that the discussed novel magnetic properties of graphene nanostructures combined with the low-dimensional nature of this material offer exciting perspectives for technological applications, especially in spintronics. The most interesting device concept was introduced by Son et al., who predicted that external electric field applied across a zigzag graphene nanoribbon induces half-metallicity [39]. Here, the half-metallic state refers to the metallic band structure for electrons in one spin channel combined with a gapped insulating state in the other. At zero field zigzag graphene nanoribbons are characterized by the energy gap Δ_z^0 in both spin channels as discussed previously and illustrated in Fig. 1.5b. An applied electric field breaks this symmetry and closes the gap in one of the spin channels. Importantly, the direction of electric field defines in which spin channel the metallic conductivity is established. First-principles calculations of [39] showed that the critical field required for the onset of the half-metallic state is $3.0/w$ V, where w is the nanoribbon width in Angstrom. Such a simple device would offer a new approach for electrical control of spin transport that is instrumental in spintronic circuits.

In practice, however, such devices would inevitably face physical limitations related to the fact that magnetic order in low-dimensional systems is strongly affected by thermal fluctuations. In particular, the Mermin–Wagner theorem [40] states that long-range magnetic order in one-dimensional systems, e.g. the magnetic edges in graphene, does not exist at any finite temperature. More specifically, the range of magnetic order is established by the spin correlation lengths ξ^α ($\alpha = x, y, z$) that define the decay of the spin correlation function

$$\langle \hat{s}_i^\alpha \hat{s}_{i+l}^\alpha \rangle = \langle \hat{s}_i^\alpha \hat{s}_i^\alpha \rangle \exp(-l/\xi^\alpha), \tag{1.11}$$

which is expected to be strongly temperature dependent. In this expression $\hat{s}_i^{\alpha}$ are the components of normalized magnetic moment vector $\hat{\mathbf{s}}_i$ at site i. The spin correlation length would thus impose practical limitations on the device dimensions.

The energetics of possible spin fluctuations that contribute to the breakdown of the ordered zero-temperature ground-state configuration was estimated by means of first-principles calculations [41]. In particular, the investigated transverse and longitudinal spin excitations are shown in Fig. 1.7a. The magnetic correlation parameters in the presence of spin-wave fluctuations, the dominant type of spin disorder in this case, were obtained with the help of one-dimensional Heisenberg model Hamiltonian

$$H = -a \sum_i \hat{\mathbf{s}}_i \hat{\mathbf{s}}_{i+1} - d \sum_i \hat{s}_i^z \hat{s}_{i+1}^z, \tag{1.12}$$

where the Heisenberg coupling $a = 2\kappa/a_z^2 = 105\,\text{meV}$ corresponds to the spin-wave stiffness $\kappa = 320\,\text{meV}\,\text{Å}^2$ calculated from first principles. The estimated small anisotropy parameter $d/a \approx 10^{-4}$ originates from the weak spin-orbit interaction in carbon. This simple model Hamiltonian has known analytic solutions [42]. Figure 1.7c shows the spin correlation lengths calculated for our particular case. Above the crossover temperature $T_x \approx 10\,\text{K}$, weak magnetic anisotropy does not play any role and the spin correlation length $\xi \propto T^{-1}$. However, below T_x the spin correlation length grows exponentially with decreasing temperature. At $T = 300\,\text{K}$ the spin correlation length $\xi \approx 1\,\text{nm}$.

From a practical point of view, this means that the dimensions of spintronic devices based on the magnetic zigzag edges of graphene and operating at normal temperature conditions are limited to several nanometers. At present, such dimensions are very difficult to achieve, which can be regarded as a pessimistic conclusion. Nevertheless, one has to keep in mind that the spin stiffness predicted for the magnetic graphene edges is still higher than the typical values for traditional magnetic materials. That is,

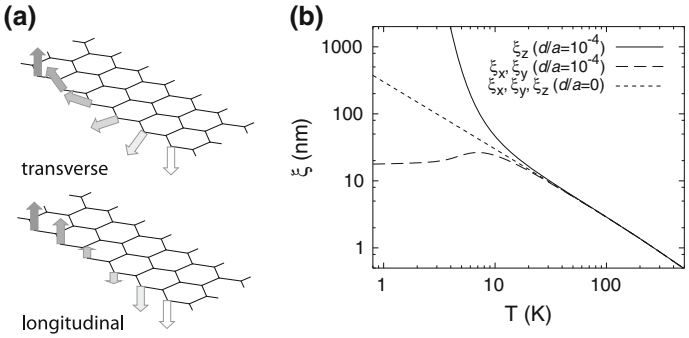

Fig. 1.7 **a** Schematic illustration of the transverse and the longitudinal spin excitation at zigzag graphene edges. The local magnetic moments at the edge atoms are shown by *arrows*. **b** Components of spin correlation length at the zigzag edges perpendicular (ξ_z) and parallel (ξ_x, ξ_y) to the graphene plane as a function of temperature. Reproduced with permission from [41]

graphene outperforms d-element based magnetic materials, and there is a room for improvement. Achieving control over the magnetic anisotropy d/a could possibly raise the crossover temperature T_x above 300 K and thus significantly extend ξ. Possible approaches for reaching this goal include chemical functionalization of the edges with heavy-element functional groups or coupling graphene to a substrate.

The low-dimensional nature of the edge-state magnetism in graphene makes its experimental detection challenging. During the past several years, the edge-state magnetism in graphene received indirect experimental confirmations from local probe measurements. Tao and co-authors reported a scanning tunneling microscopy/spectroscopy investigation performed on graphene nanoribbons produced by chemical unzipping of carbon nanotubes [43]. Such nanoribbons have well-ordered straight edges while their crystallographic orientation is inherited from the one of precursor carbon nanotubes. Due to the broad distribution of carbon nanotube chiralities, the edges of such nanoribbons typically show low-symmetry (chiral) orientation (Fig. 1.8a). Scanning tunneling spectroscopy reveals the presence of edge states localized along all such observed chiral edges. Importantly, the edge-localized states are split into a pair of peaks (Fig. 1.8b) with the magnitude of splitting showing a clear dependence on the nanoribbon width, which qualitatively agrees with the theoretical predictions involving the magnetic origin of the splitting [36, 43]. Further experimental investigation of the hydrogen etched edges of such graphene nanoribbons allowed accessing the details of their atomic structure (Fig. 1.8c, d) [44]. The latter appeared to be consistent with the simple models employed in theoretical studies.

More recently, Magda and colleagues reported an investigation [45] of 3–12 nm wide graphene nanoribbons produced using a nanofabrication technique [46] based on scanning tunneling microscopy. This approach allowed for controlling the crystallographic orientation of the edges. The scanning tunneling spectroscopy showed both the presence of confinement gap in armchair graphene nanoribbons as well as 0.2–0.3 eV band gaps in zigzag graphene nanoribbons. The latter was attributed to the magnetic ordering at the edges. In addition, the observed semiconductor-to-metal transition at nanoribbon width of approximately 7 nm was related to the change of magnetic coupling between the opposite edges from the antiferromagnetic to the ferromagnetic configuration. Importantly, the observed band gap was found stable even at room temperature.

Narrower graphene nanoribbons with well defined structure can be obtained using the bottom-up approach pioneered by Cai and co-workers [47]. This method relying on the surface-assisted self-assembly starting from precursor molecules allows producing armchair graphene nanoribbons down to sub-nanometer width. Exploiting this route for producing chiral [48] and zigzag [49] graphene nanoribbons has been reported only recently. In particular, Ruffieux et al. reported *ca.* 1 nm wide zigzag graphene nanoribbons that showed localized edge states with splittings $\Delta_z^0 = 1.5\,\text{eV}$ and $\Delta_z^1 = 1.9\,\text{eV}$ in agreement with the results of *GW* (Green's function screened interaction) calculations [49].

Other related scenarios of the onset of magnetic ordering in carbon-based materials have been investigated. For instance, with the help of scanning probe techniques, notably the magnetic force microscopy, and magnetization measurements, Červenka

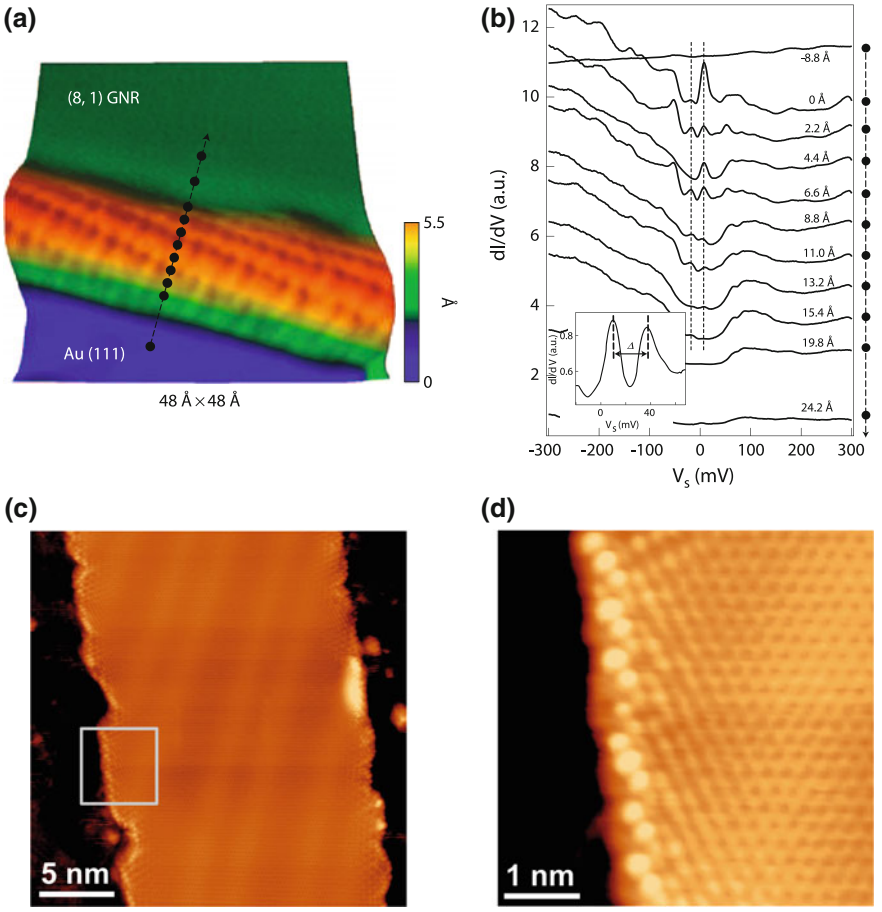

Fig. 1.8 **a** Atomically-resolved scanning tunneling microscopy (STM) image of the edge of (8, 1) chiral graphene nanoribbon on Au(111) surface. **b** dI/dV spectra of (8, 1) graphene edge measured at different points (*black dots*, panel **a**) along a line perpendicular to the edge at $T = 7\,\mathrm{K}$. Inset shows a higher resolution dI/dV spectrum for the edge of another graphene nanoribbon of (5, 2) chirality. Reprinted with permission from [43]. **c** Room-temperature STM image of a hydrogen etched chiral graphene nanoribbon. **d** Enlarged STM image ($V_S = 0.97\,\mathrm{V}$, $I_t = 50\,\mathrm{pA}$) showing the atomic structure of a straight segment of the edge with orientation that roughly corresponds to (2, 1) chirality. The localized edge states are clearly visible in the image. Reprinted with permission from [44]

and colleagues have concluded that the intrinsic ferromagnetism of highly-oriented pyrolitic graphite is related to the presence of grain boundaries [50], which are intrinsic defects in polycrystalline materials [51]. These observations have been rationalized by the fact that grain boundaries are effectively arrays of dislocations [52], and each dislocation may carry a localized magnetic moment depending on the structure of its core [53]. The electronic properties of grain boundaries in highly-oriented

pyrolitic graphite were found to be qualitatively similar to what was observed for the edges graphene nanoribbons and exhibited strong dependence on the distance between the dislocations. Regarding the results in [50], however, Martínez-Martín et al. raised serious doubts on the validity of these MFM measurements and their interpretation [54].

1.3 Defect-Induced Magnetism in Graphene and Graphite

Experimental observations of ferromagnetic ordering in irradiated graphite are responsible for the renewal of interest to carbon-based magnetism. These results are especially exciting since such defect-induced magnetic ordering persists till room temperature and well above. State-of-the-art experimental advances are covered in Chaps. 2 and 3. In this section, we shall try to understand the origin of magnetism in irradiated graphite from the theoretical point of view. The phenomena discussed in this section apply to both graphene and graphite, a three-dimensional crystalline lattice composed of graphene sheets bound by weak Van der Waals interactions.

At its very basic level, the picture of the radiation damage in carbon materials is relatively simple. Irradiation of graphite with high-energy particles (for instance protons) creates several types of defects. The defects are produced as a result of the so-called "knock-on collisions" that involve direct transfer of momentum from the high-energy incident particles to individual atoms in the crystalline lattice of irradiated material [55, 56]. If the transferred kinetic energy is sufficiently large, above the displacement threshold T_d, the affected atom may leave its equilibrium position in the crystalline lattice resulting in the formation of a pair of complementary point defects—a vacancy defect and an interstitial. Their stable structures in graphite are shown in Fig. 1.9a. The magnitude of displacement threshold T_d in graphitic materials was found to be around 20 eV in a number of investigations [57–60]. Creation of defects by means of electron stopping, that is the process involving electronic excitations and ionization of individual atoms, is less relevant to carbon materials. This is because electronic excitations in metals and narrow-gap materials are delocalized and quench instantly [55, 56].

In addition to vacancies and interstitials, certain high-energy particles after slowing down may also produce chemisorption defects. In particular, protons bind to carbon atoms in graphite lattice leading to the change of their coordination sphere from triangular to tetrahedral and rehybridization into the sp^3-state. The resulting defects are referred to as hydrogen chemisorption defects (see Fig. 1.9a). From the standpoint of single-orbital models discussed above the vacancy and hydrogen chemisorption defects very similar—one p_z-orbital is removed from the π-conjugate system of graphene sheet. In the case of vacancy, the p_z-orbital is eliminated as a result of removing the knocked-out carbon atom. In the case of hydrogen chemisorption the carbon atom remains close to its initial position in the crystalline lattice, but once rehybridized it is no longer able to provide its p_z-orbital to the π-conjugate system. Below, we will collectively refer to these two types of defects as p_z-vacancies.

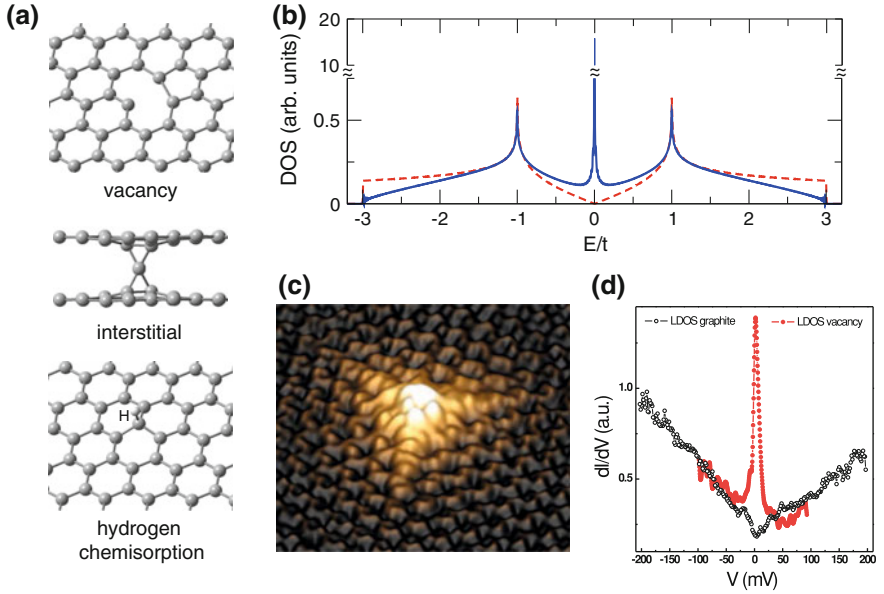

Fig. 1.9 **a** Atomic structures of three types of primary defects in graphite created upon irradiation with high-energy protons—single-atom vacancies, interstitials and hydrogen chemisorption defects. **b** Density of states curves of ideal graphene (*dashed line*) and graphene with large concentration of p_z-vacancies calculated using the tight-binding model. Reproduced with permission from [65]. **c** Scanning tunneling microscopy image of a vacancy defect on the surface of graphite. **d** Corresponding dI/dV curves recorded in vicinity of the defect and at a distance from it. Reproduced with permission from [72]

The three types of defects described above are the primary defects produced upon the radiation damage process. More complex defect structures can be formed at later stages of the process. For example, single-atom vacancies and interstitials, the later being particularly mobile, may aggregate producing extended defects. Complexes involving two or more different types of defects, such as the complexes of hydrogen with vacancies and interstitials [61], and intimate Frenkel pairs [59, 62], can also be formed upon irradiation. Radiation in graphitic materials may also result in creation of Stone–Wales defects [63, 64] and other kinds of in-plane disorder.

Single-atom vacancies and chemisorption defects have a particularly strong effect on the electronic structure of graphene and graphite. Consider a periodically repeated supercell of ideal graphene containing $2N$ carbon atoms ($N_A = N_B = N$). Removal of one carbon atom from sublattice A creates a zero-energy state localized in the complementary sublattice B ($\alpha = N_B$; thus $\eta = 2N_B - ((N_A - 1) + N_B) = 1$). Such zero-energy states giving rise to a sharp peak in the density of states (Fig. 1.9b) and extending over large distances are called quasi-localized states due to their power-law decay [65–68]. The quasi-localized states have been observed in numerous scanning tunneling microscopy (STM) measurements performed on the surface of graphite.

These states appear as triangular $\sqrt{3} \times \sqrt{3}R30°$ features typically extending over several nanometers and localized around point defects [69–72]. Figure 1.9c, d reproduce the results of one of such measurements reported in [72].

According to Lieb's theorem, a magnetic moment of $|(N_A - 1) + N_B| = 1\mu_B$ per supercell is expected for the described model with single defect in the supercell. That is, the presence of defects induces ferromagnetic ordering within this particular model. This conclusion has been widely confirmed by calculations using both density functional theory [61, 73–75] and the mean-field Hubbard model [19, 76]. Figure 1.10 reproduces the spin-resolved density-of-states (DOS) plots calculated using density functional theory for the hydrogen chemisorption and vacancy defects [74]. In the case of the hydrogen chemisorption defect, the DOS plot exhibits a sharp peak at the Fermi level that corresponds to the quasi-localized state band (Fig. 1.10a). The peak is fully exchange-split and the magnetic moment is $1\mu_B$ per supercell irrespective of its size. The spatial distribution of electron spin density around the defect site shows a clear $\sqrt{3} \times \sqrt{3}R30°$ superstructure [74]. The case of vacancy defect appears to be more complicated. The DOS exhibits a peak due to the quasi-localized state, but is shifted to lower energies compared to the Dirac point energy that is clearly recognized as a V-shaped feature (Fig. 1.10b). Such a shift is related to the structural reconstruction of the vacancy defect, which results in the formation of an additional covalent bond coupling two atoms that belong to the same sublattice [74]. In turn, the shift to lower energies gives rise to self-doping and partial suppression of the contribution of the quasi-localized state to the total magnetic moment. However, one can also observe an exchange-split DOS peak originating from the localized non-bonding state due to the presence of one σ-symmetry dangling bond at the single-atom vacancy defect (Fig. 1.10b, inset). The magnitude of exchange splitting is much larger due to the very high degree of localization of the dangling bond states, hence it contributes $1\mu_B$ to the total magnetic moment induced by the defect. The overall magnetic moment per vacancy defect varies between $1.12\mu_B$ and $1.53\mu_B$ for defect

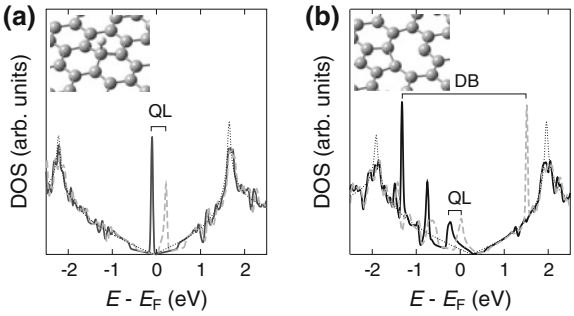

Fig. 1.10 Spin-resolved density of states (DOS) plots for **a** the hydrogen chemisorption defect and **b** the vacancy defect in graphene calculated using density functional theory. *Solid* and *dashed curves* refer to the majority and minority spin channels, respectively. *Dotted curve* shows the reference density of states of pristine graphene. Exchange-split features that correspond to the quasi-localized (QL) and dangling-bond (DB) states are indicated. Reproduced with permission from [74]

concentrations within the range of 0.5–20%. Magnetic moments can also be created by dangling bonds present in other types of defects, such as the bridge interstitial defect in graphene [77]. However, magnetic ordering due to only localized magnetic moments in graphene-based system seems improbable at high temperatures. The Ruderman–Kittel–Kasuya–Yosida interaction is weak in graphene due to its semimetallic electronic structure [78, 79]. On the other hand, magnetic ordering due to defect-induced quasi-localized states can be viewed as a scenario realizing itinerant magnetism without excluding a possible contribution of dangling-bond magnetic moments to the net magnetic moment.

The model that we considered so far, with one defect located in a periodically repeated supercell, is only a very rough approximation of disordered graphene for the following two reasons. First, in this case all defects are in the same sublattice of the graphene layer. Second, the defects themselves form an ordered periodic superlattice. A more realistic description of disorder can be realized, for example, by constructing models in which a large number of defects is randomly distributed in a sufficiently large supercell [80]. Such models eliminate any short-range structural order and allow defects to occupy both sublattices at arbitrary concentrations. However, larger supercells needed for building such disordered models render first-principles calculations difficult. Large models of disordered graphene can be treated using calculations relying on the Hubbard model within the mean-field approximation.

Results of such calculations are shown in Fig. 1.11 as average magnetic moment per carbon atom in sublattice A and sublattice B, $\langle M^A \rangle$ and $\langle M^B \rangle$, as a function of defect concentration x [80]. Additionally, the resulting values were averaged over many random distributions of defects in the simulation supercell for the following two scenarios: defects equally distributed over the two sublattices ($N_A^d = N_B^d$, Fig. 1.11a) and defects located in sublattice B only ($N_A^d = 0$, Fig. 1.11b). In the case of equal distribution, the net magnetic moments in the two sublattices are equal in magnitude

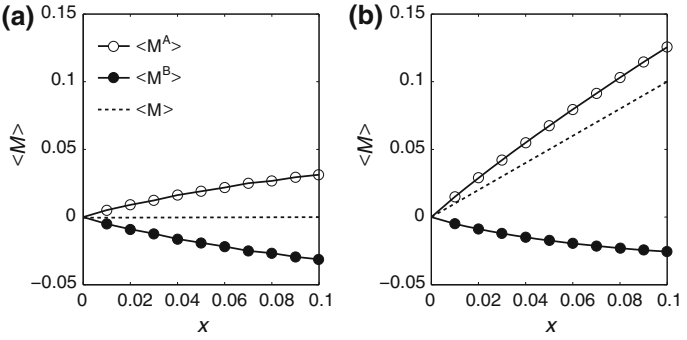

Fig. 1.11 Average magnetic moments on sublattices A and B as a function of defect concentration x calculated for large models using the mean-field Hubbard model (here, $U/t = 1.33$). The defects are either **a** distributed equally between the two sublattices or **b** belong to sublattice B only. The net magnetic moment per carbon atom (sum of the two contributions, *dotted line*) is shown. Reproduced with permission from [80]

but have opposite signs. Thus, the overall magnetic correlation is of *antiferromagnetic* type. For defects populating one of the sublattices, the system exhibits *ferromagnetic* ordering with a net magnetic moment per carbon atom $\langle M \rangle = (\langle M^A \rangle + \langle M^B \rangle)/2 = x/2$. That is, $\langle M \rangle$ scales linearly with the defect concentration x. It is easy to see that both results are in full accord with Lieb's theorem.

Experimental evidence of ferromagnetic ordering in irradiated graphite points to the evident conclusion that the concentration of defects in the two sublattices of individual graphene sheets in bulk graphite is not equal. Therefore, there must be a mechanism, which discriminates between the two sublattices. In bulk *ABA* graphite such a mechanism is provided by the stacking order of graphene layers, which breaks the equivalence of the two sublattices [80], as illustrated in Fig. 1.12a. Only local *ABA* stacking order of three adjacent graphene layers is required in order to break the sublattice equivalence in the middle sheet. For the case of hydrogen chemisorption defects, this mechanism can be demonstrated by means of first-principles calculations. Configuration with hydrogen chemisorbed on a carbon atom in sublattice *B* is 0.16 eV lower in energy than if hydrogen is chemisorbed on sublattice *A* (see Fig. 1.12b, c). Such energy difference is sufficient to produce a considerable difference in equilibrium concentration of hydrogen atoms chemisorbed in the two sublattices. The energy barrier for the hopping of hydrogen atoms is sufficiently small (∼1 eV) [81] to allow for thermally activated diffusion at temperatures that correspond to typical experimental conditions.

Similar sublattice discriminating mechanisms can not be excluded for other types of defects produced upon irradiation, for instance vacancies. Cross-sections for momentum transfer during knock-on collisions are probably very similar for both *A* and *B* carbon atoms in graphite. However, the stacking order is expected have strong effect on the recombination dynamics of interstitial and vacancy defects close to

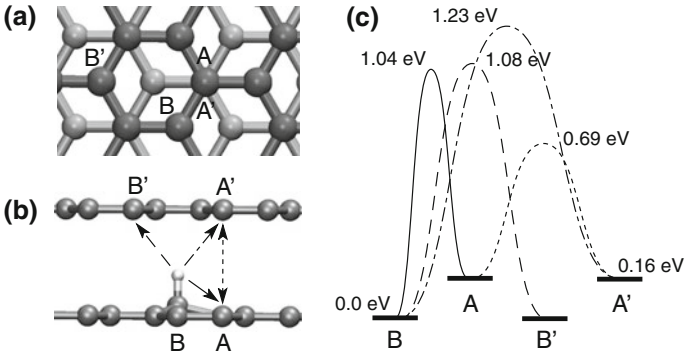

Fig. 1.12 **a** Crystalline lattice of *ABA* stacked graphite with inequivalent carbon atoms (*A* and *B*) indicated. **b** Scheme of diffusion pathways of chemisorbed hydrogen in graphite. **c** Schematic illustration of the potential energy surface for the in-plane diffusion of chemisorbed hydrogen in graphite. Relative energies of the local minima and transition states are indicated. Reproduced with permission from [80]

equilibrium conditions. It was also demonstrated by means of first-principles molecular dynamics simulations that instantaneous recombination of low-energy recoil atoms in graphite is significantly more probable for atoms belonging to the A sublattice [59]. That is, more vacancies in sublattice B are created assuming an equal number of knock-on collisions involving the atoms of both types. These results lead to a natural conclusion that the most probable physical picture of defect-induced magnetic order in irradiated graphite is ferrimagnetism. The magnetic moment in sublattice A is expected to be larger than the one induced in sublattice B.

The temperature dependence of magnetic ordering in defective graphene and graphite remains largely unaddressed. Similarly to the one-dimensional system, a two-dimensional system without magnetic anisotropy cannot develop long-range magnetic ordering at finite temperatures [40]. However, the presence of even a small magnetic anisotropy $d/a \sim 10^{-3}$ already results in very high transition temperatures [82, 83]. Weak magnetic exchange coupling between the individual graphene layers in graphite also leads to a strong effect on the magnetic transition temperature [84].

References

1. P.R. Wallace, Phys. Rev. **71**, 622 (1947)
2. A.H. Castro Neto, F. Guinea, N.M.R. Peres, K.S. Novoselov, A.K. Geim, Rev. Mod. Phys. **81**, 109 (2009)
3. S. Reich, J. Maultzsch, C. Thomsen, P. Ordejón, Phys. Rev. B **66**, 035412 (2002)
4. J.W. McClure, Phys. Rev. **108**, 612 (1957)
5. J.C. Slonczewski, P.R. Weiss, Phys. Rev. **109**, 272 (1958)
6. H. Feldner, Z.Y. Meng, A. Honecker, D. Cabra, S. Wessel, F.F. Assaad, Phys. Rev. B **81**, 115416 (2010)
7. M. Kinza, J. Ortloff, C. Honerkamp, Phys. Rev. B **82**, 155430 (2010)
8. H. Feldner, Z.Y. Meng, T.C. Lang, F.F. Assaad, S. Wessel, A. Honecker, Phys. Rev. Lett. **106**, 226401 (2011)
9. O.V. Yazyev, W.L. Wang, S. Meng, E. Kaxiras, Nano Lett. **8**, 766–766 (2008)
10. S. Kuroda, H. Bando, H. Shirakawa, Solid State Commun. **52**, 893–897 (1984)
11. H. Thomann, L.R. Dalton, M. Grabowski, T.C. Clarke, Phys. Rev. B **31**, 3141 (1985)
12. J. Fernandez-Rossier, J.J. Palacios, Phys. Rev. Lett. **99**, 177204 (2007)
13. L. Pisani, J.A. Chan, B. Montanari, N.M. Harrison, Phys. Rev. B **75**, 064418 (2007)
14. D. Gunlycke, D.A. Areshkin, J. Li, J.W. Mintmire, C.T. White, Nano Lett. **7**, 3608–3611 (2007)
15. T.O. Wehling, E. Sasioglu, C. Friedrich, A.I. Lichtenstein, M.I. Katsnelson, S. Blugel, Phys. Rev. Lett. **106**, 236805 (2011)
16. M. Schüler, M. Rösner, T.O. Wehling, A.I. Lichtenstein, M.I. Katsnelson, Phys. Rev. Lett. **111**, 036601 (2013)
17. S. Sorella, E. Tosatti, Europhys. Lett. **19**, 699 (1992)
18. S. Fajtlowicz, P.E. John, H. Sachs, Croat. Chem. Acta **78**, 195 (2005)
19. J.J. Palacios, J. Fernández-Rossier, L. Brey, Phys. Rev. B **77**, 195428 (2008)
20. E.H. Lieb, Phys. Rev. Lett. **62**, 1201 (1989)
21. W.L. Wang, O.V. Yazyev, S. Meng, E. Kaxiras, Phys. Rev. Lett. **102**, 157201 (2009)
22. E. Clar, *The Aromatic Sextet* (Wiley, London, 1972)
23. O.V. Yazyev, Acc. Chem. Res. **46**, 2319 (2013)
24. M. Ezawa, Phys. Rev. B **73**, 045432 (2006)
25. Y.-W. Son, M.L. Cohen, S.G. Louie, Phys. Rev. Lett. **97**, 216803 (2006)

26. V. Barone, O. Hod, G.E. Scuseria, Nano Lett. **6**, 2748 (2006)
27. L. Brey, H.A. Fertig, Phys. Rev. B **73**, 235411 (2006)
28. N.M.R. Peres, A.H. Castro Neto, F. Guinea, Phys. Rev. B **73**, 195411 (2006)
29. K. Nakada, M. Fujita, G. Dresselhaus, M.S. Dresselhaus, Phys. Rev. B **54**, 17954 (1996)
30. M. Fujita, K. Wakabayashi, K. Nakada, K. Kusakabe, J. Phys. Soc. Jpn. **65**, 1920 (1996)
31. J. Jung, T. Pereg-Barnea, A.H. MacDonald, Phys. Rev. Lett. **102**, 227205 (2009)
32. F. Muñoz-Rojas, J. Fernández-Rossier, J.J. Palacios, Phys. Rev. Lett. **102**, 136810 (2009)
33. K. Sawada, F. Ishii, M. Saito, S. Okada, T. Kawai, Nano Lett. **9**, 269 (2009)
34. J. Jung, A.H. MacDonald, Phys. Rev. B **79**, 235433 (2009)
35. A.R. Akhmerov, C.W.J. Beenakker, Phys. Rev. B **77**, 085423 (2008)
36. O.V. Yazyev, R.B. Capaz, S.G. Louie, Phys. Rev. B **84**, 115406 (2011)
37. M. Wimmer, A.R. Akhmerov, F. Guinea, Phys. Rev. B **82**, 045409 (2010)
38. T. Wassmann, A.P. Seitsonen, A.M. Saitta, M. Lazzeri, F. Mauri, Phys. Rev. Lett. **101**, 096402 (2008)
39. Y.-W. Son, M.L. Cohen, S.G. Louie, Nature (London) **444**, 347 (2006)
40. N.D. Mermin, H. Wagner, Phys. Rev. Lett. **17**, 1133 (1966)
41. O.V. Yazyev, M.I. Katsnelson, Phys. Rev. Lett. **100**, 047209 (2008)
42. G.S. Joyce, Phys. Rev. Lett. **19**, 581 (1967)
43. C. Tao, L. Jiao, O.V. Yazyev, Y.-C. Chen, J. Feng, X. Zhang, R.B. Capaz, J.M. Tour, A. Zettl, S.G. Louie et al., Nature Phys. **7**, 616 (2011)
44. X. Zhang, O.V. Yazyev, J. Feng, L. Xie, C. Tao, Y.-C. Chen, L. Jiao, Z. Pedramrazi, A. Zettl, S.G. Louie, H. Dai, M.F. Crommie, ACS Nano **7**, 198 (2012)
45. G.Z. Magda, X. Jin, I. Hagymasi, P. Vancso, Z. Osvath, P. Nemes-Incze, C. Hwang, L.P. Biro, L. Tapaszto, Nature **514**, 608 (2014)
46. L. Tapaszto, G. Dobrik, P. Lambin, L.P. Biro, Nature Nanotechnol. **3**, 397 (2008)
47. J. Cai, P. Ruffieux, R. Jaafar, M. Bieri, T. Braun, S. Blankenburg, M. Muoth, A.P. Seitsonen, M. Saleh, X. Feng, K. Mullen, R. Fasel, Nature **466**, 470 (2010)
48. P. Han, K. Akagi, F. Federici Canova, H. Mutoh, S. Shiraki, K. Iwaya, P.S. Weiss, N. Asao, T. Hitosugi, ACS Nano **8**, 9181 (2014)
49. P. Ruffieux, S. Wang, B. Yang, C. Sánchez-Sánchez, J. Liu, T. Dienel, L. Talirz, P. Shinde, C.A. Pignedoli, D. Passerone, T. Dumslaff, X. Feng, K. Müllen, R. Fasel, Nature **531**, 489–492 (2016)
50. J. Červenka, M.I. Katsnelson, C.F.J. Flipse, Nature Phys. **5**, 840 (2009)
51. O.V. Yazyev, Y.P. Chen, Nature Nanotechnol. **9**, 755 (2014)
52. W.T. Read, W. Shockley, Phys. Rev. **78**, 275 (1950)
53. M.A. Akhukov, A. Fasolino, Y.N. Gornostyrev, M.I. Katsnelson, Phys. Rev. B **85**, 115407 (2012)
54. D. Martínez-Martín, M. Jaafar, R. Pérez, J. Gómez-Herrero, A. Asenjo, Phys. Rev. Lett. **105**, 257203 (2010)
55. F. Banhart, Rep. Prog. Phys. **62**, 1181 (1999)
56. A.V. Krasheninnikov, F. Banhart, Nature Mater. **6**, 723 (2007)
57. V.H. Crespi, N.G. Chopra, M.L. Cohen, A. Zettl, S.G. Louie, Phys. Rev. B **54**, 5927 (1996)
58. B.W. Smith, D.E. Luzzi, J. Appl. Phys. **90**, 3509 (2001)
59. O.V. Yazyev, I. Tavernelli, U. Rothlisberger, L. Helm, Phys. Rev. B **75**, 115418 (2007)
60. A. Zobelli, A. Gloter, C.P. Ewels, G. Seifert, C. Colliex, Phys. Rev. B **75**, 245402 (2007)
61. P.O. Lehtinen, A.S. Foster, Y. Ma, A. Krasheninnikov, R.M. Nieminen, Phys. Rev. Lett. **93**, 187202 (2004)
62. C.P. Ewels, R.H. Telling, A.A. El-Barbary, M.I. Heggie, P.R. Briddon, Phys. Rev. Lett. **91**, 025505 (2003)
63. E. Kaxiras, K.C. Pandey, Phys. Rev. Lett. **61**, 2693 (1988)
64. A.J. Stone, D.J. Wales, Chem. Phys. Lett. **128**, 501 (1986)
65. V.M. Pereira, F. Guinea, J.M.B. Lopes dos Santos, N.M.R. Peres, A.H. Castro Neto, Phys. Rev. Lett. **96**, 036801 (2006)

66. T.O. Wehling, A.V. Balatsky, M.I. Katsnelson, A.I. Lichtenstein, K. Scharnberg, R. Wiesendanger, Phys. Rev. B **75**, 125425 (2007)
67. W.-M. Huang, J.-M. Tang, H.-H. Lin, Phys. Rev. B **80**, 121404 (2009)
68. F. Gargiulo, G. Autès, N. Virk, S. Barthel, M. Rösner, L.R.M. Toller, T.O. Wehling, O.V. Yazyev, Phys. Rev. Lett. **113**, 246601 (2014)
69. H.A. Mizes, J.S. Foster, Science **244**, 559 (1989)
70. K.F. Kelly, N.J. Halas, Surf. Sci. **416**, L1085 (1998)
71. P. Ruffieux, O. Gröning, P. Schwaller, L. Schlapbach, P. Gröning, Phys. Rev. Lett. **84**, 4910 (2000)
72. M.M. Ugeda, I. Brihuega, F. Guinea, J.M. Gómez-Rodríguez, Phys. Rev. Lett. **104**, 096804 (2010)
73. E.J. Duplock, M. Scheffler, P.J.D. Lindan, Phys. Rev. Lett. **92**, 225502 (2004)
74. O.V. Yazyev, L. Helm, Phys. Rev. B **75**, 125408 (2007)
75. D.W. Boukhvalov, M.I. Katsnelson, A.I. Lichtenstein, Phys. Rev. B **77**, 035427 (2008)
76. H. Kumazaki, D.S. Hirashima, J. Phys. Soc. Jpn. **76**, 064713 (2007)
77. P. Lehtinen, A.S. Foster, A. Ayuela, A. Krasheninnikov, K. Nordlund, R.M. Nieminen, Phys. Rev. Lett. **91**, 017202 (2003)
78. M.A.H. Vozmediano, M.P. López-Sancho, T. Stauber, F. Guinea, Phys. Rev. B **72**, 155121 (2005)
79. V.K. Dugaev, V.I. Litvinov, J. Barnas, Phys. Rev. B **74**, 224438 (2006)
80. O.V. Yazyev, Phys. Rev. Lett. **101**, 037203 (2008)
81. T.O. Wehling, M.I. Katsnelson, A.I. Lichtenstein, Phys. Rev. B **80**, 085428 (2009)
82. V.Y. Irkhin, A.A. Katanin, M.I. Katsnelson, Phys. Rev. B **60**, 1082 (1999)
83. J. Barzola-Quiquia, P. Esquinazi, M. Rothermel, D. Spemann, T. Butz, N. Garcia, Phys. Rev. B **76**, 161403 (2007)
84. L. Pisani, B. Montanari, N.M. Harrison, New J. Phys. **10**, 033002 (2008)

Chapter 2
Soft X-ray Dichroism Studies of Graphite

Hendrik Ohldag

Abstract With the recent advance of *spintronics*, an area of science and technology that proposes to use the spin of electrons to store and process information instead of their charge, carbon based nanomaterials have experienced increased interest. In particular the possibility to induce magnetic order through small modification of the structure has fascinated researchers for over a decade now. However, the origin of magnetism in carbon-based materials is still quite controversial from a scientific point of view. Unlike traditional magnetic materials, there are no d- or f-electrons present and contradictory experimental results have complicated theoretical work even further. To characterize the magnetic properties of an unknown sample one often uses conventional magnetometers that measure the total magnetic moment of a sample. However, these instruments do no allow to pin point the exact microscopic origin of the magnetism to rule out the presence of other magnetic impurities. For this reason it is crucial to study the magnetism of carbon based materials using element specific magnetic probes like e.g. x-ray absorption spectroscopy. In this chapter we will present an introduction to dichroism soft x-ray absorption spectroscopy and microscopy and the ability of this experimental approach to characterize the electronic, chemical and magnetic structure of a complex sample, element by element and in some cases even layer by layer.

2.1 Soft X-ray Spectroscopy and Microscopy

2.1.1 Evolution of Magnetic Devices and X-ray Technology

Magnetism is a fascinating field of physics because of its fundamental challenges as well as its technological relevance. Together with gravitation, magnetism is one of two basic physical phenomena that have been employed for the benefit of humankind

H. Ohldag (✉)
SLAC National Accelerator Laboratory,
Stanford Synchotron Radiation Lightsource, 2575 Sand Hill Road, MS 69,
Menlo Park, CA 94025, USA
e-mail: hohldag@slac.stanford.edu

P.D. Esquinazi (ed.), *Basic Physics of Functionalized Graphite*,
Springer Series in Materials Science 244, DOI 10.1007/978-3-319-39355-1_2

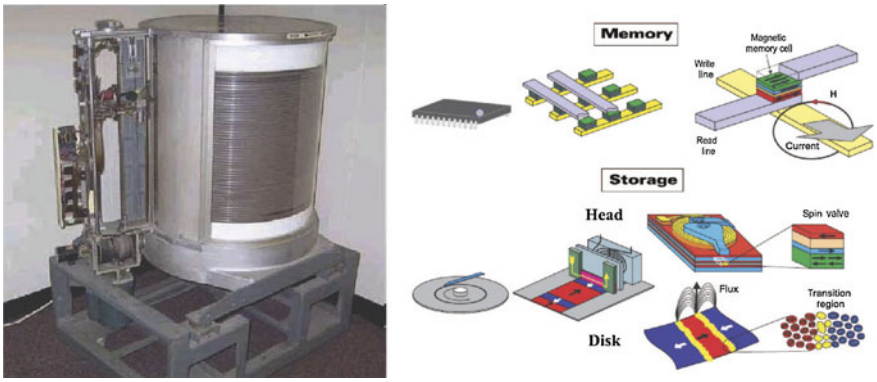

Fig. 2.1 *Left*: Picture of original IBM 350 hard disk capable of storing 5 Megabyte of data [1]. *Right*: Examples of different magnetic memory devices on the nanoscale as they are currently realized [2]. Miniaturization down to the nanoscale has been made possible by using complex materials, alloys and multilayers to control electronic and magnetic properties on an atomic or granular scale

for thousands of years. Considering the fact that magnetism is such a well studied phenomena it is remarkable that the field reached another turning point towards the end of the last millennium. Up to then it had been well established that elements like the 3d transition metals Iron, Cobalt and Nickel as well as some of the 4f materials and alloys thereof show ferromagnetic order at finite temperatures. The bulk properties of ferromagnetic materials appeared to be well understood and magnetic materials were routinely used in data storage, sensors, motors and generators to just name a few examples. In a way magnetism seemed to be heading towards becoming more relevant to engineers than physicists. However, this changed dramatically with the advent of nanotechnology and in particular with the discovery of the so called *giant magneto resistance*, independently by Albert Fert and Peter Grünberg who received the Nobel Prize for their discovery in 2007. Suddenly, the possibility to increase the functionality and decrease the size of magnetic devices by using complex material combination and multilayers instead of conventional ones opened up new avenues to take magnetism into the 21st century. Figure 2.1 is shown to demonstrate this development. In 1956 the IBM 305 RAMAC (Random Access Method of Accounting and Control) computer system was sold to the first US customers. While the central processing unit still used traditional vacuum tubes, the revolutionary new feature was that the system was equipped with a movable HEAD hard drive system. The drive was capable of storing 5 Megabytes of data on 24 disks each 610 mm in diameter. Each bit required an area of 0.1 mm^2 or 10 kbit per in^2. Modern hard drives and devices in contrast allow to store 1 Terabit per in^2, corresponding to a bit diameter of 25 nm. This increase in storage density of 10^8, has been made possible by engineering new materials with properties and nanosized shapes that are much more favorable for magnetic data storage indexmagnetic storage and processing. For example, instead of using simple magnetic alloys of Fe and Ni as for the RAMAC drive, we now use precisely designed multilayers of ferromagnetic, antiferromagnetic and non-magnetic alloys.

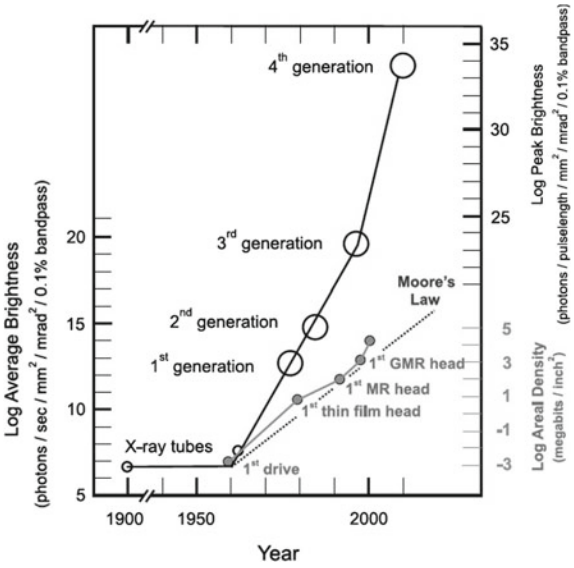

Fig. 2.2 Since the discovery of x-rays in the late 1800s x-ray sources have made significant advances. Conventional x-ray tubes were used in the early stages, while electron accelerators have been used for research purposes since the 1970s. Accelerator-based sources have been refined and advanced over the last decades. Today free electron lasers can deliver x-ray beams with unprecedented intensity into micron sized spots. For comparison the increasing storage density of hard drive devices is plotted as well indicating that advances in this field require probes that can address smaller and smaller length scales [2]

To further fundamentally explore the field of carbon based magnetism, a joint effort between advanced synthesis of magnetic systems, state-of-the-art theoretical and computational approaches is needed. Such an approach will provide guidance for the design of new magnetic materials and requires a fundamental scientific understanding obtained by cutting edge analytic tools able to address the nanoscale. Figure 2.2 shows how x-ray sources have become more and more powerful over the past few decades. From simple x-ray tubes to parasitic use electron storage rings in the early 1970 s all the way to modern free electron lasers the brightness (intensity per area) of x-ray sources has been increased by 25 orders (!) of magnitude. While the acquisition of a simple x-ray absorption spectrum of a bulk sample could take hours in 1970, it is now possible to acquire the scattering pattern of a single protein in a few femtoseconds. At the same time, magnetic devices have become smaller and often only a limited number of atoms determine their behavior. This is in particular true, since interfaces and surfaces started to play an important role. Polarization dependent x-ray absorption spectroscopy and microscopy have been shown to be an indispensable tool to understand the science behind the miniaturization of data storage devices. In the next section we will describe in more detail how polarization dependent x-ray spectroscopy can be used to address the magnetic properties on an atomic scale. In the following we will give a brief introduction into the subject.

Magneto-optical effects, i.e. the interaction of light with magnetic materials is well known since the mid 1800s, when Faraday [3] and Kerr [4] discovered that the polarization state of an electromagnetic wave will be altered if reflected from or passed through a magnetic medium. The Faraday and the Kerr effect have since been used extensively for the characterization of magnetic properties, such as measuring the magnetic hysteresis loop in a Magneto Optical Kerr (MOKE) setup or the observation of magnetic domain patterns with the Faraday effect using conventional optical microscopy [5]. Both effects manifests themselves in small changes of the optical constants by 0.1% or less. However, in view of advanced nanoscale magnetic materials, optical techniques face severe limitations. The wavelength of light, which is in the sub-micrometer regime, can not provide nanoscale information and the optical transitions occur in the conducting bands, which are not element-specific and can therefore not provide fundamental quantitative magnetic information.

Probing magnetic materials with x-rays, in particular with polarized soft x-rays, overcomes the limitations of optical techniques. The interaction of polarized soft x-rays with magnetic materials gives rise to x-ray magnetic dichroism effects, that can be seen as x-ray counterparts of magneto-optical effects. However in contrast to magneto-optical effects in the visible spectrum x-ray dichroism effects are generally large, which makes their detection rather easy. Also, since the wavelength of soft x-rays is of the order of a few nanometer, x-ray microscopy techniques naturally provide access to the nanoscale. The following list summarizes the features offered by polarized soft x-rays. Medical x-rays as well as x-ray images of magnetic devices shown in Fig. 2.3 are shown to demonstrate the capabilities of x-ray microscopy.

1. Soft x-rays are electromagnetic radiation with an energy between about 200 eV and about 2 keV, which matches the element-specific inner core binding energies of 3d, 4d, 4f, and 5d elements. Therefore, element-specific information can be obtained for these elements, which feature some of the most prominent elements

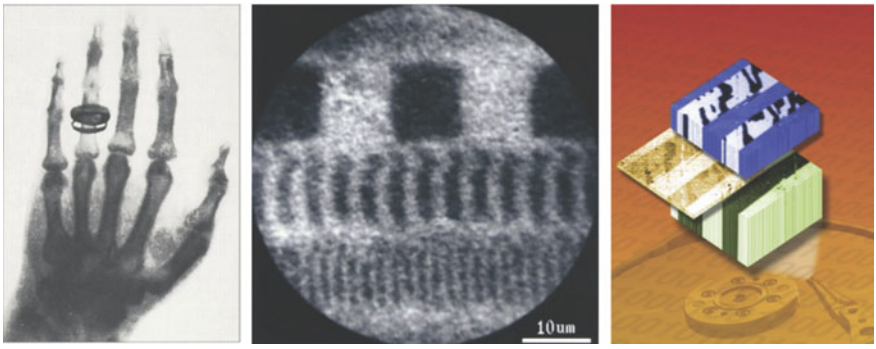

Fig. 2.3 Evolution of x-ray microscopy. The first x-ray image taken by Conrad Röntgen in 1895. Almost 100 years later polarized x-ray microscopy [6] allowed to observe magnetic bits on a real hard drive media. Only ten years later [7] the rapid increase in x-ray brightness made it possible to reveal the magnetic structure in a ferromagnetic/antiferromagnetic Co/NiO bilayer and the interface in between consisting of a mixed Co/Ni oxide

in magnetism research. The spectral resolution of state-of-the-art x-ray monochromators enables fingerprinting the (spin-resolved) electronic structure.
2. The wavelength of soft x-rays is in the nanometer regime, which inherently gives access to the nanoscale.
3. The polarization of the x-rays can be tuned so that ferro-, ferri-, and antiferromagnetic materials can be probed.

2.1.2 Soft X-ray Absorption Spectroscopy

Since we will only discuss experiments involving x-ray *absorption* spectroscopy (XAS) in the later part of this chapter we will now focus on the physics behind the x-ray absorption process. Magnetic x-ray dichroism can also be observed in x-ray reflection, scattering or incoherent as well as coherent diffraction, however this is outside the scope of this chapter. For an introduction into these areas the reader is referred to the appropriate chapters in [2].

Experimentally, the x-ray absorption cross section as a function of photon energy E can be measured e.g. in a transmission experiment. Independent of the photon energy the transmitted photon intensity $I_1(E)$ after penetrating a thickness t of the sample is related to the incoming photon intensity $I_0(E)$ by the Lambert–Beer rule,

$$I_1(E) = I_0(E)e^{-\mu(E)\cdot t}. \tag{2.1}$$

Here, $\mu(E)$ is the element specific absorption coefficient. To calculate $\mu(E)$ one can employ the so called *Fermi's Golden Rule*. An incoming electromagnetic wave polarized along the z-direction will lead to an electronic dipole transition from the initial state $|i\rangle$ to the final state $\langle f|$.

$$\Gamma_{i\to f} \approx \frac{2\pi}{\hbar} |\langle f|z|i\rangle|^2 \rho(E) \tag{2.2}$$

Some fundamental but important properties of the x-ray absorption cross section can be extracted from this simple equation.

1. A transition will occur if the energy of the incoming photon, matches the energy difference between an occupied core level and unoccupied valence state. One factor that determines the strength of the transition is given by the overlap of initial and final state. Since the initial state is a core level, transitions that involve a final state with significant probability closer to the nucleus are strong transitions.
2. $\rho(E)$ is the density of unoccupied states above the Fermi energy in a solid. That means another factor that determines the strength of the line is the availability of empty states. The line shape of the x-ray absorption spectrum will mimic the density of states above the Fermi level. This is illustrated on the right hand side of Fig. 2.4.

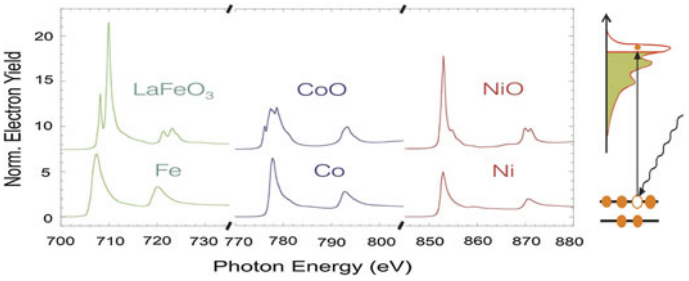

Fig. 2.4 Elemental and Chemical Sensitivity of Soft X-rays. The *left hand side* shows absorption spectra of Fe, Co, Ni and some oxides. The panel of the *right* shows a simple picture of the transition of a core level electron to a final state. Figure taken from [2]

3. X-ray absorption is capable of probing the symmetry of the electronic structure. The dipole operator exhibits axial symmetry (along z in this example). If the electronic structure is different along different, orthogonal directions of the sample the x-ray absorption cross section will be as well. This directional or polarization dependence is referred to as dichroism.
4. The x-ray absorption line is referred to as K (when the initial state is a $1s$ electrons), L (for the $2s$, p electrons), or M (for the $3s$, p, d electrons) x-ray absorption edges.

More general, one finds that the x-ray absorption cross section is a direct measure of the number of empty states of unoccupied the electronic structure. For example, for a $2p$ to $3d$, or L-transition, the integrated intensity of the x-ray absorption cross section is proportional to the number of empty d-states, which is why the Fe L-edge appears stronger than the Co L-edge or the Ni L-edge. This effect is also sometimes referred to as white line sum rule (see e.g. [2]), and it has to be considered, when spectra are analyzed quantitatively to determine relative concentrations. The white line sum rule states that the x-ray absorption cross section is proportional to the isotropic (not spin resolved) density of states where polarization or symmetry effects do not play a role. A direct consequence of this is that it allows to easily distinguish between a metal and an oxide as shown in Fig. 2.4. While the available d-states in a metal are degenerate the absorption line appears as a single peak, since all available states are centered around the Fermi energy. Hybridization of metal d-electrons and oxygen p and s electrons the resulting crystal fields will lift that degeneracy and therefore the available empty states will be spread out and grouped over a larger energy range. The resulting, spectrum, unique for each compound, can be used to identify different chemical states of the sample [8] as shown in Fig. 2.4.

In combination with the uniaxial nature of the dipole operator this also implies that one can easily detect symmetries of the electronic structure. For example, the fact that the electronic structure of a layered oxide is highly asymmetric leads to a strong L-resonance when the x-rays are polarized perpendicular to the plane, while the line vanishes otherwise [9]. Generally speaking, any deviation of the electronic structure from perfect cubic symmetry will lead to a similar asymmetry of the x-ray

absorption cross section (optical tensor), that can be detected by varying the linear or circular polarization of the incoming x-rays.

Finally we note that typical L-edge spectra consist of two main peaks, caused by the spin-orbit (LS) which leads to a splitting of e.g. the p-electron levels into a $p_{3/2}$, i.e. $(L + S)$ and a $p_{1/2}$, i.e. $(L - S)$ state, corresponding to the L_3 and L_2 absorption edges. This splitting is absent for K-edges. The spin-orbit splitting will be of particular importance for the interpretation of x-ray magnetic dichroism effects, as we will see later. Typical examples of experimental $L_{3,2}$-edge XAS spectra are shown in the left panel of Fig. 2.4. With x-ray monochromators providing an energy resolution of typically better than 0.1 eV, both the spin-orbit coupled edges separated by several eV, as well as absorption resonances of Fe, Co and Ni, which are separated by more than 50 eV can be easily distinguished.

2.1.2.1 Detection Approaches: Surface Versus Bulk

There are essentially two ways to detect the soft x-ray absorption cross section. One can either detect the transmitted photons or utilize secondary probes, such as electrons and fluorescence photons, which are generated in the x-ray absorption process as shown in Fig. 2.5.

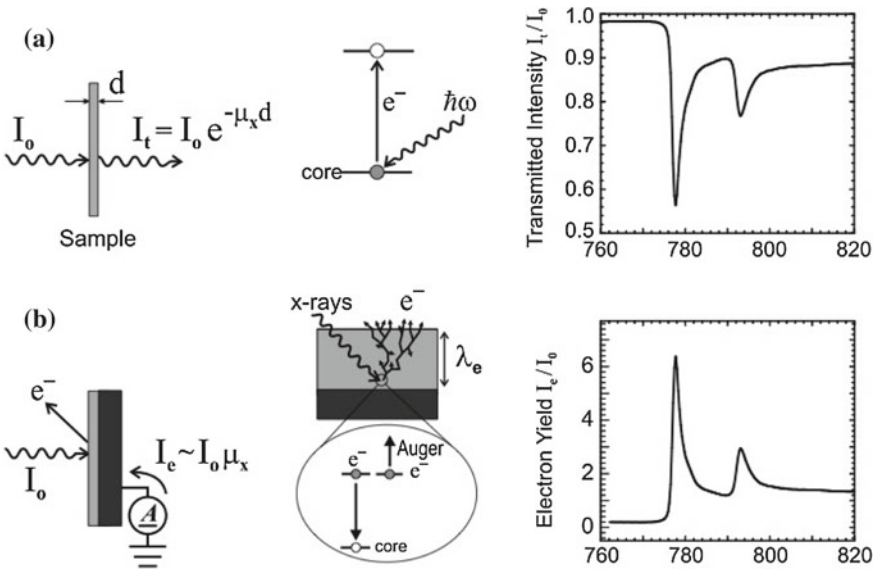

Fig. 2.5 Different approaches to measure x-ray absorption. *Top row*: Transmission through the sample is measured using appropriate photon counting devices upstream of the samples. Absorption resonances appear as strong reduction in the transmitted intensity. *Bottom row*: Collecting the (secondary) electron yield from the surface of the sample provides a surface sensitive approach. Absorption edges are characterized by an increase in electron yield

In the first case one directly records the transmitted intensity through the sample and calculates the absorption cross section using the Lambert–Beer rule (2.1). Comparing the transmitted intensity to the incoming x-ray intensity allows for a direct quantitative measurement of the x-ray optical properties of the sample. As typical penetration depths of soft x-rays are about 100 nm, XAS measured in transmission mode requires x-ray transparent specimens. X-ray detectors located downstream of the sample are used in thin films that are deposited on x-ray transparent substrates, such as Si_3N_4, which are commonly used in transmission electron microscopy and readily available. In cases, where thin films are used in conjunction with substrates where the transmitted x-ray intensity is converted into visible light (luminescence) [10] regular photo diodes can be used.

The indirect way to detect the x-ray absorption cross section is to collect the electrons or fluorescence photons emitted from the sample. Within a few attoseconds after the initial photo excitation process there is an emission of Auger electrons or fluorescence photons. The latter can be detected using appropriate photo diodes or photo multiplier. However, the fluorescence yield is strongly affected by saturation effects (self-absorption) if the magnetic film is thicker than a few nm, since the penetration depth and hence the probing volume changes and is reduced in the same way as the fluorescence yield increases. For this reason the fluorescence detection method is typically used for diluted samples e.g. magnetic semiconductors [11] or to access the magnetism of metal ligand in biological molecules [12]. In addition, the fluorescence yield is very weak for soft x-ray energies since the Auger channel dominates the recombination process. Each emitted Auger electron that is produced by x-ray absorption processes within several tens of nanometers from the surface will lead to the generation of hundreds of low energy secondary electrons, because the mean free path of the initial Auger electron is only a few nm. However, since also the mean free path of the secondary electrons is limited the vast majority of the emitted electrons will originate from the first ten nanometer of the sample, providing the high surface sensitivity using electron yield detection. In contrast to fluorescence, which is a rather bulk sensitive detection method, sample current measurements are surface sensitive, but are limited to electrically conducting samples.

2.1.2.2 Soft X-ray Dichroism

Using polarized x-rays, XAS becomes sensitive to study the magnetic properties of materials. Depending on the polarization, i.e. linear or circular polarization, two x-ray magnetic dichroism effects can be distinguished (2.6).

- **X-ray magnetic circular dichroism (XMCD)** uses circularly polarized x-rays and is used to characterize ferro- and ferrimagnetic materials, i.e. magnetic materials with a net magnetic moment. Since time reversal symmetry is broken in a magnetic material, a dichroism effect is observed using circular polarized x-rays, which exhibit a defined direction.

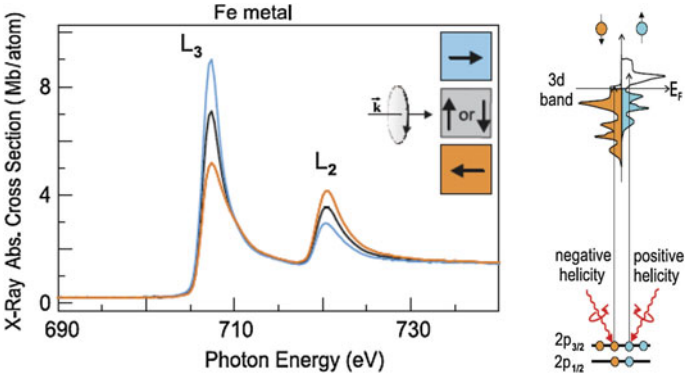

Fig. 2.6 Soft X-ray Magnetic Dichroism. Circular polarized x-rays preferably excite electrons with a particular spin as shown on the right hand side. In a magnetic material a different number of spin up and spin down electrons is observed at the Fermi level, which is why *left* and *right* circular polarized x-rays "see" a different number of final states. For this reason the line strength depends on the relative orientation of spin, orbital and x-ray angular momentum as shown for the example of Iron on the *left hand side*

- **X-ray magnetic linear dichroism (XMLD)** uses linearly polarized x-rays and allows in particular investigating antiferromagnetic materials with no net magnetic moment, but where the electronic structure exhibits a uniaxial symmetry.

The **XMCD** effect describes the fact, that the absorption of circularly polarized x-rays depends on the relative orientation of the helicity of the x-rays $\boldsymbol{\sigma}$ and the direction of the magnetization of the ferro-/ferrimagnetic sample **M**, i.e. an either parallel or antiparallel orientation projected onto the photon propagation direction,

$$\text{XMCD} \sim \boldsymbol{\sigma} \cdot \langle \mathbf{M} \rangle . \tag{2.3}$$

Experimentally, XMCD contrast can be obtained by

- modulation of circular polarization (left and right) while keeping the magnetization direction constant,
- reversing the direction of the magnetization through application of an external magnetic field for fixed polarization, and
- utilizing the reversed spin-orbit coupling at corresponding absorption edges, e.g. $L_{3,2}$ edges at fixed polarization and magnetization.

Similarly, the **XMLD** effect describes the difference in absorption of linearly polarized x-rays, where the x-ray polarization (**E**) is parallel and perpendicular to the magnetization axis. XMLD is generally assumed to be proportional to the square of the magnetization

$$\text{XMLD} \sim \mathbf{E} \cdot \langle \mathbf{M}^2 \rangle \tag{2.4}$$

and therefore, magnetic moments in both ferromagnetic and antiferromagnetic materials contribute to the XMLD signal. However, as in itinerant metallic ferromagnets the XMLD signal is much smaller than the corresponding XMCD effect, XMLD is primarily used to study antiferromagnetic systems, whereas XMCD is the dominant effect in ferro- and ferrimagnetic materials.

Figure 2.6 shows a typical experimental XMCD spectrum obtained at the $L_{3,2}$ edges in a metallic Fe thin film. Large changes in the absorption $\mu(E)$ occur at the resonant energies for the two opposite orientations between the magnetization of the sample and the helicity of the x-rays. The difference of the two absorption profiles is referred to as the XMCD signal. A pronounced feature of XMCD is the sign reversal between the L_3 and the L_2 edge. It can be understood within the physical origin of XMCD based on a simple two step model.

We consider the XMCD effect at the L edges in a $3d$ metal, such as Fe, Co, Ni. As stated above, the spin-orbit coupling splits the $2p$ electronic levels into a $j = 3/2$ and a $j = 1/2$ level, with spin and orbit being parallel in the former and antiparallel in the latter case, and which correspond to the L_3 and L_2 absorption edges, respectively. In the first step, due to angular momentum conservation and spin-orbit coupling the absorption of a circularly polarized photon with its helicity parallel (antiparallel) to the $2p$ orbital moment yields a photoelectron with its spin pointing down (up). The second step is the dipolar transition of the spin polarized photo electron into an unoccupied electronic state of the valence band above the Fermi level. As the exchange interactions shifts the majority valence band relative to the minority valence band, there is a difference of spin up and spin down holes, which the photoelectron can occupy. Following Fermi's Golden Rule (2.2) coefficients, therefore has a negative peak at the L_3 edge and, due to the reversed LS coupling a positive peak at the L_2 edge (see Fig. 2.6). As the difference in spin-up and spin-down density of states determines the local spin moment, XMCD can directly probe the spin and orbital magnetic moments separately.

The theoretical foundation for this important feature of XMCD are the magneto-optical sum rules, which were developed by Thole [13] and Carra [14]. As can be seen from Fig. 2.6 the XMCD spectrum can be split into a contribution from the L_3 resonance and one from the L_2 resonance, where the respective areas under the experimental XMCD spectrum are labelled as A_3 and A_2. The spin moment s_L can then be obtained in its general form from

$$m_S = -3n_h\mu_B(A_3 - 2A_2) + m_T \tag{2.5}$$

with n_h the number of holes and m_T taking into account an anisotropic spin density through a magnetic dipole operator. Similarly, the orbital moment m_L can be derived from

$$m_L = -2n_h\mu_B(A_3 + A_2). \tag{2.6}$$

The fact, that XMCD spectroscopy can directly and quantitatively determine local and element-specific magnetic moments [15], is one of its most important features.

2.1.3 Soft X-ray Absorption Microscopy

2.1.3.1 Instruments—Photon Out Versus Electron Out

Optical microscopies are diffraction limited in spatial resolution to the sub-micrometer regime, while the nm wavelength of soft x-rays opens the door to nanoscale spatial resolution. The major advantage of x-ray based microscopy techniques compared to magneto-optical microscopies is its elemental sensitivity and quantitative information, originating in the X-ray dichroism effect as magnetic contrast mechanism. Soon after the x-ray magnetic dichroism effects had been established [16–18], it became clear that using those effects as magnetic contrast mechanism enables magnetic x-ray microscopies providing a unique combination of high spatial and temporal resolution, inherent element-specificity and quantitative magnetic information as described in the previous section. In the following we will describe three different x-microscopy techniques, which are able of using x-ray magnetic dichroism effects as a a contrast mechanism. They are shown in Fig. 2.7.

Historically, the first x-ray magnetic microscopy images were reported using an X-ray photo emission electron microscope (X-PEEM) by Stöhr et al. [19]. There, secondary electrons, which are generated in the x-ray absorption process propagate to the surface, where they escape and are being detected by electron optics.

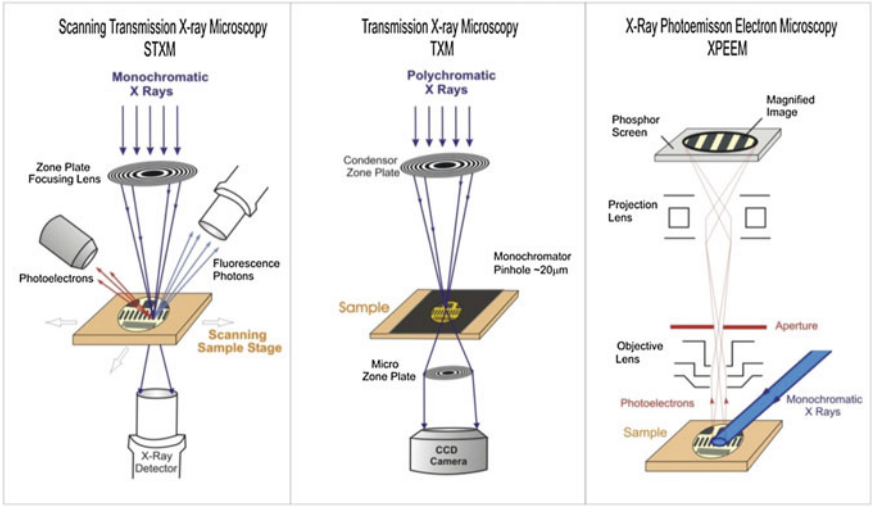

Fig. 2.7 Three different types of x-ray microscope. From *right* to *left*. Photoemission Electron Microscope (PEEM) images the spatial variation of the electron yield excited by an incoming unfocused x-ray beam. Conventional electron optics generate a magnified image on a screen. Transmission X-ray Microscope (TXM), operates very much like a conventional optical microscope but employs Fresnel zoneplates as lenses. Scanning Transmission X-rat Microscope (STXM) is a scanning probe microscope using a small x-ray spot as probe and a simple photo diode as detector

X-PEEM is a so-called *photon-in electron-out* technique [20]. Relying on classic electron optics, commercial X-PEEM systems were available early on and have been installed at nearly every synchrotron facility worldwide. Today, state-of-the-art X-PEEM systems use aberration corrections to push the spatial resolution into the nanometer regime and to increase the throughput such as the PEEM-3 instrument at the Advanced Light Source in Berkeley CA [21]. The probing depth of X-PEEM is limited to the escape depth of electrons. As this is a few nm only, X-PEEM is rather surface sensitive [22, 23].

Although X-rays have been discovered already in 1895, x-ray optics, which are needed as the refractive index of normal optics is close to unity, were not available until the mid 1980s, when the advent of electron beam lithography enabled the development of circular gratings, so-called Fresnel zone plate (FZP) lenses. Those FZPs are now commonly used as focusing x-ray optics in soft x-ray microscopes. In 1996, the first image of a magnetic domains at 59 nm spatial resolution, recorded with the full-field transmission soft x-ray microscope (TXM) at BESSY I in Berlin, was reported [24]. A few years later an interference-controlled scanning transmission x-ray microscope was developed [25]. Both the zone plate based x-ray microscopes, TXM and STXM, as well as X-PEEM, which provide real-space images of magnetic structures and their dynamical behavior, have become workhorses to the magnetic imaging communities and can be found at nearly all synchrotron laboratories worldwide. In this chapter we will discuss results obtained using STXM and PEEM microscopy. While TXM microscopy typically provide higher spatial resolution, about 10 nm compared to 20 nm, PEEM and STXM microscopy are better suited for studies that require high spectral resolution as it was the case for the examples presented here.

2.1.3.2 Carbon Based Nanostructures in X-ray Microscopy: An Application

Before we discuss some examples of x-ray microscopy and spectroscopy of carbon based materials with particular focus on their magnetic properties, we would like to show a fascinating example of how "carbon" can be used to boost the performance of an x-ray microscope. Figure 2.8 shows several PEEM images of a so called *patterned media* device.[1] These are magnetic films that are lithographically patterned so that magnetic switching occurs only in pre-defined regions. In this case a lithography process was used to define 25 by 25 nm islands, separated by 35 nm grooves. Images on the right hand side are taken of the bare sample, while the surface was covered with a self assembled monolayer of diamondoids [26] for the images shown on the left hand side of Fig. 2.8. Magnetic PEEM images are obtained by tuning the photon energy to an absorption resonance, in this case the Co L_3 resonance and acquiring two images with opposite x-ray helicity. The difference between these two images, the XMCD image, shows only magnetic contrast as we have seen in Fig. 2.6, while the sum or

[1] These samples have been provided by Olav Hellwig, Hitachi Global Storage Technology.

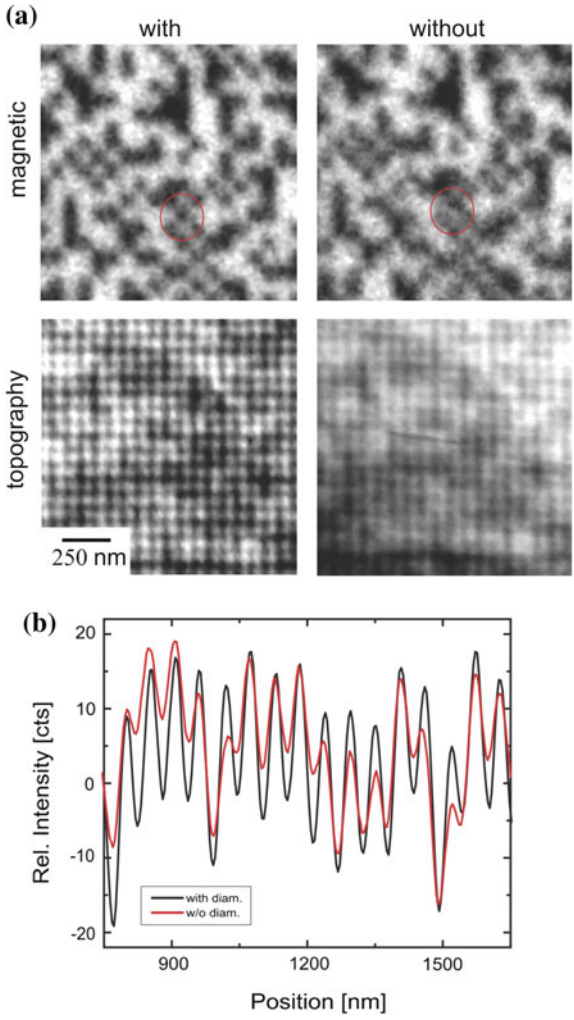

Fig. 2.8 Functionalized Carbon in Electron Microscopy. A self assembled monolayer of diamondoids improves the resolution of magnetic PEEM. See the text for a detailed explanation [26]

average contains information about variation of topography, concentration or in the case of PEEM the work function. That means that the magnetization in black squares is pointing in one direction, e.g. up, while it is pointing in the opposite direction in the white areas. The lower panel shows linescans taken from the topography images, with (black) and without (red) diamondoids . The images were taken from the same spot of the sample under identical imaging conditions. So, why is it that the diamondoid layer improves the resolution of the PEEM?

As we discussed earlier, PEEM microscopy is based on an electrostatic lens system that is used to image the lateral distribution of secondary electrons [27]. It is important to realize that the emitted secondary electrons exhibit a very large energy spread, so that without any additional filtering the resolution is limited by chro-

matic aberrations. However, the application of filters will reduce the image intensity significantly, so that ultimately, even with filtering, the resolution is limited to about 25 nm. This is confirmed in the PEEM images shown in Fig. 2.8. Without diamondoid layer the 35 nm grooves are well visible while the 25 nm islands are at the limit of the resolution. However, once the surface is covered with diamondoids the resolution improves dramatically and the islands are clearly visible int he topography images and the magnetic images appear sharper as well. The reason is that the electrons emitted from the magnetic layers are now recaptured in the diamondoid layer, because diamondoids have a significant *negative electron affinity*. In addition diamondoids exhibit a strong peak in their unoccupied valence states. That means that the captured electrons after thermalization can be re-emitted with a very small energy distribution. This particular feature of acting as a monochromator in electron emission (see [26] and references therein), makes diamondoids very fascinating tools for the development of new cathode materials. Here, it presents a simple, disruptive approach to improve the spatial resolution of a microscope without actually changing the optical column of the microscope.

2.2 X-ray Spectromicroscopy of Magnetic Graphite

In this section we will give several examples of how x-ray microscopy, x-ray spectromicroscopy and high resolution XMCD spectroscopy have provided unique insight into the origin of magnetism in carbon and the relevant physical processes. We will start with simple magnetic domain images of proton irradiated carbon that show that no magnetic impurities are needed to establish ferromagnetic order in carbon. Closer inspection of the spectroscopic signatures that are responsible for forming the image contrast will then reveal, which electronic states are responsible for the magnetic order and how these states are possibly formed during irradiation.

2.2.1 Elemental Probe of Magnetism

In 2003 Esquinazi and co-workers were able to demonstrate that pure graphite can be made magnetic by simply introducing defects using proton bombardment [28]. The possibility of magnetic order in metal-free carbon is fascinating from a fundamental as well as from a technological point of view. As mentioned before, classical magnetism is observed in elements with d and f electrons, while one would not expect to observe long range magnetic order in a light element with only s and p electrons. Also, due to the "renaissance" of carbon based materials over the past two decades thanks to the development of reproducible methods to fabricate carbon nanotubes, bucky balls and graphene, the technological implication of making these devices magnetic would be far reaching.

There have been numerous reports of ferromagnetism in virgin graphite [29] as well as graphite treated by ion bombardment [28, 30, 31] and carbon nanoparticles [32–34] in recent years. It could be shown that the observed magnetism in proton irradiated carbon is not caused by magnetic impurities but is related to the π-states of carbon [35] as we will discuss later. However, the question how it is possible to establish ferromagnetic order in carbon-based systems without any metallic magnetic or non-magnetic elements still remains in general unanswered. Several theoretical studies in the past have suggested that absorption of hydrogen at the edges of [36] or on [37] graphene sheets as well as hydrogen chemisorption in graphite [38] may lead to the formation of a spin polarized band at the Fermi level and robust ferromagnetic order. While it is obvious that defects or ad-atoms play a central role, the origin of the magnetic moment observed in graphite [29] is still under discussion, see Chap. 1. Another intriguing question arises from the observation that the apparent magnetization (calculated taking the whole sample mass) detected in magnetic graphite is typically many orders of magnitude smaller than the one found for “classical"magnets like the 3*d*-transition metals. Apart from the fact that this makes it challenging to obtain a reliable and detailed understanding of the relevant processes that cause the ferromagnetic order in graphite [39], it also leads to the question of how such a system exhibiting a small magnetization and presumably negligible magnetic exchange coupling can be a ferromagnet at room temperature. The explanation of such extremely small magnetization resides in the uncertainty of the total ferromagnetic mass in the measured samples and in the role of non-metallic defects. Recent studies on proton- [30] and carbon-irradiated [31] graphite managed to provide maximum limits for the induced ferromagnetic mass allowing to estimate magnetization values exceeding 5 emu/g. Although important evidence has been obtained that supports the role of vacancies in the graphite ferromagnetism [40], the very origin and extent of surface magnetism [41] remains open [39].

Any study that addresses the magnetism of carbon has to address the purity of the samples or the presence of magnetic contaminants first. Again, the element specificity of x-ray absorption is crucial. The upper panel in Fig. 2.9 shows conventional laboratory based scanning probe microscopy images of a proton irradiated spot on a 200 nm thick graphite film. Atomic force microscopy is sensitive to the topography of the samples, showing that at the point of impact material has been removed. In addition a ring of magnetic material has formed around the irradiated spot as evident from the magnetic force microscopy image on the right. The sample was then transported to a scanning transmission x-ray microscope to determine if the impact area shows any presence of ferromagnetic 3*d* metals like Fe, Co or Ni. However, none of these materials could be observed within the detection limit of the setups which is around 100 parts per million.

Local x-ray absorption spectra acquired in this area at the carbon K-edge using linear polarization also showed that the number of occupied electronic states is reduced in the area around the point of impact, essentially indicating that this area is less metallic or the p-electrons are more localized [42] as we will discuss in detail in the next section. Evidently, the proton irradiation introduces defects that help to localize p-electrons, which in turn leads to the existence of long range ferromagnetic order of

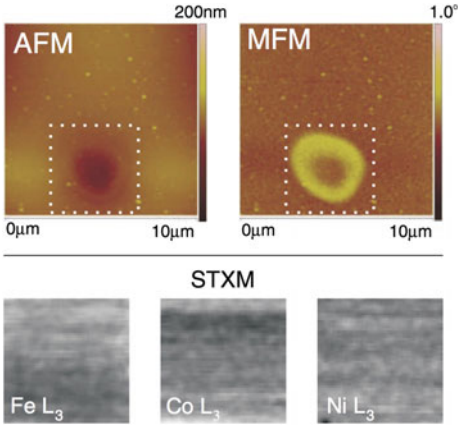

Fig. 2.9 The *top row* compares atomic force and magnetic for microscopy images of a proton irradiated spot on graphite. The *bottom row* shows x-ray microscopy images of the same area obtained at the Fe-, Co- and Ni-L absorption resonance [35]

the slightly distorted graphite lattice. However, if the distortion becomes too large, like in the center of the impact area, the ferromagnetic order is destroyed and one observes an increase in delocalization of the *p*-electrons again. The fact that ferromagnetism exists only in a very small window of defect concentration explains why the observed magnetization values are small since the optimum doping level is generally not realized throughout a macroscopic sample.

However, stable ferromagnetic order at room temperature may be realized in small regions or nanostructures as it is the case in this example. The diameter of the magnetic ring is about 3 μm and its width is less than 1 μm. In general it will be very difficult to detect the magnetic moment using macroscopic probes, which is why conventional approaches usually require a sample with thousands of irradiated spots. On the other hand typical scanning probes like magnetic force microscopy are sensitive enough to detect the magnetic stray field originating from such a spot as seen in Fig. 2.9, however without element specificity it remains unclear what the origin of the magnetic signal is. Using XMCD as a contrast mechanism in an x-ray microscope finally allow the successful observation of an element specific magnetic signal originating only from carbon atoms in the sample as shown in Fig. 2.10. Again the magnetic ring can be identified, this time as a result of the difference between two images of the spot obtained with circular polarized x-rays. The image contrast

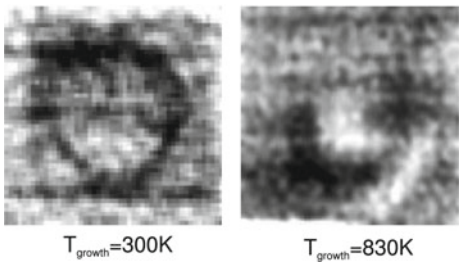

Fig. 2.10 XMCD images of proton irradiated carbon prepared at different temperatures. Higher preparation temperature lead to a more robust magnetic order that exists over a wider range of irradiation fluences and even the formation of magnetic domains [35]

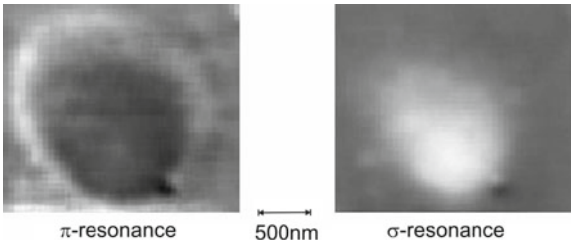

Fig. 2.11 STXM images of the same irradiated spot as discussed previously. Images were obtained by averaging over two images acquired at a resonance with opposite helicity. The images were also normalized to an image acquired off resonance to account for small thickness variations as seen by AFM similar to Fig. 2.9

is a direct measure of the magnetic moment aligned with the polarization vector of the x-rays. In [35] the authors conclude that the magnetic order is caused by an atomic magnetic moment of the order of $0.1 \ldots 0.5\,\mu_B$, which is consistent with the full magnetic moment of a single carbon atom. This means that indeed the full magnetization can be obtained in small structures and furthermore explains why the ordering temperature is above room temperature for these materials (Fig. 2.11).

2.2.2 Magnetic Order and Electronic Structure

In Sect. 2.1.3.2 we discussed how one can compare difference and sum images in x-ray microscopy to obtain information about the magnetic order as well as topography and concentration. In the proton irradiated samples the typography does not play a role since film roughness ($\approx$1 nm) is small compared to the total thickness of the sample (200 nm), at least on the scale of the resolution of the microscope (25 nm). Also the samples are pure carbon, so we would not expect any variation of the concentration. However, if we evaluate the sum images acquired at the π and σ resonance we find a variation of available empty π and σ states in the irradiated area. The grey scale represent the transmitted x-ray intensity through the sample. Bright areas mean that the transmission is high or absorption is low. For a given resonance the absorption is directly proportional to the number of available final states in this case π or σ, as described in (2.2). This means the bright areas in the images represent areas in the sample with a reduced number of empty states π or σ states, or vice versa an increase in the (occupied) π or σ electron density. What we can clearly deduce from these images is that the proton irradiation leads to a shift of π-type electron density from the center of the area towards the magnetic ring, leaving behind an area with an electronic structure that has more σ-type character. The size of the contrast is of the order of 10% and because of the white line sum rule we can therefore estimate that the relative changes of π to σ bonds in the irradiated area of similar order of magnitude.

Altogether, polarization dependent x-ray absorption spectromicroscopy has shown us that:

1. Magnetic impurities are not required to establish long range magnetic order in carbon.
2. One requirement for establishing ferromagnetic order is the correct balance between π and σ type bonds between carbon atoms. This can be achieved by irradiation with protons, which disturb the crystallographic structure and therefore redistribute electronic weight.

2.2.3 *High Resolution XMCD Spectroscopy of Magnetic Carbon*

The last question we will address regarding the magnetism of carbon in this chapter is which electronic states are responsible for the magnetic order as shown in Fig. 2.12. For this purpose XMCD spectra of irradiated graphite samples were acquired using an XMCD spectroscopy setup. The magnetization of the sample was reversed in a magnetic field of 0.5 T for every data point while the photon energy was scanned through the carbon 1*s* resonance. This was done for virgin as well as irradiated samples. The most obvious difference between the two samples is the drastic decrease in intensity of the so called $\pi^\star$ resonance, which can be readily understood by the decrease in crystallographic order due to proton irradiation and the redistribution of spectral weight as discussed in the previous section.

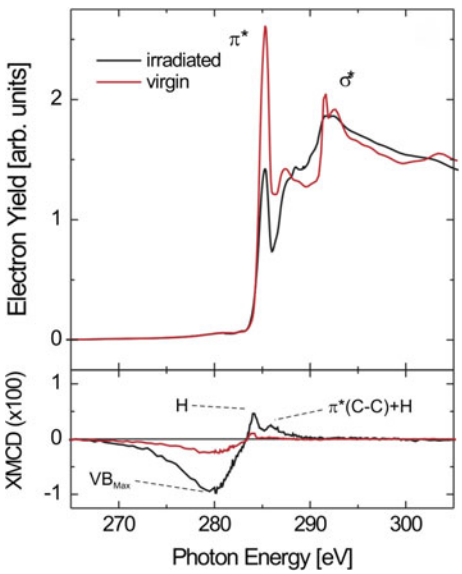

Fig. 2.12 X-ray absorption spectra of irradiated (*black*) and virgin (*red*) HOPG samples measured using EY at room temperature, as well as the XMCD difference ($\times 100$) detected using an applied field of ± 0.5 T. The spectra were obtained at 30° grazing incidence using circular polarization. From [43]

The XMCD spectra of both samples show a broad feature in the valence band around 280 eV. The feature can already be observed in the virgin sample, which exhibits very weak ferromagnetic signal (not to be mixed up with a "weak ferromagnetic order") [29]. However, the magnetization increases upon proton irradiation leading to a significant increase in the XMCD intensity originating from the spin polarized valence band. In addition proton irradiation leads to the formation of a peak in the XMCD spectra around 286 eV that can be readily attributed to C-H bonds due to the implantation of protons into the graphite lattice. This feature is absent in the virgin sample. The fact that we observe a rather strong XMCD signature from the valence band is consistent with our observations in the previous section, in which we found that proton irradiation leads to a redistribution of electronic states.

References

1. E. Thelen, The ramac 350 resoration web site. http://www.ed-thelen.org
2. J. Stöhr, H.C. Siegmann, *Magnetism: from Fundamentals to Nanoscale Dynamics* (Springer, Berlin, 2006)
3. M. Faraday, Phil. Trans. R. Soc. **136**, 1 (1846)
4. J. Kerr, Phil. Mag. **3**, 321 (1877)
5. A. Hubert, R. Schäfer, *Magnetic Domains* (Springer, Berlin, 1998)
6. J. Stöhr, Y. Wu, B.D. Hermsmeier, M.G. Samant, G.R. Harp, S. Koranda, D. Dunham, B.P. Tonner, Science **259**, 658 (1993)
7. H. Ohldag, A. Scholl, F. Nolting, S. Anders, F.U. Hillebrecht, J. Stöhr, Phys. Rev. Lett. **86**, 2878 (2001)
8. T. Regan, H. Ohldag, C. Stamm, F. Nolting, J. Lüning, J. Stöhr, Phys. Rev. B **64**, 214422 (2001)
9. C.T. Chen, L.H. Tjeng, J. Kwo, H.L. Kao, P. Rudolf, F. Sette, R.M. Fleming, Phys. Rev. Lett. **68**(16), 2543 (1992)
10. C. Jacobsen, S. Lindaas, S. Williams, X. Zhang, J. Microsc. **172**(2), 121 (1993)
11. H. Ohldag, V. Solinus, F.U. Hillebrecht, J.B. Goedkoop, M. Finazzi, F. Matsukara, H. Ohno, Appl. Phys. Lett. **76**, 2928 (2000)
12. T. Funk, S. Friedrich, A. Young, E. Arenholz, S. Cramer, Rev. Sci. Instrum. **73**, 1649 (2002)
13. B. Thole, P. Carra, F. Sette, G.V. der Laan, Phys. Rev. Lett. **68 (12)**(12), 1943 (1992)
14. P. Carra, B.N. Harmon, B.T. Thole, M. Altarelli, G.A. Sawatzky, Phys. Rev. Lett. **66**, 2495 (1991)
15. C.T. Chen, Y.U. Idzerda, H.J. Lin, N.V. Smith, G. Meigs, E. Chaban, G.H. Ho, E. Pellegrin, F. Sette, Phys. Rev. Lett. **75**, 152 (1995)
16. G. van der Laan, B.T. Thole, G.A. Sawatzky, J.B. Goedkoop, J.C. Fuggle, J.M. Esteva, R. Karnatak, J.P. Remeika, H.A. Dabkowska, Phys. Rev. B **34**, 6529 (1986)
17. G. Schütz, W. Wagner, W. Wilhelm, P. Kienle, R. Zeller, R. Frahm, G. Materlik, Phys. Rev. Lett. **58**(7), 737 (1987)
18. C.T. Chen, F. Sette, Y. Ma, S. Modesti, Phys. Rev. B **42**, 7262 (1990)
19. J. Stoehr, Y. Wu, B.D. Hermsmeier, M.G. Samant, G. Harp, S. Koranda, D. Dunham, B.P. Tonner, Science **259**, 658 (1993)
20. X.M. Cheng, D.J. Keavney, Rep. Prog. Phys. **75**, 026501 (2012)
21. J. Feng, E. Forest, A. MacDowell, M. Marcus, H. Padmore, S. Raoux, D. Robin, A. Scholl, R. Schlueter, P. Schmid, J. Stoehr, W. Wan, D.H. Wei, Y. Wu, J. Phys. Cond. Matt. **17**, S1339 (2005)
22. D. Wei, Y.L. Chan, Y.J. Hsu, J. Electron Spectrosc. Relat. Phenom. **185**(10), 429 (2012)

23. P. Fischer, M.Y. Im, C. Baldasseroni, C. Bordel, F. Hellman, J.S. Lee, C.S. Fadley, J. Electron Spectrosc. Relat. Phenom. **189**, 196 (2013)
24. P. Fischer, G. Schütz, G. Schmahl, P. Guttmann, D. Raasch, Z. Phys, B Cond. Matt. **101**(3), 313 (1996)
25. A. Kilcoyne, T. Tyliszczak, W. Steele, S. Fakra, P. Hitchcock, K. Franck, E. Anderson, B. Harteneck, E.G. Rightor, G.E. Mitchell, A.P. Hitchcock, L. Yang, T. Warwick, H. Ade, J. Synchrotron Radiat. **10**, 125 (2003)
26. H. Ishiwata, Y. Acremann, A. Scholl, E. Rotenberg, O. Hellwig, E. Dobisz, A. Doran, B. Tkachenko, A. Fokin, P. Schreiner, J. Dahl, R. Carlson, N. Melosh, Z. Shen, H. Ohldag, Appl. Phys. Lett. **101**, 163101 (2012)
27. A. Scholl, Curr. Op. in Solid State & Mater. Sci **7**, 59 (2003)
28. P. Esquinazi, D. Spemann, R. Höhne, A. Setzer, K.H. Han, T. Butz, Phys. Rev. Lett. **91**, 227201 (2003)
29. P. Esquinazi, A. Setzer, R. Höhne, C. Semmelhack, Y. Kopelevich, D. Spemann, T. Butz, B. Kohlstrunk, M. Lösche, Phys. Rev. B **66**, 024429 (2002)
30. J. Barzola-Quiquia, P. Esquinazi, M. Rothermel, D. Spemann, T. Butz, N. García, Phys. Rev. B **76**, 161403(R) (2007)
31. H. Xia, W. Li, Y. Song, X. Yang, X. Liu, M. Zhao, Y. Xia, C. Song, T.W. Wang, D. Zhu, J. Gong, Z. Zhu, Adv. Mater. **20**, 1 (2008)
32. Y. Kopelevich, R.R. da Silva, J.H.S. Torres, A. Penicaud, T. Kyotani, Phys. Rev. B **68**, 092408 (2003)
33. R. Caudillo, X. Gao, R. Escudero, M. José-Yacaman, J.B. Goodenough, Phys. Rev. B **74**, 214418 (2006)
34. N. Parkanskya, B. Alterkopa, R.L. Boxmana, G. Leitusb, O. Berkhc, Z. Barkayd, Y. Rosenberg, N. Eliaz, Carbon **46**, 215 (2008)
35. H. Ohldag, T. Tyliszczak, R. Höhne, D. Spemann, P. Esquinazi, M. Ungureanu, T. Butz, Phys. Rev. Lett. **98**(18), 1 (2007)
36. K. Kusakabe, M. Maruyama, Phys. Rev. B **67**, 092406 (2003)
37. E.J. Duplock, M. Scheffler, P.J.D. Lindan, Phys. Rev. Lett. **92**, 225502 (2004)
38. O.V. Yazyev, Phys. Rev. Lett. **101**, 037203 (2008)
39. P. Esquinazi, J. Barzola-Quiquia, D. Spemann, M. Rothermel, H. Ohldag, N. Garcia, A. Setzer, T. Butz, J. Magn. Magn. Mater. **322**, 1156 (2010)
40. X. Yanga, H. Xiab, X. Qinc, W. Lia, Y. Daia, X. Liua, M. Zhaoa, Y. Xiaa, S. Yana, B. Wangc, Carbon **47**, 1399 (2009)
41. M. Dubman, T. Shiroka, H. Luetkens, M. Rothermel, F.J. Litterst, E. Morenzoni, A. Suter, D. Spemann, P. Esquinazi, A. Setzer, T. Butz, J. Magn. Magn. Mater. **322**, 1228 (2010)
42. K. Schindler, N. Garcia, P. Esquinazi, H. Ohldag, Phys. Rev. B **74**, 045433 (2008)
43. H. Ohldag, P. Esquinazi, E. Arenholz, D. Spemann, M. Rothermel, A. Setzer, T. Butz, New J. Phys. **12**, 123012 (2010)

Chapter 3
Evidence for Magnetic Order in Graphite from Magnetization and Transport Measurements

Daniel Spemann and Pablo D. Esquinazi

Abstract This chapter reviews the experimental evidence obtained for the existence of magnetic order triggered by defects and/or non-magnetic ions in graphite with very low magnetic impurities concentrations. We demonstrate how and where this magnetically ordered state is produced in graphite bulk, thin flakes and powders in a reproducible manner. The experimental evidence obtained in the last 12 years leaves no doubt that this ferro- or ferrimagnetism is intrinsic of the graphite structure containing certain defects and not related to magnetic impurities. The main aim of this chapter is to provide the reader the key experimental facts and characterisation methods necessary to arrive at such a conclusion. We restrict the discussion to results obtained from two main magnetic characterisation methods, namely magnetization and transport measurements. In addition, we describe in Sect. 3.2 the main characterization method for trace element analysis to obtain the magnetic and non-magnetic impurities concentration. The chapter is concluded with an overview of further, independently obtained evidence for magnetic order in graphitic materials from literature.

3.1 Magnetic Signals from Defects in Graphite

As we learn in Chap. 1 of this book, a carbon vacancy or a hydrogen atom bonded to a carbon *p*-electron, or carbon atoms near a vacancy of the graphite structure can produce a finite magnetic moment. Several theoretical descriptions of possible magnetic states in the graphite/graphene structure were published since 2003, see [1–3] and supported, e.g., by STM measurements on single carbon vacancies [4]. The

D. Spemann (✉)
Physical Department, Leibniz Institute for Surface Modification (IOM),
Permoserstrasse 15, 04318 Leipzig, Germany
e-mail: daniel.spemann@iom-leipzig.de

P.D. Esquinazi
Division of Superconductivity and Magnetism, Institute for Experimental Physics II,
University of Leipzig, Linnéstrasse 5, 04103 Leipzig, Germany
e-mail: esquin@physik.uni-leipzig.de

P.D. Esquinazi (ed.), *Basic Physics of Functionalized Graphite*,
Springer Series in Materials Science 244, DOI 10.1007/978-3-319-39355-1_3

idea that graphite or a carbon-based material can show ferromagnetism is, however, much older, see the review in [5]. From theory and experiments we have learned that a delicate balance between the defect density, i.e. distance between defects, and at which positions within the graphite lattice those are located, is necessary to produce a magnetically ordered state. As will be shown below, ion irradiation proved to be a suitable method for the controlled introduction of defects in the graphite lattice. In the last years several reviews were published on defect-induced magnetism in graphite and other carbon-based materials [5–7].

Though the appearance of a magnetically ordered state through defects depends on the details of the lattice structure and the elements involved, the main concepts gained from the physics of defect-induced magnetism (DIM) in graphite can nevertheless be used to understand qualitatively how this state can occur in other materials, like in non-magnetic oxides [8].

3.1.1 Ion Irradiation: A Simple Way to Produce Defects

As shown in Chap. 1, a C-vacancy or a H-chemisorption defect can produce a magnetic moment in the graphite structure. The key to get a magnetically ordered state lies in the position and the distance between these vacancies/defects, i.e. their concentration. A simple way to produce them is via irradiation with protons or heavier ions. Were the formation energy of a vacancy or H-chemisorption defect equal in both sublattices A and B of graphite, we would have a completely balanced (anti)ferrimagnetically ordered state with zero total magnetic moment, e.g. after proton irradiation. This is due to the fact that the spin direction of a given C-vacancy or H-chemisorption defect in a graphene layer depends on which sublattice it resides, see for example [9]. As we shall demonstrate below, this, however, does not happen because both the formation energies of a C-vacancy and H-chemisorption defect differ in the A and B sublattices of graphite due to the stacking of the graphene sheets [10–12]. In a single graphene sheet, however, the formation energies are the same for both sublattices and the number of defects created in a statistical process, e.g. due to ion irradiation, is expected to be the same on both sublattices. Consequently, no magnetic order is expected for this type of defective graphene in line with experimental findings [13–17].

3.1.1.1 Defect Production in Graphite by Proton Irradiation

When a highly energetic proton traverses matter it interacts with the electrons and nuclei of the atoms in the material via Coulomb interaction thereby transferring its kinetic energy to the electrons and nuclei in a large number of binary collisions. As a consequence, the proton slows down, a process called *stopping* until it exits the target material or is stopped completely at a depth called *range*. There are two contributions to stopping, *electronic* and *nuclear* stopping originating from interactions

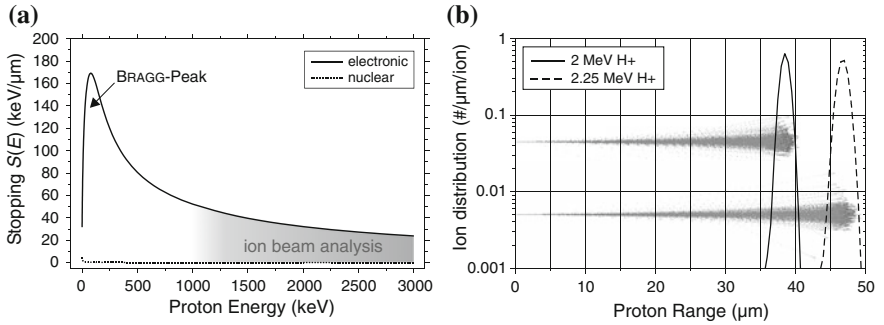

Fig. 3.1 **a** Electronic and nuclear stopping of protons in graphite calculated using SRIM. **b** Ion trajectories of 2 and 2.25 MeV protons in graphite as well as the resulting range distributions calculated from Monte Carlo simulations using SRIM. The scale for the lateral spread of the proton beam is the same as the depth scale which demonstrates the low amount of lateral straggling compared to the proton range

with electrons and nuclei, respectively. The amount of stopping strongly depends on the atomic number and velocity of the ion as well as the electron density and the mean ionization potential of the target material. Figure 3.1a shows the stopping of protons in graphite as a function of kinetic energy calculated using the Stopping and Range of Ions in Matter (SRIM) software package [18]. As can be seen, the stopping increases with decreasing proton energy until a maximum, the *Bragg-Peak*, is reached. The energy loss due to interactions with electrons vastly exceeds the energy lost to nuclei, which only becomes noticable at the end of proton range. Since the stopping of the protons typically requires a huge number of single collision events the initial direction of the proton remains well preserved with a low amount of lateral straggling and the range is characterized by a narrow depth distribution, see Fig. 3.1b.

The energy transfer to the electrons can lead to breakage of chemical bonds and creation of vacancies in the electron shells of atoms which will subsequently be refilled under the emission of Auger electrons or characteristic X-rays. The latter can be employed for trace element analysis as described in Sect. 3.2. The energy transfer to nuclei on the other hand can lead to the production of point defects, e.g. vacancy-interstitial-pairs (Frenckel defects). This requires that the energy transfer to a single nucleus is equal or greater than the material-specific lattice displacement energy E_d. Figure 3.2 shows the depth profile of the C-vacancies produced in graphite by 2 and 2.25 MeV protons calculated using SRIM. Starting from the surface the vacancy concentration shows a moderate increase with depth until it steeply rises to the maximum close to the proton range where the nuclear stopping is largest. From theses plots defect densities can be calculated as a function of depth and ion fluence.

The range and the number of C-vacancies are listed in Table 3.1 for 2 and 2.25 MeV protons and compared to 2 MeV He^+ ions. Whereas the protons penetrate several tens of microns into graphite, the 2 MeV He^+ ion is already stopped after 5.5 µm. The total number and density of C-vacancies differ substantially between the ion types

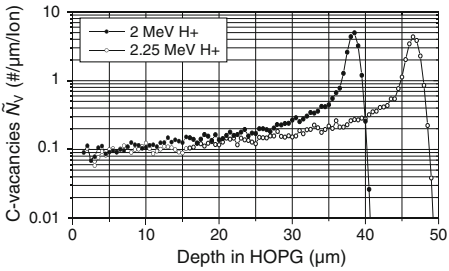

Fig. 3.2 Number of C-vacancies per 1 µm depth interval and incident proton for 2 and 2.25 MeV protons in graphite (SRIM simulation assuming a displacement energy of $E_d = 32$ eV)

Table 3.1 Ion range and number of carbon vacancies for MeV protons and He^+ ions extracted from SRIM simulations

Ion	Range R	Carbon vacancies $\tilde{N}_v$		
	µm	Surface	Maximum	Total
		$\mu m^{-1} \cdot ion^{-1}$	$\mu m^{-1} \cdot ion^{-1}$	ion^{-1}
2 MeV He^+	5.5	1.6	200	83
2 MeV H^+	38.5	0.09	5.0	15.9
2.25 MeV H^+	46.5	0.08	4.3	16.7

too with a 2 MeV He^+ ion creating 83 vacancies on average whereas the protons only produce around 16 vacancies each in total.

The number of vacancies n_v produced per unit volume of the target material can be calculated as $n_v = \Phi \cdot \tilde{N}_v$ with Φ being the ion fluence, i.e. the number of ions incident per unit area. In case of 2 MeV protons, a fluence of $\Phi = 10^{17}$ cm^{-2} will result in $n_v = 900$ cm^{-1} ion$^{-1} \times 10^{17}$ ion cm$^{-2} = 9 \times 10^{19}$ cm^{-3} C-vacancies in the near-surface area which corresponds to an atomic vacancy concentration of $c_v = n_v M/(\rho N_A) = 7.9 \times 10^{-4}$ with the molar mass $M = 12$ g/mol of carbon and the density $\rho = 2.26$ g/cm^3 of graphite.

3.1.1.2 Localization of Hydrogen After Proton Irradiation

Since H-chemisorption defects provide magnetic moments and therefore might contribute to the observed magnetic order in graphite, 3D hydrogen microscopy was employed to study the location of the hydrogen after proton implantation (see [19] for more details). The results can be summarized as follows: (i) The intrinsic hydrogen content of virgin ZYA grade HOPG from Advanced Ceramics is <0.3 at.-ppm which represents the minimum detection limit (MDL) of the method; (ii) There is an amount of $\sim 5 \times 10^{15}$ cm^{-2} hydrogen adsorbed on the surface of the graphite sample. This is a very important observation as will become clear below; (iii) The implanted protons remain localized in the regions where they came to rest after the

stopping process, i.e. there is no indication of hydrogen diffusion over length scales more than 2 μm which represents the lateral and depth resolution of this microscopy technique.

3.1.2 Curie Paramagnetism and Magnetic Order

One of the clearest ways to check for the effect of irradiation on the magnetic properties of graphite is through the measurement of the temperature dependence of the magnetic moment before and after irradiation. This experiment has been realized in 2007 using a 3.5 mg HOPG sample of size $2 \times 3 \times 0.3$ mm^3 glued with varnish on a high-purity Si substrate [20]. The possibility of measuring the sample before and after irradiation without detaching it from the sample holder has the advantage that direct handling of the sample is avoided which might otherwise introduce impurities if done without care. Figure 3.3a shows the magnetic moment of this sample (sample 1) as a function of temperature in a semilogarithmic scale. The temperature dependence of the virgin curve shows a minimum (maximum diamagnetism) at $T \sim 30$ K, which is usual for HOPG samples of good quality. After a broad proton

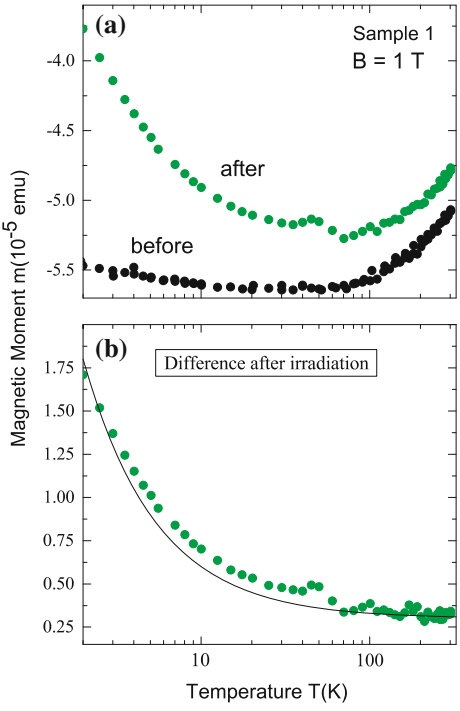

Fig. 3.3 **a** Total magnetic moment (HOPG sample 1 with the Si substrate) as a function of temperature at a constant magnetic field applied parallel to the graphene planes for the sample before and after proton irradiation with a broad beam of 0.8 mm diameter (total charge 450 μC at 100 nA proton current). **b** The difference between the two curves from (**a**). This difference reveals directly the irradiation effect. The continuous line is the function 3×10^{-5}[emu K]$/T + 3 \times 10^{-6}$[emu]. Taken from [20]

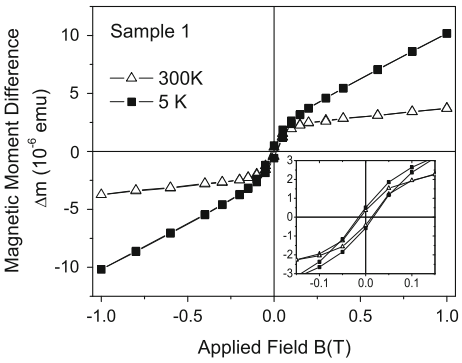

Fig. 3.4 Hysteresis loops for the same sample as in Fig. 3.3 obtained for 5 and 300 K as the difference between the loops measured after and before irradiation at the same magnetic fields. The *inset* blows up the data in a smaller field range. After [20]

beam irradiation covering most of the sample area, the magnetic moment shows a clear increase in the whole temperature range, see Fig. 3.3a.

Figure 3.3b shows the difference between the magnetic moment after the irradiation minus that of the virgin state as a function of temperature at a constant field of 1 T. This difference can be understood as the sum of two contributions, namely, a paramagnetic one, which follows roughly the Curie law $3 \times 10^{-5}/T$ emu, and a constant ferromagnetic contribution 3×10^{-6} emu, i.e. $m(T, B > B_s) \simeq \frac{3\times10^{-5}}{T} + 3 \times 10^{-6}$ in emu, where B_s is the minimum saturation field for the ferromagnetic part. The small but clear deviation between the fit and the data shown in Fig. 3.3b can be interpreted as being due to a small deviation from the Curie law, which is only valid for low enough fields and high enough temperatures, i.e. only for $x \propto B/T \ll 1$ one is allowed to keep the first term only of the Brillouin function that provides the simple $1/T$ Curie law. Part of the deviation may also come from the assumption of a strictly temperature-independent ferromagnetic contribution.

The hysteresis loops shown in Fig. 3.4, obtained at two temperatures by subtracting the loops after irradiation from those obtained in the virgin state, justify the assumption of the two magnetic contributions. The increase of the magnetic moment after irradiation at room temperature is mainly due to the increase of the ferromagnetism of the sample; only ∼25% of the increase is due to a paramagnetic contribution at 300 K and 1 T. The paramagnetic contribution is clearly recognized in Fig. 3.4 from the slope of the loops at fields above ∼0.25 T. The inset in this figure shows clearly the finite irreversibility produced by the irradiation with coercivity fields of the order of 0.02 T. The results shown in Fig. 3.3 clearly indicate that broad beam irradiation—at the used proton current and fluence—triggers two magnetic contributions, one due to independent, localized magnetic moments and a second one with all the characteristics of magnetic order with a Curie temperature above room temperature. Note that the effect on the magnetic properties of graphite due to proton irradiation depends on several parameters as the total implanted or irradiated charge, fluence and proton current as well as on the geometry of the used proton beam, see [20] for more details.

In [21] different ions were used to check the correspondence between Curie paramagnetism and a magnetically ordered state with the density of nominally expected

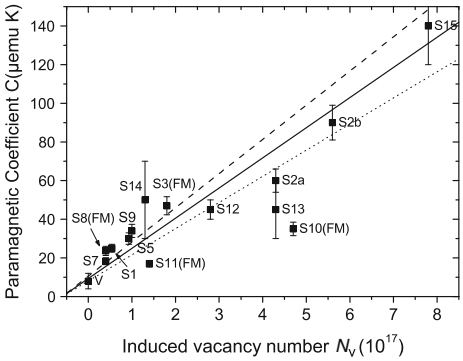

Fig. 3.5 Paramagnetic parameter C, see (3.1), obtained from the fits to the magnetic moment difference data as a function of the nominal total vacancy number produced by the irradiation for all measured samples. The labels show the sample number and the label "FM" in brackets means that this sample shows ferromagnetism induced by the irradiation. The point with the label "V" refers to the samples in virgin, non-irradiated state, with similar sample volumes. The continuous line is the function $C = 0.075 \cdot 2.08 \times 10^{-15}(N_V + 6 \times 10^{16})$ μemu K. The *dashed* and *dotted lines* follow the same function but with the first numerical coefficient equal to 0.085 and 0.065, respectively. From [21]

total vacancies N_V produced in the sample by ion irradiation. In general, the induced paramagnetic contribution is clearly observed at $T < 100$ K in all samples, see e.g. Fig. 3.3. From the fits to the data one obtains the paramagnetic coefficient or Curie constant C shown in Fig. 3.5 as a function of N_V [21]. Note that only single C-vacancies were taken into account because at MeV ion energies it is expected that these are produced with the highest probability in comparison with multi-vacancy defects. These multi-vacancy defects are, however, produced at low-energy irradiation and may play an important role in the induced effects there [22]. Measurements of electron spin resonance (ESR) line widths and signal intensity as a function of temperature of graphite samples irradiated with protons, deuterons and helium ions indicate that the spins produced by the irradiation are of a localized nature [23].

For the case that the temperature dependence of the magnetic moment is obtained always at a fixed field of $\mu_0 H = 1$ T, as done in [21], the classical paramagnetic contribution of N paramagnetic centers, each with an effective magnetic moment $\mu_{\text{eff}} = p\mu_B$ (μ_B is the Bohr magneton), is given by:

$$m_P = C/T, \tag{3.1}$$

$$C = N\frac{{\mu_{\text{eff}}}^2}{3k_B} = N\,p^2\,2.08 \times 10^{-15}\ \mu\text{emu K}. \tag{3.2}$$

For atomic paramagnetic centers the effective Bohr magneton number is given by [24] $p = g(JLS)\sqrt{J(J+1)}$ where $g(JLS)$ is the Landé factor. The case presented here to estimate p from experimental data assumes a single multiplet, whereas the case of a paramagnetic contribution due to more than one multiplet was observed experimentally and described in detail in [21].

Roughly speaking and within the data dispersion we can take a linear correlation between C and N_V given by the equation $C = (0.075 \pm 0.01) \cdot 2.08 \times 10^{-15}(N_V + 6 \times 10^{16})$ μemu K, see Fig. 3.5. Then, the effective magneton number for a vacancy would be given by $p = (0.27 \pm 0.02)\ \mu_B$ according to (3.2). We can compare this number with the simplest atomic multiplet case. For example, using $p = g(JLS)\sqrt{J(J+1)}$ with $J = S = 1/2, L = 0, g = 2$ gives $p = 1.73$. One may speculate that a vacancy itself has no spin, i.e. $S = 0$ and $J = L = 1/2$, yielding $p = 0.87$. On the other hand, from theoretical estimates [2, 3, 11, 25–28] one expects $p \sim 0.5 \ldots 1$. Assuming that each vacancy would have an effective magnetic moment of 0.5 μ_B the experimentally obtained p is a factor two smaller than expected.

Some of the irradiated samples show also a ferromagnetic contribution triggered by the generation of defects with a certain density, those samples are marked with "(FM)" in Fig. 3.5 [21]. With the estimated average distance of the produced C-vacancies at 50 nm depth from the samples' surface one obtains the correlation shown in Fig. 3.6, which implies a rather narrow window for the average distance between C-vacancies to obtain a ferromagnetic contribution. The reason for the absence of more experimental data in Fig. 3.6 is due to self-heating effects during irradiation, which detrimentally influence the defect density and impede their accurate estimation, making a comparison between differently irradiated samples difficult. The increase of temperature during irradiation has been measured in [21] and is, in general even for reasonably low ion beam currents, not negligible.

It should be noted that apart from defect generation in the bulk of graphite, ion irradiation might also result in chemisorption of the hydrogen adsorbed on the surface on graphite samples. This would provide additional magnetic moments and possibly magnetic order in the near-surface region.

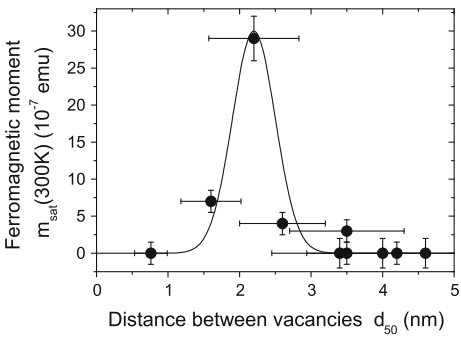

Fig. 3.6 Ferromagnetic moment at saturation as a function of the nominal distance between induced vacancies calculated at 50 nm depth from the HOPG surface for most of the samples prepared in [21]. The error bars are the maximum estimated ones considering the sensitivity and reproducibility of the SQUID measurements as well as the range of parameters needed to estimate the average vacancy distance within a graphene layer using SRIM. The continuous line follows a Gaussian function and is a guide to the eye only. Taken from [21]

3.1.3 *Localization of the Ferromagnetism Triggered by Proton Irradiation*

For the following let us assume that C-vacancies are responsible for the observed magnetic order. As shown in Fig. 3.6 the mean distance between vacancies needs to be in a comparably small range to trigger ferromagnetism in graphite. Starting from SRIM simulations of the vacancy production shown in Fig. 3.2 we can estimate the mean distance between vacancies for the 2D (graphene) and 3D (graphite) case as a function of ion fluence [29]. Let us assume a vacancy production of $\tilde{N}_v = 0.1\ \mu m^{-1}\ ion^{-1}$ (see Table 3.1) as found for 2 and 2.25 MeV protons in the near-surface region and a fluence of $\Phi = 10^{15}\ cm^{-2}$. The defect density then is $n_v^{2D} = 10^{15}\,cm^{-2} \cdot 3.35 \times 10^{-5} = 3.35 \times 10^{10}\,cm^{-2}$ taking into account the distance between the basal planes of graphite of 0.335 nm and $n_v^{3D} = 10^{15}\,cm^{-2} \cdot 0.1\,\mu m^{-1} = 10^{18}\ cm^{-3}$. Comparing with the atomic density of $n^{2D} = 3.82 \times 10^{15}\ cm^{-2}$ of graphene and $n^{3D} = 1.14 \times 10^{23}\ cm^{-3}$ of graphite one gets the same relative vacancy concentration of 8.78×10^{-6} for both cases. In order to calculate the mean distance between vacancies we assume that each vacancy is in the center of a square (2D) or cube (3D) of sidelength a and we take the average of the distance to the next neighbors. For the 2D case we get an area of $a^2 = 2.98 \times 10^3\ nm^2$ per vacancy and an average distance of $d^{2D} = 66$ nm. In the 3D graphite case we get a volume $a^3 = 1000\ nm^3$ per vacancy, yielding an average distance of $d^{3D} = 14.2$ nm. Figure 3.7a shows the dependence of the mean distance between vacancies as a function of proton fluence Φ for the 2D and the 3D graphite lattice.

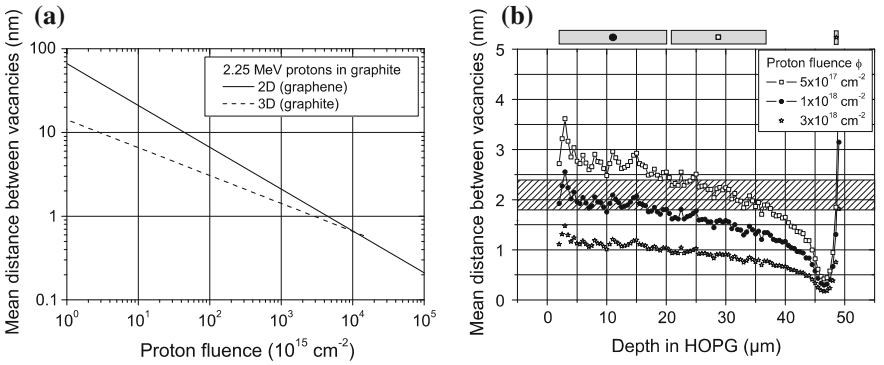

Fig. 3.7 **a** Mean distance between next neighboring vacancies versus fluence of 2.25 MeV protons for the two dimensional graphene case (*straight line*) and the three dimensional graphite lattice (*dashed line*) assuming a vacancy production of 0.1 per micron depth interval and incident proton [18]. **b** Mean distance between vacancies in the graphene case versus depth from the surface of a graphite sample estimated using Monte Carlo simulations [18] for three fixed fluences. The shadowed area is a guide to the eye to realize the different depths and total sample mass ($\propto$ to the boxes drawn at the top of the figure) at which a mean distance between vacancies of (2.1 ± 0.3) nm exists

The depth dependency of the vacancy production rate given by the SRIM simulation [18] can be used to calculate the mean distance as a function of depth, see Fig. 3.7b. Assuming that the largest signal due to the induced magnetic order is produced at a distance between vacancies of (2.1 ± 0.3) nm in the 2D case, different depth intervals contribute to the magnetic signals for different fluences. The calculations indicate that from the three selected fluences in Fig. 3.7b the largest ferromagnetic signal would be given for $\phi \simeq 10^{18}$ protons per cm^2 from the first $\sim$20 μm depth. These estimates indicate also that the largest ferromagnetic mass one can produce with a single energy proton beam will be located within the first $\sim$30 μm depth where the curve is rather flat. In [30] the maximum magnetic moment was observed for 2.0 MeV protons at a fluence of $\phi \sim 2 \times 10^{17}$ cm^{-2}, whereas the magnetic moment already decreased for $\phi \sim 4 \times 10^{17}$ cm^{-2}, compatible with the rough estimates above. Raman and XPS measurements on 2.25 MeV proton implanted HOPG showed that sp^3 hybridization increases upon irradiation, but that the lattice structure is still preserved at fluences of $\phi \sim 2 \times 10^{17}$ cm^{-2} [31]. This proves that a mostly intact graphite lattice with preserved stacking order is required for magnetic order, see also [32].

Figure 3.8 shows results that indicate the measured magnetic signal is located in the first micrometers depth [34] in qualitative agreement with the estimates presented in Fig. 3.7 and also with the results in [12]. It is interesting to note that the H-chemisorption defects created at the end of ion range of $\sim$40 μm do not trigger magnetic order, most probably because the graphite lattice is too heavily damaged by the proton implantation at this depth. On the other hand, the restriction of the observed magnetic order to the near-surface region might also indicate that the hydrogen adsorbed on the surface of the sample indeed undergoes chemisorption assisted by

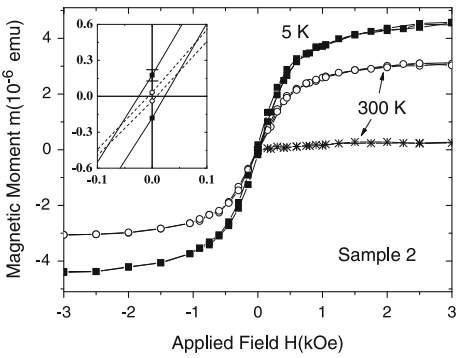

Fig. 3.8 Magnetic moment as a function of applied field for the irradiated sample 2 at 300 K (o) and 5 K (■) obtained after subtracting the data of the non-irradiated sample. The points (⋆) are obtained for the same sample at 300 K after taking out the first $\sim$5 micrometers from the irradiated surface side. The *inset* blows up the data at low fields to show the finite hysteresis and the clear temperature dependence of the coercive field and remanent magnetic moment. Sample 2 mass was 12.5 mg of a HOPG sample of grade A. The sample was irradiated with 25600 spots of $\sim$2 μm diameter each and separated by a distance of 10 μm. The fluence was 5.0×10^{16} cm^{-2}, total irradiated charge 44.8 μC and 1 nA proton current at 110 K. Taken from [33]

the proton irradiation as already discussed above. In fact, hydrogenation has been found to effectively trigger magnetic order in graphite [35, 36] or other graphitic materials [37–41].

In contrast, neutron irradiation of bulk graphite only led to spin 1/2 paramagnetism in [42], but no magnetic order induced by defects in the bulk. A comparison with the Raman spectra in [43] indicates that the damage introduced in the graphite lattice by the neutron irradiation was substantial for the data presented in [42]. Therefore, it cannot be excluded that magnetic order was suppressed due to the loss of the Bernal stacking order required for the coupling of the magnetic moments.

Following the estimates done in [9] based on the ferromagnetic contribution of coupled defects from the same sublattice of a graphene lattice, a mean distance between vacancies of 1.5 nm would give a critical temperature of ∼450 K in very good agreement with experimental observations [34, 44]. We note that due to the statistical process of vacancy production and the simplicity of the model used for the estimate of the vacancy density, an error of at least a factor of two is expected for the calculated damage production rates and the derived mean vacancy distance. Note that in our energy range a lower proton energy will decrease the distance between vacancies at a given depth.

3.2 Magnetic Impurities: Trace Element Analysis Using PIXE

In order to prove the intrinsic nature of the magnetic order in graphite a reliable trace element analysis of the samples was mandatory as this allowed to calculate the maximum possible contribution of magnetic impurities to the magnetic moment. Later, XMCD measurements could successfully prove that the magnetic moments are associated with π-electrons of carbon atoms and are not due to impurities [45].

Since the magnetic moments of the samples are typically small, tiny amounts of contamination can already be sufficient to dominate their magnetic properties—e.g. the sample in Fig. 3.8 has a magnetization $M = 4.5 \times 10^{-6}$ emu/12.5 mg = 3.6×10^{-4} emu/g at 5 K after irradiation, a magnetization that would correspond to a Fe concentration in the sample of 1.6 μg/g. This illustrates that careful sample handling to avoid contamination, but also the possibility of successive trace element analysis after any sample treatment is important. Therefore, a method is required that allows an accurate measurement of impurity concentrations in the ppm and sub-ppm range, preferably in a non-destructive manner. Furthermore, the ability to image the distribution of impurities would be welcome. Particle Induced X-ray Emission (PIXE) [46] using MeV protons for excitation has the necessary requirements for this kind of studies as will be shown below. Another technique with excellent sensitivity and quantification is Instrumental Neutron Activation Analysis (INAA) which however lacks imaging capabilities and is not easily available on a daily basis, not to mention the analysis times that can easily take days for sufficient sensitivity. X-ray Fluorescence analysis (XRF) on the other hand will in general not be sensitive enough.

In this section we show the results of PIXE analysis of commercial HOPG samples and compare this with measurements using Energy Dispersive X-ray analysis (EDX), a wide-spread technique that has been used for analysis of HOPG in the literature [47–49].

3.2.1 *Trace Element Content of Commercial HOPG Samples*

The samples studied are commercially available HOPG from Advanced Ceramics (now Momentive Performance Materials), NT-MDT and SPI Supplies with three available structural grades designated as ZYA, ZYB and ZYH. In case of SPI Supplies the corresponding designation is SPI-1, -2 and -3. In the following of Sect. 3.2, the samples are named by the company (Advanced Ceramics is abbreviated as AC) and the structural grade, e.g. AC ZYA denotes the ZYA-grade sample from Advanced Ceramics.

Trace elemental analysis was performed at the LIPSION facility of the University of Leipzig [50] with PIXE [46] and Rutherford Backscattering Spectrometry (RBS) [51] using a 2.28 MeV proton microbeam focused to $1-2\,\mu$m diameter. The protons penetrate 47 μm deep into graphite where they generate 90% of the total X-ray yield from Fe atoms within the first 27 μm [52] making PIXE a truly bulk-sensitive technique. More details of the sample preparation, experiments and results can be found in [53].

Figure 3.9 shows a typical PIXE spectrum from ZYA-grade HOPG from Advanced Ceramics together with the extracted elemental concentrations. We note that the

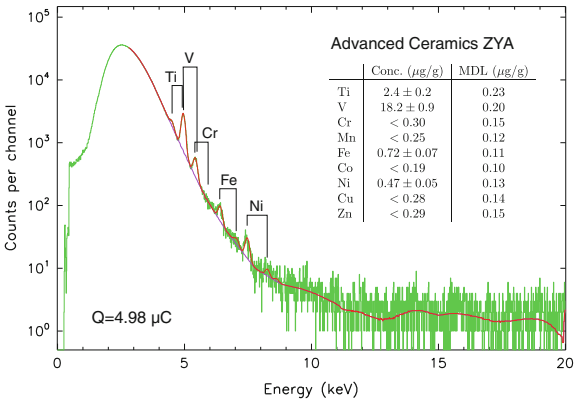

Fig. 3.9 PIXE spectrum from ZYA-grade HOPG from Advanced Ceramics recorded with a collected proton charge of $Q = 4.98\,\mu$C. The *green curve* are the measured data, the *violet* and *red curve* are the background simulation and fit to the data, respectively, from GeoPIXE II [52]. The extracted concentrations as well as minimum detection limits are given and the corresponding X-ray lines for the detected elements indicated. Taken from [53]

measured concentration of 0.72 μg/g Fe, if magnetic, would imply a contribution to the magnetization at saturation of the order of 1.6×10^{-4} emu/g.

3.2.1.1 Sideface Contamination of As-Received Samples

In order to check for contaminations in the as-received state the HOPG samples of ZYA grade were analyzed with the proton beam incident on both top surface and sideface designated as "surface" and "sideface" in Fig. 3.10 where the X-ray yields, i.e. elemental concentrations, are displayed in false color scale for the SPI-1 sample. As can be seen in Fig. 3.10a, the sideface is strongly contaminated with Cr, Fe, and Ni, all three showing an identical distribution indicating that they originate from the same source. The quantitative analysis of this contamination reveals a composition of 16.0% Cr, 77.2% Fe and 6.8% Ni by weight which fits with the frequently used non-magnetic, austenitic SAE grade 301 stainless steel [54]. It is therefore reasonable to assume that this contamination originates from the cutting of the samples prior shipping using a stainless steel tool.

Contaminations of similar distribution and composition can be found on the sidefaces of AC ZYA and NT-MDT ZYA samples as well, however, to a less severe

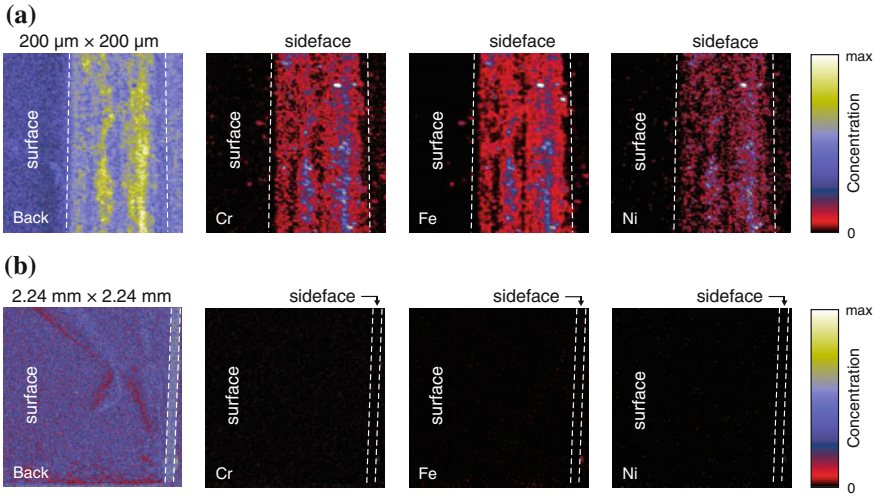

Fig. 3.10 X-ray yield in false color scale for the background and the elements Cr, Fe and Ni: **a** SPI-1 sample in the as-received state (200 μm × 200 μm scan size, $Q = 0.87$ μC applied proton charge) showing a severe sideface contamination with Cr, Fe and Ni, probably originating from a stainless steel tool used for sample cutting. Some loose particles of contamination can even be found on the top surface close to the sideface; **b** SPI-1 after ultrasonic cleaning (2.24 mm × 2.24 mm scan size, $Q = 5.24$ μC applied proton charge) with the same maximum concentration values of the color scale as in (**a**). As can be seen between the *two dashed lines*, the sideface is not contaminated anymore and therefore appears *black*. Taken from [53]

Table 3.2 Sideface contamination with Fe and bulk concentrations of trace elements in HOPG

Sample	Sideface	Concentrations in HOPG bulk (μg/g)					
	Fe (ng/cm^2)	Ti	V	Cr	Fe	Co	Ni
AC ZYA	15.8 ± 1.1	2.4 ± 0.2	18.2 ± 0.9	<0.30	0.72 ± 0.07	<0.19	0.47 ± 0.05
AC ZYB	n.d.	4.9 ± 0.4	10.5 ± 0.5	<0.32	<0.23*	<0.21	<0.28
AC ZYH	n.d.	1.9 ± 0.2	24.5 ± 1.2	<0.30	22.6 ± 1.1	<0.25	4.2 ± 0.3
NT-MDT ZYA	155 ± 8	<0.50	<0.40	<0.28	0.55 ± 0.05	<0.20	<0.27
NT-MDT ZYB	n.d.	12.6 ± 0.9	0.80 ± 0.10	<0.29	10.4 ± 0.5	<0.23	<0.31
NT-MDT ZYH	n.d.	5.6 ± 0.3	1.40 ± 0.14	0.30 ± 0.04	10.2 ± 0.5	<0.22	<0.28
SPI-1	702 ± 35	<0.50	<0.40	<0.27	0.66 ± 0.06	<0.19	<0.27
SPI-2	n.d.	1.5 ± 0.2	<0.40	<0.31	9.4 ± 0.5	<0.24	<0.31
SPI-3	n.d.	2.1 ± 0.2	5.4 ± 0.5	<0.33	8.4 ± 0.4	<0.23	<0.33

With the exception of AC ZYB the ZYA samples with the highest structural quality have the lowest Fe concentrations <1 μg/g. In addition to the elements listed the concentrations of Mn, Cu and Zn were determined for all samples as well and found to be <0.28 μg/g for Mn, <0.33 μg/g for Cu and <0.34 μg/g for Zn. Reproduced from [53]
n.d.: not determined; *Fe concentration in a similar AC ZYB sample: (0.17 ± 0.03) μg/g [29]

degree. As Table 3.2 shows, 702 ng Fe per cm^2 sideface area was found for SPI-1, whereas for the AC and NT-MDT samples Fe concentrations amount to 15.8 ng/cm^2 and 155 ng/cm^2, respectively. Even though they were not measured it is reasonable to assume that the sidefaces of the ZYB and ZYH samples are contaminated as well in the as-received state.

After thorough ultrasonic cleaning, however, the sidefaces are free of contaminants as can be seen from the large scan shown Fig. 3.10b. We conclude that ultrasonic cleaning is mandatory prior use of these HOPG samples in contamination-critical applications.

3.2.1.2 Bulk Concentrations of Trace Elements

PIXE trace element analysis was performed by simply scanning the proton beam over a 2.24 mm × 2.24 mm sized area covering a substantial portion of the whole sample and collecting the X-ray photons from the trace element atoms. The PIXE spectra (see as example Fig. 3.9 for the AC ZYA sample) were analyzed and the concentrations extracted are given in Table 3.2.

The findings can be summarized as follows: (i) The ZYA-grade samples have Fe concentrations below 1 μg/g; (ii) The ZYB and ZYH samples of NT-MDT and SPI all

have similar Fe concentrations of the order of 10 μg/g, whereas the AC ZYB has the lowest Fe contamination of <0.23 μg/g ((0.17 ± 0.03) μg/g was determined for a similar sample a few years ago [29]) and the AC ZYH the highest Fe concentration of 22.6 μg/g; (iii) Most of the samples also contain Ti and V with varying concentrations between the different samples.

We would like to point out that, with the exception of AC ZYA and AC ZYB samples, we have not analyzed any of the other samples before and can therefore not make any statement about the variation of the concentration values between different batches of these samples. AC ZYA samples have been used in our studies on DIM and therefore frequently analyzed in the last ten years. We found that their trace element content shows little variation between different batches.

The impurities are not distributed homogeneously within the sample, but located in micrometer large grains that are homogeneously dispersed within the bulk [29, 47, 49]. This is illustrated in Fig. 3.11 where the Ti, V and Fe maps are shown for the AC ZYA and SPI-3 sample. A detailed inspection of the maps reveals that Ti and V are strongly correlated showing identical distributions within the scan area. In most of the (Ti,V) grains Fe is present too. However, there are a few (Ti,V) grains that do not contain Fe and a few Fe grains that do not contain Ti or V. The maps indicate that the grain density is significantly higher in SPI-3 and that the grains itself are slightly smaller compared to AC ZYA. Assuming that grains can be detected up to a depth of 27 μm their density in AC ZYA can be estimated to about 6×10^6 cm^{-3}.

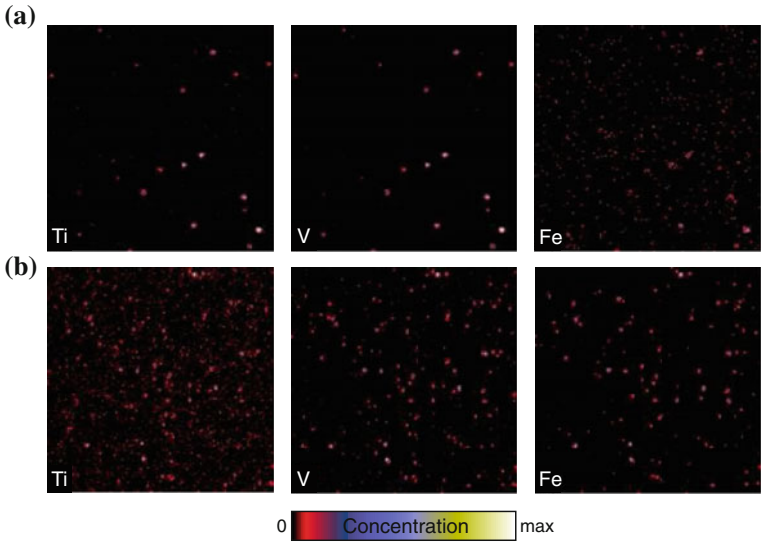

Fig. 3.11 Ti, V and Fe distribution in a 400 μm × 400 μm sized scan area for **a** AC ZYA and **b** SPI-3. Taken from [53]

3.2.1.3 Analysis of Single Metallic Grains

In order to draw some conclusions on their magnetic properties single grains of contamination were selected from larger scan areas and analyzed in detail by simultaneous PIXE and RBS. As an example, Fig. 3.12a, b show the PIXE and RBS analysis, respectively, of a single grain in the AC ZYA sample. As stated above, Ti and V have identical distributions, different from Fe and Ni that are located at the outside of the grain, both with a similar and irregular distribution along the grain's perimeter. This is also illustrated in the composite map of Fig. 3.12a showing the distribution of Ti, Fe, Ni in red, green and blue color, respectively, with brighter colors referring to higher concentrations of the respective element.

Figure 3.12b shows the RBS spectrum extracted from the grain alone. The broad peak around channel 720 are protons backscattered from the metals where peak width and area reflect grain thickness and the total number of metal atoms, respectively. The grain is also visible as "missing" carbon in the dip around channel 530. From this dip position the depth of the grain can be determined. As quantitative analysis shows, this 7.0 μm × 5.5 μm sized grain has a mass thickness of (0.13 ± 0.01) mg/cm^2, consists on average of 13.7% Ti, 82.0% V, 2.4% Fe and 1.9% Ni by weight and is located 4.35 μm below the graphite surface. It contains (1.2 ± 0.1) pg Fe and (0.96 ± 0.10) pg Ni. Assuming for simplicity that the grain is made of pure Vanadium with a mass density of $\rho = 6.1$ g/cm^3, the geometrical thickness can be calculated to $d \approx 210$ nm. This and the analysis of other grains show that they are not spherical, but flat disks that are oriented parallel to the graphene planes. This finding agrees well with the EDX and TEM analysis of an AC ZYA sample reported in [49]. Taking into account the high temperatures $T > 2000$ °C and pressures used in the production

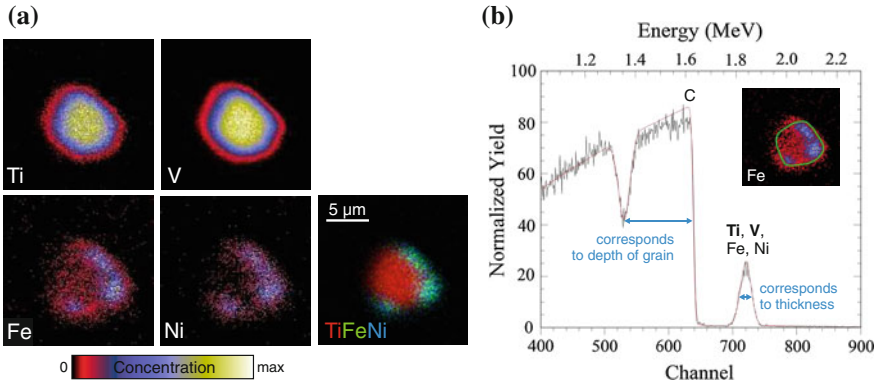

Fig. 3.12 Ion beam analysis of a single grain in AC ZYA (17.5 μm × 17.5μm scan area): **a** Element maps and composite map of Ti, Fe and Ni showing a homogeneous distribution of Ti and V inside the grain and the location of Fe and Ni at the perimeter; **b** RBS spectrum extracted from the grain (the *green curve* in the Fe map represents the extracted scan area). From the XRUMP [55] analysis (*red curve*) the metallic content, thickness and depth of the grain can be determined. Taken from [53]

of HOPG from pyrocarbons [56], this flat shape is to be expected. Metallic particles in the pyrocarbons, whatever their origin might be, melt at these temperatures and spread out perpendicular to the direction of pressure, i.e. perpendicular to the *c*-axis of the formed HOPG. Furthermore, the formation of iron carbides is to be expected under these conditions. Indeed, electron diffraction analysis showed that Fe in the grain is not metallic, but present as cementite Fe_3C [49] in agreement with the findings in [57–59]. It might be interesting to note that DFT calculations of the influence of small iron clusters on graphene showed that a possible intrinsic carbon magnetism is in fact reduced due to the spin pairing between Fe and C atoms [60].

Figure 3.13 shows composite maps of grains for all investigated samples with the exception of SPI-1 and NT-NDT ZYA where no grains could be detected within the detection limits of PIXE imaging. Indeed, these two samples are the only ones that do not contain Ti or V (see Table 3.2). They do, however, contain Fe of comparable amount as AC ZYA, presumably more or less homogeneously distributed within the bulk and not concentrated in grains as for the latter one. As can be seen, the grains differ substantially in size from 2 µm (NT-MDT ZYB) to ≈30 µm (AC ZYH) and composition between different samples, but also within the same sample as is demonstrated for AC ZYH. Here, three grains of very different shape and size are displayed. In view of these variations, it is obvious, that the estimation of bulk concentrations from the analysis of a few single grains only can lead to substantial errors. Indeed, taking the 1.2 pg Fe from the grain in Fig. 3.12 and the grain density of

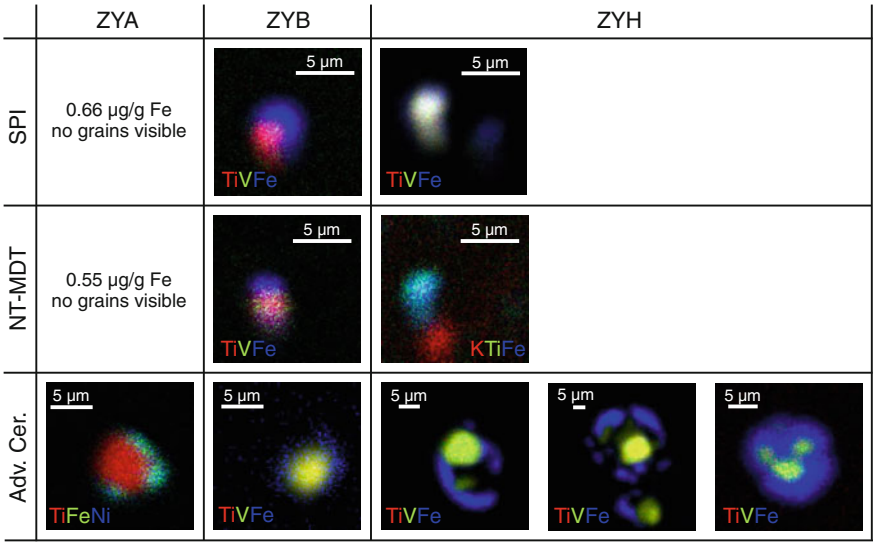

Fig. 3.13 Composite maps of single grains for all investigated samples except SPI-1 and NT-MDT ZYA where no grains could be found. The displayed elements and assigned colors are given in each map. As demonstrated, size and composition of the grains differ substantially between different samples, but also within the same sample (see AC ZYH). Taken from [53]

$6 \times 10^6\,\mathrm{cm}^{-3}$ estimated from Fig. 3.11 one gets about 3 μg/g Fe as bulk concentration for AC ZYA where the true value is (0.72 ± 0.07) μg/g. Obviously, the metal content of this grain is above the average compared to the other grains in AC ZYA.

3.2.2 *Comparison with EDX Analysis*

EDX is a wide-spread technique for elemental analysis and imaging and has been used recently in the characterization of contaminations in HOPG in [47–49]. In order to compare its capabilities and limitations with those of ion beam microscopy some of the HOPG samples were studied with EDX using 20 keV electrons. Figure 3.14 shows the X-ray spectra recorded from a NT-MDT ZYB sample with EDX and PIXE, respectively, using a large scan area. Whereas the PIXE spectrum shows peaks for Ti, V and Fe, no peaks can be discerned for these trace elements in the EDX spectrum, despite Ti and Fe having concentrations $\gtrsim$10 μg/g. As a detailed analysis shows, a typical MDL for Fe amounts to ∼200 μg/g in EDX analysis, about a factor 1000 larger than for PIXE and far above the Fe bulk concentrations in all the HOPG samples. It is clear, that EDX cannot be used to measure the bulk concentrations of trace elements in HOPG directly.

In case of HOPG samples, where the trace elements are strongly concentrated in grains, EDX can at least be performed on single grains. Figure 3.15 shows such an EDX analysis on a grain in AC ZYA. First, Backscattered Electron (BE) imaging is used to detect single grains directly below the graphite surface due to the *Z*-contrast in electron yield. Then, a small scan is made and the emitted X-rays are recorded (see

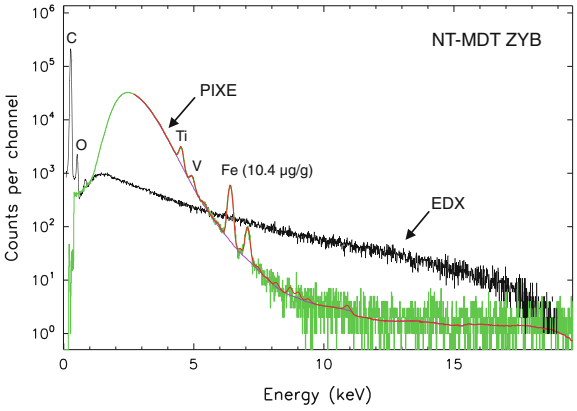

Fig. 3.14 EDX spectrum (*black line*) and PIXE spectrum (*green line*, together with GeoPIXE II fit, see Fig. 3.9 for explanation) recorded on NT-MDT ZYB. In both cases, a large scan was made to obtain reliable bulk concentration values, however, no peaks for the trace elements can be detected in the EDX spectrum, demonstrating its insufficient sensitivity for trace element analysis in HOPG. Taken from [53]

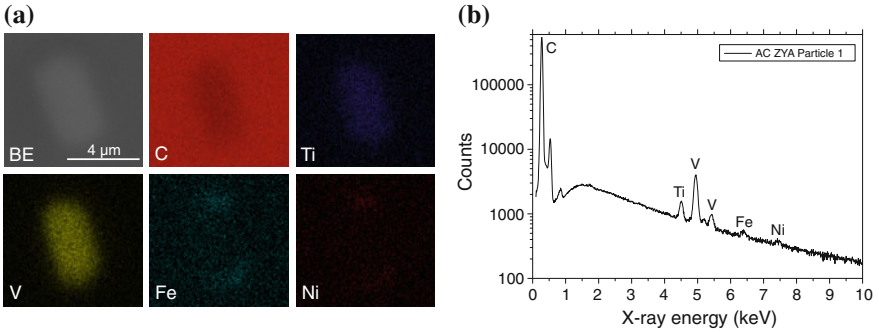

Fig. 3.15 EDX analysis of a single grain in AC ZYA: **a** BE and elemental maps of a 2.5 μm × 4.5 μm sized grain. The Fe and Ni map indicate that both elements are enriched at the outer edge as already seen in Fig. 3.12. **b** EDX spectrum showing peaks for the 3d-metals inside the grain. The peaks of Fe and Ni suffer from a comparably poor statistics. Taken from [53]

Fig. 3.15). From the spectrum, however, no direct information on depth and thickness of the grain can be obtained making a quantitative analysis, e.g. the determination of the metallic content, difficult. Qualitative analysis though shows that the Ti/V concentration ratio matches quite well the results from PIXE/RBS on the grain in Fig. 3.12 from the same sample, whereas the Fe and Ni concentrations are both twice as large as for PIXE. This might be due to differences in the composition of individual grains as pointed out earlier and/or due to the rather poor statistics in the EDX spectrum (see Fig. 3.15b) and the insufficient knowledge of grain thickness and depth.

Let us assume that the metallic content of single grains can be accurately determined with EDX, then bulk concentrations can in principle be estimated from these data with the help of the grain density as was done in [47–49]. This approach, however, has several weaknesses: (i) It requires that all the grains in a sample are comparable in metallic content and composition which is not necessarily the case as Fig. 3.13 shows; (ii) The number density of grains must be determined, e.g. using BE imaging. Since only a very low number of grains is present in HOPG in the near-surface area of $\lesssim$1 μm depth even for large scan areas (e.g. in [49] only three grains are visible for AC ZYA in a 1.0 mm × 0.9 mm scan area) substantial statistical errors exist; (iii) Trace elements not enriched in grains are not taken into account at all. These difficulties lead us to the conclusion that EDX is useful for identifying and imaging metallic grains in HOPG, but cannot be considered as a reliable method for quantitative trace element analysis in graphite. Indeed, the Fe concentration in AC ZYA estimated from SEM analysis (and magnetization data) was 6 μg/g in [49], whereas PIXE analysis always gave $<$1 μg/g Fe for numerous of AC ZYA samples in the last ten years.

3.3 Quasi Two-Dimensional Spin Waves Excitations in the Ferromagnetic Response in Virgin and Ion Irradiated Graphite

As will be shown below in Sect. 3.3.1 and Fig. 3.16 therein, the ferromagnetic contribution to the magnetization of proton irradiated HOPG decreases linearly with temperature T. This indicative result suggests the existence of 2D spin waves excitations [61–63], either in the saturated region (field applied much above the coercive field), at intermediate fields or, as we shall see below, also in the remanent state at zero field [29, 33, 44].

The analysis of the measured temperature dependence of the magnetization is done in terms of the two-dimensional Heisenberg model 2DHM with anisotropy that provides a linear dependence with temperature [34]. The discrete Hamiltonian describing the 2DHM reads:

$$H = -J \sum_{ij} [S_{iz} S_{jz} + (1 - \Delta)(S_{ix} S_{jx} + S_{iy} S_{jy})] \,, \tag{3.3}$$

where $S_i = (S_{ix}, S_{iy}, S_{iz})$ is a unit vector pointing in the direction of the classical magnetic moment placed at site i of a 2D lattice. The sum (i, j) is taken over all nearest neighbor pairs with J being the exchange coupling. The parameter Δ is the uniaxial anisotropy in the z-direction. Whereas $\Delta = 0$ represents the isotropic 2DHM which is known to have $T_C = 0$, a small anisotropy already raises T_C considerably because $T_C \propto -1/\ln \Delta$ for $\Delta \to 0$.

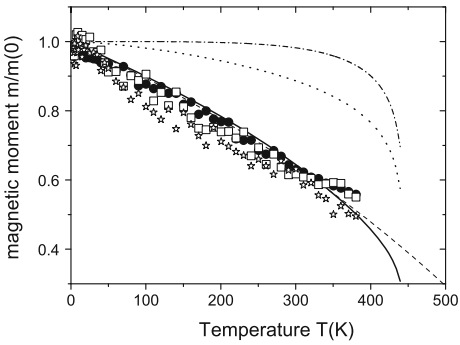

Fig. 3.16 Normalized magnetic moment ($m(0) = 4.9$ μemu at 10 kOe) obtained for a 6 mg sample (sample 4 in [33]) at (10,3,1) kOe (•, □, ⋆) after subtracting the data from the same sample before irradiation and a paramagnetic (Curie) contribution $m_p(T) = 1.18H/T$ [μemu K/kOe]. The different theoretical curves are: The continuous line follows (3.5), the *dashed-dotted line* the Ising model, the *dotted line* the 3D case Bloch $T^{3/2}$-law that includes spin waves in 3D systems, and the *dashed line* the 2D spin waves case that follows (3.4). The used parameters are: $T_C = 450$ K and $T_C^{sw} = 1050$ K. Taken from [34]

As can be shown [61–63], the normalized spin wave magnetization in the anisotropic axis can be expressed as:

$$M_z^{sw} = 1 - T/T_C^{sw} - 2T^2/(T^\star T_C^{sw}) - (2/3)(T/T_C^{sw})^3\,, \tag{3.4}$$

at low temperatures ($T^\star = 4J$) [61–65]. Here, T_C^{sw} is the spin wave critical temperature due to low-energy spin wave excitations, given by $k_B T_C^{sw} = 2\pi J/K(1-\Delta)$ with $K(x)$ being the elliptic function. Note that near the Curie temperature T_C the 2D Ising model provides a better description of the spin flip excitations. In this case $T_C(\hat{J}) = 1.52\hat{J}$ [64], where $\hat{J}$ is the renormalized exchange due to spin waves excitations and given by $\hat{J}(T) = J(1 - 2T/T_C^{sw})$. Finally, the measured magnetization $M_z(T < T_C)$ can be described as:

$$M_z(T) \approx M_z^{sw}(T, J)\, M_z^I[T, \hat{J}(T)]. \tag{3.5}$$

The first factor $M_z^{sw}(T, J)$ on the right hand side of (3.5) is the magnetization due to spin waves, whereas the second one, $M_z^I[T, \hat{J}(T)]$ describes the magnetization based on an Ising model with the exchange $\hat{J}$ renormalized by the spin waves. In [33, 63] this theoretical result was checked against Monte Carlo calculations and good agreement was obtained, especially for low anisotropies.

There is one more issue that deserves a discussion, namely how to treat the lattice disorder in case the magnetic phase transition does survive. Remember that irradiation produces C-vacancies everywhere and the graphite lattice remains intact only up to a certain density, let us say around 5%. At much larger densities of defects the graphite lattice will collapse and no magnetic order will appear. In fact, amorphous carbon shows no magnetic order but paramagnetism [66]. In case of "soft" disorder the stiffness $2\langle S\rangle J$ is modified to $2\langle S\rangle J[1 - (pz/(z-2))]$ with z being the number of nearest neighbors and $0 \le p \le p_c$, where $p = 0$ means no disorder and p_c is a critical percolation disorder parameter ($p_c \approx 0.4$) above which no spontaneous magnetization occurs [67, 68]. For the effective stiffness that fits the experiment this renormalization should be taken into account.

3.3.1 2D Spin Waves in Irradiated and Virgin HOPG Samples

Figure 3.16 shows the normalized magnetic moment obtained from a HOPG sample irradiated with 6 spots of 2.0 MeV protons, each of 0.8 mm diameter and 1.9×10^{17} cm^{-2} fluence (total irradiated charge 900 μC) at a proton current of 100 nA [34]. In addition, different 3D and 2D models, including spin waves using an anisotropy $\Delta \lesssim 10^{-4}$ are plotted which demonstrate that the temperature dependence of the magnetic moment can be best described by the 2D spin wave model.

It is worth noting that the data in Fig. 3.16 show the direct influence of the irradiation on the magnetic response of the sample, because the signal before irradiation

was subtracted, as well as a paramagnetic signal (due to irradiation) that contributes significantly only at $T \lesssim 25$ K. As we clarify below, if the measurement is done under a magnetic field, the subtraction of the signal before irradiation is necessary because of the non-negligible temperature dependent background of the HOPG samples. For all measurements done under a magnetic field, the temperature dependence of the total magnetic moment of a HOPG sample (in the case discussed here with field parallel to the graphene layers) is given by the sum of: (i) The intrinsic Landau diamagnetism of the HOPG sample, which is given by a small misalignment between the field and the parallel to the graphene planes direction; (ii) The possible temperature dependence of the magnetic contribution from the substrate/sample holder, which in general should be negligible, if an appropriate holder is used; (iii) The temperature dependence of the ferromagnetic contribution itself. We note that there is an uncertainty in the temperature dependence of the corresponding diamagnetic background. This is a non-negligible source of error when a quantitative comparison of the temperature dependence of the saturation magnetization $M_{\rm sat}(T)$ with appropriate models is required. Therefore, one possible way to avoid this uncertainty is to compare the remanent magnetization measured at zero applied field, see Fig. 3.17. In the case of the ferromagnetism found in the HOPG samples the remanent (zero field) magnetization $M_{\rm rem}(T)$ can show a similar temperature dependence as the saturation one $M_{\rm sat}(T)$ (or at applied fields below saturation as shown in Fig. 3.17).

This is expected when the applied field does not change the energy landscape of the domain walls and when there is no magnetic anisotropy that strongly changes with temperature. The similarity between the temperature dependence of $M_{\rm sat}(T)$ and $M_{\rm rem}(T)$ can be observed in hard as well as soft ferromagnets. As an example of some

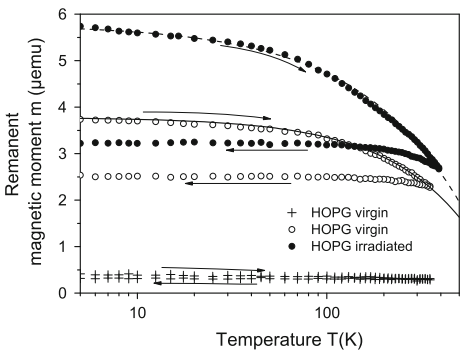

Fig. 3.17 Remanent moment versus temperature of: (○) virgin HOPG sample of mass 14.2 mg. The continuous line is the function $m[\mu\text{emu}] = 3.78 - 0.43 \times 10^{-2} T$ with T in Kelvin. (+): virgin HOPG sample of mass 11.1 mg. (●): HOPG sample (mass 14.2 mg) irradiated with low proton fluence ($\Phi \lesssim 6 \times 10^{16}$ cm^{-2}) with a broad proton beam. The *dashed line* follows the function $m[\mu\text{emu}] = 5.78 - 2.65 \times 10^{-2} T^{0.8}$. Note that the absolute values of the diamagnetic signals are rather meaningless due to the large influence of the sample misalignment with respect to the applied field direction on the diamagnetic contribution, a misalignment that changes from sample to sample. Taken from [29]

soft ferromagnets where $M_{\text{rem}}(T)/M_{\text{sat}}(T) \lesssim 0.1$ and constant in the temperature region clearly below the corresponding Curie temperature, see [69].

The unequivocal quasi-linear temperature dependence is an indication of 2D magnetism, see Fig. 3.16, and the slope of $m(T)$ can be interpreted as due to the excitation of 2D spin waves [34]. Because virgin HOPG samples are not ideal and can also have lattice defects as vacancies and/or hydrogen, we expect that, if the magnetic impurities contribution is negligible, they also should show the 2D spin waves influence in their magnetic response. Figure 3.17 shows the temperature dependence of the remanent magnetic moment of two virgin samples and an irradiated one, for comparison. The samples with a finite remanent magnetization show also a quasi-linear irreversible temperature dependence in the warming up state, see Fig. 3.17. Ferromagnetic order in pristine HOPG was also observed by Miao et al. [70] who demonstrated that sample annealing at 2300 °C leads to the extinction of the magnetic order, indicating that the magnetic order is related to vacancies, defect and localized edge states.

3.4 Transport Measurements: Magnetoresistance and Anisotropic Magnetoresistance Results

A direct, alternative method to detect and study magnetic order is to measure the magnetoresistance (MR). The MR develops a characteristic butterfly loop when measured versus magnetic field. Additionally, for a ferromagnet we might expect that the MR depends on the orientation of the magnetization with respect to the electric current direction, i.e. the so called Anisotropic MR (AMR), see for example [61, 71–73]. The AMR was discovered by William Thomson (Lord Kelvin) in 1867 and is nowadays considered one key transport property of a magnetically ordered material. To understand the origin of the angular dependence of the resistance on θ, the angle between the magnetization and the input current directions, in conventional, e.g. d-ferromagnets, one takes the following concepts into account: (i) There are two bands, s- and d-band, where the d-band has a spin splitting due to the exchange interaction; (ii) The resistivity increases due to the scattering of s-electrons into the d-band, a band where the carriers have higher effective mass and less mobility; (iii) If due to the spin splitting the d-band remains full (i.e. below the Fermi level E_F) for one spin direction, s-electrons with the same spin direction cannot be scattered into that spin part of the d-band so that a decrease of the resistivity is expected as long as no spin-flips occur; (iv) However, if spin-flips occur, then the above mentioned scattering process is still possible.

A spin-flip process is introduced in the Hamiltonian via the **LS** coupling. In this case s-electrons can be scattered in free $3d$-states (or other states that are involved in the magnetic order) only if their momentum $\mathbf{k}$ is in the same plane as the classical orbital of the free $3d$-states. The occupation of the $3d$-orbital states (spin-up and -down) is given by the magnetization direction. Note that the free $3d$-states will

have a **L**-component always normal to the magnetization direction. For example, if we consider free $3d$-states of the type $3d_{x^2-y^2}$ and the current **I** is parallel to the magnetization **M** and both are parallel to the (x, y) plane, the free $3d$-states will have an angular momentum component normal to **I**. That means that the classical orbits will be on the same plane as the electron momentum originating in a larger scattering cross section, increasing in this case the resistance. Neglecting the explicit dependence of the resistivity on the angle to the principal axes of the crystal (i.e. the magneto-crystalline anisotropy) and for a large enough applied magnetic field, the angular dependence of the AMR is given by:

$$\rho(\theta) = \rho_{\perp} + (\rho_{\parallel} - \rho_{\perp}) \cos^2(\theta) \,, \tag{3.6}$$

where $\rho_{\parallel}$ ($\rho_{\perp}$) denotes the longitudinal resistivity measured for **I** $\parallel$ ($\perp$)**M** [73]. This angular dependence is common for the AMR of polycrystalline magnetic samples.

Clearly, in graphite there are no d-bands. Nevertheless, in case the graphite sample shows magnetic order there is a spin splitting in the π- but also, and in a broader energy range, in the σ-band as XMCD results indicate [12, 45]. Therefore, we may expect that an AMR should be measurable. Leaving apart details of the orbital moments involved in this property, the origin of the AMR in magnetic graphite should be qualitatively similar to that in conventional transition metals-based ferromagnets, instead of $s - d$ scattering one should think on a $\pi - \sigma$ one. A rigorous theoretical description of the AMR in magnetic graphite on this basis is, however, not yet done.

Figure 3.18 shows the results of the resistance versus applied field at a constant temperature and at different angles between current and field direction of an irradiated HOPG sample. The HOPG sample of dimensions $4.4 \times 1.0 \times 0.01$ mm^3 was irradiated with 12 spots, 0.8 mm diameter each, of 2 MeV protons of nominal 6×10^{16} cm^{-2} fluence [29], see the sketch in Fig. 3.18a. The four-point van der Pauw arrangement and experimental conditions used in [29] allowed for low-noise transport measurements with a relative resolution of $\sim$10 ppm in the resistance R. The irradiated sample had 100 times larger resistivity than in its virgin state. Firstly, a negative MR is observed independently of the field direction (within the plane). This negative MR means that the scattering probability for, e.g., $s - \pi$ or $s - \sigma$ scattering decreases with increasing spin-ordering of the magnetic moments in the sample. Therefore, the solely negative MR already suggests the existence of magnetic ordering in the irradiated sample. The clear magnetic hysteresis loop within the negative MR, see Fig. 3.18b, leaves no doubt on the magnetic state and the existence of magnetic domains.

Figure 3.18a shows the MR at 25 K for three angles θ between the field and the external input current ($\theta = 0$ means field parallel to the current and the sample's main axis). The observed behavior as well as the absolute change of the MR is compatible with the AMR effect (see, for example, the results in ferromagnetic Co-nanowires [74]). In the upper inset of Fig. 3.18a the MR at 6 T field versus angle θ follows the expected $\cos^2(\theta)$ dependence given by (3.6). From the AMR data one can estimate the change of the magnetization at saturation $M_{\rm sat}$ assuming that $M_{\rm sat} \propto (\mathrm{MR})^{1/2}$ at high enough fields. The obtained $M_{\rm sat}$ decreases linearly with T in agreement with

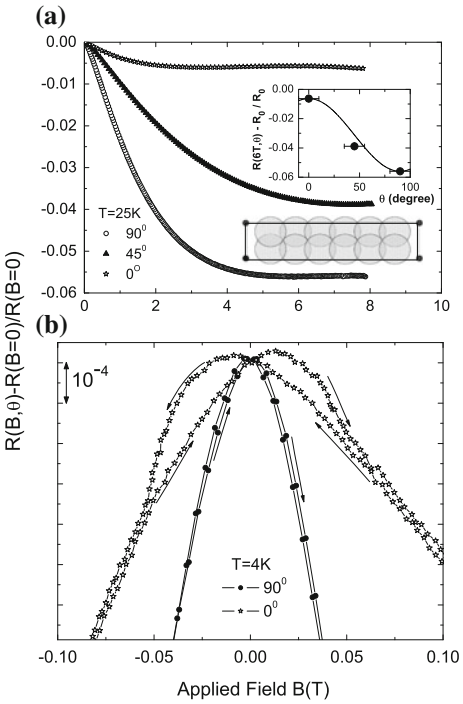

Fig. 3.18 **a** Magnetoresistance (MR) versus magnetic field at 25 K for three angles between field and current of a HOPG sample irradiated with 12 spots (see sketch). The error in the angle θ was $\pm 10°$. The *inset* shows the MR ($R_0 = R(0, \theta)$) versus θ and the continuous line follows a $\cos^2(\theta)$ dependence. The magnetic field is always parallel to the surface of the sample, i.e. to the graphene layers. **b** Hysteresis loops in the MR for the same sample. The measurements were done starting at a field of +8 T. The asymmetry in the hysteresis at $\theta = 0°$ might be due to different domain structures between the positive and negative direction of the applied field and/or the contribution of a Hall-like signal. Taken from [29]

SQUID results in other, irradiated and non-irradiated ferromagnetic graphite samples, see Fig. 3.17, and indicate a critical temperature $T_C \sim (190 \pm 10)$ K. With the simple model from [9] and this T_C we expect a distance between vacancies between 2.5 and 3 nm, in reasonable agreement with the estimated distance the magnetic moments from vacancies should have in the first 10 μm depth for the nominal fluence [29].

In [75] the changes in the ferromagnetic behavior of graphite powder and graphite flakes after treatment with diluted sulphuric acid have been studied. This kind of acid treatment enhances substantially the ferromagnetic magnetization of virgin micrometer-sized graphite powder as well as in graphite flakes. In that study, the anisotropic magnetoresistance (AMR) has been measured in a graphite flake before and after acid treatment.

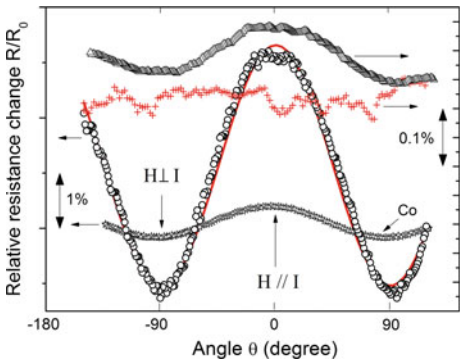

Fig. 3.19 Relative change of the electrical resistance versus the angle between the magnetic field ($\mu_0 H = 0.5$ T) and the applied current for the graphite flake at 300 K before (+, *right* $y-$axis) and after acid treatment ($\triangle$, right $y-$axis). ($\bigcirc$): data obtained after acid treatment at 30 K under same conditions (*left* y-axis). The continuous line follows the $\cos^2(\theta)$ function. For comparison the AMR measured in a Co polycrystalline film at 300 K is also shown ($\star$, *left* $y-$axis). Taken from [75]

Figure 3.19 shows the change in resistance with the angle between the magnetic field and input current, where the field was always applied parallel to the main area of the graphite flake. Whereas the graphite flake does not reveal any AMR within experimental resolution before acid treatment, the change is clearly resolved after acid treatment, even at room temperature, see Fig. 3.19. One can also see that the AMR follows very well the expected $\cos^2(\theta)$ dependence. It is worth emphasizing that the remarkable observation of the AMR in irradiated as well as in acid-treated graphite indicates the existence of a spin-splitting, or a non-spherical symmetry of the charge distribution, and a non-negligible spin-orbit interaction. A theoretical study of the anisotropy of the MR has yet to be done and several details are to be clarified in future studies.

3.5 Further Evidence for DIM in Graphite: A Literature Review

In the following, we will concentrate on further experimental evidence for defect-induced magnetism in graphite taken from literature. However, DIM was also found in numerous other materials, e.g. carbon nanotubes [76–79], carbon nanofoam [80–84], ion irradiated fullerene films [85–87], ion implanted nano-sized diamond [88], diamond-like carbon [89] as well as SiC irradiated with ions [90–95] or neutrons [96].

3.5.1 DIM in HOPG by Ion Irradiation

The first independent proof of defect-induced magnetism in HOPG created by ion irradiation was published in 2008, five years after the first report of DIM induced by proton irradiation in HOPG [30]. Xia et al. demonstrated room-temperature ferromagnetism with a Curie temperature of $T_C = 460$ K in HOPG after 70 keV $^{12}C^+$ ion implantation [97]. The maximum magnetization achieved was 9.3 emu/g for an ion fluence of $\phi = 2 \times 10^{15}$ cm^{-2}. The temperature dependence of the remanent magnetic moment was found to follow an uniaxial anisotropic 2D Heisenberg model in line with the findings on MeV proton irradiated HOPG [34]. Furthermore, impurity concentrations were determined to $\sim$1 μg/g using PIXE, clearly demonstrating the intrinsic nature of the magnetic order.

In 2009, Yang et al. reported room-temperature ferromagnetism, again in 70 keV $^{12}C^+$ implanted HOPG [98]. Using various positron annihilation techniques for depth profiling of the defect density and DFT calculations they concluded that the magnetic order is closely related to vacancies and vacancy clusters, the authors cannot exclude a contribution from hydrogen though. It is interesting to note, that sample annealing at 200 °C was found to reduce the vacancy density and led to a complete loss of the magnetic order.

In 2011, medium energy 225 keV proton and He^+ irradiation was used by Makarova et al. to trigger magnetic order in HOPG [32]. The magnetic moments of the samples were in the range of $(2 - 25) \times 10^{-6}$ emu, clearly above potential contributions from the $\sim$1 μg/g impurities determined with high-resolution ICP-MS and PIXE. Whereas for high ion fluences the magnetic response was found to be isotropic, an anisotropic response was reported for low fluences. Raman studies indicate that the degradation of the magnetic ordering at high ion fluences starts well before the amorphization of the graphite lattice.

In the same year, He et al. used successive $^{12}C^+$ implantations with various ion energies in the range from 15 keV to 70 keV in order to get a homogeneous depth profile of the defects [99]. In this way, room-temperature ferromagnetism was induced with magnetization M_{sat} up to 17.6 emu/g. This value is in agreement with that obtained in [12] for a proton irradiated HOPG sample where the graphite mass to which the ferromagnetism is restricted is known. The average magnetic moment was estimated to 0.02–0.03 μ_B per carbon atom [99], consistent with proton irradiated HOPG [34].

Several studies on this topic were published in 2012. Mohanta et al. studied the magnetic response of HOPG after 40 MeV $^{12}C^+$ irradiation with SQUID magnetometry and γ-ray differential perturbed angular distribution (TDPAD) measurements of the hyperfine field using ^{19}F nuclei recoil-implanted into a depth $\sim$7 μm below the surface [100]. Whereas SQUID data show a ferromagnetic response, the hyperfine field data only show enhanced paramagnetism, but no long-range magnetic ordering. The authors therefore believe that the magnetic ordering is restricted to the near-surface region, in line with XMCD measurements on proton irradiated HOPG [12].

Shukla et al. reported magnetic moments up to $m_{sat} \sim 1.4 \times 10^{-4}$ emu for 1 MeV $^{12}C^{+}$ irradiated HOPG [101], approximately 100 times larger than reported for MeV proton irradiation and still a factor 10 larger than for 70 keV $^{12}C^{+}$ irradiation. For the sample with the largest magnetic moment the defect separation was estimated to be 0.3–0.7 nm varying with depth below surface, significantly smaller than reported in [21]. The magnetic moment decreases again on further increasing ion fluences.

Near edge X-ray absorption fine structure angular resolved (NEXAFS) combined with magnetization measurements were used by He et al. to study the role of defect electronic states in the magnetism of HOPG implanted with 15–70 keV $^{12}C^{+}$ ions [102]. They found a clear correlation of pre-edge features in X-ray absorption with the observed magnetization for different fluences and annealing temperatures and attribute the origin of the ferromagnetism to defect-induced electronic states near the Fermi level. The authors admitted that C-H bonds might contribute to the magnetic order as well.

Pires et al. implanted 120 keV Na in HOPG with concentrations up to 2 at% and studied the magnetization and planar magnetoresistance—both showing a strong correlation [103]. The maximum magnetic moment was observed for a Na concentration of 1 at% and the ferromagnetic response attributed to point defects or small vacancy clusters.

In the study of Shukla et al. 2 MeV proton and 1 MeV $^{12}C^{+}$ irradiation was used to trigger ferromagnetic ordering in HOPG [104]. Magneto-resistance measurements showed that the magnetic ordering sensitively depends on defect separation which ranges between 1.7 nm at the surface and 0.5 nm near the ion range for the sample irradiated with $\Phi \sim 2 \times 10^{17}$ cm^{-2} protons. The authors state that under these conditions magnetic ordering can only be achieved in part of the sample. The findings for the $^{12}C^{+}$ implanted sample are similar.

3.5.2 *Defective Graphitic Materials*

Besides the deliberate introduction of defects into graphite by ion irradiation defective graphitic material can also be obtained by chemical synthesis, e.g. from suitable precursor compounds. One example is the pyrolytic carbon obtained by Kamishima et al. from triethylamine [105]. The authors report ferromagnetism with a magnetization at saturation of $M_{sat} \sim 0.5$ emu/g at room temperature. From XRD measurements they conclude that this magnetic order cannot be attributed to impurities but may be related to a graphite-like structure.

In 2008, Li et al. produced Pb-C nanocomposites from which carbon nanocomposites were extracted by chemical treatment [106]. XRD and magnetization measurements allowed to relate magnetic properties to the degree of crystallization. It was found that disordered carbon is diamagnetic while oriented pyrolytic graphite shows ferromagnetism. For HOPG nanospheres magnetizations at saturation up to $M_{sat} \sim 0.18$ emu/g were obtained at $T = 2$ K.

Local room-temperature ferromagnetism at the grain boundaries of untreated ZYH-grade HOPG was reported by Červenka et al. [107]. Bulk magnetization measurements showed hysteresis and magnetization up to $M_{sat} \sim 2.5 \times 10^{-3}$ emu/g at room temperature, whereas magnetic force microscopy was used to study the magnetic response at grain boundaries. Those, forming a two-dimensional array of point defects, were proposed to be the most probable source of magnetism in graphite. It should be noted, however, that Martínez-Martín et al. raised serious doubts on the validity of these MFM measurements and their interpretation [108].

In 2015, Wang et al. reported strong magnetism in pure carbon films grown by electron irradiation assisted PVD [109]. In the amorphous film matrix, which only showed weak paramagnetism, the development of graphene nanocrystallites was observed exhibiting strong ferromagnetism with M_{sat} up to 0.37 emu/g at room temperature. This magnetism was attributed to spin magnetic moments at the edges of the graphene layer.

Finally, we note that the magnetic order in graphite-related materials should be detectable by carbon nuclei in the surroundings of the defects responsible for the magnetism. Recently, Freitas et al. determined the hyperfine magnetic field at the atomic ^{13}C nucleus using nuclear magnetic resonance (NMR) technique [110]. The direct measurement of the hyperfine field, its value ($\simeq$24 T) and the agreement with the results of the Density Functional Theory calculations confirm further the intrinsic, defect-related origin of the magnetic order in carbon-based materials, and rule out magnetic impurities as possible source for the observed behavior.

References

1. K. Kusakabe, M. Maruyama, Phys. Rev. B **67**, 092406 (2003)
2. Y. Ma, P.O. Lehtinen, A.S. Foster, R.M. Nieminen, New J. Phys. **6**, 68 (2004)
3. P.O. Lehtinen, A.S. Foster, A. Ayuela, A. Krasheninnikov, K. Nordlund, R.M. Nieminen, Phys. Rev. Lett. **91**, 017202 (2003)
4. M.M. Ugeda, I. Brihuega, F. Guinea, J.M. Gómez-Rodríguez, Phys. Rev. Lett. **104**, 096804 (2010)
5. P. Esquinazi, *Magnetic Carbon, Handbook of Magnetism and Advanced Magnetic Materials*, vol. 4, pp. 2256–2281, ed. by H. Kronmüller, S. Parkin (Wiley, Chichester, 2007)
6. O.V. Yazyev, Rep. Prog. Phys. **73**, 056501 (2010)
7. M. Stoneham, J. Phys.: Condens. Matter **22**, 074211 (2010)
8. P. Esquinazi, W. Hergert, D. Spemann, A. Setzer, A. Ernst, IEEE Trans. Magn. **49**(8), 4668 (2013)
9. L. Pisani, B. Montanari, N. Harrison, New J. Phys. **10**, 033002 (2008)
10. E.J. Duplock, M. Scheffler, P.J.D. Lindan, Phys. Rev. Lett. **92**, 225502 (2004)
11. O.V. Yazyev, Phys. Rev. Lett. **101**, 037203 (2008)
12. H. Ohldag, P. Esquinazi, E. Arenholz, D. Spemann, M. Rothermel, A. Setzer, T. Butz, New J. Phys. **12**, 123012 (2010)
13. M. Sepioni, R.R. Nair, S. Rablen, J. Narayanan, F. Tuna, R. Winpenny, A.K. Geim, I.V. Grigorieva, Phys. Rev. Lett. **105**(20), 207205 (2010)
14. A. Ney, P. Papakonstantinou, A. Kumar, N.G. Shang, N. Peng, Appl. Phys. Lett. **99**(10), 102504 (2011)

15. M. Ricco, D. Pontiroli, M. Mazzani, M. Choucair, J.A. Stride, O.V. Yazyev, Nano Lett. **11**(11), 4919 (2011)
16. R.R. Nair, M. Sepioni, I.L. Tsai, O. Lehtinen, J. Keinonen, A.V. Krasheninnikov, T. Thomson, A.K. Geim, I.V. Grigorieva, Nat. Phys. **8**(3), 199 (2012)
17. S. Just, S. Zimmermann, V. Kataev, B. Buechner, M. Pratzer, M. Morgenstern, Phys. Rev. B **90**(12), 125449 (2014)
18. J. Ziegler, M. Ziegler, J. Biersack, Nucl. Instrum. Methods B **268**, 1818 (2010)
19. P. Reichart, D. Spemann, A. Hauptner, A. Bergmaier, V. Hable, R. Hertenberger, C. Greubel, A. Setzer, T. Butz, G. Dollinger, D. Jamieson, P. Esquinazi, Nucl. Instrum. Meth. Phys. Res. B **249**, 286 (2006)
20. J. Barzola-Quiquia, P. Esquinazi, M. Rothermel, D. Spemann, T. Butz, Nucl. Instrum. Methods Phys. Res. B **256**, 412 (2007)
21. M.A. Ramos, J. Barzola-Quiquia, P. Esquinazi, A. Muñoz, Martin, A. Climent-Font, M. García-Hernández, Phys. Rev. B **81**, 214404 (2010)
22. X. Yang, H. Xia, X. Qin, W. Li, Y. Dai, X. Liu, M. Zhao, Y. Xia, S. Yan, B. Wang, Carbon **47**, 1399 (2009)
23. Y. Virmani, J. Zimbrick, E. Zeller, Carbon **10**(5), 613 (1972)
24. N.W. Ashcroft, N.D. Mermin, *Solid State Physics*, p. 653 ff (Holt-Saunders International Editions, Philadelphia, 1981)
25. P.O. Lehtinen, A.S. Foster, Y. Ma, A. Krasheninnikov, R.M. Nieminen, Phys. Rev. Lett. **93**, 187202 (2004)
26. O.V. Yazyev, L. Helm, Phys. Rev. B 75, 125408 (2007). See also O.V. Yazyev, Phys. Rev. Lett. **101**, 037203 (2008)
27. Y. Zhang, S. Talapatra, S. Kar, R. Vajtai, S.K. Nayak, P.M. Ajayan, Phys. Rev. Lett. **99**, 107201 (2007)
28. E.V. Castro, M.P. López-Sancho, M.A.H. Vozmediano, arXiv:0906.4126
29. P. Esquinazi, J. Barzola-Quiquia, D. Spemann, M. Rothermel, H. Ohldag, N. García, A. Setzer, T. Butz, J. Magn. Magn. Mater. **322**, 1156 (2010)
30. P. Esquinazi, D. Spemann, R. Höhne, A. Setzer, K.H. Han, T. Butz, Phys. Rev. Lett. **91**, 227201 (2003)
31. S. Mathew, B. Joseph, B.R. Sekhar, B.N. Dev, Nucl. Instrum. Methods **266**(14), 3241 (2008)
32. T.L. Makarova, A.L. Shelankov, I.T. Serenkov, V.I. Sakharov, D.W. Boukhvalov, Phys. Rev. B **83**(8), 085417 (2011)
33. J. Barzola-Quiquia, J.L. Yao, P. Rödiger, K. Schindler, P. Esquinazi, Phys. Stat. Sol. (a) **205**, 2924 (2008)
34. J. Barzola-Quiquia, P. Esquinazi, M. Rothermel, D. Spemann, T. Butz, N. García, Phys. Rev. B **76**, 161403(R) (2007)
35. K.M. McCreary, A.G. Swartz, W. Han, J. Fabian, R.K. Kawakami, Phys. Rev. Lett. **109**(18), 186604 (2012)
36. M. Moaied, J.V. Alvarez, J.J. Palacios, Phys. Rev. B **90**(11), 115441 (2014)
37. A.L. Friedman, H. Chun, Y.J. Jung, D. Heiman, E.R. Glaser, L. Menon, Phys. Rev. B **81**(11), 115461 (2010)
38. T. Saito, K. Terashima, Y. Utsushikawa, J. Appl. Phys. **107**(7), 073522 (2010)
39. L. Xie, X. Wang, J. Lu, Z. Ni, Z. Luo, H. Mao, R. Wang, Y. Wang, H. Huang, D. Qi, R. Liu, T. Yu, Z. Shen, T. Wu, H. Peng, B. Oezyilmaz, K. Loh, A.T.S. Wee, A.W. Chen, Appl. Phys. Lett. **98**(19), 193113 (2011)
40. C.N.R. Rao, H.S.S.R. Matte, K.S. Subrahmanyam, U. Maitra, Chem. Sci. **3**(1), 45 (2012)
41. S.C. Ray, N. Soin, T. Makgato, C.H. Chuang, W.F. Pong, S.S. Roy, S.K. Ghosh, A.M. Strydom, J.A. McLaughlin, Sci. Rep. **4**, 3862 (2014)
42. Y. Wang, P. Pochet, C. Jenkins, E. Arenholz, G. Bukalis, S. Gemming, M. Helm, S. Zhou, Phys. Rev. B **90**, 214435 (2014)
43. R. Krishna, A.N. Jones, B.J. Marsden, Radiat. Phys. Chem. **107**, 121 (2015)
44. H. Xia, W. Li, Y. Song, X. Yang, X. Liu, M. Zhao, Y. Xia, C. Song, T.W. Wang, D. Zhu, J. Gong, Z. Zhu, Adv. Mater. **20**, 4679 (2008)

45. H. Ohldag, T. Tyliszczak, R. Höhne, D. Spemann, P. Esquinazi, M. Ungureanu, T. Butz, Phys. Rev. Lett. **98**, 187204 (2007)
46. S. Johansson, J. Campbell, K. Malmqvist, *Particle-Induced X-Ray Emission Spectrometry (PIXE)* (Wiley, New York, 1995)
47. M. Sepioni, R. Nair, I. Tsai, A. Geim, I. Grigorieva, EPL **97**, 47001 (2012). See also comment by D. Spemann et al., EPL **98**, 57006 (2012) and reply by Sepioni et al. EPL **98**, 57007 (2012)
48. R. Nair, M. Sepioni, I. Tsai, O. Lethinen, O. Keinonen, A. Krasheninnikov, T. Thomson, A. Geim, I. Grigorieva, Nat. Phys. **8**, 199, Supplementary information #4 (2012)
49. M. Venkatesan, P. Dunne, Y. Chen, H. Zhang, J. Coey, Carbon **56**, 279 (2013)
50. D. Spemann, T. Reinert, J. Vogt, T. Andrea, N. Barapatre, R. Feder, A. Jakob, N. Liebing, C. Meinecke, F. Menzel, M. Rothermel, T. Butz, Nucl. Instrum. Methods B **269**, 2175 (2011)
51. W. Chu, J. Mayer, M. Nicolet, *Backscattering Spectrometry* (Academic Press, New York, 1978)
52. C. Ryan, Nucl. Instrum. Methods B **181**, 170 (2001)
53. D. Spemann, P. Esquinazi, A. Setzer, W. Böhlmann, AIP Adv. **4**, 107142 (2014)
54. E. Oberg, *Machinery's Handbook*, 25th edn. (Industrial Press Inc., New York, 1996)
55. L. Doolittle, Nucl. Instrum. Methods B **9**, 344 (1985)
56. MIKROMASCH. Highly ordered pyrolytic graphite. www.spmtips.com/test-structures-HOPG.html. Accessed 4 Sept 2014
57. A. Tsuzuki, S. Sago, S. Hirano, S. Naka, J. Mater. Sci. **19**, 2513 (1984)
58. A. Vočadlo, J. Brodholt, D. Dobson, K. Knight, W. Marschall, G. Price, I. Wood, Earth Planet. Sci. Lett. **203**, 567 (2002)
59. A. Talyzin, A. Dzwilewski, L. Dubrovinsky, A. Setzer, P. Esquinazi, Eur. Phys. J. B **55**, 57 (2007)
60. R. Faccio, H. Pardo, F.M. Araujo-Moreira, A.W. Mombru, Chem. Phys. **449**, 14 (2015)
61. W. Döring, Z. Naturforsch. **A16**, 1008 (1961)
62. A.P. Levanyuk, N. García, J. Phys.: Condens. Matter **4**, 10277 (1992)
63. P.A. Serena, N. García, A.P. Levanyuk, Phys. Rev. B **47**, 5027 (1993)
64. E. Brezin, J. Zin-Justin, Phys. Rev. B **14**, 3110 (1976)
65. D.R. Nelson, R.A. Pelcovitz, Phys. Rev. B **16**, 2191 (1977)
66. R. Höhne, K.H. Han, P. Esquinazi, A. Setzer, H. Semmelhack, D. Spemann, T. Butz, J. Magn. Magn. Mater. **272–276**, e839 (2004)
67. S. Kirkpatrick, Rev. Mod. Phys. **45**, 574 (1972)
68. R.C. Jones, G.J. Yates, J. Phys. C: Solid State Phys. **8**, 1705 (1975)
69. R. Sanz, M. Cerdán, M.D.M.M.E. McHenry, EEE Trans. Magn. **47**, 4124 (2011)
70. X. Miao, S. Tongay, A.F. Hebard, Carbon **50**, 1614 (2012)
71. W. Döring, G. Simon, Ann. Phys. **460**, 373 (1960)
72. C. Fert, *Ferromagnetic Materials*, vol. 3 (North-Holland, Amsterdam, 1982) (chap. 9)
73. R.C. O'Handley, *Modern Magnetic Materials* (Wiley, New York, 2000)
74. G. Dumpich, T.P. Krome, B. Hausmanns, J. Magn. Magn. Mater. **248**, 241 (2002)
75. J. Barzola-Quiquia, W. Böhlmann, P. Esquinazi, A. Schadewitz, A. Ballestar, S. Dusari, L. Schultze-Nobre, B. Kersting, Appl. Phys. Lett. **98**, 192511 (2011)
76. D.-C. Yan, S.-Y. Chen, M.-K. Wu, C.C. Chi, J.H. Chao, M.L.H. Green, Appl. Phys. Lett. **96**, 242503 (2010)
77. A.L. Friedman, H. Chun, Y.J. Jung, D. Heiman, E.R. Glaser, L. Menon, Phys. Rev. B **81**, 115461 (2010)
78. A.L. Friedman, H. Chun, D. Heiman, Y.J. Jung, L. Menon, Phys. B: Condens. Matter **406**(4), 841 (2011)
79. J. Barzola-Quiquia, P. Esquinazi, M. Lindel, D. Spemann, M. Muallem, G. Nessim, Carbon **88**, 16 (2015)
80. A.V. Rode, E.G. Gamaly, A.G. Christy, J.G.F. Gerald, S.T. Hyde, R.G. Elliman, B. Luther-Davies, A.I. Veinger, J. Androulakis, J. Giapintzakis, Phys. Rev. B **70**(5), 054407 (2004)
81. A.W. Mombru, H. Pardo, R. Faccio, O.F. de Lima, E.R. Leite, G. Zanelatto, A.J.C. Lanfredi, C.A. Cardoso, F.M. Araujo-Moreira, Phys. Rev. B **71**(10), 100404 (2005)

82. H. Pardo, R. Faccio, F.M. Araujo-Moreira, O.F. de Lima, A.W. Mombru, Carbon **44**(3), 565 (2006)
83. A.V. Rode, A.G. Christy, N.R. Madsen, E.G. Gamaly, S.T. Hyde, B. Luther-Davies, Current Appl. Phys. **6**(3) Raith GmbH; FRST; Ind Res Ltd; Royal Soc New Zealand (2006)
84. D. Arcon, Z. Jaglicic, A. Zorko, A.V. Rode, A.G. Christy, N.R. Madsen, E.G. Gamaly, B. Luther-Davies, Phys. Rev. B **74**(1), 014438 (2006)
85. A. Kumar, D.K. Avasthi, J.C. Pivin, A. Tripathi, F. Singh, Phys. Rev. B **74**(15), 153409 (2006)
86. S. Mathew, U.M. Bhatta, J. Ghatak, B.R. Sekhar, B.N. Dev, Carbon **45**(13), 2659 (2007)
87. A. Kumar, D.K. Avasthi, J.C. Pivin, Appl. Phys. Express **1**(12), 125002 (2008)
88. S. Talapatra, P.G. Ganesan, T. Kim, R. Vajtai, M. Huang, M. Shima, G. Ramanath, D. Srivastava, S.C. Deevi, P.M. Ajayan, Phys. Rev. Lett. **95**(9), 097201 (2005)
89. T. Saito, T. Ozeki, K. Terashima, Solid State Commun. **136**(9–10), 546 (2005)
90. L. Li, W. Hua, S. Prucnal, S.D. Yao, L. Shao, K. Potzger, S. Zhou, Nucl. Instrum. Methods **275**, 33 (2012)
91. X. He, J. Tan, B. Zhang, M. Zhao, H. Xia, X. Liu, Z. He, X. Yang, X. Zhou, Appl. Phys. Lett. **103**(26), 262409 (2013)
92. Y. Wang, L. Li, S. Prucnal, X. Chen, W. Tong, Z. Yang, F. Munnik, K. Potzger, W. Skorupa, S. Gemming, M. Helm, S. Zhou, Phys. Rev. B **89**(1), 014417 (2014)
93. Y. Wang, X. Chen, L. Li, A. Shalimov, W. Tong, S. Prucnal, F. Munnik, Z. Yang, W. Skorupa, M. Helm, S. Zhou, J. Appl. Phys. **115**(17), 17C104 (2014)
94. Y. Wang, Y. Liu, G. Wang, W. Anwand, C.A. Jenkins, E. Arenholz, F. Munnik, O.D. Gordan, G. Salvan, D.R.T. Zahn, X. Chen, S. Gemming, M. Helm, S. Zhou, Sci. Rep. **5**, 8999 (2015)
95. R.W. Zhou, X.C. Liu, H.J. Wang, W.B. Chen, F. Li, S.Y. Zhuo, E.W. Shi, AIP Adv. **5**(4), 047146 (2015)
96. Y. Liu, G. Wang, S. Wang, J. Yang, L. Chen, X. Qin, B. Song, B. Wang, X. Chen, Phys. Rev. Lett. **106**(8), 087205 (2011)
97. H. Xia, W. Li, Y. Song, X. Yang, X. Liu, M. Zhao, Y. Xia, C. Song, T.W. Wang, D. Zhu, J. Gong, Z. Zhu, Adv. Mater. **20**(24), 4679 (2008)
98. X. Yang, H. Xia, X. Qin, W. Li, Y. Dai, X. Liu, M. Zhao, Y. Xia, S. Yan, B. Wang, Carbon **47**(5), 1399 (2009)
99. Z. He, X. Yang, H. Xia, X. Zhou, M. Zhao, Y. Song, T. Wang, Carbon **49**(6), 1931 (2011)
100. S.K. Mohanta, S.N. Mishra, S.M. Davane, S.K. Srivastava, J. Phys. Condens. Matter **24**(8), 085601 (2012)
101. N. Shukla, M. Sarkar, N. Banerji, A.K. Gupta, H.C. Verma, Carbon **50**(5), 1817 (2012)
102. Z. He, X. Yang, H. Xia, T.Z. Regier, D.K. Chevrier, X. Zhou, T.K. Sham, Phys. Rev. B **85**(14), 144406 (2012)
103. R.F. Pires, P. Pureur, M. Behar, J.L. Pimentel, J. Schaf, Y. Kopelevich, J. Appl. Phys. **111**(9), 093922 (2012)
104. N. Shukla, S.K. Bose, S.K. Choudhary, H. Pandey, M. Sarkar, N. Banerji, A.K. Gupta, H.C. Verma, J. Magn. Magn. Mater. **324**(22), 3887 (2012)
105. K. Kamishima, T. Noda, F. Kadonome, K. Kakizaki, N. Hiratsuka, J. Magn. Magn. Mater. **310**(2), E346 (2007)
106. D. Li, Z. Han, B. Wu, D. Geng, Z. Zhang, J. Phys. D: Appl. Phys. **41**(11), 115005 (2008)
107. J. Červenka, M.I. Katsnelson, C.F.J. Flipse, Nat. Phys. **5**(11), 840 (2009)
108. D. Martínez-Martín, M. Jaafar, R. Pérez, J. Gómez-Herrero, A. Asenjo, Phys. Rev. Lett. **105**, 257203 (2010)
109. C. Wang, X. Zhang, D. Diao, Nanoscale **7**(10), 4475 (2015)
110. J.C.C. Freitas, W.L. Scopel, W.S. Paz, L.V. Bernardes, F.E. Cunha-Filho, C. Speglich, F.M. Araújo-Moreira, D. Pelc, T. Cvitanić, M. Požek, Sci. Rep. **5**, 14761 (2015)

Chapter 4
Phase Transitions Induced by a Magnetic Field in Graphite

Benoît Fauqué and Kamran Behnia

Abstract The subject of this chapter is the the so-called quantum limit of a three-dimensional metal, which is attained at a sufficiently strong magnetic field with only a few occupied Landau levels. Graphite, which has a small Fermi surface, is an ideal candidate to explore this limit. A magnetic field of 7.5 T confines the carriers to their lowest Zeeman-split Landau level. In the early 1980s, a sharp increase in the in-plane magneto-resistance of graphite at high magnetic field (typically $B > 20$ T) was discovered and attributed to a phase transition induced by the magnetic field. Numerous studies followed, and this phase transition is generally believed to be a density-wave instability triggered by the one-dimensional nature of the electronic spectrum and the enhancement of the electron–electron interactions in the quantum limit. Recent transport measurements up to 80 T revealed that not one but two successive field-induced instabilities are present. After a brief description of the quantum limit, we review the rich and complex field phase diagram of graphite as a function of temperature and magnetic field. We discuss possible electronic states associated with these instabilities and end the chapter with a study of the quantum limit in other dilute metals, such as bismuth or lightly-doped semiconductors.

4.1 Introduction: The Effect of a Large Magnetic Field on a Three Dimensional Electron Gas

In the presence of a magnetic field, electrons of a three-dimensional (3D) Fermi sea, while still propagating freely along the magnetic field (B), circulate in quantized orbits in the plane perpendicular to it. As the magnetic field is swept, the radius of the orbits (the cyclotron radius r_c) shrinks with increasing B and crosses the different characteristic length scales of the system. When r_c becomes shorter than

B. Fauqué (✉) · K. Behnia
ESPCI ParisTech, PSL Research University, CNRS, Sorbonne Universities, UPMC Univ, Paris 6; LPEM, 10 rue Vauquelin, 75231 Paris Cedex 5, France
e-mail: benoit.fauque@espci.fr

K. Behnia
e-mail: kamran.behnia@espci.fr

P.D. Esquinazi (ed.), *Basic Physics of Functionalized Graphite*,
Springer Series in Materials Science 244, DOI 10.1007/978-3-319-39355-1_4

the electronic mean free path (l_e), electrons can follow a complete orbit without being scattered. In this regime, quantum oscillations become observable by various probes, such as magnetization and electrical transport [1]. This is a consequence of the quantification of the Fermi sea by the magnetic field. In the simplest picture, where there is only one type of carrier, no Zeeman splitting and no anisotropy, the electronic dispersion can be written as:

$$E = (n + 1/2)\hbar\omega_c + \frac{\hbar^2}{2m_0}k_z^2 \tag{4.1}$$

where n is the Landau level index, $\omega_c = \frac{eB}{m_0}$, m_0 and e are the mass and the charge of the electrons and k_z is the momentum in the z-direction, i.e. parallel to the field. As sketched in Fig. 4.1, the magnetic field redistributes the states among the n Landau levels (LLs). With the magnetic field, the degeneracy in each Landau level increases [2] and the number of occupied LLs decreases. At high magnetic field, all the carriers are confined in the $n = 0$, the lowest Landau level (LL) and one attains the *quantum limit*, where the shape of the electronic spectrum is very different from what it is in absence of a magnetic field: starting from a 3D Fermi sea, we are ending with a one-dimensional spectrum, which has numerous electronic instabilities [3].

While the physics of the quantum limit has been intensively studied for two-dimensional electron gas systems [4], it has been a longstanding problem for three-dimensional gases, and it remains an open question [5]. One of the reasons for this is that the magnetic field required to attain this regime for a standard 3D metal is out of reach with current technology. Typically for a metal with a carrier density of one electron per formula unit, the quantum limit would be reached for a magnetic field as high as several thousand Tesla. However, it is possible to overcome this difficulty by studying systems with larger Fermi wavelengths: *dilute metals*. The quantum limit of the semimetals bismuth, graphite or narrow-gap doped semiconductors can be reached using a moderate magnetic field, i.e. of the order of few Tesla. Therefore,

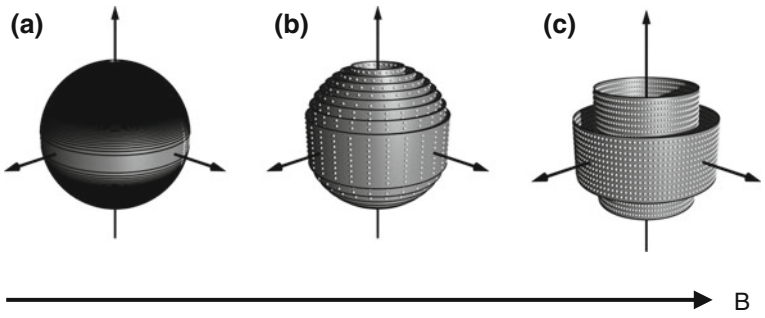

Fig. 4.1 **a**, **b** and **c** Sketches of the Fermi surface of a 3D dimensional electron system as a function of magnetic field, starting at zero (**a**). As the magnetic field increases, there are fewer Landau levels (LLs) occupied, until all the carriers are confined in the $n = 0$, the lowest Landau level (LL)

these simple elements are ideal to explore the nature of the electronic organization in the quantum limit regime, which is the subject of this chapter.

Each system is characterized by a number of properties (orbital mass anisotropy, g-factor, number of valleys, etc.) which deeply affect its electronic spectrum in the quantum limit regime. As an example, let us compare two simple cases: the first is the simplest, a single isotropic electron pocket; the second is a compensated system with a Fermi surface consisting of two pockets, one isotropic electron-like and another isotropic hole-like.

At zero field, both systems have the same carrier concentration ($n = 2.5 \times 10^{17}$ cm^{-3}) and the same Fermi energy (E_F). Once the magnetic field is applied, the systems begin to differ significantly, as shown on Fig. 4.2. In the case of uncompensated system, E_F adjusts in order to keep the carrier concentration constant. As a result, E_F changes with the magnetic field. In particular, each time a LL is depopulated, there is a sharp change in E_F. Once all carriers are confined to the $n = 0$ LL (at about 10 T), E_F increases linearly, following the cyclotron energy of the electrons at $n = 0$ LL. In the case of a compensated system, on the other hand, it is the carrier concentration, which is fixed by the overlap between the hole and electron bands. Contrary to the uncompensated case, the carrier concentration can vary with the magnetic field as long as the charge neutrality is preserved. In this simple picture where we assume a perfect electron-hole symmetry, the Fermi energy is thus field independent. Once the holes and electrons are in their lowest Landau level, the carrier concentration decreases to reach zero at about 25 T. This is simply the result of the difference of behavior of the hole and electron lowest Landau levels: one moves up when the other moves down. Thus, when the cyclotron energy becomes larger than the overlap energy, the carrier concentration goes to zero. This simple example illustrates that the electronic ground state in the quantum limit has not a unique fate and is sensitive to the specific properties of the Fermi surface (FS) under consideration. In the first case, the system stays metallic, but in the second it becomes an insulator.

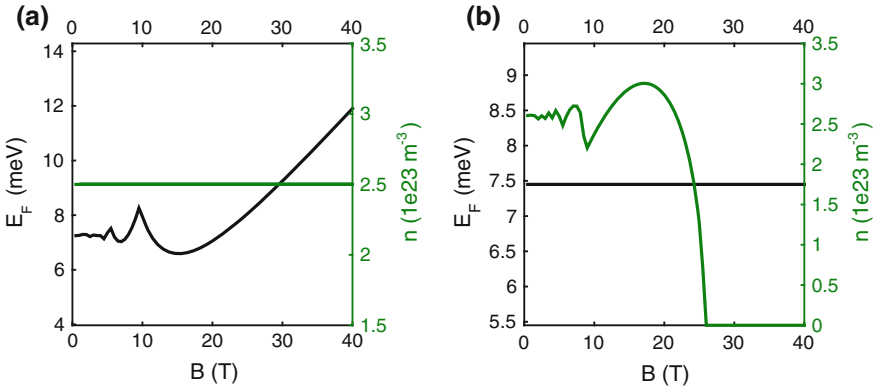

Fig. 4.2 Field dependence of the Fermi energy and the carrier concentration for an isotropic electron pocket with $n = 2.5 \times 10^{17}$ cm^{-3} on **(a)** and for a compensated system formed by one hole and one electron pockets ($n = p = 2.5 \times 10^{17}$ cm^{-3}) on **(b)**

The focus of this chapter is graphite, a compensated system, in which electronic instabilities have been found in the quantum limit. In Sect. 4.2 we review and discuss the most recent experimental studies at high magnetic fields, which establish the existence of a complex phase diagram. In Sect. 4.3, we discuss the theoretical ideas put forward to explain this phase diagram. Finally, in Sect. 4.4, we compare graphite to other dilute systems for which one can go deep into the ultraquantum limit.

4.2 Field-Induced Phase Transitions in Graphite

The FS of graphite has been intensively studied over the last fifty years, by numerous experiments including quantum oscillations and magneto reflection measurements. It is well captured by the Slonczewski–Weiss–McClure (SWM) model [6, 7]. A sketch of this FS is shown in Fig. 4.3a. It is formed by one electron and one hole pocket elongated along the two inequivalent edges H-K-H and H′-K′-H′ of the Brillouin

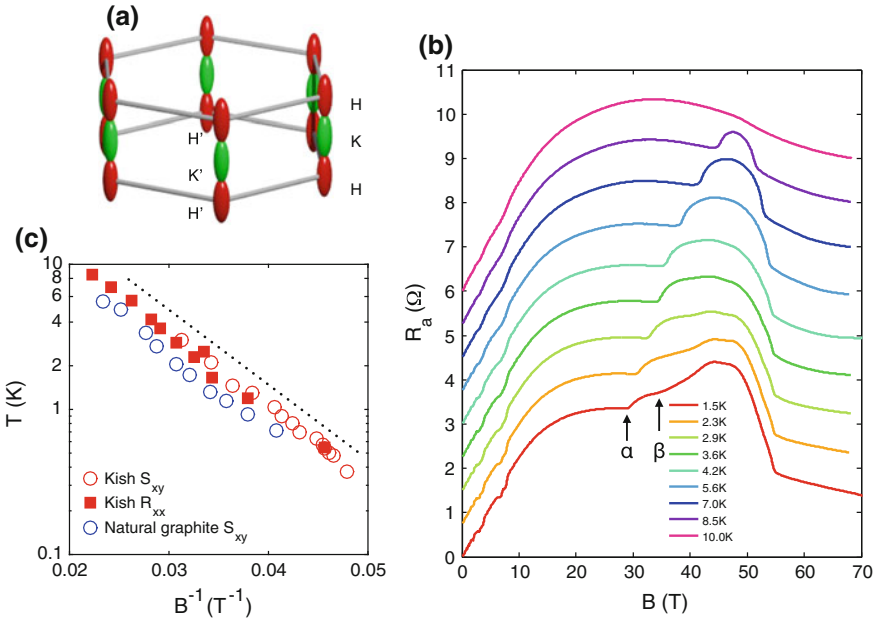

Fig. 4.3 **a** Sketch of the Fermi surface of graphite: the electron and hole pockets located along the H-K-H and H′-K′-H′ direction of the graphite Brillouin zone. **b** In-plane magnetoresistance (R_a) of kish sample with a thickness of 50 μm, up to 70 T for temperatures between 1.5 and 10 K. The magnetic field is applied along the *c*-axis. The curves are shifted for clarity. **c** The magnetic field dependence of the transition temperature plotted as log T versus B^{-1}. Data for kish and natural graphite obtained from the in-plane resistance (R_{xx}) and Nernst effect (S_{xy}) are shown. The *dot line* corresponds to the behavior expected from (4.2)

zone. The electronic density is very low ($n \approx p \approx= 3 \times 10^{18}$ cm^{-3}), four orders of magnitude lower than in copper. When the magnetic field is applied along the c-axis, two frequencies of quantum oscillation can be detected. They are as low as $F_{hole} = 4.6 \pm 0.1$ T for holes and 6.2 ± 0.1 T for electrons [8]. A magnetic field as low as 7.5 T is sufficient to confine both the electrons and holes into the $n = 0$ (spin splitted) LL, respectively labeled $(0, \pm)$ and $(-1, \pm)$.

4.2.1 Evidence for a Field Induced State in Graphite

In 1981, Tanuma et al. [9] reported a sharp increase in the in-plane magnetoresistance of graphite at around $B = 25$ T. Following this pioneering work, numerous experimental studies confirmed the existence of a field-induced many-body state beyond a temperature-dependent critical magnetic field. A detailed review on this work is provided by Yaguchi and Singleton [11]. To illustrate the signature of this phase transition on in-plane resistivity, we present in Fig. 4.3 our own data for a kish graphite sample, as a function of the magnetic field up to 70 T for temperatures ranging from 1.5 to 10 K. In this figure (and the following), the magnetic field is oriented along the c-axis. At $T = 10$ K, upon the application magnetic field, the resistivity increases by several orders of magnitude, before saturating around 15 T and then starting a slow decrease when the field exceeds 30 T. As the temperature decreases, we observe the emergence of a sudden increase in resistivity (labeled α) on top of this monotonic background. This sharp increase indicates a change in the electronic ground state. The onset of the α-transition is shifting to lower magnetic fields as the temperature decreases. A close look of the low temperature curves reveals the existence of additional structures, possibly associated with another transition [10, 12]. In particular at $T = 1.5$ K, a plateau in the in-plane resistance R_a has been observed near 35 T and has been attributed to a second transition, labeled β on Fig. 4.4b. At higher magnetic field (typically 53 T) in-plane resistivity drops and erases the field-induced enhancement. Remarkably, and contrary to the onset of the transition, the field at which this re-entrance occurs is temperature-independent.

Soon after the discovery reported by Tanuma et al. [9], Yoshokia and Fukuyama [15] suggested that this field-induced state was the result of the formation of charge density waves (CDW) along the magnetic field in the $(n = 0, +)$ LL of the electrons. As we will discuss in the next Sect. 4.3, while there is currently no consensus on the precise nature of the density wave (DW) state, three experimental observations are in agreement with a DW scenario. They are detailed below:

(i) The temperature dependence of the onset of the transition: in a mean-field approach the onset of the transition T_c depends on the magnetic field following a BCS-like result [14]:

$$T_c = T^* \exp\left(-\frac{B^*}{B}\right) \tag{4.2}$$

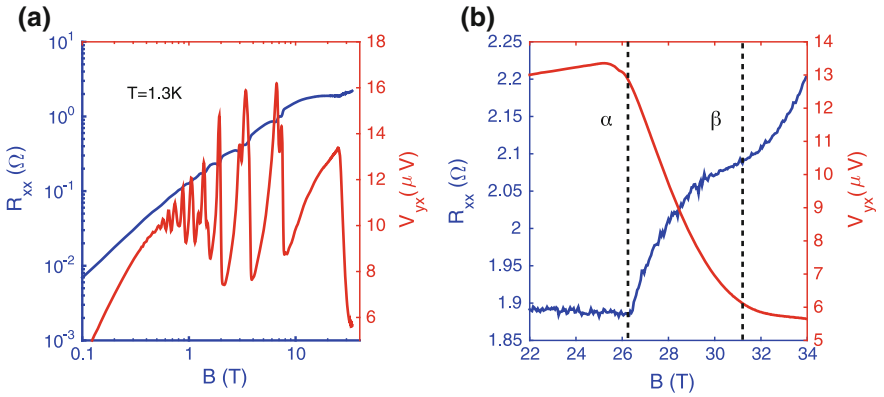

Fig. 4.4 **a** Field dependence of the in-plane resistance in log scale (*in blue*) and of the Nernst voltage (*in red*) at $T = 1.3$ K measured in the same sample. The magnetic field is applied along the c-axis. **(b)** A zoom of **(a)** in the magnetic field window from 22 T to 34 T. Sample thickness : 0.2 mm

where T^* is a temperature scale related to the Fermi energy [15]. Figure 4.3c presents the onset temperature of the transition, deduced by the resistance and Nernst effect in two different types of graphite (kish and natural) as a function of the inverse of magnetic field. In good agreement with early [14, 17–19] and with recent results [12, 13], we find that $\log T_c$ follows B^{-1} linearly and Equation (4.2) captures the evolution of the onset of the α-transition with temperature and magnetic field, using $T^* = 80$ K and $B^* \approx 110$ T as fitting parameters.

(ii) The re-entrance at 53 T: as the magnetic field increases, the distance between the Landau levels ($n = 0, \pm$) of the electrons and ($n = -1, \pm$) of the holes increases due to the Zeeman energy. According to [16], close to 53 T, both Landau levels (0, +) and (−1, −) depopulate, which leads to the collapse of the DW that had formed within these Landau levels [14].

(iii) Non-linear transport: an electric field can make a density wave to move collectively and provide an additional contribution to electric conductivity. Non-ohmic behavior was first observed in the case of in-plane measurements [20] (i.e. in the direction perpendicular to the CDW state). It was also observed in c-axis measurements [21], which is more consistent with the sliding motion of a CDW state given that the nesting vector is expected to be along the c-axis. It should be noted that the electrical field threshold crucially depends on defects, which pin the DW and is therefore sample-dependent.

4.2.2 Nernst Effect in the Field Induced State

Experimentally, the field-induced state in graphite has been mainly studied using electronic transport measurements [11]. No evidence of this field-induced state has

been reported by magnetization measurements or any other thermodynamic probe [13, 19]. In this section we discuss the consequences of this phase transition for the Nernst effect, which is a probe of entropy transport by electrons. The Nernst effect ($S_{xy} = \frac{E_y}{\Delta T_x}$) corresponds to the generation of a transverse electrical field by a thermal gradient in the presence of a magnetic field.

The study of electrical and entropy transport in graphite at low magnetic field has revealed that among four transport coefficients ρ_{xx}, ρ_{xy}, S_{xx} and S_{xy}, the Nernst effect is the most sensitive probe to the quantum oscillations [23]. Figure 4.4a compares the in-plane resistance (R_{xx}) and the Nernst voltage (V_{xy}) as a function of the magnetic field at $T = 1.3$ K. For R_{xx}, the amplitude of the quantum oscillations is about $\approx 10\%$ of the overall signal. On the other hand, the amplitude of the quantum oscillations in the Nernst response dominate the signal. The remarkable sensitivity of the Nernst response still holds at high magnetic field, as reported on Fig. 4.4b. A drop of a factor two in the Nernst voltage is concomitant with an increase of the resistance of about 10% [24]. At first sight, a decrease in the Nernst effect seems to contradict the DW scenario. Typically, in DW state systems such as the iron pnictide [25], the Nernst effect increases at the onset of the Fermi surface reconstruction that occurs with the formation of a spin density wave. This is qualitatively understood in the semi-classical limit where the Nernst coefficient ($\nu = \frac{S_{xy}}{B}$) is roughly set by the ratio of electron mobility to Fermi energy [26]. When the Fermi surface reconstruction leads to a decrease in the Fermi energy, one expects the Nernst coefficient to increase.

In the specific case of graphite, we are in the quantum limit with only a few occupied Landau levels. Bergman and Oganesyan [27] proposed a general theory for the transverse thermoelectric conductivity (α_{xy}), $\alpha_{xy} = -\frac{ek_B}{\hbar}\frac{\pi^2}{3}\sum_{n=0}^{n_{\max}}\frac{k_B T}{2\pi\hbar v_{Fn}}$ where $n_{\max} = [\nu]$, the index of the highest occupied Landau level, equal to the integer part of $\nu = (E_F/\hbar\omega_c - \nu_0)$ and $v_{Fn} = \sqrt{2(E_F - \hbar\omega_c(n + \frac{1}{2}))/m_z}$, the Fermi velocity along the magnetic field for the Landau level n. In the limit where only the $(0, \pm)$ and $(-1, \pm)$ Landau levels are occupied, the amplitude of α_{xy} is imposed by the Fermi velocity of the $(0, \pm)$ and $(-1, \pm)$ LLs. In the case of graphite (a compensated system), α_{xy} is simply related to S_{xy} through $\alpha_{xy} = \frac{S_{xy}}{\rho_{xx}}$. The opening of a gap along one of the four Landau levels would result in a loss of the contribution of this Landau level to α_{xy}. A decrease of Nernst voltage is therefore expected. The discrepancy is simply the result of the difference in the nature of the electronic spectrum between the semi classical (where the Landau quantification does not play a major role) and the quantum limit (where only few Landau levels are occupied). Quantitatively, the drop of a factor two in V_{xy} suggests that the contribution of two Landau levels has been lost [24], possibly as a result of simultaneous nesting of the electron and/or hole pockets.

4.2.3 *In Plane Versus c-Axis Transport*

First observed in natural graphite, the field induced state has been observed over years in synthetic graphite such as kish and HOPG (Highly Oriented Pyrolytic Graphite) [9, 14, 29], mainly using in-plane resistance measurements. In comparison, c-axis transport (when both the electrical current and the magnetic field are parallel to the c-axis) were studied less intensely over the years, even though the field-induced state dramatically affects c-axis transport [21, 22], as we will see in the next section in more detail. One reason is that it is extremely difficult to measure the c-axis resistance (R_c) without any in-plane contribution. In addition, the anisotropy ratio varies significantly from one type of graphite to another. For example, the resistivity anisotropy between the c-axis and the in-plane is around 20 for kish graphite and around 1000 for HOPG at room temperature. Moreover, the field dependence of R_c differs between the two systems. In Fig. 4.5b we compare the field dependence of R_c for a kish sample (in black) and a HOPG sample (in green), at $T = 1.5$ K. Below the transition, R_c remains weak in Kish graphite, but becomes very large in HOPG. These differences have been a subject of debate. Ono et al. [30] suggest that HOPG is more anisotropic than kish graphite due to a larger number of stacking faults. Thus, a current applied along the c-axis of a HOPG sample would not only be perpendicular but also parallel to graphene layers. R_c can be then described by two parallel resistors, one coming from the intrinsic c-axis contribution and the other from in-plane resistance [31]. As a result, R_c in HOPG is naturally more contaminated by the large in-plane resistance than in kish samples, giving rise to a large magnetoresistivity below the field-induced state in HOPG.

In spite of this difficulty, the study of the c-axis transport in the field-induced state has been very fruitful [21, 22]. The remarkable sensitivity of R_c to the field induced state can be realized in Fig. 4.5a where we show a comparison of the in-plane (R_a)

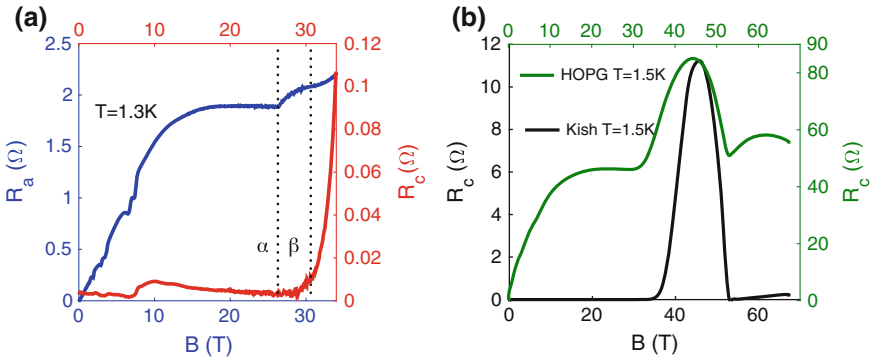

Fig. 4.5 **a** Comparison of the in-plane (R_{xx}) and longitudinal (R_c) magnetoresistance for kish sample (thickness 0.2 mm) at $T = 1.3$ K, **b**, c-axis resistance R_c (B//I//c) for kish samples (*in black*, *left* axis) and HOPG sample (*in green*, *right* axis, thickness 1.2 mm) as a function of the magnetic field at $T = 1.5$ K

and the c-axis (R_c) resistance in kish graphite at the same temperature $T = 1.3$ K and up to 32 T. While R_a increases by about 10%, R_c increases by at least one order of magnitude in this field window. In addition, there are different onsets of the transition in R_a and in R_c. As first noticed by Yaguchi et al. [22], R_c increases sharply at a magnetic field slightly higher than the onset of the α-transition. The increase in R_c has been identified as a second, β transition. Thus, R_c is not sensitive to the α-transition, but is very sensitive to the β-transition.

4.2.4 *c-Axis Transport Measurement: Multiple Instabilities in the Quantum Limit of Graphite*

Motivated by the recent progress in magnetic field technology [32] and the large variation of R_c at the β-transition, we extended the measurements of the out-of-plane resistivity at LNCMI-Toulouse up to 80 T [28]. In Fig. 4.6 we present the field dependence of R_c at temperatures from $T = 0.44$ K to $T = 10$ K. In good agreement with previous reports [21, 22], we find that at low temperatures R_c dramatically increases when the magnetic field lies between 30 and 53 T. Surprisingly, beyond 53 T and up to 75 T, we find a second field window of dramatic R_c enhancement. The temperature dependence of R_c at the maximum of the two domes of Fig. 4.6a at B = 47 and 64 T is shown in Fig. 4.6b. In both states, log R_c varies linearly with T^{-1}, over several orders of magnitude, and then saturates at low temperatures. This is the typical behavior associated with the opening of a gap (labeled Δ). Using an Arrhenius

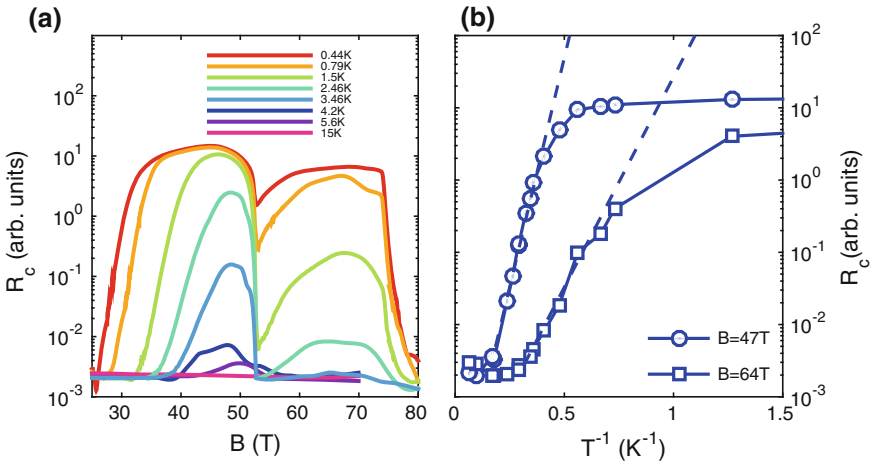

Fig. 4.6 **a** Out-of-plane magnetoresistance in semi-logarithmic scale for a kish graphite sample (*thickness* 100 μm) up to 80 T and to 0.44 K. **b** R_c as a function of T^{-1} at $B = 47$ T (*circles*) and $B = 64$ T (*squares*). *Dashed lines* are Arrhenius fits to R_c. Both plots are adapted from [28]

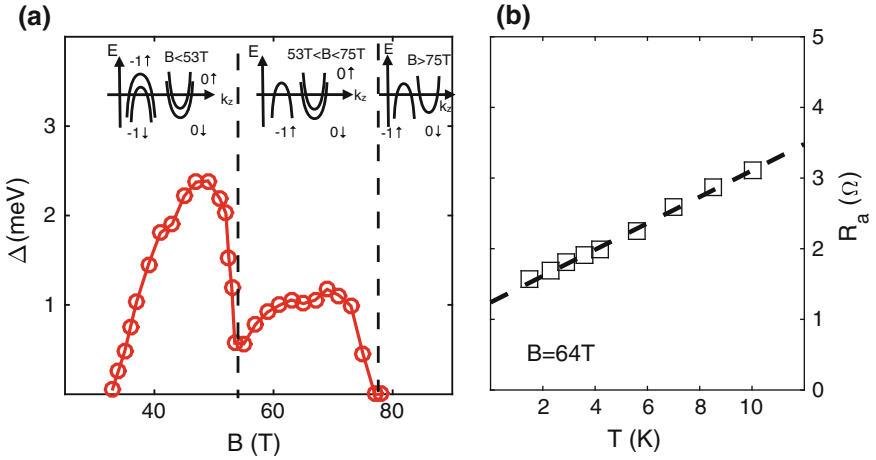

Fig. 4.7 Field dependence of the gap deduced from the thermally activated behavior of R_c. Sketch of occupied Landau sub-levels with increasing magnetic field. When $B > 7.5$ T, there are four occupied sub-levels. The onset of the field-induced transition at 30 T opens a gap in all these sub-levels. At $B = 53$ T, one sub-level crosses the Fermi energy and the field-induced state is destroyed. At $B > 53$ T, a second field-induced state emerges, opening a gap in the last three occupied sub-levels. At $B = 75$ T, another sub-level becomes empty and the second field-induced state vanishes

law (blue dotted lines on Fig. 4.6b) we estimate $\Delta \simeq 2.4$ and 1.1 meV at B = 47 T and 64 T, respectively. The determination of the gap can indeed be performed at all magnetic fields. The field dependence of the gap estimated from R_c measurement is shown in Fig. 4.7a. We note that the amplitude of the gap first increases to reach a maximum at $B = 47$ T where $\Delta = 2.4$ meV and then sharply decreases at the (first) re-entrance field. Afterwards, the gap increases again and saturates between 60 and 75 T at a value of about 1 meV, and then sharply decreases at 75 T, the second re-entrance field. It is interesting to note that the ratios of the activation gap with the critical temperature (defined as the temperature at which the Arrhenius fit crosses the normal state resistance value) at B = 47 T and 64 T are almost the same and equal to $\frac{2\Delta}{k_B T_c} = 3.7$.

The existence of multiple instabilities in the quantum limit regime of graphite, first observed in kish samples, was later confirmed in HOPG samples, see Fig. 4.5b, in super graphite made by graphitization of piled polyimide sheets [13] and in natural graphite [73]. Besides the large magnetoresistance discussed previously, a double-peak structure emerges above 25 T. This structure is similar to what was observed in kish samples. Thus, according to R_c measurements, the magnetic field induces not one but two successive phase transitions, consisting of two distinct ordered states. The existence of another field-induced state above 53 T modifies deeply the high-magnetic field phase diagram of graphite and raises several questions.

(i) How does the Landau level spectrum of graphite evolve with magnetic field above 7.5 T? What is the nature of the instability above 53 T? Following the scenario of Yaguchi et al. [14] and supported by theoretical work [16], only the two LLs (0,-) (for the electrons) and $(-1, +)$ (for the holes) are occupied above 53 T. As in the case of the first instability, one can speculate on the formation of a CDW in the two LLs or an exciton-like state combining the $(0, -)$ and $(-1, +)$ LLs [13, 73]. However, this picture is challenged by the second re-entrance field at 75 T. If both LL $(0, -)$ and $(1, +)$ are occupied, the depopulation of one LL implies the depopulation of the other due to charge conservation. As a result, if one attributes the 75 T re-entrance to the depopulation of LL ($(0, -)$ or $(1, +)$), the system should become an insulator, which would contradict the result of the experiment. We have proposed another scenario, sketched in the insert of Fig. 4.7. At 53 T, only one (and not two) Landau level is depopulated. The LL $(0, +)$ would then be depopulated at 75 T, which would explain the collapse of the second phase. Indeed, the only difference between both scenarios is the number of LLs, which depopulate close to 53 T (i.e. one or two). Recently, Arnold et al. [12] have observed two resistance hysteresis (slightly below and above 53 T) possibly associated with the destruction of two CDW states concomitant with the depopulation of two LLs. We note, however, that in this scenario the existence of a second re-entrance transition at $B = 75$ T remains unexplained.

(ii) Why the in-plane resistivity would have a phase transition at 53 T? As one can see in Fig. 4.3, at low temperatures and above 53 T, R_a has a monotonic behavior, which does not suggest a dramatic change in the electronic ground state. More precisely, at $B = 64$ T, as it is shown in Fig. 4.5b, R_a has a *metallic* behavior with a linear T-dependence. This is in contrast with $R_c(T)$, which displays an activated behavior. This residual in-plane metallicity is indeed surprising and different from the case of Bechgaard salts, which is a well-documented family of quasi-one dimensional conductors hosting a density-wave transition. In the spin-density-wave system $(TMTSF)_2PF_6$, all three components of resistivity display an activated behavior with a gap of similar amplitude [44]. In the case of graphite, the in-plane kinetic energy is quenched by the magnetic field and a gap is formed along the c-axis. As the result, the spectrum is fully gapped and an activated behavior is expected for any direction of the current injection. This remarkable dichotomy between in-plane and out-of-plane transport is the hallmark of a peculiar electronic organization that will be discussed in the next section.

4.3 Theoretical Overview of Different Electronic States Expected for a Three-Dimensional Electron Gas in the Quantum Limit

We review below theoretical ideas describing the electronic organization in the quantum limit regime of graphite.

4.3.1 Field Induced Density Waves

Within the Hartree–Fock approximation for a repulsive interaction Celli and Mermin found in 1968 [33] that the ground state of a 3D electron gas system in a uniform magnetic field is subject to an electronic instability. According to their work, at sufficiently low temperatures, there is always a spin density wave directed along the field. This instability is the result of a logarithmic divergence of the electronic polarization function at zero energy when the values of q_z connecting the Fermi-surface points in the z-direction in momentum space. Over years, a large number of theoretical works have extended and refined this early work [34–37]. A consensus emerged on the essential ingredients in favor of an electronic instability in the quantum limit: (i) the change in the effective dimensionality of the charge carriers induced by the magnetic field from 3D to 1D, as discussed in Sect. 4.1, and (ii) the enhancement of the electron-electron interaction, in particular when the magnetic field is near a field at which the low LLs start to depopulate.

Yet, no consensus has emerged on the precise nature of the instability. In the case of an attractive interaction, the numerical solution of the parquet equation confirmed the formation of a DW [37], and both SDW and CDW states have been proposed as possible candidates. Depending on the parameters of the system (such as the number of valleys, the anisotropy of the mass tensor and the Zeeman factor), the SDW or CDW state may have lower energy [35]. For example, in a system with two valleys, even if the SDW is more favorable in each valley, the cancellation of the direct energy by a shift of 180° of the CDW in each valley can favor a (charge) valley density wave state [36]. It should be noted that more exotic instabilities have also been proposed, such as Wigner crystallization [38], Luttinger-liquid phase [40] and even a re-entrant superconductor [41] in the case of an attractive interaction. More recently, based on the works of Abrikosov et al [39], an excitonic phase have been also proposed [73].

Most of these theories have been developed for multi-valley dilute doped semiconductors. In the case of graphite, the compensated nature of the FS has to be considered in addition to the valley degree of freedom. As discussed in the Sect. 4.2, above 7.5 T, four Landau levels are occupied (respectively $(0, \pm)$ for the hole pocket and $(-1, \pm)$ for the electron pocket), and therefore several instabilities involving either a CDW or a SDW have been proposed. Quickly after the discovery of a field induce state in graphite, Yoshokia and Fukuyama [15] suggested the formation of two CDWs along the c-axis in the two valleys along the H-K-H and H'-K'-H' directions of the Brillouin zone. These CDWs are out of phase in order to minimize the Coulomb interaction. However, this scenario has been challenged by Takahashi et al. [43], who argued that the electrons along the (H,K,H) and (H',K',H') directions do not belong to the same layers. In other words, the cancellation of the Coulomb interaction cannot be at work in each layer. Instead, they suggest that a transverse SDW forms in the $(n = 0, \pm)$ LLs. There is thus currently no consensus on the nature of instability observed at high magnetic field in graphite.

The experimental results discussed in the previous section impose novel constraints on the theory. First, the observation of an activated gap for transport along

the c-axis means that all Landau levels are gapped at the β-transition. Not only the electrons (considered in the theory of [15, 43]) but also the holes have a gapped spectrum following the formation of the DW state. However, in most theories, only two (instead of four) Landau levels have been considered: either $(0, \pm)$ [15, 43] or $(0, +)$ and $(-1, -)$ [12, 15, 43]. Second, the field induced state in graphite is the only case in which an activated conductivity along one axis coexists with metallic conductivity perpendicular to it. This dichotomy contrasts with what has been reported in other 1D density-wave systems. Thus, beyond the DW scenario, other ingredients are required to capture the physics of the electrical transport properties of graphite at high magnetic fields.

4.3.2 The Three Dimensional Quantum Hall Effect

Since the early work of Tanuma et al. [9], the understanding of the electron organization in the presence of a large magnetic field has been deeply affected by the physics of the quantum Hall effect. In particular, the discovery of particular types of quantum Hall effects (QHE) in graphene and multilayer graphene [45, 46] opens new perspectives in understanding the high-field physics in graphite. For instance, one can wonder whether it would be possible to adiabatically connect the quantum Hall state of the multilayer graphene to the field-induced states of graphite.

The possibility of a 3D quantum Hall effect has been discussed since the 80's. As pointed out by Halperin [36], if the Fermi level lies inside the gap, one expects the conductivity tensor of a 3D system to take the form: $\sigma_{ij} = \frac{e^2}{2\pi h} \sum_k \epsilon_{i,j,k} G_k$, where $\epsilon_{i,j,k}$ is the fully antisymmetric tensor and G a reciprocal tensor of the lattice or of the incommensurate potential produced by a DW state. A theory of the 3D QHE in graphite has been proposed [47]. In that work, the Fermi energy was shifted into the bulk gap. A plateau in the Hall conductance was predicted as a result of the formation of chiral surface states. Experimentally, plateaus in the Hall resistivity have been reported in HOPG samples. They are a possible signature of the fractional quantum Hall effect in graphite [29]. However, no quantum-Hall plateau-like structure was observed in kish or natural graphite samples [13]. The understanding of the quantum Hall conductance in graphite is non trivial due to the compensated nature of its FS.

These chiral states were first postulated for layered samples (which exhibit a bulk quantum Hall effect) such as the Bechargard salts and for 2D electron gas multi layers system [49]. They correspond to the formation of a metallic sheet on the surface of the system as the result of the interlayer coupling of independent 2D quantum Hall systems. Experimentally, such states have been tested and observed in multilayer structures formed by 50 periods of 150 Å GaAs quantum Hall alternated with 150 Å $Al_{0.1}Ga_{0.9}As$ barriers [50]. Within the QH states, the conductivity σ_{zz} has an activated behavior. At low temperature, σ_{zz} saturates and scales with the perimeter of the mesa structure, which establishes that the transport is mainly dominated by the edge state, not by the bulk state.

Our work has revealed the existence of a gap along the c-axis. From a theoretical point of view, this means that graphite would thus fulfill the condition required for the quantification of the conductivity tensor [47]. Yet, no evidence of a metallic surface state has been reported so far. In the simplest picture, the modulation of the charge or the spin is fixed by the nesting vector, which continually changes with the magnetic field. However, for the two lowest Landau level (0,+) and (−1,−), in the field range of (30 T, 60 T), $2k_F$ is about half of the c-axis length of the Brillouin zone.

It is instructive to think of graphite as a stack of "weakly-coupled graphene bilayers" in the $n = 0$ LL. Note that the tight-binding parameters for graphite in the so-called SWM picture are such that the coupling energy between such adjacent bilayers would be 50–70 meV. This is much lower than the intra-bilayer coupling energies, but an order of magnitude larger than the energy gaps, which according to our results, the field-induced phase transition opens in the energy spectrum of graphite.

Seen from another perspective, in a magnetic field of 54 T, the magnetic length is $l_B = 35$Å, shorter than the in-plane inter-electron distance r_0 in each graphene plane. This implies that strong correlations have to be considered [16], known to generate a variety of electronic phases in the two dimensions [4]. What happens to them once the third dimension is turned on, remains an open question. Interestingly, in most DW scenarios, the spin or charge modulation is along the field and the possibility of an in-plane DW state [34] has not been considered in detail.

Even though the link between quantum Hall physics and field-induced states is appealing, it is still speculative. Further experimental and theoretical works should be carried out to clarify its relevance to field induced states in graphite.

4.4 Discussion

Since the early work of Celli and Mermin [33], it is theoretically expected that at a sufficiently high magnetic field and at a sufficiently low temperature, any system in the quantum limit regime is unstable towards a DW instability. Yet, evidence for such a phase transition has only been reported in graphite. In this last section, we discuss the case of other dilutes metals.

As in the case of graphite, the FS of bismuth (sketched in Fig. 4.8) is compensated, and both carriers are characterized by a very large mobility (even larger than in the case of graphite) and a total number of electrons (and holes) as low as $n = 3 \times 10^{17}$ cm^{-3} [51]. When the field is oriented along the bisectrix direction, the quantum limit for the three electron pockets can be reached for a magnetic field as low as 2.5 T, which makes bismuth another ideal system to explore the physics of the quantum limit. Experimentally, a sharp increase of the magneto-transmission has been observed for a magnetic field as high as 88 T oriented along the binary axis. This sharp increase has been attributed to a field induced transition from a semi-metal to a semiconductor state [61] and later observed in $Bi_{1-x}Sb_x$ by transport measurements [62]. As discussed in section , for a compensated metal with only one valley, when the

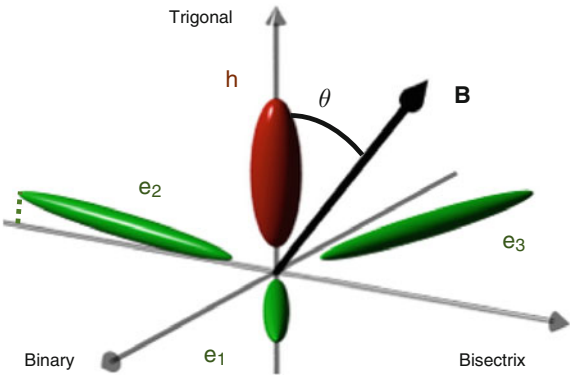

Fig. 4.8 Sketch of the Fermi surface of bismuth. The three electron pockets labeled $e_{1,2,3}$ (*in green*) are almost orthogonal to the single hole pocket (*in red*), while for graphite, both the hole and the electron pockets are elongated along the same axis

0^- LL of the hole (and the electron) pocket depopulates, a gap forms and the system becomes insulating. We note that in the case of graphite, the field scale associated with SM-SC is still unknown. Theoretical estimates vary from around 85 T [12] to 200 T [16].

More recently, several anomalies have been reported in the quantum limit of bismuth. Firstly, Nernst effect measurements have revealed the existence of unexpected peaks in the Landau level spectrum at high magnetic fields [52, 53]. The study of their angular dependence has shown that they can be attributed to the Landau level spectrum of a twin minor domain of the rhombohedral crystallographic structure of bismuth [54]. Interestingly, as the magnetic field increases, the electronic density in each domain changes in a different way, resulting in a significant field induced discontinuity in carrier density across the twin boundary. This allows studying the electronic organization at the junction of two compensated systems when only few Landau levels are populated.

Second, a first order field-induced phase transition has been reported by torque magnetometry for a field above 15 T and oriented close to the trigonal axis [55]. This phase transition was first attributed to the formation of a valley-polarized state, and later to the crossing of the Fermi energy and the LL 0^+ of the electron pockets [56]. However, no evidence of an hysteresis behavior at this crossing was reported by transport measurements [54].

Third, the angular dependence of the magnetoresistance of bismuth has shown that at low temperatures and high magnetic fields, the threefold symmetry of the lattice is suddenly lost [57, 58]. Since the work of Kapitza, it has been known that bismuth displays a very large magnetoresistance [59]. When the magnetic field is oriented in the (binary, bisectrix) plane, the magnetoresistance (measured along the trigonal axis) shows large oscillations associated with the contribution of the three anisotropic Dirac electron valleys. At low temperatures and high magnetic fields, the C_3 symmetry in the angular dependence of the magnetoresistance is lost. The three Dirac valleys cease to be rotationally invariant, which could be related to the formation of a "valley-nematic Fermi liquid state" [60].

However, none of these features resembles the field induced state of graphite. The fate of the three-dimensional electron gas in bismuth and in graphite diverges. Let us point out several differences between the electronic structure of bismuth and graphite that could explain the absence of a DW state in bismuth. First, the orientation of the hole and electron pockets is different. For graphite, both the hole and electron pockets are elongated along the c-axis, while for bismuth the hole and electrons pockets are almost perpendicular to each other. Indeed, holes and electrons have much more in common in the case of graphite than in the case of bismuth. For bismuth, even when all the electrons are in the lowest Landau level, at $B = 2.5$ T and parallel to the bisectrix direction, the $n = 8$ LL of holes is still occupied and the holes in bismuth are still far away from the quantum limit. Second, the amplitude of the Zeeman energy is different. In the case of graphite, the Zeeman energy is rather small. In the case of bismuth, the Zeeman energy is large, and very anisotropic for the hole pocket. These differences may prevent the formation of a common nesting vector for both carriers. Third, the number of valleys is different. While graphite has two valleys for each carrier, bismuth has one valley for holes and three valleys for electrons. As discussed in Sect. 4.3.1, the valley degrees of freedom could play an essential role to stabilize the DW state. The presence of only one valley for holes could be another factor that prevents the stabilization of a DW state in bismuth. Finally, beyond the difference in the electronic spectrum, we can also invoke the difference in the dielectric constant between both systems. The dielectric constant is smaller for graphite ($\epsilon = 9$ [63]) than for bismuth ($\epsilon = 80$). As a result, the amplitude of the Coulomb interaction—the motor of the electronic instability in graphite—would be smaller in the case of bismuth.

The second set of candidate systems are doped semiconductors, where a well-defined Fermi surface is experimentally resolved to low concentrations (i.e. low enough to allow for the exploration of the quantum limit with a reasonably low magnetic field). The simplest system is certainly Bi_2Se_3. Due to anti-site defects, E_F is pinned down in the conduction band and a well-defined FS is experimentally resolved down to a carrier concentration of $n \approx 1 \times 10^{17}$ cm^{-3} [64]. The FS is one single pocket with a modest anisotropy. At high magnetic fields, a large increase of the Nernst effect has been reported and attributed to field-dependence of E_F [65]. A similar behavior has been also reported in the thermopower of $Pb_{1-x}Sn_xSe$ [66]. No evidence of a field induced state has been reported in any of these systems.

Even more dilute systems, such as InSb, $Hg_{1-x}Cd_xTe$ or PbTe, can be used to probe the physics deep inside the quantum limit. A metal-insulator transition (MIT) induced by a magnetic field has been observed in these systems [67, 68]. Figure 4.9 shows log-log plots of the longitudinal (ρ_{zz}), transverse (ρ_{xx}), and Hall (ρ_{xy}) resistivities as a function of the magnetic field for a n-type InSb sample with a carrier concentration $n = 2.2 \times 10^{15}$cm^{-3}. For such a low carrier concentration, all carriers are confined to the (0,−) LL when magnetic field exceeds 0.8 T. Above this field, a second field scale, labeled $B_{MI} = 3.3$ T, can be identified when ρ_{xy} rises suddenly. In the case of InSb, both ρ_{xx} and ρ_{zz} change by several orders of magnitude when the magnetic field increases and the temperature decreases. This contrasts with the case of graphite where only R_c has an activated behavior. The origin of the MIT has been

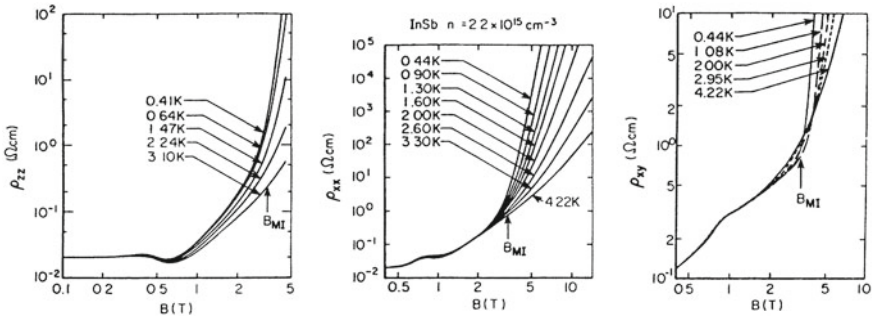

Fig. 4.9 Longitudinal (ρ_{zz}), transverse (ρ_{xx}), and Hall (ρ_{xy}) resistivities of an n-type InSb sample as a function of the magnetic field B in a log-log scale. These figures are extracted from [67]

a subject of debate and several explanations have been proposed, such as magnetic freezeout, Wigner crystallization or Anderson localization. While in the case of InSb and $Hg_{1-x}Cd_xTe$, a consensus emerged in favor of the magnetic freezeout scenario [67, 69], the case of PbTe remains controversial [68].

Contrary to semimetals, in which the FS is the result of an overlap between two bands, the FS of doped semiconductors is the result of the population of the conduction (or valence) band through the ionization of a dopant. The overlap energy is then replaced by the interaction energy between the electrons and the distributed ionized impurities. In the presence of a magnetic field, the reduced spatial extension of the wave function can favor a situation where the electrons prefer to bound to the impurity sites [70, 71], pushing the system towards an insulating state: this is the so-called magnetic freezeout. The Mott criterion predicts an insulating state when the dopant density n becomes smaller than a critical value n_c that satisfies $a_B n_c^{\frac{1}{3}} \approx 0.25$, where a_B is the average Bohr radius.

In principle, the magnetic freezeout scenario should not apply to semi metals due to the absence of a dopant. Nonetheless, graphite samples are not free from impurities and it is interesting to compare the different length scales involved in the metal-insulator transition in graphite. At zero field, $a_B = (a_\perp^2 a_{//})^{1/3} = 41$Å with $a_{//} \approx 7$ Å and $a_\perp \approx 100$ Å, where $a_{//}$ and $a_\perp$ correspond to the longitudinal and transverse Bohr radius of graphite, respectively [72]. At $B = 54$ T the magnetic length l_B is equal to 34 Å, which is of just below a_B. In contrast to InSb, this is outside the "strong field limit", where the MIT is expected to occur. Yet, in both systems, the magnetic field induces an insulating state at least from the point of view of longitudinal transport. Further work should be carried out to clarify the difference in origin and nature of these insulating states.

4.5 Conclusion

In this chapter, we reviewed the electronic phase transitions induced by the magnetic field in graphite. At low temperature, where only the two lowest hole-like and electron-like Landau levels are populated, graphite hosts a succession of electronic instabilities induced by the one-dimensional nature of the electronic spectrum and the enhancement of electron-electron interaction with the magnetic field. Despite numerous experimental studies many question remain unsolved. In particular, the evolution of the Landau level spectrum above 7.5 T and the nature of the instabilities have not been settled yet. Interestingly, thanks to the formation of a gap along the *c*-axis the system is qualified (at least from a theoretical point of view) to host the 3D quantum Hall effect, providing another theoretical route to understand these electronic instabilities. Thus, the field-induced states of graphite offer an interesting opportunity to understand the electronic organization of quantum Hall edge states when the interlayer coupling between independent graphene layers increases, i.e. as a third dimension is added to the two-dimensional electron gas. The comparison with other dilute systems has shows that the electronic ground state in the quantum limit is not unique and that a rich variety of electronic grounds state may be formed in this context.

Acknowledgments It is our pleasure to thank our colleagues from the high magnetic facility laboratory at LNCMI-Toulouse and Grenoble: Stephane Kramers, David LeBoeuf, Marc Nardone, Cyril Proust, Baptiste Vignolles and Gabriel Seyfarth without whom all these experiments could not have been carried out. We also thank Jason Alicea, Duncan Maude, Yasutami Takada and Zengwei Zhu for stimulating discussions. This work was supported by the Agence Nationale de la Recherche, as a part of the SUPERFIELD and QUANTUMLIMIT projects, by a grant attributed by the Ile-de-France regional council and by EuroMagNET II under the EU contract number 228043.

References

1. D. Schoenberg, *Magnetic Oscillations in Metals* (Cambridge University Press, Cambridge, 1984)
2. J.M. Ziman, *Theory of Solids* (Cambridge University Press, Cambridge, 1972)
3. T. Giamarchi, Quantum Physics in One Dimension (Oxford University Press, Oxford, 2004)
4. D. Yoshioka, *The Quantum Hall Effect* (Springer, New York, 2001)
5. B.I. Halperin, Jap. J. Appl. Phys. **26**, 1913 (1987)
6. J.C. Slonczewski, P.R. Weiss, Phys. Rev. **80**, 272279 (1979)
7. J.W. McClure, Phys. Rev. **108**, 612 (1957)
8. J.M. Schneider, *Electronic Properties of Graphite* (Physics Grenoble, Universite Joseph-Fourier) (2010)
9. S. Tanuma et al., in *Physics in High Magnetic Fields*, ed. by S. Chikazumi and N. Miura (Springer, Berlin, 1981)
10. H. Yaguchi, Y. Iye, T. Takamasu, N. Miura, Phys. B **184**, 332 (1993)
11. H. Yaguchi, J. Singleton, J. Phys. Condens. Matter **21**, 344207 (2009)
12. F. Arnold et al., http://xxx.lanl.gov/pdf/1411.3323.pdf
13. K. Akiba, A. Miyake, H. Yaguchi, A. Matsuo, K. Kindo, M. Tokunaga, J. Phys. Soc. Jpn. **84**, 054709-1-6 (2015)

14. H. Yaguchi, J. Singleton, Phys. Rev. Lett. **81**, 5193 (1998)
15. D. Yoshioka, H. Fukuyama, J. Phys. Soc. Jpn. **50**, 725 (1981)
16. Y. Takada, H. Goto, J. Phys. Condens. Matter **10**, (1998)
17. Y. Iye et al., Phys. Rev. B **25**, 5478 (1982)
18. Y. Iye, P.M. Berglund, L.E. McNeil, Solid State Commun. **52**, 975 (1984)
19. S. Uji, J.S. Brooks, Y. Iye, Phys. B **299**, 246 (1998)
20. Y. Iye, G. Dresselhaus, Phys. Rev. Lett. **54**, 1182 (1985)
21. H. Yaguchi, J. Singleton, T. Iwata, Phys. B **298**, 546 (2001)
22. H. Yaguchi et al., J. Phys. Soc. Jpn. **68**, 181 (1999)
23. Z. Zhu et al., Nat. Phys. **6**, 26 (2010)
24. B. Fauqué et al., Phys. Rev. Lett. **106**, 246405 (2011)
25. C. Hess, *Properties and Applications of Thermoelectric Materials - II* (Springer, New York, 2012)
26. K. Behnia, J. Phys. Condens. Matter **21**, 113101 (2009)
27. D.L. Bergman, V. Oganesyan, Phys. Rev. Lett. **104**, 066601 (2010)
28. B. Fauqué et al., Phys. Rev. Lett. **110**, 266601 (2013)
29. Y. Kopelevich et al., Phys. Rev. Lett. **103**, 116802 (2009)
30. Ono et al., J. Phys. Soc. Jpn. **14**(498) (1976)
31. Y. Kopelevich et al., Phys. Lett. A **374** (2010)
32. J. Béard et al, Eur. Phys. J. Appl. Phys. **59**, 30201 (2012)
33. V. Celli, N.D. Mermin, Phys. Rev. 1 **40**, A 839 (1965)
34. H. Fukuyama, Solid State Commun. **26**, 783 (1978)
35. Z. Tezanovic et al., Phys. Rev. B **36**, 488 (1987)
36. B.I. Halperin, Japanese J. Appl. Phys. **26** (1987)
37. V.M. Yakovenko et al., Phys. Rev. B **47**, 8851 (1993)
38. W.G. Kleppmann, R.J. Elliott, J. Phys. C Solid State **8**, 2729 (1975)
39. A.A. Abrikosov, J. Low Temp. Phys. **2**(37), 175 (1970)
40. C. Biagini et al., Europhys. Lett. **55**, 383 (2001)
41. M. Rasolt, Z. Tesanovic, Rev. Mod. Phys. **64**, 709 (1992)
42. D. Yoshioka, H. Fukuyama, J. Phys. Soc. Jpn. **50**, 725 (1981)
43. K. Takhashi, Y. Takada, Phyisca C **201**, 384 (1994)
44. M. Dressel et al., Phys. Rev. B **71**, 075104 (2005)
45. K.S. Novoselov et al., Nat. Phys. **2**, 177 (2006)
46. A. Kumar et al., Phys. Rev. Lett. **107**, 126806 (2011)
47. B.A. Bernevig et al., Phys. Rev. Lett. **99**, 146804 (2007)
48. F.J. Burnell, B.A. Bernevig, D.P. Arovas, Phys. Rev. B **79**, 155310 (2009)
49. L. Balents, M.P.A. Fisher, Phys. Rev. Lett. **76**, 2782 (1996)
50. D.P. Druist et al., Phys. Rev. Lett. **80**, 365 (1998)
51. Z. Zhu et al., Phys. Rev. B **84**, 115137 (2011)
52. K. Behnia et al., Science **317**, 1729 (2007)
53. B. Fauqué et al., New J. Phys. **11** 113012 (2009)
54. Z. Zhu et al., PNAS **109**(37), 14813 (2012)
55. L. Li et al., Science **321**, 547 (2008)
56. J. Alicea, L. Balents et al., Phys. Rev. B **79**, 241101(R) (2009)
57. Zengwei Zhu et al., Nat. Phys. **8**, 89 (2011)
58. A. Collaudin et al., Phys. Rev. X 5, 021022 (2015)
59. P.L. Kapitza, Proc. R. Soc. A **119**, 358443 (1928)
60. D. Abanin et al., Phys. Rev. B **82**, 035428 (2010)
61. N. Miura et al., Phys. Rev. Lett. **49**, 1339 (1982)
62. K. Hiruma et al., J. Phys. Soc. Jpn. **52**, 2118 (1983)
63. E.A Taft, H.R Philipp, Phys. Rev. A **138**, 197 (1965)
64. N. Butch et al., Phys. Rev. B **10**, 241301(R) (2010)
65. B. Fauqué et al., Phys. Rev. B **87**, 035133 (2013)
66. T. Liang et al., Nat. Commun. **4**, 2696 (2013)

67. M. Shayegan, V.J. Goldman, D. Drew, Phys. Rev. B **38**, 5585 (1988)
68. J. Oswald et al., Phys. Rev. B **40**, 3032 (1989)
69. S. Ishida, E. Otsuka, J. Phys. Soc. Jpn. **42**, 542 (1977)
70. R.W. Keyes, R.J. Sladek, J. Phys. Chem. Solids **1**(8), 515 (1958)
71. Y. Yafet, R.W. Keyes, E.N. Adams, J. Phys. Chem. Solids 1,**13**, 71956 (1958)
72. N.B Brandt, S.M Chudinov, Y.G. Ponomarev, *Semimetals Graphite and its Compounds, Modern Problems in Condensed Matter Sciences* (North-Holland Physics Publishing, Amsterdam, 1988)
73. Z. Zhu et al., http://lanl.arxiv.org/pdf/1508.03645v1

Chapter 5
Superconductivity in Layered Systems of Dirac Electrons

Eduardo C. Marino and Lizardo H.C.M. Nunes

Abstract Dirac electrons have been discovered in many advanced materials including, among others, graphene, cuprates, pnictides and rare-earth dichalchogenides. These materials are either two-dimensional, such as graphene or exhibit a layered structure formed by planes where the most relevant physics occurs. Interestingly many of them undergo a transition to a superconducting phase, under appropriate conditions. However, the kinematical properties of Dirac electrons, which imply the absence of a Fermi surface at zero doping, rules out the traditional, phonon-mediated BCS mechanism of superconductivity. In this chapter, we describe a theoretical study of the superconducting properties of layered systems of Dirac electrons, assuming the existence of some mechanism behind it. We analyze in detail the phase diagram identifying quantum critical points, the effects of temperature, magnetic field, chemical potential (doping), number of layers, as well as the interplay of the SC with an excitonic interaction. The results unequivocally indicate that a novel mechanism, other than the traditional BCS, is required to explain the superconductivity of Dirac electrons.

5.1 Introduction

Dirac electrons have been discovered in many advanced materials including, among others, graphene, cuprates, pnictides and rare-earth dichalchogenides [1]. These materials are either two-dimensional, such as graphene or exhibit a layered structure formed by planes where the most relevant physics occurs. Interestingly many of them undergo a transition to a superconducting phase, under appropriate conditions. However, the kinematical properties of Dirac electrons, which imply the absence

E.C. Marino (✉)
Instituto de Física, UFRJ, Cx.P. 68528, Rio de Janeiro, RJ 21941-972, Brazil
e-mail: marino@if.ufrj.br

L.H.C.M. Nunes
Departamento de Ciências Naturais, UFSJ, Pça Dom Helvécio, 74, São João Del-rei, MG 36301-160, Brazil
e-mail: lizardonunes@ufsj.edu.br

P.D. Esquinazi (ed.), *Basic Physics of Functionalized Graphite*,
Springer Series in Materials Science 244, DOI 10.1007/978-3-319-39355-1_5

of a Fermi surface at zero doping, rules out the traditional, phonon-mediated BCS mechanism of superconductivity. In this chapter, we describe a theoretical study of the superconducting properties of layered systems of Dirac electrons, assuming the existence of some mechanism behind it. We analyze in detail the phase diagram identifying quantum critical points, the effects of temperature, magnetic field, chemical potential (doping), number of layers, as well as the interplay of the SC with an excitonic interaction. The results unequivocally indicate that a novel mechanism, other than the traditional BCS, is required to explain the superconductivity of Dirac electrons.

5.1.1 Dirac Fermions in the Honeycomb Lattice

In this section we explain how Dirac fermions appear in the honeycomb lattice. We start our analysis considering the honeycomb lattice presenting a bipartite lattice formed of sublattices A and B, such as in graphene.

Let $a^\dagger_{i,\sigma} = \sum_k e^{i\mathbf{k}\cdot\mathbf{r}_i} a^\dagger_{\mathbf{k},\sigma}$ and $b^\dagger_{i,\sigma} = \sum_{\mathbf{k}} e^{i\mathbf{k}\cdot\mathbf{r}_i} b^\dagger_{\mathbf{k},\sigma}$ be, respectively, electron creation operators, with spin σ, on site i of sublattices A and B respectively. (For the sake of simplicity, $\hbar = 1$, as usual.) The Hamiltonian, which describes the hopping of electrons between adjacent sites of different sublattices A and B, is given by [2, 3]

$$H_t = -t \sum_{\mathbf{k},\sigma} s_{\mathbf{k}} \left(a^\dagger_{\mathbf{k},\sigma} b_{\mathbf{k},\sigma} + \text{h.c.} \right), \tag{5.1}$$

where $t \approx 2.8$ eV is the hopping energy between nearest neighbors and $s_{\mathbf{k}} = 1 + e^{i\mathbf{k}\cdot\mathbf{a}_1} + e^{i\mathbf{k}\cdot\mathbf{a}_2}$, with $\mathbf{a}_1 = a\hat{e}_x$, $2\mathbf{a}_2 = a\left(\hat{e}_x - \sqrt{3}\hat{e}_y\right)$, as shown in Fig. 5.1, and the lattice parameter is $a = 2.46$ Å.

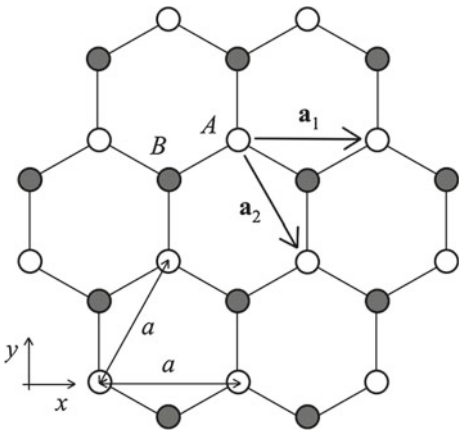

Fig. 5.1 Lattice structure of graphene

Since we have two atoms per unit cell, we may introduce the two component spinorial field $\psi^{\dagger}_{\mathbf{k},\sigma} = \left(a^{\dagger}_{\mathbf{k},\sigma}\ b^{\dagger}_{\mathbf{k},\sigma}\right)$ in order to rewrite the hopping Hamiltonian in (5.1) as

$$H_t = \sum_{\mathbf{k},\sigma} \psi^{\dagger}_{\mathbf{k},\sigma} \mathscr{A}_{\mathbf{k}} \psi_{\mathbf{k},\sigma}\,, \tag{5.2}$$

where the 2×2 matrix $\mathscr{A}_{\mathbf{k}}$ is given by

$$\mathscr{A}_{\mathbf{k}} = -t \begin{pmatrix} 0 & s_{\mathbf{k}} \\ s^{*}_{\mathbf{k}} & 0 \end{pmatrix}. \tag{5.3}$$

It is straightforward to calculate the dispersion relation,

$$\pm t|s_{\mathbf{k}}| = \pm t \sqrt{3 + 2\left[\cos(ak_x) + 2\cos\left(\frac{ak_x}{2}\right)\cos\left(\frac{\sqrt{3}ak_y}{2}\right)\right]}, \tag{5.4}$$

which is plotted in Fig. 5.2. We see that there are six Dirac points at the corners of the first Brillouin zone in the honeycomb lattice, as indicated by the inset; however, only two of them are non-equivalent and we choose the Dirac points to be $\mathbf{K} = -4\pi/3a\,\hat{e}_x$ and $\mathbf{K}' = 4\pi/3a\,\hat{e}_x$. Taking $q = |\mathbf{k} - \mathbf{K}| = |\mathbf{k} - \mathbf{K}'|$ as the momentum measured relatively from the Dirac points, we expand (5.4) in the vicinity of $\mathbf{K}$ and $\mathbf{K}'$ collecting only the linear term. Hence, the low energy dispersion becomes $\pm v_F q$, which is the relativistic dispersion from the Dirac equation. However, $v_F = \sqrt{3}ta/2$ is the Fermi velocity, which replaces the velocity of light in ordinary relativistic systems, but for a much lower value, $v_F \approx 10^6$ m/s. This result was first obtained by Wallace [4].

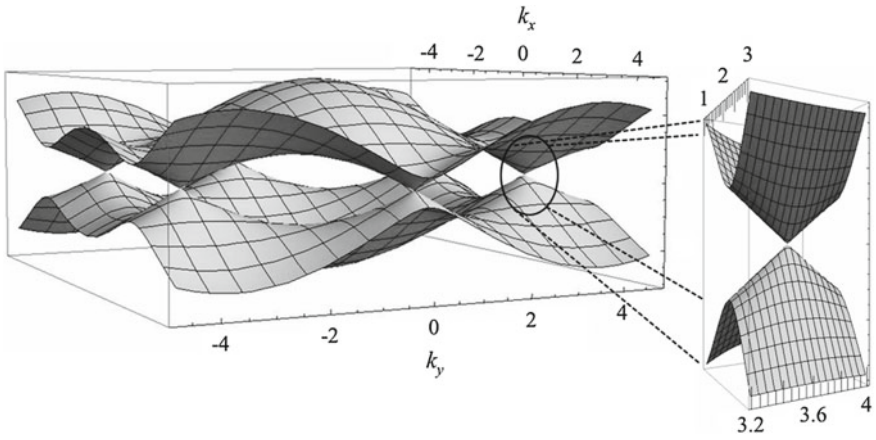

Fig. 5.2 Dispersion relation as defined by (5.4). k_x and k_y are given in units of $1/a$

Now, we obtain the continuum limit of the non-interacting Hamiltonian given by (5.1) in the vicinity of the two Dirac points. First, we take $\mathbf{q} = \mathbf{k} - \mathbf{K}$ and redefine the momentum components as

$$\mathbf{k} = \left(\frac{q_x}{2} + \frac{\sqrt{3}q_y}{2}, -\frac{\sqrt{3}q_x}{2} + \frac{q_y}{2} \right), \tag{5.5}$$

which represents a $\pi/3$ clockwise rotation of the original reference frame. We may expand the non-interacting Hamiltonian in (5.1) around the Dirac point $\mathbf{K}$, so that (5.3) becomes

$$\mathscr{A}_K(k) = v_F \begin{pmatrix} 0 & k_x - ik_y \\ k_x + ik_y & 0 \end{pmatrix}, \tag{5.6}$$

which is simply expressed as $\mathscr{A}_K(k) = v_F \sigma \cdot \mathbf{k}$, with $\sigma = \left(\sigma_x, \sigma_y\right)$ given in terms of the well-known Pauli matrices. Analogously, the momentum may be redefined as a $4\pi/3$ clockwise rotation of the original reference frame in order to expand the hopping Hamiltonian in the vicinity of $\mathbf{K}'$, so that $\mathscr{A}_{K'}(k) = v_F \sigma^\dagger \cdot \mathbf{k}$. Therefore, the continuum approximation of the non-interacting Hamiltonian is given by

$$H_t = \sum_{\kappa = K, K', \sigma} \int \frac{d^2k}{(2\pi)^2} \, \psi^\dagger_{\sigma,\kappa}(k) \mathscr{A}_\kappa(k) \psi_{\sigma,\kappa}(k), \tag{5.7}$$

where we have introduced the fermion field $\psi^\dagger_{\sigma,\kappa}(k) = \left(a^\dagger_{\sigma,\kappa}(k) \; b^\dagger_{\sigma,\kappa}(k)\right)$ and $\kappa = K, K'$ denotes the Dirac points. We see that the above expression is essentially the Dirac Hamiltonian with v_F replaced by the velocity of light.

In the following we investigate the conditions for the appearance of superconductivity in the system introducing a phenomenological interaction, which is responsible for the Cooper pair creation in the singlet state [5].

5.2 Superconductivity in Dirac Fermions Systems

Motivated by the discussion above, in this section we analyze the conditions for the appearance of superconductivity in two dimensional (2D) spatial Dirac fermion systems.

Let us consider a fermionic system consisting of a stack of planes containing two Dirac points. We introduce an internal index $a = 1, \ldots, N$ that characterize the different planes to which the fermions belong. For the case of graphene, there are two inequivalent Dirac points at the corners of the first Brillouin zone. Therefore, presently the fermionic operator is denoted by $\psi^\dagger_{i\sigma a}$, where the Dirac indices $i = 1, 2$ correspond to those two Fermi points, the z-component of the fermionic spin are $\sigma = \uparrow, \downarrow$. Moreover, we assume that there is a BCS-type superconducting interaction, produced by some underlying microscopic mechanism, whose origin is not important

for our purposes at the moment, so that the interaction Lagrangian contains four terms, describing the various possible BCS interactions in which a Cooper pair would form between electrons with opposite spins, belonging to different Fermi points but in the same plane. Nevertheless, the interaction of electrons belonging to different planes is allowed. The complete Lagrangian of our system is given by

$$\mathscr{L} = \mathrm{i}\overline{\psi}_{\sigma a}\ \partial\!\!\!/\ \psi_{\sigma a} + g\left(\psi^{\dagger}_{1\uparrow a}\,\psi^{\dagger}_{2\downarrow a} + \psi^{\dagger}_{2\uparrow a}\,\psi^{\dagger}_{1\downarrow a}\right)\left(\psi_{2\downarrow b}\,\psi_{1\uparrow b} + \psi_{1\downarrow b}\,\psi_{2\uparrow b}\right), \quad (5.8)$$

where $g > 0$ is the strength of the interaction coupling and the sum over a, b is implicit. Notice that we use the following convention for the Dirac matrices: $\gamma^0 = \sigma^z$, $\gamma^0\gamma^1 = \sigma^x$, $\gamma^0\gamma^2 = \sigma^y$. Moreover, $\partial\!\!\!/ = \gamma^\mu\partial_\mu$ and $\overline{\psi}_{\sigma a} = \psi^{\dagger}_{\sigma a}\gamma^0$.

As usual, we may now introduce the order parameter for the superconducting phase,

$$\Delta^* = -g\,\langle\psi^{\dagger}_{1\uparrow a}\,\psi^{\dagger}_{2\downarrow a} + \psi^{\dagger}_{2\uparrow a}\,\psi^{\dagger}_{1\downarrow a}\rangle\,, \quad (5.9)$$

where $\langle\cdots\rangle$ denotes the the expectation value in the grand canonical ensemble. Notice that $|\Delta|$ is the superconducting gap. Introducing the Nambu fermion field $\Phi^{\dagger}_a = (\psi^{\dagger}_{1\uparrow a}\ \psi^{\dagger}_{2\uparrow a}\ \psi^{\dagger}_{1\downarrow a}\ \psi^{\dagger}_{2\downarrow a})$, our model Lagrangian in momentum space can be written in terms of Δ as

$$\mathscr{L} = -\frac{1}{g}\,\Delta^*\Delta\ +\ \Phi^{\dagger}_a\mathscr{A}\Phi_a\,, \quad (5.10)$$

where the matrix $\mathscr{A}$ is given by

$$\mathscr{A} = \begin{pmatrix} -k_0 & k_- & 0 & -\Delta \\ k_+ & -k_0 & -\Delta & 0 \\ 0 & -\Delta^* & -k_0 & -k_+ \\ -\Delta^* & 0 & -k_- & -k_0 \end{pmatrix}, \quad (5.11)$$

with $k_\pm = v_{\mathrm{F}}\,(k_2 \pm \mathrm{i}k_1)$ (the Planck's constant $\hbar = 1$, for the sake of simplicity). The determinant of the matrix $\mathscr{A}$ is $\det\mathscr{A}[\Delta] = \left[(k_0^2 - v_{\mathrm{F}}^2|\mathbf{k}|^2) - |\Delta|^2\right]^2$.

5.2.1 *Quantum Phase Transition*

We now consider the $T = 0$ case. We shall see that there is a quantum critical point connecting the superconducting and normal phases at a certain critical coupling. We start our analysis considering the free energy (effective potential) per plane for the Lagrangian in (5.10), which is denoted by V_{eff}. We assume that there must be constant configurations of Δ that minimize the effective potential per plane, which indicates a superconducting phase.

Since the partition function may be written as a functional integral in the complex time representation,

$$\mathscr{Z} = \frac{1}{\mathscr{Z}^0} \int \mathscr{D}\Phi^\dagger \mathscr{D}\Phi \, \exp\left\{ \mathrm{i} \int d^3k \, \mathscr{L} \right\}, \tag{5.12}$$

we perform the standard gaussian integration over the fermionic fields in order to obtain the effective potential per plane at $T = 0$,

$$V_{\mathrm{eff}}\left(|\Delta|\right) = \frac{|\Delta|^2}{\lambda} - 2 \int \frac{d^2k}{(2\pi)^2} \int \frac{dk_0}{2\pi} \left\{ \ln \left[\frac{\det \mathscr{A}[\Delta]}{\det \mathscr{A}[0]} \right] \right\}, \tag{5.13}$$

where we have introduced the new coupling λ in terms of the numbers of layers, $g = \lambda/N$. The above expression corresponds to a mean field approximation. Conversely, this would be the leading order approximation in an $1/N$ expansion and it becomes the exact result for $N \to \infty$.

We may evaluate the effective potential by introducing a physical cutoff in energy or momentum [5]. When considering applications in condensed matter systems, one usually finds a natural energy cutoff Λ (momentum cutoff Λ/v_{F}). In this case, no renormalization is needed and the coupling λ is the physical one. The results are obtained in terms of an arbitrary energy cutoff Λ, which is always provided by the lattice in condensed matter systems. Indeed, we have $\Lambda = 2\pi\hbar v_{\mathrm{F}}/a$. For the particular case of graphene, Λ is estimated about 17 eV for $a = 2.65$ Å and $v_{\mathrm{F}} = 10^6$ m/s. Since a is the smallest distance scale, Λ becomes a natural high-energy cutoff. A familiar example is the Debye frequency (energy), a natural cutoff that emerges in the BCS theory in the case of conventional phonon mediated superconductivity. However, we would like to stress that we are not assuming that Λ is large compared to $|\Delta|$, rather, we are considering a completely arbitrary finite cutoff. This is not the situation usually found in conventional BCS superconductors. However, it is likely to be found in nonconventional ones such as high-Tc cuprates.

We evaluate (5.13) with a finite physical momentum cutoff Λ/v_{F},

$$V_{\mathrm{eff}}\left(|\Delta|\right) = \frac{|\Delta|^2}{\lambda} - \frac{2}{3\alpha} \left[\left(|\Delta|^2 + \Lambda^2 \right)^{\frac{3}{2}} - |\Delta|^3 - \Lambda^3 \right], \tag{5.14}$$

where $\alpha = 2\pi v_{\mathrm{F}}^2$. Let us study now the minima of the effective potential per plane. For a real order parameter, the first derivative of V_{eff} with respect to Δ is given by

$$V'_{\mathrm{eff}}\left(\Delta\right) = 2\Delta \left[\frac{1}{\lambda} - \frac{\left(\Delta^2 + \Lambda^2 \right)^{\frac{1}{2}}}{\alpha} + \frac{\Delta}{\alpha} \right] = 0 \tag{5.15}$$

This admits two solutions, namely, $\tilde{\Delta}_0 = 0$ or

$$\tilde{\Delta}_0 = \frac{\lambda\alpha}{2}\left[\frac{\Lambda^2}{\alpha^2} - \frac{1}{\lambda^2}\right]. \tag{5.16}$$

The second derivative of the potential, evaluated at $\tilde{\Delta}_0 = 0$ is

$$V''_{\text{eff}}\left(\tilde{\Delta}_0 = 0\right) = \frac{1}{\lambda} - \frac{\Lambda}{\alpha} \tag{5.17}$$

and we conclude that $\tilde{\Delta}_0 = 0$ is a solution only for $\lambda < \tilde{\lambda}_c$, with $\tilde{\lambda}_c = \alpha/\Lambda$. Conversely, the second derivative of (5.14) evaluated at $\tilde{\Delta}_0 \neq 0$ (given by (5.16)) is positive for $\lambda > \tilde{\lambda}_c$. As a consequence the superconducting gap now will be given by

$$\tilde{\Delta}_0 = \begin{cases} 0 & \lambda < \tilde{\lambda}_c \\ \frac{\alpha\lambda}{2}\left(\frac{1}{\tilde{\lambda}_c^2} - \frac{1}{\lambda^2}\right) & \lambda > \tilde{\lambda}_c \end{cases} \tag{5.18}$$

Therefore, we find a quantum phase transition at the critical coupling $\tilde{\lambda}_c = \alpha/\Lambda$, see Fig. 5.3. Observe that, since Λ is a physical parameter, the value of the quantum critical point $\tilde{\lambda}_c$ is predicted by the theory.

Moreover, observe that for $\lambda > \tilde{\lambda}_c$,

$$\tilde{\Delta}_0 = \alpha\left(\frac{1}{\tilde{\lambda}_c} - \frac{1}{\lambda}\right)\left(\frac{\lambda + \tilde{\lambda}_c}{2\tilde{\lambda}_c}\right) \tag{5.19}$$

and in the region where $\lambda \gtrsim \tilde{\lambda}_c$, we have $\tilde{\Delta}_0 \simeq \Delta_0$, with Δ_0 given by the result for the weak coupling limit, the regime where $\Lambda \gg \tilde{\Delta}_0$ [5].

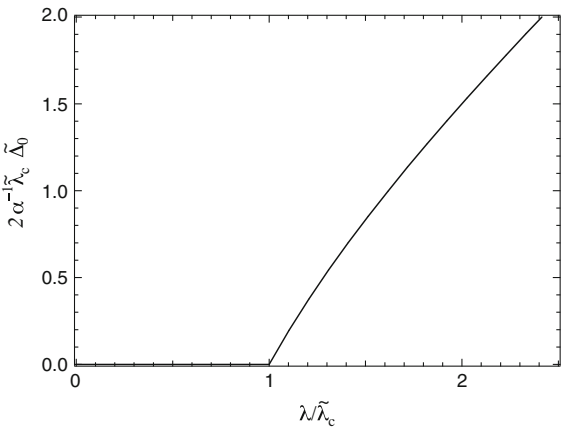

Fig. 5.3 The zero temperature superconducting gap as a function of the interaction coupling $\lambda/\tilde{\lambda}_c$

5.2.2 Finite Temperature Results

In this section we calculate the superconducting transition temperature (also denoted critical temperature T_c) analyzing the minima of the effective potential. The nonzero solutions for Δ at a finite temperature are supposed to hold a priori only in the $N \to \infty$ limit. This limit corresponds to a physical situation where the three-dimensionality of the system is explicitly taken in account. Otherwise temperature phase transitions for lower dimensions are ruled out by the Coleman-Mermin-Wagner-Hohenberg theorem [6]. For finite values of N and $T \neq 0$ the situation is quite subtle and it will be discussed in Sect. 5.2.3. Furthermore, we set the Boltzmann's constant to be one henceforth, for the sake of simplicity as a shorthand notation.

At $T \neq 0$, the effective potential from (5.10) must be

$$V_{\text{eff}}\left(|\Delta|, T\right) = \frac{|\Delta|^2}{\lambda} - 2T \int \frac{d^2k}{(2\pi)^2} \sum_{n=-\infty}^{\infty} \left\{ \ln \left[\frac{\det \mathscr{A}[\Delta]}{\det \mathscr{A}[0]} \right] \right\}, \tag{5.20}$$

where $\omega_n = (2n+1)\pi T$ are the fermionic Matsubara frequencies (with the Boltzmann constant $k_B = 1$).

Since we are looking for the minima of the V_{eff} with respect to the order parameter, we consider the following condition,

$$V'_{\text{eff}}\left(|\Delta|, T\right) = 2|\Delta| \left\{ \frac{1}{\lambda} - \frac{1}{2\alpha} \int_0^{\Lambda^2} dx \frac{1}{\sqrt{x + |\Delta|^2}} \tanh\left(\frac{\sqrt{x + |\Delta|^2}}{2T} \right) \right\} = 0, \tag{5.21}$$

which must be satisfied by the order parameter. Notice that in the above expression we have performed the sum over the Matsubara frequencies and also performed the derivative of (5.20) with respect to $|\Delta|$. Furthermore, Λ is the same cutoff used before.

As in the $T = 0$ case, this admits two solutions, either $\Delta(T) = 0$ or $\Delta(T) \neq 0$. In the latter case, the superconducting order parameter satisfies the gap equation

$$1 = \frac{\lambda}{\alpha} \int_{\tilde{\Delta}}^{\sqrt{\tilde{\Delta}^2 + \Lambda^2}} dy \tanh\left(\frac{y}{2T} \right). \tag{5.22}$$

Solving the integral, we find an implicit equation at an arbitrary temperature for the superconducting energy gap in the presence of a physical cutoff Λ, namely

$$\tilde{\Delta}(T) = 2T \cosh^{-1}\left[e^{-\frac{\alpha}{2T\lambda}} \cosh\left[\frac{\left(\tilde{\Delta}^2(T) + \Lambda^2 \right)^{\frac{1}{2}}}{2T} \right] \right]. \tag{5.23}$$

Using the fact that $\tilde{\Delta}_0$ satisfies the equation $V'_{\text{eff}} = 0$, where the effective potential is given by (5.14), we may verify that indeed

$$\tilde{\Delta}(T) \overset{T\to 0}{\sim} 2T \cosh^{-1}\left[\frac{e^{\frac{\tilde{\Delta}_0}{2T}}}{2}\right] \overset{T\to 0}{\longrightarrow} \tilde{\Delta}_0, \tag{5.24}$$

where $\tilde{\Delta}_0$ is given by (5.18).

Since $\tilde{\Delta}(T_c) = 0$, one can determine the T_c for the onset of superconductivity in the presence of a physical cutoff from (5.23),

$$\cosh\left(\frac{\Lambda}{2T_c}\right) = e^{\frac{\alpha}{2T_c\lambda}}. \tag{5.25}$$

This equation yields the following relation between T_c and the zero temperature gap,

$$\tilde{\Delta}_0 = \left(\frac{\lambda + \tilde{\lambda}_c}{2\tilde{\lambda}_c}\right) 2T_c \ln\left[\frac{2}{1 + e^{-\frac{\Lambda}{T_c}}}\right], \tag{5.26}$$

where $\tilde{\lambda}_c = \alpha/\Lambda$.

It is remarkable that the expression we find for the superconducting energy gap in the case of Dirac fermions, strongly differs from the one obtained in the BCS theory in any dimensions. There the gap has an exponential dependence on the inverse of the coupling λ. Here, in spite of still being non-analytical in the coupling constant λ, the gap has a power-law dependence on it and vanishes below a critical value at zero temperature. The different behavior can be traced back to the fact that in the case of Dirac fermions the density of states vanishes at the Fermi points. In the BCS case, however, we have a Fermi surface with a non-vanishing density of states at the Fermi level and the momentum integrals used for obtaining the effective potential may be evaluated as

$$\int \frac{d^2k}{(2\pi)^2} \simeq N(\varepsilon_{\text{F}}) \int_{-\Lambda}^{\Lambda} d\xi, \tag{5.27}$$

where $N(\varepsilon_{\text{F}})$ is the density of states at the Fermi level. This leads to a gap proportional to $\exp\{-\frac{1}{N(\varepsilon_{\text{F}})\lambda}\}$.

We conclude this section calculating $\Delta(T)$ numerically. But first, we investigate the Δ_0/T_c ratio. A particular regime that is frequently studied is the one where the cutoff is large compared to the critical temperature and to $\tilde{\Delta}_0$, namely, when $\Lambda \gg T_c$ and $\lambda \gtrsim \tilde{\lambda}_c$. This last condition guarantees that $\Lambda \gg \tilde{\Delta}_0$, according to (5.18) and (5.19). Since the previous relations imply

$$T_c \ll \Lambda = \frac{\alpha}{\tilde{\lambda}_c} \simeq \frac{\alpha}{\lambda}, \tag{5.28}$$

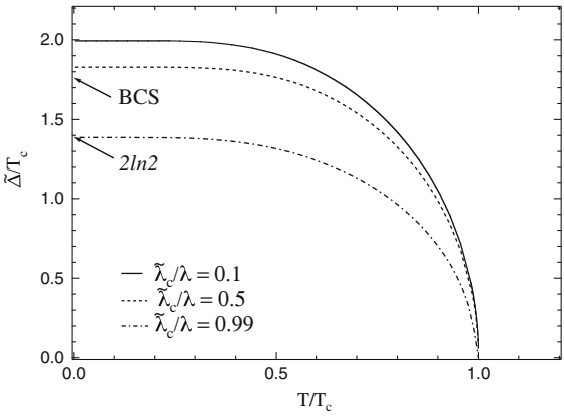

Fig. 5.4 The superconducting gap $\tilde{\Delta}(T)$ divided by T_c as a function of the normalized temperature T/T_c for several values of $\tilde{\lambda}_c/\lambda$. The two arrows indicate the values for $\tilde{\Delta}_0/T_c$ given by the BCS theory and the $\lambda \simeq \tilde{\lambda}_c$ case ($\tilde{\lambda}_c = \alpha/\Lambda$)

we may infer that the conditions above hold in the weak coupling regime. In this case, (5.26) simply becomes $\tilde{\Delta}_0/T_c = 2\ln 2$ [5, 7]. This relation gives the ratio $\tilde{\Delta}_0/T_c \sim 1.39$, which should be compared with the corresponding ratio in the BCS theory for conventional superconductors, namely, 1.76, which is also derived in the weak coupling limit. The pre-factor in the latter expression, describing the behavior of the gap around T_c, is 2.36, whereas the corresponding value in BCS theory is 3.06. We solve (5.23) numerically for $\tilde{\Delta}$, using different values for the ratio $\lambda/\tilde{\lambda}_c$ and display the result in Fig. 5.4. We observe that in the weak coupling regime the ratio Δ_0/T_c approaches the $2\ln 2$ result indeed. On the other hand, as the coupling increases, we see that this ratio surpasses the value obtained in BCS theory and approaches the values obtained experimentally in strongly coupled systems.

We finish this section with a final remark, there are condensed matter systems for which the weak coupling condition (5.28) is not valid, if such systems contain Dirac fermions, we should use (5.18) and (5.23) for the superconducting gap, respectively at $T = 0$ and $T \neq 0$. The critical temperature, by its turn, would be given by (5.26).

5.2.3 *Dynamical Gap Generation Versus Spontaneous Symmetry Breaking*

We know that the Coleman-Mermin-Wagner-Hohenberg theorem [6] forbids the occurrence of spontaneous breakdown of a continuous symmetry at a nonzero temperature for systems below the three spatial dimensions. Therefore, in this section we analise the nature of the superconducting critical temperature calculated above. However, for $N \to \infty$ the system is effectively three-dimensional and the occurrence of a nonzero gap $\Delta(T)$ for finite temperature is not in conflict with the theorem. For $T = 0$, either for finite or infinite N, we have a non-vanishing superconducting gap, which was investigated above, in Sect. 5.2.1. In both cases the Coleman-Mermin-Wagner-Hohenberg theorem does not apply.

We start pointing out that our model Lagrangian given by (5.8), in addition to a complex valued O(N) symmetry [8] and the chiral U(1) symmetry, also possesses the U(1) symmetry,

$$\psi_{i\Delta a} \to e^{\mathrm{i}\theta}\psi_{i\Delta a} \qquad \psi^{\dagger}_{i\Delta a} \to e^{-\mathrm{i}\theta}\psi^{\dagger}_{i\Delta a} \qquad i = 1, 2\,. \tag{5.29}$$

Assuming that the superconducting order parameter $\Delta = \langle\Delta\rangle$ is complex, it can be expressed in terms of polar coordinates as

$$\langle\Delta\rangle = \Delta e^{\mathrm{i}\theta}\,, \tag{5.30}$$

where Δ in the rhs of the above equation is in fact the real superconducting energy gap. Hence, from the above, we infer that a nonzero value for the gap would imply, in principle, the spontaneous breakdown of the U(1) symmetry, (5.29) and a nonzero gap leads to a nonzero order parameter according to (5.30).

In the case of finite N and $T \neq 0$, in order to have a a superconducting phase and yet complying with the Coleman-Mermin-Wagner-Hohenberg theorem, we may invoke the mechanism proposed by Witten [9], by means of which we may have dynamical generation of a superconducting gap without the corresponding U(1) symmetry breakdown. It goes as follows: whenever the gap is nonzero, according to (5.30), we must shift the field Δ as

$$\Delta \to \Delta - \Delta e^{\mathrm{i}\theta}\,. \tag{5.31}$$

This will produce an extra term in the effective Lagrangian

$$\begin{aligned}\mathscr{L}\,[\Psi, \Delta] = \mathrm{i}\overline{\psi}_{\Delta a}\;\partial\!\!\!/\;\psi_{\Delta a} - \frac{1}{g}\,\Delta^{*}\Delta \\ - \Delta^{*}\left(\psi_{2\downarrow b}\;\psi_{1\uparrow b} + \psi_{1\downarrow b}\;\psi_{2\uparrow b}\right) - \Delta\left(\psi^{\dagger}_{1\uparrow a}\;\psi^{\dagger}_{2\downarrow a} + \psi^{\dagger}_{2\uparrow a}\;\psi^{\dagger}_{1\downarrow a}\right).\end{aligned} \tag{5.32}$$

in terms of new fermion fields, defined as $\hat{\psi}_{i\Delta a} \equiv e^{-\mathrm{i}\frac{\theta}{2}}\psi_{i\Delta a}$. The extra term in (5.32) above reads

$$\Delta\left[\left(\hat{\psi}^{\dagger}_{1\uparrow a}\;\hat{\psi}^{\dagger}_{2\downarrow a} + \hat{\psi}^{\dagger}_{2\uparrow a}\;\hat{\psi}^{\dagger}_{1\downarrow a}\right) + \left(\hat{\psi}_{2\downarrow b}\;\hat{\psi}_{1\uparrow b} + \hat{\psi}_{1\downarrow b}\;\hat{\psi}_{2\uparrow b}\right)\right]. \tag{5.33}$$

This is an explicit superconducting gap term that will make

$$\langle\hat{\psi}^{\dagger}_{1\uparrow a}\;\hat{\psi}^{\dagger}_{2\downarrow a} + \hat{\psi}^{\dagger}_{2\uparrow a}\;\hat{\psi}^{\dagger}_{1\downarrow a}\rangle \neq 0. \tag{5.34}$$

Since the U(1) symmetry acts as $\psi_{i\Delta a} \to e^{\mathrm{i}\omega}\psi_{i\Delta a}$ and $\theta \to \theta + 2\omega$ we immediately see that the field $\hat{\psi}_{i\Delta a}$ is invariant under U(1) rotations and therefore the non-vanishing expectation value above does not imply spontaneous breakdown of the

U(1) symmetry. Thus, we can have dynamical generation of a superconducting gap without the associated spontaneous symmetry breaking [9]. Moreover, it should be noticed that the chiral U(1) symmetry, $\psi_{i\Delta a} \to e^{i\theta}\psi_{i\Delta a}$, is also unbroken.

The investigation of the thermodynamic conditions for the occurrence of this mechanism has been done in detail for the case of the Gross-Neveu model in 2+1D [10] and also in the case of the semimetal-excitonic insulator transition that occurs in layered materials [11], both related to the potential spontaneous breakdown of the chiral symmetry. The results of these analysis also apply here. The basic point is that, in order to check whether the order parameter (5.30) is zero or not, we must analyze the thermodynamics of the phase θ of the superconducting order parameter. It turns out that this phase decouples and suffers a Kosterlitz-Thouless [12] transition at a temperature T_{KT}. For temperatures above T_{KT} there is no phase coherence and the superconducting order parameter vanishes because then $\langle\cos\theta\rangle = \langle\sin\theta\rangle = 0$ (even though Δ may be different from zero). Below T_{KT} there is a phase ordering and there will be a nonvanishing gap provided the condition $T < T_c$ is also met (otherwise $\Delta = 0$). As it is, $T_{KT} \leq T_c$ [10] and, therefore, the actual superconducting transition occurs at T_{KT}. However, it can be shown that $T_{KT} \overset{N\to\infty}{\longrightarrow} T_c$ [10]. This clearly indicates that, in spite of the fact that we may have a nonzero superconducting gap at $T = T_c$, only in a really three-dimensional system we will have phase coherence developing at the same temperature that the modulus of the order parameter becomes nonzero, as determined by the gap equation. Therefore, T_c presently calculated may be regarded as a mean-field upper bound critical temperature for the KT transition, which sets the actual temperature for the appearance of superconductivity in the $N \to \infty$ limit.

We conclude this section with a final remark: it has been speculated [13] that the above scenario could provide a framework for explaining the pseudogap transition that precedes the superconducting transition in high-Tc cuprates in the underdoped region. Our model provides a concrete realization of this mechanism.

5.3 Superconductivity in Graphite

In this section we investigate the superconducting phase diagram of a system consisting in a stack of graphene layers with a interlayer hopping between adjacent sheets, where we have assumed the existence of a specific on-site attractive interaction between the electrons [14]. We will see that the hopping between adjacent layers increases the critical temperature for small values of the chemical potential, what might explain why intrinsic superconductivity is observed in graphite and not in graphene [15, 16]. For higher values of chemical potential, our results predict a crossover and the 2D T_c is greater than the 3D T_c, but that only happens to higher values of the chemical potential.

We start our discussion considering a stack of N graphene layers with a hopping term between adjacent planes, where the upper layer has its B sublattice on top of sublattice A of the underlying layer (Bernal stacking), as can be seen in Fig. 5.5. The

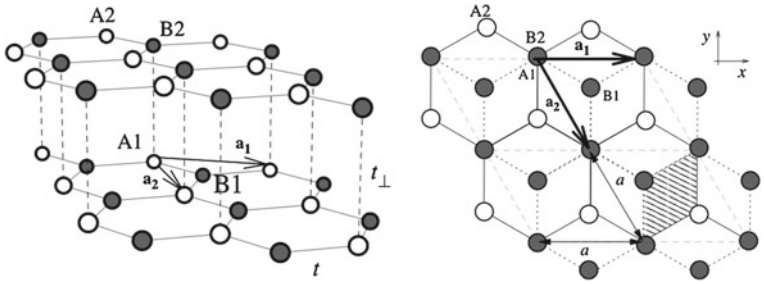

Fig. 5.5 Lattice structure of two adjacent graphene layers (after [2])

Hamiltonian of each coupled layer is described by the following [2],

$$\begin{aligned} H_{t,l} = &-\mu \sum_{\mathbf{k},\sigma} \left(a^\dagger_{\mathbf{k},\sigma,l} a_{\mathbf{k},\sigma,l} + b^\dagger_{\mathbf{k},\sigma,l} b_{\mathbf{k},\sigma,l} \right) \\ &- t \sum_{\mathbf{k},\sigma} s_k \left(a^\dagger_{\mathbf{k},\sigma,l} b_{\mathbf{k},\sigma,l} + a^\dagger_{\mathbf{k},\sigma,l+1} b_{\mathbf{k},\sigma,l+1} \right) + \text{h.c.} \\ &- t_\perp \sum_{\mathbf{k},\sigma} a^\dagger_{\mathbf{k},\sigma,l} b_{\mathbf{k},\sigma,l+1} + \text{h.c.}, \end{aligned} \tag{5.35}$$

where the index $l = 1, \ldots, N$ characterizes the different planes and μ is the chemical potential. The second line in the rhs of the above equation describes the hopping between electrons of different sublattices within a graphene sheet, while the third line describes the hopping between layers. As already seen in Sect. 5.1.1, The hopping parameter is about $t \approx 2.8$ eV, and now we also have added the out-of-plane hopping parameter $t_\perp \approx t/10$. Moreover, for the honeycomb lattice, $s_k = 1 + e^{i\mathbf{k}\cdot\mathbf{a}_1} + e^{i\mathbf{k}\cdot\mathbf{a}_2}$, where $\mathbf{a}_1 = a\hat{e}_x$ and $2\mathbf{a}_2 = a\left(\hat{e}_x - \sqrt{3}\hat{e}_y\right)$, as shown in Fig. 5.5. and also seen in Sect. 5.1.1 as well.

In order to investigate the conditions for the appearance of superconductivity in the system, we add an on-site attractive interaction between the electrons within each graphene layer forming Cooper pairs in the *s*-wave state,

$$\begin{aligned} H_{\text{SC},l} = -\lambda_{\text{sc}} \sum_{\mathbf{k},\mathbf{k}',\sigma,l} &\left(a^\dagger_{\mathbf{k},\sigma,l} a^\dagger_{-\mathbf{k},-\sigma,l} a_{-\mathbf{k}',-\sigma,l} a_{\mathbf{k}',\sigma,l} \right. \\ &\left. + b^\dagger_{\mathbf{k},\sigma,l} b^\dagger_{-\mathbf{k},-\sigma,l} b_{-\mathbf{k}',-\sigma,l} b_{\mathbf{k}',\sigma,l} \right), \end{aligned} \tag{5.36}$$

with $\lambda_{\text{sc}} > 0$. The origin of the interaction is to be determined by some underlying microscopic theory, which is not considered here. However, the symmetry of the gap originated from this interaction is consistent with the isotropic *s*-wave symmetry gap observed in some graphite intercalation compounds (GICs) [17]. Moreover, we assume λ_{sc} to be a free parameter of the Hamiltonian which takes any arbitrary positive value.

Introducing the superconducting order parameter

$$\Delta = -g \sum_{\mathbf{k}} \langle a^{\dagger}_{\mathbf{k},\uparrow,l} a^{\dagger}_{-\mathbf{k},-\downarrow,l} \rangle = -g \sum_{\mathbf{k}} \langle b^{\dagger}_{\mathbf{k},\uparrow,l} b^{\dagger}_{-\mathbf{k},-\downarrow,l} \rangle \tag{5.37}$$

and the Nambu fermion field $\Phi^{\dagger}_{\mathbf{k},l} = \left(\psi^{\dagger}_{\mathbf{k},l}, \psi^{\dagger}_{\mathbf{k},l+1} \right)$, where

$$\psi^{\dagger}_{\mathbf{k},l} = \left(a^{\dagger}_{\mathbf{k},\uparrow,l} \, b^{\dagger}_{\mathbf{k},\uparrow,l} \, a_{-\mathbf{k},\downarrow,l} \, b_{-\mathbf{k},\downarrow,l} \right), \tag{5.38}$$

we may now rewrite the combined Hamiltonian as $H_{t,l} + H_{\mathrm{SC},l}$

$$H = \sum_{\mathbf{k}} \Phi^{\dagger}_{\mathbf{k},l} \, \mathscr{A} \, \Phi_{\mathbf{k},l} - \frac{|\Delta|^2}{g}, \tag{5.39}$$

where the 8×8 matrix $\mathscr{A}$ in (5.39) is given by

$$\mathscr{A} = \begin{pmatrix} \mathscr{A}_1 & \mathscr{A}_{12} \\ \mathscr{A}_{21} & \mathscr{A}_2 \end{pmatrix}, \tag{5.40}$$

with

$$\mathscr{A}_1 = \mathscr{A}_2 = \begin{pmatrix} -\mu & -ts_k & 0 & \Delta \\ -ts_k^* & -\mu & \Delta & 0 \\ 0 & \Delta^* & \mu & ts_k^* \\ \Delta^* & 0 & ts_k & \mu \end{pmatrix} \tag{5.41}$$

and

$$\mathscr{A}_{12} = \mathscr{A}_{21}^T = \begin{pmatrix} 0 & -t_{\perp} & 0 & 0 \\ 0 & 0 & 0 & 0 \\ 0 & 0 & 0 & t_{\perp} \\ 0 & 0 & 0 & 0 \end{pmatrix}. \tag{5.42}$$

5.3.1 Phase Diagram for Bilayer Graphene

Graphene dispersion relation has six Dirac points at the corners of the first Brillouin zone; however, only two of them are non-equivalent [2, 3] Therefore, the low energy of our model Hamiltonian is obtained expanding (5.39) in the vicinity of the Dirac points. Redefining the coupling $g = \lambda/N$, the effective potential per bilayer for each Dirac point will be [14]

$$V_{\mathrm{eff}} = 2\frac{|\Delta|^2}{\lambda} - \frac{1}{\beta} \sum_{n} \left[\int \frac{d^2k}{(2\pi)^2} \ln \left(\frac{\det \mathscr{A}'_{K,n}[\Delta]}{\det \mathscr{A}'_{K,n}[0]} \right) \right], \tag{5.43}$$

where $\mathscr{A}'_{\alpha,n} = -i\omega_n \mathbf{1} + \mathscr{A}_\alpha$ and $\mathbf{1}$ is the 8×8 unity matrix. As in Sect. 5.2, the above expression in (5.43) is the leading order in a $1/N$ expansion and would be the exact result for $N \to \infty$.

The occurrence of superconductivity corresponds to the existence of nonzero solutions of the superconducting gap that minimizes the effective potential. Taking the derivative of V_{eff} with respect to the order parameter and summing over the Matsubara frequencies, we obtain

$$V'_{\text{eff}}(T) = \Delta^* \left[\frac{2}{\lambda} - \frac{1}{2} \sum_{j=1}^{4} \int \frac{d^2k}{(2\pi)^2} \frac{1}{\sqrt{|\Delta|^2 + \xi_j^2}} \tanh\left(\frac{\beta}{2} \sqrt{|\Delta|^2 + \xi_j^2} \right) \right], \tag{5.44}$$

where

$$\xi_j = \pm \sqrt{v_{\text{F}}^2 k^2 + \left(\frac{t_\perp}{2} \right)^2} \pm \frac{t_\perp}{2} - \mu \tag{5.45}$$

and $v_{\text{F}} = \sqrt{3}ta/2$ ($\hbar = 1$) for graphene. The nonzero solutions for $|\Delta|$ are given equalizing to zero the expression within brackets in (5.44), which provides the self-consistent gap equation. Introducing the momentum cutoff Λ/v_{F}, we get

$$\frac{1}{\lambda} - \frac{1}{8\alpha} \sum_{a,b} \int_0^{\Lambda^2} dx \, \frac{1}{E_{ab}(x)} \tanh\left[\frac{E_{ab}(x)}{2T} \right] = 0 \,, \tag{5.46}$$

where

$$E_{ab}(x) \equiv \sqrt{|\Delta|^2 + \xi_{ab}^2(x)} \,, \tag{5.47}$$

with

$$\xi_{ab} = a \sqrt{\Lambda^2 + \left(\frac{t_\perp}{2} \right)^2} + b \frac{t_\perp}{2} - \mu \,, \tag{5.48}$$

$\alpha = 2\pi v_{\text{F}}^2$ and $a, b = \pm 1$.

A priori, the nonzero solutions for Δ are supposed to hold only in the $N \to \infty$ limit at a finite temperature, because, otherwise, they are ruled out by the Coleman-Mermin-Wagner-Hohenberg theorem [6], as previously discussed in Sect. 5.2.3. However, T_c calculated in the present section for an arbitrary N may be regarded as a mean-field upper bound critical temperature for the Berezinskii-Kosterlitz-Thouless transition, which sets the actual temperature for the appearance of superconductivity in the $N \to \infty$ limit.

In particular, notice that for $T = \mu = t_\perp = 0$ in (5.46), the nonzero solutions for the superconducting gap yields the same result in (5.18) for $\lambda > \alpha/\Lambda$, which is the quantum critical point calculated in Sect. 5.2.1. Moreover, the case $T = t_\perp = 0$ and finite μ with different values of interaction couplings will be discussed in Sect. 5.4.2.

Presently, we calculate the T_c making $\Delta = 0$ at $T = T_c$ in (5.46). We also constrain ourselves to positive values of the chemical potential up to $\mu/\Lambda = 0.9$, given the half

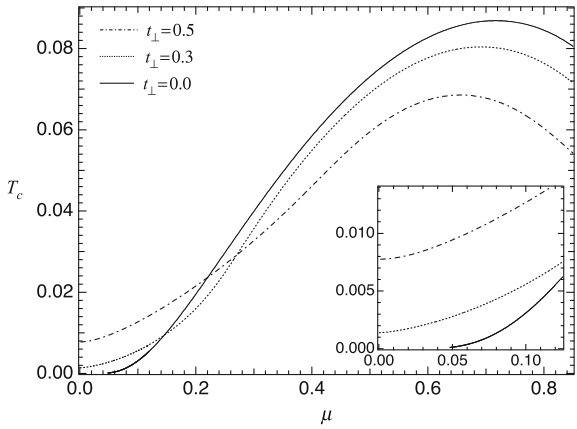

Fig. 5.6 The superconducting critical temperature as a function of the chemical potential for $t_\perp = 0,\ 0.3$ and 0.5. The inset shows the same plot for a smaller range of the chemical potential. $\lambda/\lambda_c = 0.8$ and all the other quantities are given in unities of Λ

bandwidth Λ. Our numerical results for T_c are shown in Fig. 5.6 for several values of $t_\perp$. The inset of Fig. 5.6 shows that, for a small value of μ ($\mu/\Lambda < 0.13$), given in terms of the cutoff, T_c increases as $t_\perp$ increases, indicating that the hopping between layers favours the appearance of superconductivity in the system for small values of the chemical potential.

5.3.2 Phase Diagram for Graphite

We now consider calculating the superconducting phase diagram of many coupled graphene layers for a finite chemical potential. To simplify the problem, we consider only the minimal model where only the electron tunneling amplitudes between the nearest sites in the plane t and out of the plane $t_\perp$ are regarded. The same approach was employed in [18].

Consider a graphene bilayer described by the following Hamiltonian in the vicinity of each non-equivalent [2],

$$H_{\rm BL} = \sum_{\mathbf{k},\sigma} \Phi^\dagger_{\mathbf{k},\sigma} \mathscr{B}_{\mathbf{k}} \Phi_{\mathbf{k},\sigma}\ , \tag{5.49}$$

where the above 4×4 matrix $\mathscr{B}_{\mathbf{k}}$ is given by

$$\mathscr{B}_{\mathbf{k}} = \begin{pmatrix} v_F\, \mathbf{k}\cdot\boldsymbol{\sigma} & \mathscr{B}_{12} \\ \mathscr{B}_{21} & v_F\, \mathbf{k}\cdot\boldsymbol{\sigma} \end{pmatrix}, \tag{5.50}$$

the vector $\boldsymbol{\sigma} = \left(\sigma_x, \sigma_y\right)$ is written in terms of the well-known Pauli matrices, the matrix $\mathscr{B}_{12}$ is

$$\mathscr{B}_{12} = \mathscr{B}_{21}^{T} = \begin{pmatrix} 0 & t_{\perp} \\ 0 & 0 \end{pmatrix}, \tag{5.51}$$

and $\Phi_{\mathbf{k},\sigma}^{\dagger} = \left(\psi_{\mathbf{k},\sigma,1}^{\dagger}, \psi_{\mathbf{k},\sigma,2}^{\dagger}\right)$, with $\psi_{\mathbf{k},\sigma,j}^{\dagger} = \left(a_{\mathbf{k},\sigma,j}^{\dagger}\, b_{\mathbf{k},\sigma,j}^{\dagger}\right), j = 1, 2$ denotes the layer index.

The model Hamiltonian for graphite is assumed to be described as an infinite number of graphene layers coupled by the hopping between adjacent sheets. Therefore, introducing the operator

$$\tilde{\Phi}_{\mathbf{k},\sigma}^{\dagger} = \left(\cdots \psi_{\mathbf{k},\sigma,l-1}^{\dagger}\, \psi_{\mathbf{k},\sigma,l}^{\dagger}\, \psi_{\mathbf{k},\sigma,l+1}^{\dagger} \cdots\right), \tag{5.52}$$

the Hamiltonian becomes

$$H_{\mathrm{Gr}} = \sum_{\mathbf{k},\sigma} \tilde{\Phi}_{\mathbf{k},\sigma}^{\dagger} \mathscr{C}_{\mathbf{k}} \tilde{\Phi}_{\mathbf{k},\sigma}, \tag{5.53}$$

where

$$\mathscr{C}_{\mathbf{k}} = \begin{pmatrix} \ddots & & & & \\ & v_F\, \mathbf{k}\cdot\boldsymbol{\sigma} & \mathscr{B}_{12} & & \\ & \mathscr{B}_{21} & v_F\, \mathbf{k}\cdot\boldsymbol{\sigma} & \mathscr{B}_{12} & \\ & & \mathscr{B}_{21} & v_F\, \mathbf{k}\cdot\boldsymbol{\sigma} & \\ & & & & \ddots \end{pmatrix}. \tag{5.54}$$

Introducing the momentum k_z in the z direction, it is possible to re-express the Hamiltonian for graphite taking the first-neighbors hopping between adjacent layers in the momentum representation, which is written in terms of a 4×4 matrix similar to $\mathscr{B}_{\mathbf{k}}$ in (5.50) [18],

$$H_{\mathrm{Gr}} = \sum_{\mathbf{k},k_z,\sigma} \Phi_{\mathbf{k},k_z,\sigma}^{\dagger} \mathscr{D}_{\mathbf{k},k_z} \Phi_{\mathbf{k},k_z,\sigma}, \tag{5.55}$$

where

$$\mathscr{D}_{\mathbf{k},k_z} = \begin{pmatrix} v_F\, \mathbf{k}\cdot\boldsymbol{\sigma} & 2\,\mathscr{B}_{12}\cos k_z d \\ 2\,\mathscr{B}_{21}\cos k_z d & v_F\, \mathbf{k}\cdot\boldsymbol{\sigma} \end{pmatrix}, \tag{5.56}$$

and d is the distance between layers.

For this minimal model, the dispersion relation is given by

$$E_{\mathrm{Gr}} = \pm\sqrt{|v_{\mathrm{F}}\,\mathbf{k}|^2 + (t_{\perp}\cos k_z d)^2} \pm t_{\perp}\cos k_z d \tag{5.57}$$

and, for $k_z d = \pi/2$, we recover the Dirac-type dispersion found in graphene.

Taking into account the attractive interaction forming Cooper pairs within each graphene layer, as seen in (5.36), and introducing the operator

$$\tilde{\Psi}^{\dagger}_{\mathbf{k},\sigma} = \left(\cdots \psi^{\dagger}_{\mathbf{k},\sigma,l-1} \, \psi^{\dagger}_{\mathbf{k},\sigma,l} \, \psi^{\dagger}_{\mathbf{k},\sigma,l+1} \cdots \right), \tag{5.58}$$

where $\psi^{\dagger}_{\mathbf{k},\sigma,l}$ is given by (5.38), the model Hamiltonian which describes the superconducting graphite becomes

$$H_{\mathrm{Gr,SC}} = \sum_{\mathbf{k},\sigma} \tilde{\Psi}^{\dagger}_{\mathbf{k},\sigma} \mathscr{E}_{\mathbf{k}} \tilde{\Psi}_{\mathbf{k},\sigma}, \tag{5.59}$$

where

$$\mathscr{E}_{\mathbf{k}} = \begin{pmatrix} \ddots & & & & \\ & \mathscr{A}_1 & \mathscr{A}_{12} & & \\ & \mathscr{A}_{21} & \mathscr{A}_2 & \mathscr{A}_{12} & \\ & & \mathscr{A}_{21} & \mathscr{A}_1 & \\ & & & & \ddots \end{pmatrix}, \tag{5.60}$$

with $\mathscr{A}_1 = \mathscr{A}_2$ and $\mathscr{A}_{12} = \mathscr{A}_{21}^T$ given by the (5.41) and (5.42) respectively.

Accordingly, taking $\Delta \equiv \langle 0|\sigma|0\rangle$, it is possible to re-express the Hamiltonian for the superconducting graphite in terms of an 8×8 matrix, which is similar to $\mathscr{A}_{\mathbf{k}}$ in (5.40),

$$H_{\mathrm{Gr,SC}} = \sum_{\mathbf{k},k_z,\sigma} \Psi^{\dagger}_{\mathbf{k},k_z,\sigma} \mathscr{F}_{\mathbf{k},k_z} \Psi_{\mathbf{k},k_z,\sigma}, \tag{5.61}$$

where

$$\mathscr{F}_{\mathbf{k},k_z} = \begin{pmatrix} \mathscr{A}_1 & 2\mathscr{A}_{12}\cos k_z d \\ 2\mathscr{A}_{21}\cos k_z d & \mathscr{A}_2 \end{pmatrix} \tag{5.62}$$

and the dispersion is given by the 8 eigenvalues

$$E_{\pm}(\mathbf{k}, k_z) = \pm\sqrt{|\Delta|^2 + (E_{\mathrm{Gr}} - \mu)^2}, \tag{5.63}$$

with E_{Gr} given by (5.57).

Therefore, the self-consistent equation for the superconducting gap becomes

$$\frac{2}{\lambda} = \frac{1}{2} \sum_{j=1}^{4} \int_{-\frac{\pi}{d}}^{\frac{\pi}{d}} \frac{dk_z}{2\pi d} \int \frac{d^2k}{(2\pi)^2} \frac{1}{E_+(\mathbf{k}, k_z)} \tanh\left[\frac{\beta}{2} E_+(\mathbf{k}, k_z) \right], \tag{5.64}$$

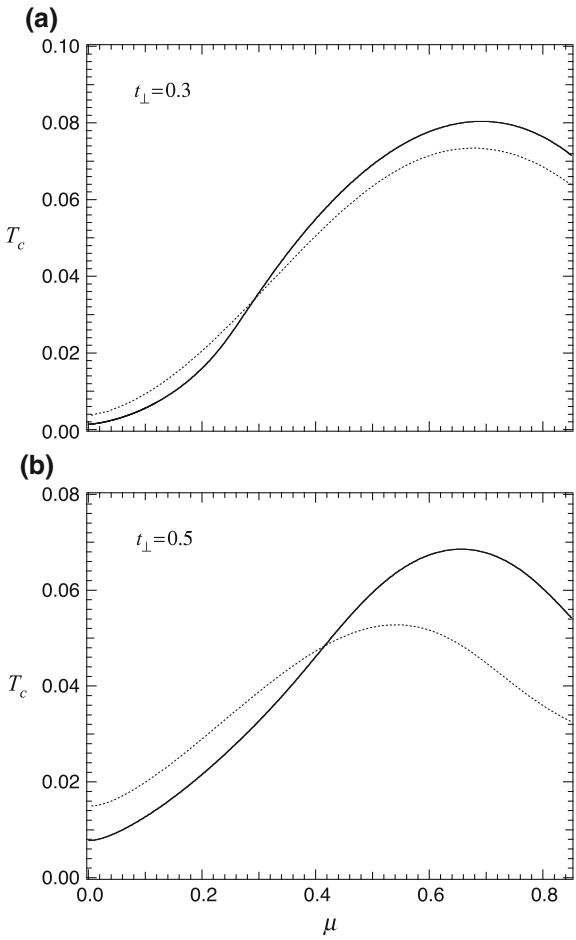

Fig. 5.7 The superconducting critical temperature as a function of the chemical potential for **a** $t_\perp = 0.3$ and **b** $t_\perp = 0.5$ for both graphene bilayer (*solid line*) and graphite (*dotted line*). The inset in each pane shows the same plot for a smaller range of the chemical potential. $\lambda/\lambda_c = 0.8$ and all the other quantities are given in unities of Λ

where the four values of $E_+(\mathbf{k}, k_z)$, labeled by the index j in the above expression, are given by $E_{\rm Gr}$ in (5.57), in analogy to the discussions in the previous sections.

We calculate the superconducting transition temperature from (5.64) and our results are compared with T_c obtained for graphene bilayer, from the former section. Our results are shown in Fig. 5.7 and we see that for small values of the chemical potential the critical temperature for graphite is bigger than the T_c obtained for graphene bilayer for a given value of $t_\perp$, indicating that the first neighbors hopping between adjacent sheets favors the superconductivity in the system. This might explain why intrinsic superconductivity is observed in highly oriented pyrolytic graphite (HOPG) [15] and also with critical temperature $T_c \sim 25$ K in thin samples [16].

5.4 Interplay Among Superconducting Phase Transitions, Excitonic Phase Transitions and Doping

A remarkable feature presented by the high-temperature superconductivity of the cuprates is the insulator-superconductor transition as charge carriers are pumped into the system. Motivated by this, in this section we investigate the conditions for the appearance of excitons or the superconducting gap in planar Dirac fermion systems with two Dirac points.

We start our analysis assuming that the excitonic gap is similar to the one appearing in the chiral symmetry-breaking phenomenon, which has been largely studied in relativistic fermion theories [19]. The same approach has been employed previously [20] and the interaction controlling the excitonic phase should be

$$H_{\text{exc}} = \lambda_{\text{exc}} \sum_{i,\sigma} \left(a^{\dagger}_{i,\sigma} a_{i,\sigma} - b^{\dagger}_{i,\sigma} b_{i,\sigma} \right) \left(a^{\dagger}_{i,\sigma} a_{i,\sigma} - b^{\dagger}_{i,\sigma} b_{i,\sigma} \right) , \tag{5.65}$$

where λ_{exc} should be treated as a free parameter here.

Introducing the excitonic order parameter,

$$\sigma = \lambda_{\text{exc}} \sum_{i,\sigma} \langle a^{\dagger}_{i,\sigma} a_{i,\sigma} - b^{\dagger}_{i,\sigma} b_{i,\sigma} \rangle , \tag{5.66}$$

we can rewrite the combined Hamiltonian $H_t + H_{\text{SC}} + H_{\text{exc}}$, where H_t denotes the hopping of electrons within a layer, which is given by (5.35) for $t_{\perp} = 0$, and the superconducting interaction is seen in (5.36). For a particular layer, our model Hamiltonian in a mean-field approximation becomes

$$H = \sum_{\mathbf{k}} \Phi^{\dagger}_{\mathbf{k}} \mathscr{A}_{\mathbf{k}} \Phi_{\mathbf{k}} , \tag{5.67}$$

where the auxiliary Nambu field is $\Phi^{\dagger}_{\mathbf{k}} = \left(a^{\dagger}_{\mathbf{k},\uparrow} \; b^{\dagger}_{\mathbf{k},\uparrow} \; b_{-\mathbf{k},\downarrow} \; b_{-\mathbf{k},\downarrow} \right)$ and the matrix $\mathscr{A}_{\mathbf{k}}$ is given by

$$\mathscr{A}_{\mathbf{k}} = \begin{pmatrix} \mu + \sigma & -ts_k & 0 & \Delta \\ -ts_k^* & \mu - \sigma & \Delta & 0 \\ 0 & \Delta^* & \sigma - \mu & ts_k^* \\ \Delta^* & 0 & ts_k & -(\mu - \sigma) \end{pmatrix} . \tag{5.68}$$

Notice that we have Fourier transformed (5.65) in order to obtain our model Hamiltonian above. Moreover, the chemical potential has been introduced as well.

At zero temperature, the effective potential per Dirac point becomes [19]

$$V_{\text{eff}} = \frac{|\Delta|^2}{\lambda_{\text{sc}}} + \frac{\sigma^2}{\lambda_{\text{exc}}} - \int \frac{d^2k}{(2\pi)^2} \left[\sum_l \sqrt{|\Delta|^2 + \xi_l^2} - 2v_{\text{F}}k \right] , \tag{5.69}$$

where $\xi_l(x) = \sqrt{x+\sigma^2} + l\mu$, with $l = +1$ or -1. Introducing the momentum cutoff Λ/v_F, we arrive at the following expression for the effective potential,

$$V_{\text{eff}} = \frac{|\Delta|^2}{\lambda_{\text{sc}}} + \frac{\sigma^2}{\lambda_{\text{exc}}} + \frac{2\Lambda^3}{3\alpha} - \frac{1}{3\alpha}\sum_l \left[E_l^3(\Lambda^2) - E_l^3(0)\right] + \frac{1}{2\alpha}\sum_l l\mu \left\{\xi_l(x)E_l(x) + |\Delta|^2 \log\left[\xi_l(x) + E_l(x)\right]\right\}\Big|_0^{\Lambda^2}, \quad (5.70)$$

where $\alpha = 2\pi v_F^2$ and $E_l(x) = \sqrt{|\Delta|^2 + \xi_l^2(x)}$. In particular, for $\mu = \sigma = 0$, (5.70) is reduced to (5.14), which is exactly the same result obtained for a single layer of Dirac electrons interacting via a BCS-type superconducting interaction.

In the remaining of this section, we analyze the conditions for the appearance of superconductivity or excitonic fluctuations at zero temperature, taking into account the two competing interactions present in our model.

5.4.1 Zero Chemical Potential

From (5.69), introducing the momentum cutoff Λ/v_F and integrating over k, the effective potential for $\mu = 0$ becomes

$$\tilde{V}_{\text{eff}} \equiv \frac{\alpha}{\Lambda^3} V_{\text{eff}} = \frac{\tilde{\Delta}^2}{\tilde{\lambda}_{\text{sc}}} + \frac{\tilde{\sigma}^2}{\tilde{\lambda}_{\text{exc}}} - \frac{2}{3}\left[\left(\tilde{\Delta}^2 + \tilde{\sigma}^2 + 1\right)^{\frac{3}{2}} - \left(\tilde{\Delta}^2 + \tilde{\sigma}^2\right)^{\frac{3}{2}} - 1\right], \quad (5.71)$$

where now the order parameters are expressed in terms of the cutoff, $\tilde{\sigma} = \sigma/\Lambda$ and $\tilde{\Delta} = |\Delta|/\Lambda$ and also the interaction couplings are written as $\tilde{\lambda}_{\text{sc}} = \lambda_{\text{sc}}/\tilde{\lambda}_c$ and $\tilde{\lambda}_{\text{exc}} = \lambda_{\text{sc}}/\tilde{\lambda}_c$, with $\tilde{\lambda}_c = \alpha/\Lambda$.

We start our analysis considering the particular case where the excitonic and superconducting interactions are the same, $\lambda = \lambda_{\text{sc}} = \lambda_{\text{exc}}$. In such case, from a simple inspection of (5.71), it is straightforward to see that a new order parameter $\zeta^2 = |\Delta|^2 + \sigma^2$ can be defined so that V_{eff} becomes exactly the same effective potential already analysed in Sect. 5.2.1. As previously, we find a quantum phase transition at the critical coupling $\lambda_c = \alpha/\Lambda$. But now we also have the possibility of coexistence of superconductivity and the excitonic fluctuations. Indeed, as can be seen in the tridimensional plot shown in Fig. 5.8, the minima of the V_{eff} presents a radial symmetry. Therefore, it is possible to find simultaneously nonzero values for σ and Δ which minimize the effective potential, indicating that excitons and Cooper pairs coexist in the system.

The same result was obtained in the framework of nuclear physics [21], where the formation of chiral and diquark condensates involving two quark flavours in QCD was investigated. In their case, the values for the quark-antiquark and quark-quark interactions strengths were set equal by construction, via a Fierz transformation

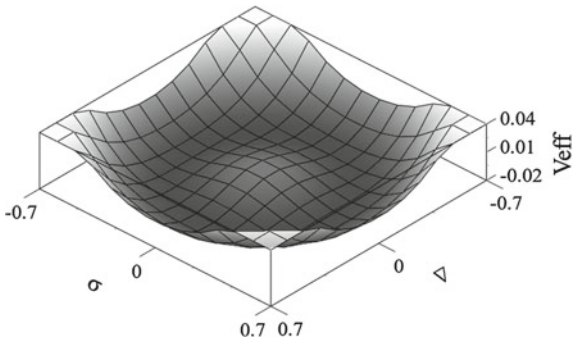

Fig. 5.8 Effective potential including both cases: excitonic and superconducting interactions. The parameters are taken as $\mu = 0$, $\tilde{\lambda}_{\rm exc} = \tilde{\lambda}_{\rm sc} = 1.5$. All parameters are in units of Λ

applied to the Nambu-Jona-Lasinio model. In our case, on the other hand, we are not restricted to the relation $\lambda_{\rm sc} = \lambda_{\rm exc}$ and therefore we shall analyze the situation for which $\lambda_{\rm sc} \neq \lambda_{\rm exc}$ below.

First, we assume the case $\lambda_{\rm sc} > \lambda_{\rm exc}$. The nonzero point for which the effective potential $V_{\rm eff}(\Delta, \sigma)$, given by (5.71), reaches its minimum for positive superconducting energy gap Δ and and excitonic order parameter σ is

$$(\Delta_0,\ \sigma_0) = \left(\frac{\tilde{\lambda}_{\rm sc}^2 - 1}{2\tilde{\lambda}_{\rm sc}},\ 0 \right), \tag{5.72}$$

but only if $\tilde{\lambda}_{\rm sc} > 1$ and $\delta > 0$. Inserting (5.72) in the above definition of ζ, we get the minimum $\zeta_0 = \Delta_0$ and there is only superconductivity in the system, provided $\lambda_{\rm sc} > \lambda_{\rm exc}$, and also $\tilde{\lambda}_{\rm sc} > 1$.

The same discussion follows for $\lambda_{\rm sc} < \lambda_{\rm exc}$ and the effective potential reaches its minimum for positive values at

$$(\Delta_0,\ \sigma_0) = \left(0,\ \frac{\tilde{\lambda}_{\rm sc}^2 - 1}{2\tilde{\lambda}_{\rm sc}} \right), \tag{5.73}$$

if $\tilde{\lambda}_{\rm exc} > 1$. Therefore, we only have excitons in the system.

In summary, for $\mu = 0$, we have seen that excitons and Cooper pairs can coexist whenever the corresponding interactions couplings are equal. If one of the interactions is stronger than the other, then only its corresponding order parameter is non-vanishing.

5.4.2 Finite Chemical Potential

Now we consider the conditions for the appearance of the superconducting energy gap or excitons in the system at $T = 0$. From (5.69), we notice that $V_{\rm eff}(\mu) = V_{\rm eff}(-\mu)$.

Therefore the minima for positive $\mu > 0$ are exactly the same for negative $\mu < 0$, and we constrain the analysis to positive values of the chemical potential in this section.

We start taking into account only the presence of superconducting interactions (in the absence of excitonic interactions). In such case (5.69) becomes

$$\tilde{V}_{\text{eff}} = \frac{|\tilde{\Delta}|^2}{\tilde{\lambda}_{\text{sc}}} + \frac{2}{3} - \frac{1}{2\alpha}\sum_l \int_0^1 dy \sqrt{|\tilde{\Delta}|^2 + \left(\sqrt{y} + l\tilde{\mu}\right)^2}\,. \tag{5.74}$$

where $\tilde{\mu} = \mu/\Lambda$. Notice that replacing $\mu = 0$ in the above expression was already investigated above. Moreover, some results for $\mu \neq 0$ have been previously reported considering the s-wave and an exotic p-wave pairing [22]. We can calculate numerically the positive values of $\tilde{\Delta}$ that minimize the effective potential in (5.74), as long as the values for the parameters $\tilde{\mu}$ and $\tilde{\lambda}_{\text{sc}}$ are furnished.

For the case $\tilde{\lambda}_{\text{sc}} < 1$, our results are shown in Fig. 5.9. Starting at $\tilde{\mu} = 0$, the system is in the normal state. However, as $\tilde{\mu}$ increases, the system asymptotically becomes superconducting and the order parameter also increases up to a maximum value at an optimal chemical potential. As $\tilde{\mu}$ increases even further, $\tilde{\Delta}_0$ decreases and the energy gap displays a dome-shaped plot.

Our results are consistent with [23], where chiral and diquark condensates are calculated for two-color and two-flavor QCD. For a certain choice of parameters, the authors obtain the same dispersion relation we have found and their numerical results for Δ also display a dome-shaped plot, as can be seen in Fig. 1 of [23], for the choice of parameters I, referred as the *weak-coupling case*.

Since the energy gap and the superconducting critical temperature T_c are proportional, our results qualitatively reproduce the superconducting phase diagram of several compounds, like 122 pnictides and cuprate superconductors, where the crit-

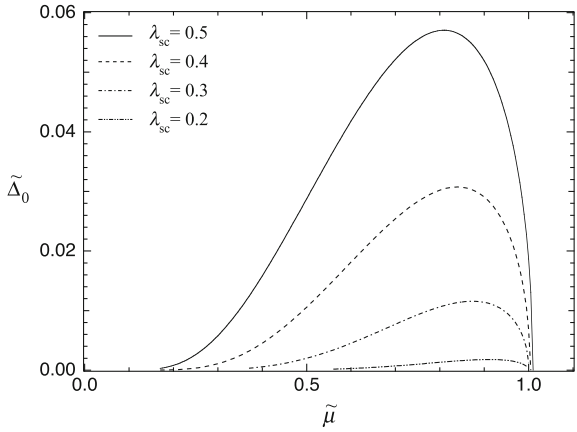

Fig. 5.9 Plots of the superconducting gap $\tilde{\Delta}_0$ as a function of the chemical potential $\tilde{\mu}$ for several values of $\tilde{\lambda}_{\text{sc}} < 1$. All parameters are in units of Λ

ical temperature displays a characteristic dome as charge carriers are doped into the system. Also, a dome-like structure of the superconducting phase for strongly interacting two-dimensional Dirac fermions has been previously obtained in [24], where the authors observed a dome-shaped plot of the superconducting phase at intermediate filling fractions, surrounded by the normal phase for fillings close to unity or zero, which is consistent to our results. Also, a dome for T_c as a function of hole concentrations has been previously obtained in a brief letter by some of us [25] for a relativistic version of the spin-fermion Hamiltonian to describe the Cu-O planes in the cuprates. Those results and the phase diagram presently calculated suggest that Dirac fermions may play a relevant role in the description of systems containing Dirac fermions, like cuprates and iron pnictides [26, 27].

Regarding the conditions for the appearance of superconductivity in the system: contrary to what happens at $\mu = 0$, where superconductivity appears in the system only when $\lambda_{\rm sc} > \lambda_c$, at finite chemical potential we could always find a finite $\tilde{\mu}$ that provided nonzero superconducting gaps, even at small values of $\lambda_{\rm sc}$, as can be seen in Fig. 5.9, where plots of $\tilde{\Delta}_0$ as a function of $\tilde{\mu}$ for small values of $\tilde{\lambda}_{\rm sc}$ are shown. This result suggests that even for very small superconducting interaction strengths, one can always find superconductivity as charge carriers are added to the system.

We conclude this section analysing the conditions for the appearance of a nonzero superconducting gap or excitons in the system as the chemical potential is varied. Taking into account both the excitonic and superconducting interactions, the effective potential in (5.69) can be written as

$$\tilde{V}_{\rm eff} = \frac{|\tilde{\Delta}|^2}{\tilde{\lambda}_{\rm sc}} + \frac{\tilde{\sigma}^2}{\tilde{\lambda}_{\rm exc}} + \frac{2}{3} - \frac{1}{2}\sum_l \int_0^1 dy \sqrt{|\tilde{\Delta}|^2 + \left(\sqrt{y+\tilde{\sigma}^2} + l\tilde{\mu}\right)^2} \tag{5.75}$$

and, once again, we constrain ourselves to positive values of the chemical potential, since $V_{\rm eff}$ is even with respect to μ.

When both $\tilde{\lambda}_{\rm exc}, \tilde{\lambda}_{\rm sc} < 1$, we do not have the presence of superconductivity or excitonic fluctuations in the system at zero value of the chemical potential. However, as the chemical potential increases we can find a nonzero superconducting gap and this indicates that, as charge carriers are added to the system, superconductivity sets in, as we have discussed above.

On the other hand, taking $\tilde{\lambda}_{\rm exc}, \tilde{\lambda}_{\rm sc} > 1$, and assuming that $\tilde{\lambda}_{\rm exc}$ is larger then $\tilde{\lambda}_{\rm sc}$ we cannot have coexistence of superconductivity and excitonic fluctuations at $\tilde{\mu} = 0$, since the interaction strengths are different, as we have discussed above. Actually, since $\tilde{\lambda}_{\rm exc} > \tilde{\lambda}_{\rm sc}$, we have zero superconducting order parameter and $\tilde{\sigma}_0 = (\tilde{\lambda}_{\rm exc}^2 - 1)/2\tilde{\lambda}_{\rm exc}$. Indeed, as can be seen in Fig. 5.10a, the point $(0, \tilde{\sigma}_0)$ is the minimum of the effective potential for non-negative values of $\tilde{\sigma}_0$ and $\tilde{\Delta}_0$. Moreover, as we start to increase the values of the chemical potential, the minimum of the effective potential remains the same as long as we constrain ourselves to small values of $\tilde{\mu}$ and we have no superconductivity even for finite values of chemical potential.

However, when $\tilde{\mu}$ continues to increase, we regain the radial symmetry of the minima for the effective potential, as can be seen in Fig. 5.10b. In other words, we

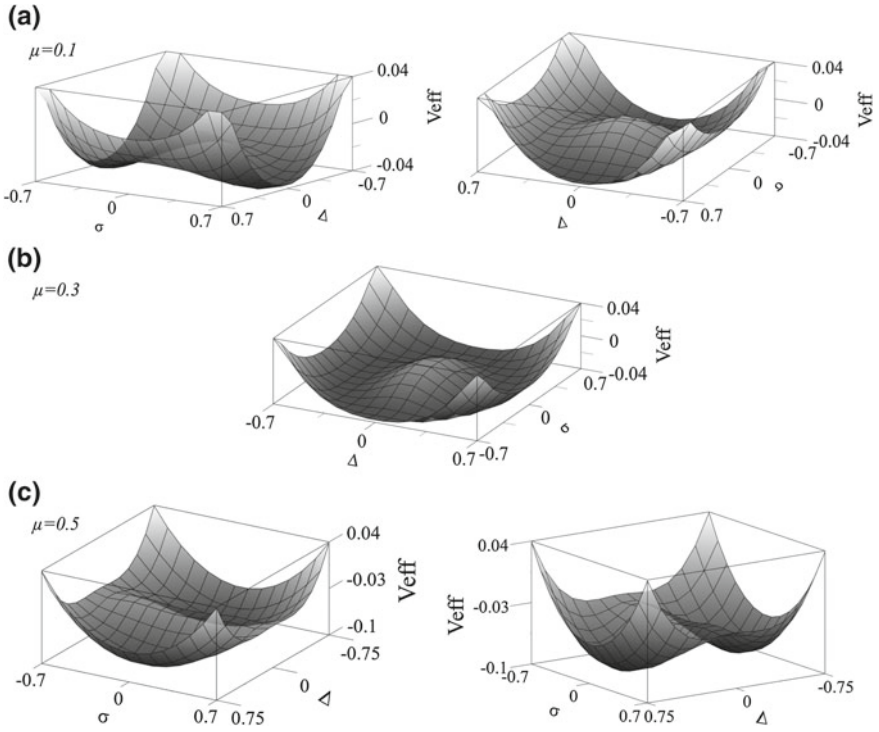

Fig. 5.10 Effective potential including both cases: excitonic and superconducting interactions.The parameters are taken as $\tilde{\lambda}_{\text{exc}} = 1.75$, $\tilde{\lambda}_{\text{sc}} = 1.5$. and **a** $\mu = 0.1$; **b** $\mu = 0.3$; **c** $\mu = 0.5$. All quantities are given in units of Λ

recover the coexistence of superconductivity and excitonic order fluctuations even if $\tilde{\lambda}_{\text{exc}} > \tilde{\lambda}_{\text{sc}}$.

Furthermore, as the chemical potential increases even more, other interesting results show up, as can be seen in Fig. 5.10c. In that case, the plot for the effective potential shows the minimum at the point $\tilde{\sigma}_0 = 0$ and finite $\tilde{\Delta}_0$, which means that the excitonic fluctuations were suppressed from the system and only superconductivity remains. In other words, even if $\tilde{\lambda}_{\text{exc}} > \tilde{\lambda}_{\text{sc}}$, as charge carriers are added to the system, doping effects eliminate the excitonic order parameter and favours superconductivity.

These results are consistent to the results obtained in hadronic physics, where, as the baryonic chemical potential increases, chiral symmetry in the system is restored and color superconductivity sets in [28].

Moreover, we see that the insulating excitonic gap is suppressed and it becomes superconducting as charge carriers are added to the system, which is the same feature observed in some strongly correlated systems, as the cuprates, for instance. Therefore, our results resemble the insulator-superconductor transition observed in the cuprates.

5.5 Conclusions and Overview

We have studied the superconductivity of Dirac electrons in monolayered systems, bilayers and multilayers, either at $T = 0$ or at a finite temperature. The effects of doping, associated to a finite chemical potential were also included. Then, the interplay of the superconductivity and excitonic interactions was also considered. In all cases, a detailed phase diagram was determined. The study of superconductivity of Dirac electrons in layered systems contained in this chapter clearly indicates that the mechanism behind it must be different from the traditional BCS mechanism.

References

1. T.O. Wehling, A.M. Black-Schaffer, A.V. Balatsky, Adv. Phys. **76**, 1 (2014)
2. E.V. Castro et al., *An Introduction to the Physics of Graphene Layers, in Strongly Correlated Systems, Coherence and Entanglement* (World Scientific, Singapore, 2007)
3. A.H. Castro Neto et al., Rev. Mod. Phys. **81**, 109 (2009)
4. P.R. Wallace, Phys. Rev. **71**, 622 (1947)
5. E.C. Marino, L.H.C.M. Nunes, Nucl. Phys. B **741**, 404 (2006)
6. N.D. Mermin, H. Wagner, Phys. Rev. Lett. **17**, 1133 (1966); P.C. Hohenberg, Phys. Rev. **158**, 383 (1967); S. Coleman. Commun. Math. Phys. **31**, 259 (1973)
7. A.H. Castro Neto, Phys. Rev. Lett. **86**, 4382 (2001)
8. E.C. Marino, M.J. Martins, Phys. Rev. D **33**, 3121 (1996)
9. E. Witten, Nucl. Phys. B **145**, 110 (1978)
10. E. Babaev, Phys. Lett. B **497**, 323 (2001)
11. D.V. Khveshchenko, H. Leal, Nucl. Phys. B **687**, 323 (2004)
12. V.L. Berezinskii, Zh. Eksp. Teor. Fiz. **59**, 907 (1970); J. Kosterlitz, D. Thouless, J. Phys. C **6**, 118 (1973)
13. V.M. Loktev, R.M. Quick, S.G. Sharapov, Phys. Rep. **349**, 1 (2001)
14. L.H.C.M. Nunes, A.L. Mota, E.C. Marino, Solid State Commun. **152**, 2082 (2012)
15. Y. Kopolevich, J. Low Temp. Phys. **119**, 691 (2000); Y. Kopelevich et al., Phys. Solid State **41**, 1959 (1999) (Fizika Tverd. Tela (St. Petersburg) **41**, 2135 (1999))
16. P. Esquinazi et al., Phys. Rev. B **78**, 134516 (2008)
17. R.K. Kremer, J.S. Kim, A. Simon, *Carbon Based Superconductors, in High Tc Superconductors and Related Transition Metal Oxides* (Springer, Berlin, 2007)
18. S.S. Pershoguba, V.M. Yakovenko, Phys. Rev. B **82**, 205408 (2010)
19. L.H.C.M. Nunes, R.L.S. Farias, E.C. Marino, Phys. Lett. A **376**, 779 (2012)
20. D.V. Khveshchenko, Nucl. Phys. B **687**, 323 (2004). Phys. Rev. Lett. **87**, 246802 (2001)
21. C. Ratti, W. Weise, Phys. Rev. D **70**, 054013 (2004)
22. B. Uchoa, A.H. Castro Neto, Phys. Rev. Lett. **98**, 146801 (2007)
23. K. Fukushima, K. Iida, Phys. Rev. D **76**, 054004 (2007)
24. L.-K. Lim et al., Eur. Phys. Lett. **88**, 36001 (2009)
25. L.H.C.M. Nunes, E.C. Marino, Phys. B **378–380**, 704 (2006)
26. Y. Kamihara, et al., J. Am. Chem. Soc. **130**, 3296 (2008)
27. M. Rotter, M. Tegel, D. Johrendt, Phys. Rev. Lett. **101**, 107006 (2008)
28. M.G. Alford et al., Rev. Mod. Phys. **80**, 1455 (2008)

Chapter 6
Flat Bands as a Route to High-Temperature Superconductivity in Graphite

Tero T. Heikkilä and Grigory E. Volovik

Abstract Superconductivity is traditionally viewed as a low-temperature phenomenon. Within the BCS theory this is understood to result from the fact that the pairing of electrons takes place only close to the usually two-dimensional Fermi surface residing at a finite chemical potential. Because of this, the critical temperature is exponentially suppressed compared to the microscopic energy scales. On the other hand, pairing electrons around a dispersionless (flat) energy band leads to very strong superconductivity, with a mean-field critical temperature linearly proportional to the microscopic coupling constant. The prize to be paid is that flat bands can probably be generated only on surfaces and interfaces, where high-temperature superconductivity would show up. The flat-band character and the low dimensionality also mean that despite the high critical temperature such a superconducting state would be more vulnerable to strong fluctuations than ordinary superconductors. Here we discuss the topological and non-topological flat bands discussed in different systems, and show that graphite is a good candidate for showing high-temperature flat-band interface superconductivity.

The purpose of this chapter is to propose a route to increasing the critical temperature of superconductivity by searching for special electronic dispersion that would promote the superconducting strength. We first show that a huge increase in the (mean-field) critical temperature is possible, if a dispersionless energy spectrum, a *flat band* can be created in the system in the absence of the interaction leading to superconducting correlations. We then discuss a few known schemes to generate such (approximate or exact) flat bands.

T.T. Heikkilä (✉)
Department of Physics and Nanoscience Center, University of Jyväskylä,
P.O. Box 35, 40014 Jyvaskyla, Finland
e-mail: Tero.T.Heikkila@jyu.fi

G.E. Volovik
Low Temperature Laboratory, Department of Applied Physics, Aalto University,
P.O. Box 15100, 00076 Aalto, Finland
e-mail: volovik@boojum.hut.fi

G.E. Volovik
L. D. Landau Institute for Theoretical Physics, 117940 Moscow, Russia

P.D. Esquinazi (ed.), *Basic Physics of Functionalized Graphite*,
Springer Series in Materials Science 244, DOI 10.1007/978-3-319-39355-1_6

6.1 Superconductivity: Pairing Energy Versus Dispersion

Within the BCS mean-field theory, the occurrence of Cooper pairing at zero temperature can be studied via the free energy density for the pairing energy Δ:

$$F_\Delta = -\frac{1}{2}\int \frac{d^d p}{(2\pi\hbar)^d}\left(E_{\mathbf{p}}(\Delta) - E_{\mathbf{p}}(\Delta = 0)\right) + \frac{\Delta^2}{2|g|}, \tag{6.1}$$

where d is the dimensionality, $g < 0$ describes the interaction strength, and $E_{\mathbf{p}}(\Delta) = \sqrt{\varepsilon_{\mathbf{p}}^2 + \Delta^2}$ is the quasiparticle excitation energy at momentum value $\mathbf{p}$, evaluated in a system with the normal-state dispersion $\varepsilon_{\mathbf{p}}$. The first term in (6.1) demonstrates that the formation of a gap Δ decreases the energy of quasiparticles, which fill the negative energy levels of Dirac vacuum. The second term is the cost of the formation of the gap, which perturbs the vacuum. For simplicity, we consider spinless fermions and the gap that does not depend on momentum.

Requiring Δ to minimize F_Δ, we get the self-consistency relation

$$\Delta = \frac{|g|}{2}\int \frac{d^d p}{(2\pi\hbar)^d}\frac{\Delta}{E_{\mathbf{p}}(\Delta)}, \tag{6.2}$$

or

$$1 = \frac{|g|}{2}\int \frac{d^d p}{(2\pi\hbar)^d}\frac{1}{E_{\mathbf{p}}(\Delta)}. \tag{6.3}$$

Equation (6.3) dictates the behavior of Δ at different dimensionalities d and for different normal-state energy spectra $\varepsilon_{\mathbf{p}}$.

For s-wave superconductivity in conventional metals with an isotropic Fermi surface and dispersion $\varepsilon = v_F(p - p_F)$ expanded around the Fermi energy ε_F, the integral in (6.3) is concentrated in the vicinity of the Fermi surface

$$1 = \frac{|g|A_d}{(2\pi\hbar)^d N_F}\int_0^{\varepsilon_{\rm uv}} \frac{d\varepsilon}{\sqrt{\varepsilon^2 + \Delta^2}} \overset{\varepsilon_{\rm uv}\gg\Delta}{\approx} |g|\nu_F \ln\frac{\varepsilon_{\rm uv}}{\Delta}. \tag{6.4}$$

Here $N_F = \frac{A_d}{(2\pi\hbar)^d v_F}$ is the density of states in the normal metal; A_d is the area of the d-dimensional Fermi surface; and $\varepsilon_{\rm uv} \ll \varepsilon_F$ is the ultraviolet cut-off of the logarithmically diverging integral, such as the Debye temperature. This leads to the exponentially suppressed gap:

$$\Delta = \varepsilon_{\rm uv}\exp\left(-\frac{1}{|g|\nu_F}\right), \tag{6.5}$$

and correspondingly to the exponential suppression of the transition temperature T_c.

Situation drastically changes when the spectrum of the normal state has a flat band—a region in momentum $\mathbf{p}$ where $\varepsilon_{\mathbf{p}} = 0$. Since within the flat band $E_{\mathbf{p}}(\Delta) = \Delta$, (6.3) becomes

$$1 = \frac{|g|V_d}{2(2\pi\hbar)^d \Delta}, \tag{6.6}$$

where V_d is the volume of the flat band in momentum space. Hence instead of the usual exponentially suppressed behavior in (6.5) we have the gap Δ that is linearly proportional to the interaction strength:

$$\Delta = \frac{|g|V_d}{2(2\pi\hbar)^d}, \tag{6.7}$$

Since the critical temperature of the superconductors is typically of the same order of magnitude as the gap at zero temperature, the resulting superconductivity may exist at high temperatures.

It is instructive to consider the intermediate case when the quasiparticle spectrum is

$$\varepsilon(p) = \varepsilon_0 \left(\frac{p}{p_0}\right)^M. \tag{6.8}$$

Then for $M > d$, (6.3) gives the power law dependence of transition temperature on the coupling constant:

$$\Delta \propto |g|^{\frac{M}{M-d}}. \tag{6.9}$$

In the limit of large $M \gg 1$, the spectrum (6.8) transforms to the flat band concentrated at $p < p_0$, and the gap (6.9) asymptotically approaches the linear dependence on the coupling g in (6.7). The case with $d = 1$ and $M = 2$, where $\Delta \propto g^2$, has been considered by Kopaev [1] and Kopaev–Rusinov [2].

In the sections below, we consider different systems where the exact or approximate flat bands could be realized.

6.2 Flat Band Induced by Interaction

6.2.1 Landau Phenomenology

We start with the flat bands induced by interaction between the fermions. As was found by Khodel and Shaginyan [3], the interaction may lead to the merging of different fermionic energy levels, which results in the formation of a dispersionless band, see also [4, 5]. The effect of the merging of discrete energy levels due to interaction has been reported in a recent paper, [6].

Their argument is based on the phenomenological Landau's consideration on the derivation of the distribution function $n_{\mathbf{p}}$ of fermions at $T = 0$. It is determined by the energy functional $\mathscr{E}\{n(\mathbf{p})\}$, whose variational derivative $\varepsilon_{\mathbf{p}}$ is the quasiparticle energy. The variation of this functional gives the equation for $n_{\mathbf{p}}$ and $\varepsilon_{\mathbf{p}}$:

$$\delta\mathscr{E}\{n(\mathbf{p})\} = \int \frac{d^d p}{(2\pi\hbar)^d}\, \varepsilon_{\mathbf{p}} \delta n_{\mathbf{p}} = 0. \tag{6.10}$$

Since the quasiparticle distribution function is constrained by the Pauli principle $0 \le n_{\mathbf{p}} \le 1$, there are two classes of solutions of the variational problem. One class is $\varepsilon_{\mathbf{p}} = 0$, which is valid if $0 < n_{\mathbf{p}} < 1$; another one is $\delta n_{\mathbf{p}} = 0$ with $n_{\mathbf{p}} = 0$ or $n_{\mathbf{p}} = 1$. In the following we illustrate these two classes of solutions.

6.2.2 *Landau Fermi Liquid and Its Topological Stability*

Let us start with the Fermi gas—the system of free fermions with the spectrum $\varepsilon_{\mathbf{p}} = p^2/2m - \mu$, where $\mu > 0$. The energy functional for free fermions is $\mathscr{E}\{n(\mathbf{p})\} = \int \frac{d^d p}{(2\pi\hbar)^d}\, \varepsilon_{\mathbf{p}} n_{\mathbf{p}}$, which gives the solution shown in Fig. 6.1 (*left*). The solution of the class $\varepsilon_{\mathbf{p}} = 0$ forms the Fermi surface with radius p_F, where $p_F^2/2m = \mu$. Outside of

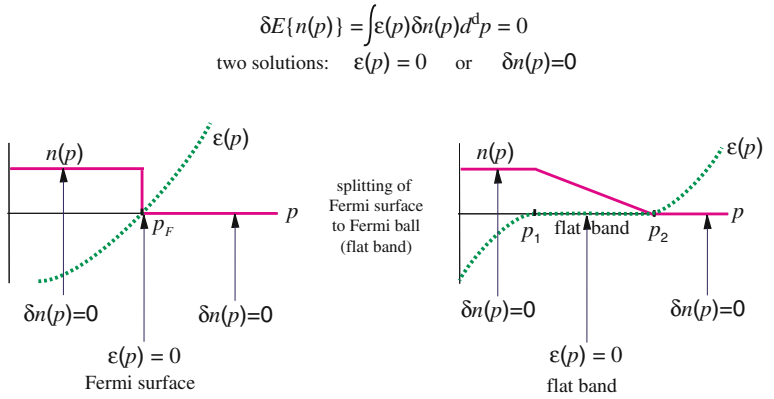

Fig. 6.1 Illustration of the formation of the Khodel–Shaginyan flat band due to interaction between fermions. *Top* the Landau model of the Fermi liquid considers the energy $\mathscr{E}\{n(\mathbf{p})\}$ as the functional of the distribution function $n(\mathbf{p})$ of quasiparticles. The variation of the functional gives two types of solutions: $\varepsilon_{\mathbf{p}} = 0$ or $\delta n_{\mathbf{p}} = 0$. *Left* distribution of quasiparticles in the class of Fermi liquids. Two regions with solutions $\delta n_{\mathbf{p}} = 0$ are separated by the surface with solution $\varepsilon_{\mathbf{p}} = 0$. This is the Fermi surface. Topological stability of this class is demonstrated in Fig. 6.2. *Right* for strong interaction (large interaction constant), the intermediate region with the solution $\varepsilon_{\mathbf{p}} = 0$, may become finite. This is the flat band. Topological structure of such flat band is demonstrated in Fig. 6.3

the Fermi surface the distribution function $n_{\mathbf{p}} = \text{const}$, with $n_{\mathbf{p}} = 1$ for $p < p_F$ and $n_{\mathbf{p}} = 0$ for $p > p_F$. This corresponds to the class of solutions with $\delta n_{\mathbf{p}} = 0$.

The structure with the Fermi surface is topologically protected. The topological stability can be illustrated using the $d = 2$ system, when the Fermi surface $p = p_F$ is the 1d circle. For that one has to consider the Green's function at imaginary frequency:

$$G(\omega, \mathbf{p}) = \frac{1}{i\omega - \left(\frac{p^2}{2m} - \mu\right)}. \tag{6.11}$$

The Green's function in (6.11) has singularities at $\omega = 0$ for $\mathbf{p}$ belonging to the Fermi surface. These points form a closed line in the three dimensional (ω, p_x, p_y)-space, see Fig. 6.2 for $d = 2$. This line has a topological winding number: the phase Φ of the Green's function, $G = |G|e^{\Phi}$ changes by 2π along an arbitrary contour C around the line. In other words, the Fermi surface represents the p-space analog of the vortex lines in superfluids and superconductors, where the phase of the order parameter changes by 2π around the vortex. The 2π winding of the phase Φ cannot change under small deformations of the parameters of the system, and thus is robust to the interactions between the particles, if we do not consider the superconducting, magnetic or other phase transition, which drastically (non-perturbatively) reconstructs the energy spectrum. This topological stability is the reason why interacting Fermi liquids preserve the Fermi surface.

For more complicated cases, when the Green's function has spin, band and other indices, and for arbitrary dimension d the winding number N of the Fermi surface is expressed analytically in terms of the matrix Green's function in the following form:

$$N = \mathbf{tr} \oint_C \frac{dl}{2\pi i} G(\omega, \mathbf{p}) \partial_l G^{-1}(\omega, \mathbf{p}). \tag{6.12}$$

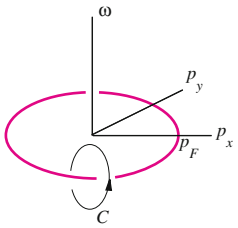

Fig. 6.2 Illustration of the topological stability of the Fermi surface on an example case with dimension $d = 2$, when the Fermi surface forms a closed loop. Green's function has singularities on the line $\omega = 0, p_x^2 + p_y^2 = p_F^2$ in the three-dimensional space (ω, p_x, p_y). Stability of the Fermi surface is protected by the invariant (6.12) which is represented by an integral over an arbitrary contour C around the Green's function singularity

Here the integral is taken over an arbitrary contour C around the Green's function singularity in the $d+1$ momentum-frequency space. For the Green's function in (6.11) the topological invariant $N = 1$.

6.2.3 Khodel–Shaginyan Flat Band and Its Topology

When the interaction between the particles is strong enough, so that it starts dominating over the fermionic statistics, a more classical behavior of the distribution function may emerge, in which the natural solution of the variational problem corresponds to a zero value of the variational derivative, $\delta\mathscr{E}\{n(\mathbf{p})\}/\delta n_{\mathbf{p}} = 0$. Therefore, with an increasing interaction strength one may expect the topological quantum phase transition to the distribution in Fig. 6.1 (*right*), where the solution $\varepsilon_{\mathbf{p}} = 0$ is spread over a finite region in momentum space, i.e., forming a flat band.

The topological structure of the Khodel–Shaginyan flat band is shown in Fig. 6.3. The vortex line with 2π winding transforms to a domain wall in the momentum frequency space, at which the Green's function has a jump, $G(\omega = +0, p_x, p_y) - G(\omega = -0, p_x, p_y) \neq 0$. This domain wall terminates on π vortices.

6.2.4 Flat Band Near the Saddle Point

Here we consider the formation of the Khodel–Shaginyan flat band in the vicinity of a saddle point in the $d = 2$ quasiparticle spectrum using the phenomenological Landau theory [7] and compare it with the results of numerical simulations of the Hubbard model [8].

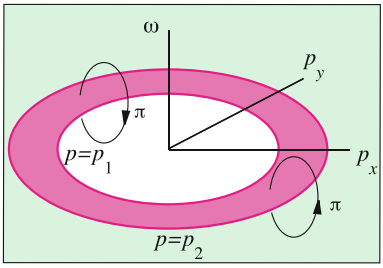

Fig. 6.3 Illustration of the topological structure of the Khodel–Shaginyan flat band in a $d = 2$ system. According to Fig. 6.1 (*right*) the Fermi surface at $p = p_F$ spreads into a flat band concentrated in the region $p_1 < p < p_2$. Correspondingly the line of the Green's function singularities in Fig. 6.2—a vortex line—is spreading to an analog of a domain wall terminating on a pair of π-vortices at $p = p_1$ and $p = p_2$ [4]

The simple Landau-type functional for the interacting Fermi liquid is

$$\mathscr{E}\{n(\mathbf{p})\} = \sum_{\mathbf{p}} n_{\mathbf{p}} \varepsilon_{\mathbf{p}}^{(0)} + \frac{1}{2} \sum_{\mathbf{p},\mathbf{p}'} f(\mathbf{p}, \mathbf{p}') n_{\mathbf{p}} n'_{\mathbf{p}} \,. \tag{6.13}$$

We illustrate the flat band solution using an even simpler functional with contact interaction:

$$\mathscr{E}\{n(\mathbf{p})\} = \sum_{\mathbf{p}} \left[\varepsilon_{\mathbf{p}}^{(0)} n_{\mathbf{p}} + \frac{1}{2} U \left(n_{\mathbf{p}} - \frac{1}{2} \right)^2 \right], \tag{6.14}$$

where $U > 0$. This functional has always a flat band solution with $0 < n_{\mathbf{p}} < 1$:

$$\varepsilon_{\mathbf{p}} = \frac{\delta \mathscr{E}}{\delta n_{\mathbf{p}}} = \varepsilon_{\mathbf{p}}^{(0)} + U \left(n_{\mathbf{p}} - \frac{1}{2} \right) = 0, \tag{6.15}$$

$$n_{\mathbf{p}} = \frac{1}{2} - \frac{\varepsilon_{\mathbf{p}}^{(0)}}{U} \quad , \quad 0 < n_{\mathbf{p}} < 1. \tag{6.16}$$

In the vicinity of the saddle point the non-perturbed spectrum (i.e. at $U = 0$) has the form $\varepsilon_{\mathbf{p}}^{(0)} = \frac{p_x p_y}{m} - \mu$. For $\mu \neq 0$, there are two hyperbolic Fermi surfaces. They interconnect at the Lifshitz transition, which takes place at $\mu = 0$. When the interaction U is switched on, the flat bands emerge. Figure 6.4 (*left*) demonstrates the flat band at $\mu = 0$. The same shape of the region with the flat band has been obtained from the numerical simulations of the Hubbard model [8], see Fig. 6.4 (*right*).

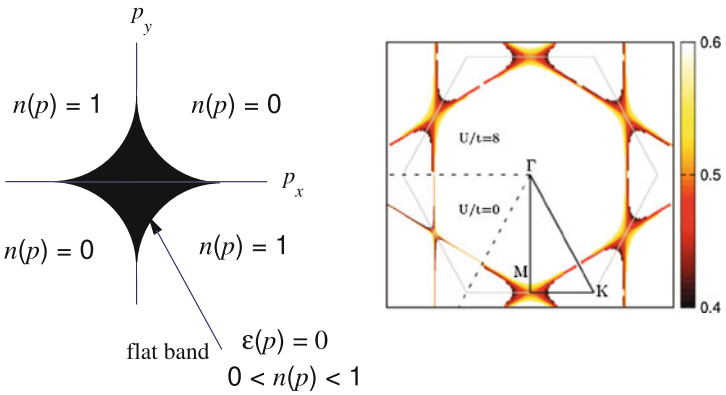

Fig. 6.4 Flat band emerging near a saddle point. *Left* from the simplified Landau-type theory in (6.14)–(6.16) with $\mu = 0$. The flat band is concentrated in the black region. *Right* from the numerical solution of the Hubbard model [8], showing the spectral function within the reciprocal space of an interacting triangular lattice. The lower left sextant corresponds to the noninteracting case $U = 0$. For large U the band flattening is clearly seen near the saddle points

6.3 Flat Bands in Topological Semimetals

In the previous section we discuss the fermion condensate—a flat band emerging due to interactions in the vicinity of a singularity in the non-interacting spectrum. There are also other ways to generate flat bands or approximate flat bands. Historically the flat bands first appeared as Landau levels of charged particles in a magnetic field [9]. Here we discuss the flat bands that have purely topological origin. They may exist without a magnetic field, and they are not very sensitive to disorder. The flat band may emerge as the surface or interface state in topological semimetals [10–12], which we discuss in this section. The flat band may also appear at the strained interfaces with misfit dislocations, which play the role of effective magnetic field. Such flat bands are discussed in Sect. 6.4.

In this section we characterize semimetals that have an internal spin-like structure. All the examples discussed here can be characterized via the topological invariant of the form [13]

$$N_1 = \mathbf{tr} \oint_C \frac{\mathbf{d}l}{4\pi i} \cdot [\Gamma H^{-1}(\mathbf{p}) \partial_l H(\mathbf{p})], \tag{6.17}$$

where H is the Hamiltonian in the momentum space; Γ is a matrix which commutes or anti-commutes with the Hamiltonian, such as the third Pauli matrix σ_3 acting on the spin-like degree of freedom; and C is a contour in momentum space, specified separately for each semimetal.

In semimetals, the flat bands are realized as a particular consequence of the bulk-boundary correspondence of topological media (see [14–16] or Sect. 22.1 in [17]). If for example a 3D bulk system contains Weyl points, then an interface with a topologically trivial material, or with a material having a different value of topological invariants contains a line of zeroes—the Fermi arc [18]. The termination points of the Fermi arc are given by projections of the Weyl points to the interface. In the same manner the Dirac lines in 3D bulk or Dirac points in 2D bulk, characterized by an invariant of the form (6.17), give rise to the to nodes of higher dimension at the interface—the flat band [10–12]. The boundaries of the flat band are determined by the projection of the Dirac line or Dirac points to the interface.

6.3.1 Topological Nodes: Dirac Lines and Dirac Points

Let us consider an example semimetal characterized by an even number of 2-dimensional Dirac points, such as that found in graphene around the two valleys. Close to the Dirac point the Hamiltonian can be written as a 2×2 matrix in (pseudo)spin space,

$$H = v_F \begin{pmatrix} 0 & p_x - ip_y \\ p_x + ip_y & 0 \end{pmatrix} = v_F \mathbf{p} \cdot \boldsymbol{\sigma}, \tag{6.18}$$

where $\mathbf{p} = (p_x, p_y)$ and $\boldsymbol{\sigma} = (\sigma_x, \sigma_y)$, where σ_j are Pauli matrices. The eigenvalues of H satisfy $\varepsilon^2 = v_F^2|p|^2$ having a node $\varepsilon(\mathbf{p} = 0)$ in a single point in momentum space. To illustrate the topological protection of this node, let us add a perturbation of the form $V(\mathbf{p}) = \mathbf{v}(\mathbf{p}) \cdot \sigma$, where $\mathbf{v} = (v_x, v_y)$ does not break the (pseudo)spin symmetry. As a result, the dispersion becomes $\varepsilon^2 = (v_F p_x + v_x)^2 + (v_F p_y + v_y)^2$, which again has a single node at $(p_x, p_y) = -(v_x, v_y)/v_F$. The only effect of the potential is thus to shift the node, but not annihilate it. This property can be expressed via the presence of the topological charge of the form (6.17), where $\Gamma = \sigma_z$ and the contour C goes around the Dirac point in the 2D momentum space (see Fig. 6.5). For the Hamiltonian in (6.18), we get $N_1 = 1$. In graphene, there are two Dirac points: the first one has the form in (6.18), and the second is otherwise the same but $p_y \mapsto -p_y$. In that case the second Dirac point has $N_1 = -1$. These topological charges stay invariant to perturbations of the form $V(\mathbf{p})$, as long as we shift the contour of integration along with the shift of the Dirac point, and as long as the two nodes do not merge due to such a perturbation.

In 3D materials, the topological charge in (6.17) characterizes lines of nodes—the Dirac lines. The Dirac lines are readily obtained in superfluids and superconductors, where the symmetry operator Γ contains the particle-hole symmetry. In particular, the Dirac line exists in the polar phase of superfluid ^{3}He [19] and may appear in superconductors without inversion symmetry [12]. The topologically stable Dirac lines give rise to the topologically protected surface flat band. According to the bulk-surface correspondence, the boundary of the flat band is determined by the projection of the nodal line on to surfaces. In nonsuperconducting materials the corresponding symmetry which enters (6.17) can be only approximate, being violated by spin-orbit interaction, or by the higher order hopping elements. This leads to formation of approximately flat surface bands as it happens for example in graphite [20], graphene networks [21] and possibly in some other materials [22, 23].

We first consider the case of graphene, whose energy spectrum within the valence and conduction bands is plotted in Fig. 6.6. This spectrum follows for example from the nearest-neighbour tight-binding model on a honeycomb lattice, see [24, 25]. Around the specific points, marked K and K' in the figure, the low-energy Hamiltonian is of the form of (6.18). These points are described by the topological charge N_1, such that $N_1(K) = +1$ and $N_1(K') = -1$.

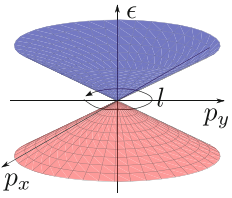

Fig. 6.5 2D Dirac point in momentum space and the line of integration for the topological invariant N_1

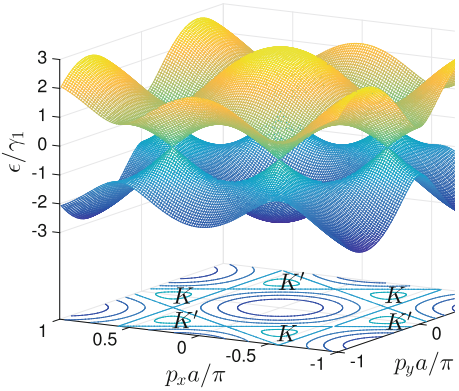

Fig. 6.6 Energy spectrum in the conduction and valence bands of graphene. Here a is the lattice constant, and γ_1 denotes the nearest-neighbour hopping parameter in the tight-binding lattice. The underlying contour plot shows the positions of the Dirac points. Only two of these points are non-equivalent, the others are connected via reciprocal lattice vectors

Figure 6.7 shows the formation of flat bands at the edges of graphene [10]. There, we show the locations of the K and K' points in the 2d momentum plane, and consider the presence of an edge placed in the x-direction. Now, the edge marks a boundary between graphene, which is a nodal semimetal, and vacuum, which is a trivial insulator. By the bulk-boundary correspondence we may hence expect flat band states at the edge. Since we maintain translational invariance along the x direction, p_x remains a good quantum number and it also parametrizes the edge states and their dispersion $\varepsilon_e(p_x)$. According to the bulk-boundary correspondence, the projections of the Dirac points to the boundary determine the end points of the flat band. From Fig. 6.7 it is clear that the termination points of the flat band must be located at p_x values corresponding to the p_x-component of the K and K' points. When p_x crosses these points, the normal to the interface runs across either K or K' points and the topological invariant in (6.17) along the normal changes. However, from the figure alone one cannot say which of the regions between the K and K' points contain flat bands and which not. The solution is to construct the system by repeating a set of infinite chains, and construct the topological invariant, in this case called the Zak phase [26] for these chains. As shown for example in [10, 26], the details of this procedure depend on the microscopic form of the edge, which is either of the "bearded" or the "zigzag" type. Figure 6.7 illustrates the resulting positions of the flat band dispersion in momentum space.

If we were to place the interface in the y direction (in which case we would obtain the "armchair" edge), there would be no flat band due to the fact that the normal to the interface would run across both K and K' points. In this case the change of the topological charge across this normal line would be $N_1(K) + N_1(K') = 0$.

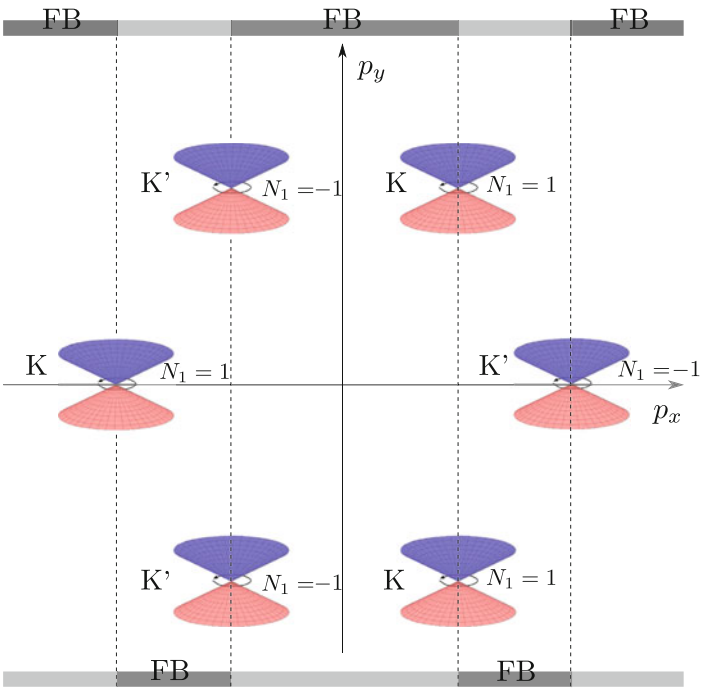

Fig. 6.7 Formation of a flat band in the zigzag (*lower part* of the figure) or bearded (*upper part*) edges of graphene

In the following sections we explain the topological invariants in multilayer graphene structures and discuss the consequent (approximate) flat band surface states.

6.3.2 *From Graphene to Graphite*

In graphite, the coupling between the graphene layers is much weaker than that within the atoms producing the hexagonal lattice in individual layers. Because of this, we may assume that the individual layers remain to be described by the two-dimensional low-energy momentum-space Hamiltonian of the form in (6.18). In the (most stable) AB stacking, the pair of layers is arranged so that the graphene hexagons are rotated with respect to each other by 30°. As a result, one pair of atoms (say, A on the bottom layer and B on the top layer) reside on top of each other, whereas the other atom of the unit cell (B on the bottom and A on the top) are on the bottom/top of the other hexagon. Therefore, the interlayer coupling between the first pair of atoms is much stronger than the coupling between the second pair. Taking into account only this strongest coupling then produces the Hamiltonian of the form

$$H_K = \begin{pmatrix} v_F \mathbf{p}\cdot\boldsymbol{\sigma} & -\gamma_1\sigma_\downarrow \\ -\gamma_1^*\sigma_\uparrow & v_F\mathbf{p}\cdot\boldsymbol{\sigma} \end{pmatrix} \tag{6.19}$$

around one of the graphene valleys (K-point) for this pair of layers. Here γ_1 quantifies the interlayer hopping. Around the other valley (K' point) the Hamiltonian is $H_{K'}(p_x, p_y) = H_K(p_x, -p_y)$. It is straightforward to show that $H_{K/K'}$ have four branches of eigenvectors, two gapped ones (with $\varepsilon(|p| = 0) = \pm\gamma_1$) and two with a quadratic dispersion around a Fermi node, $\varepsilon^2 = |\gamma_1|^2(p/p_{FB})^4$, where $p_{\mathrm{FB}} = |\gamma_1|/v_F$. The topological invariant for the Dirac point with quadratic touching demonstrates summation rule for the topological invariants, $N_1 = 2$ (-2) for H_K $(H_{K'})$.

Beyond the bilayer, the graphene layers can be stacked in two qualitatively different ways by respecting the AB stacking for each pair of layers. In Bernal stacking, the line of strongest interlayer coupling is straight, i.e., connects the same atoms in each layer whereas for rhombohedral (ABC) stacking, it follows an armchair-type pattern, i.e., the strongly coupled atoms differ between neighbouring pairs of layers. The corresponding elements of the momentum space Hamiltonians coupling layers n and m for 2D momenta around the K point are

$$H_{mn}^{\mathrm{Bernal}} = v_F\mathbf{p}\cdot\boldsymbol{\sigma}\,\delta_{mn} - \gamma_1\delta_{m,n+1}\left\{\sigma_\uparrow[(-1)^m - 1] + \sigma_\downarrow[(-1)^m + 1]\right\}/2 + \mathrm{h.c.} \tag{6.20}$$

$$H_{mn}^{\mathrm{rhombohedral}} = v_F\mathbf{p}\cdot\boldsymbol{\sigma}\,\delta_{mn} - \gamma_1\delta_{m,n+1}\sigma_\uparrow + \mathrm{h.c.} \tag{6.21}$$

In H^{Bernal} the terms in square brackets take care of indexing the even and odd layers separately. Note that since the choice of the A/B indices for the graphene sublattice atoms is arbitrary, we could have also chosen to write the coupling in $H^{\mathrm{rhombohedral}}$ in terms of $\sigma_\uparrow$ instead of $\sigma_\downarrow$. These two choices of description give different signs of the bulk topological invariant in (6.17), but the sign of the invariant becomes important only in the presence of (Bernal) stacking faults that change the coupling around some particular interface.

6.3.3 Bulk Dirac Line in Bernal Graphite

We first derive the bulk dispersion of Bernal graphite by including only the strongest interlayer hopping term γ_1. We make the bulk Ansatz

$$\psi_n^T = e^{ip_z na/\hbar}\begin{cases} \begin{pmatrix}\alpha_o & \beta_o\end{pmatrix}, & n \text{ odd} \\ \begin{pmatrix}\alpha_e & \beta_e\end{pmatrix}, & n \text{ even}\end{cases} \tag{6.22}$$

for the wave function on the nth layer. Here p_z is the momentum in the direction perpendicular to the layers and a is the distance between the layers. This is an eigenfunction with energy ε provided that the coefficients $\alpha_{e/o}$, $\beta_{e/o}$ satisfy

$$\underbrace{\begin{pmatrix} 0 & v_F p_- & 0 & -2\gamma_1 \cos(p_z a/\hbar) \\ v_F p_+ & 0 & 0 & 0 \\ 0 & 0 & 0 & v_F p_- \\ -2\gamma_1^* \cos(p_z a/\hbar) & 0 & v_F p_+ & 0 \end{pmatrix}}_{H_B} \begin{pmatrix} \alpha_o \\ \beta_o \\ \alpha_e \\ \beta_e \end{pmatrix} = \varepsilon \begin{pmatrix} \alpha_o \\ \beta_o \\ \alpha_e \\ \beta_e \end{pmatrix}, \quad (6.23)$$

where $p_\pm = p_x \pm i p_y \equiv p_\perp e^{i\phi}$, $p_\perp \geq 0$. This has (four) zero-energy solutions at $p_x = p_y = 0$, regardless of the value of p_z. Within this approximation, Bernal graphite has therefore two Dirac lines, running through the K and K' points of the 2D graphene band structure, or between the H points in the 3D graphite band structure, see Fig. 6.8. Including higher-order hopping terms in the Hamiltonian expands this line into electron and hole pockets [27–29]. However, let us first analyze the topology of H_B. The topological charge in this case is of the form of (6.17), where the contour C runs around the Dirac lines as indicated in Fig. 6.8, and σ_z should be replaced by $(\sigma_z \otimes 1)$. This produces $N_1 = \pm 2$, where the factor 2 takes care of the additional layer degree of freedom in (6.23).

This is thus nothing but the generalization of the graphene topological charge to graphite and it yields $N_1 = \pm 2$ for the momenta along the lines $H - K - H/H' - K' - H$ [27], where the $H^{(\prime)}$ point is shifted from the $K^{(\prime)}$ point in the p_z direction by $\hbar\pi/(2a)$. Based on the bulk-boundary correspondence we may therefore expect to have surface states at the lateral boundaries of Bernal graphite, as extensions of the flat band states in zigzag graphene, but now the flat band extends throughout the first Brillouin zone in the p_z direction.

Let us now consider the effect of higher-order hopping elements. First they split the Dirac line with multiple charge $N_1 = 2$ into elementary Dirac lines. The natural splitting would be into two lines with charges $N_1 = 1$. However, the situation is more interesting, see Fig. 6.9 and [27, 29, 30]. The $N_1 = 2$ line splits into 4 Dirac lines: three lines with trigonal arrangement have $N_1 = 1$, while the central line has $N_1 = -1$. The total topological invariant remains the same, $N_1 = 1 + 1 + 1 - 1 = 2$. In addition, the higher-order hoppings break the symmetry Γ [20] underlying the topological protection. Without the topological protection the four Dirac lines are electron and hole pockets move to a non-zero energy, creating. As a result the surface

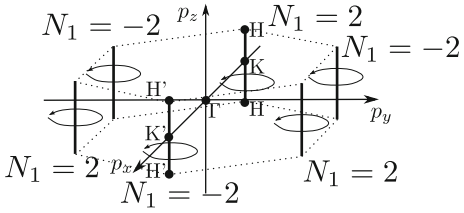

Fig. 6.8 Dirac lines in Bernal graphite within the nearest-neighbour interlayer approximation. This picture expands the 2D momentum space (p_x/p_y plane) of graphene to the 3D space where p_z runs between $-\hbar\pi/(2a)$ to $\hbar\pi/(2a)$ (a is the interlayer spacing)

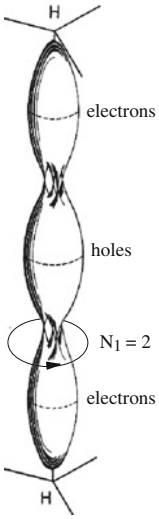

Fig. 6.9 Bernal graphite Fermi surface from [27]. It consists of the electron and hole pockets connected at four points. Each point is described by topological invariant in (6.17): the point in the center has $N_1 = -1$ and the other three points have $N_1 = 1$. Such structure originates from the nodal line with $N_1 = 2$ in the Hamiltonian (6.23), when the higher order hopping elements are taken into account

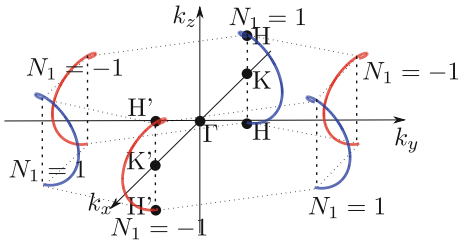

Fig. 6.10 Fermi spirals in rhombohedral graphite

states of Bernal graphite cease to be flat on the energy scale related to those higher-order hoppings [31] (Fig. 6.10).

6.3.4 Spiral Dirac Line in Rhombohedral Graphite

To obtain the bulk dispersion of rhombohedral graphite, it is enough to make the Ansatz

$$\psi_n = \begin{pmatrix} \alpha \\ \beta \end{pmatrix} e^{ip_z na/\hbar}. \tag{6.24}$$

This is an eigenfunction of $H^{\text{rhombohedral}}$ if α and β satisfy

$$\underbrace{\begin{pmatrix} 0 & v_F p_- - \gamma_1 \exp(ip_z a/\hbar) \\ v_F p_+ - \gamma_1^* \exp(-ip_z a/\hbar) & 0 \end{pmatrix}}_{H_{\text{RHG}}} \begin{pmatrix} \alpha \\ \beta \end{pmatrix} = \varepsilon \begin{pmatrix} \alpha \\ \beta \end{pmatrix} \tag{6.25}$$

for some energy ε. The zero-energy solutions are found along a spiral in the momentum space,

$$p_z a = \arctan\left(\frac{p_y}{p_x}\right) = \phi, \quad v_F p_\perp = |\gamma_1|. \tag{6.26}$$

In this case the topological charge corresponds to the spiral helicity, and can be defined by (6.17) where the integration contour runs over the 1st Brillouin zone ($-\pi/a$ to π/a) in the p_z-direction. For p_z running close to the line from the H point via K back to H, $N_1 = 1$ whenever the transverse momentum $p_x \pm ip_y$ is inside the spiral, i.e., $p_\perp < |\gamma_1|/v_F$. For larger momenta away from the $H - K - H$ line, $N_1 = 0$. On the other hand, for the path $H' - K' - H'$ the spiral is defined by (6.26), where $p_y \leftrightarrow -p_y$, inverting the helicity and the sign of N_1 to -1.

As a result of the existence of the non-trivial topological charge, the surface layers of rhombohedral graphite contain flat bands, i.e., $\varepsilon(p_\perp < |\gamma_1|/v_F) = 0$. This can be understood as follows. For each $\mathbf{p}_\perp$ with $p_\perp \neq |\gamma_1|/v_F$, the Hamiltonian $H_{\mathbf{p}_\perp}(p_z)$ describes a 1D insulator. For $p_\perp < |\gamma_1|/v_F$, this insulator is topological, since it has the topological charge $N_1(\mathbf{p}_\perp) = 1$. According to the bulk-boundary correspondence, each topological insulator has an edge state with zero energy. These states form a flat band in the region $p_\perp < |\gamma_1|/v_F$.

The robustness of the topological protection in an anisotropic rhombohedral graphite is investigated in [32].

The flattening of the surface spectrum was recently experimentally demonstrated in five-layer rhombohedral graphite [33].

6.4 Flat Band at Strained Interfaces

Recently another possible source of the topological flat band has been discussed in two materials: highly oriented pyrolytic Bernal graphite (HOPG) [34] and heterostructures SnTe/PbTe, PbTe/PbS, PbTe/PbSe, and PbTe/YbS consisting of a topological crystalline insulator and a trivial insulator [39]. In both cases the flat band comes from a misfit dislocation array, which is spontaneously formed at the interface between two crystals due to the lattice mismatch. In [34] the lattice of screw dislocations has been considered, which emerges at the interface between two domains of HOPG with different orientations of crystal axes. In [39] the misfit dislocation array is formed at the interface between topological and trivial insulators (Fig. 6.11).

The above two systems exhibit a similar phenomenon. In both cases superconductivity related with the interfaces has been found [35, 36]. The reported transition temperature essentially exceeds the typical transition temperature expected for the bulk materials. A possible origin of this phenomenon is the flat band at the interfaces, where the transition temperature could be proportional to the coupling constant and the area of the flat band.

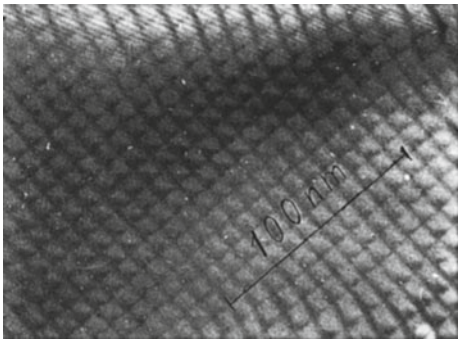

Fig. 6.11 Misfit dislocation grid at the interface from N. Ya. Fogel, Phys. Rev. B **66**, 174513 (2002) [35]

The topological origin of the flat bands in these systems can be understood either in terms of the overlapping of the 1D flat bands formed within the dislocations or using the following consideration. In case of the heterostructures, on one side of the interface the insulator is topological, and thus the interface contains Dirac fermions. The strain at the interface (with its dislocations) acts on Dirac fermions as the effective magnetic field. Such emergent field is now extensively discussed for strained graphene, see e.g. the most recent paper [37] and references therein. The effective magnetic field B produces the required flat band, since the first Landau level for massless Dirac fermions has zero energy. When the period decreases, the field B increases, giving rise to enhanced density of states, which is proportional to B. This is equivalent to an increase of the area of the flat band in the scenario discussed in Sect. 6.3. Such an increase of the transition temperature is discussed in [38, 39].

In particular, [39] considered the case where the massless Dirac Hamiltonian of the topological insulator experiences a periodic field. The analogue case for graphene in the presence of a periodic array of ripples was considered in [40]. They arrived at the Hamiltonian of the form

$$H_{TF} = -i\partial_x\sigma_x + [k_y - A(x)]\sigma_y, \tag{6.27}$$

written in terms of (scaled) momentum k_y along the dislocation, and a scaled strain-induced gauge field $A(x)$ satisfying $A(x+d) = A(x)$ and $\int_0^d A(x)dx = 0$. In the case of [39], $A(x) = \beta\cos(2\pi x/d)$, but the approach works for a more general periodic vector potential as well. Due to the position dependent vector potential, there is no translation symmetry in the x direction and the momentum in the x-direction is not a good quantum number. However, due to the periodicity of the potential we can use Bloch's theorem and define the pseudomomentum $\tilde{k}_x$. This allows for calculating the spectrum of (6.27), plotted in Fig. 6.12 and exhibiting (an approximate) flat band for $k_y < \beta/2$ and for all values of $k_x \in [-\pi/d, \pi/d]$.

The emergence of the approximate flat band in (6.27) can be understood by first considering the case $k_y = 0$. In that case the Hamiltonian has two (unnormalized) zero-energy solutions,

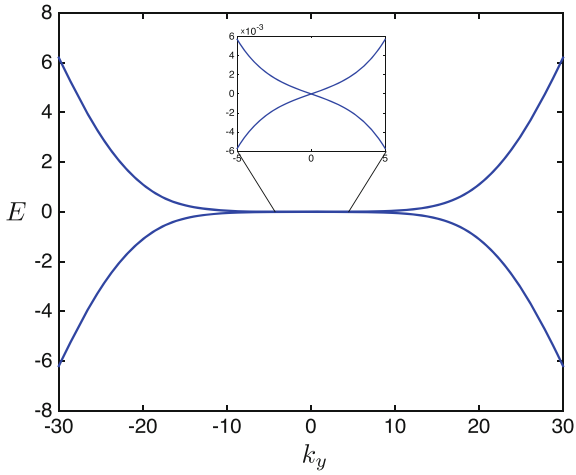

Fig. 6.12 Spectrum of (6.27) with $\beta = 30$. Inset shows the (approximate) linear dispersion with low values of k_y, and with a speed as in (6.28)

$$\psi_+ = \begin{pmatrix} 0 \\ 1 \end{pmatrix} \exp\left[\int_0^x A(x')dx'\right]$$
$$\psi_- = \begin{pmatrix} 1 \\ 0 \end{pmatrix} \exp\left[-\int_0^x A(x')dx'\right].$$

Let us include the term $H_1 = k_y\sigma_y$ as a perturbation. The second order secular equation produces the 2×2 Hamiltonian constructed from the matrix elements of the Hamiltonian H_1:

$$\begin{pmatrix} 0 & H_{+-}^{(1)} \\ H_{-+}^{(1)} & 0 \end{pmatrix} = c \begin{pmatrix} 0 & k_y \\ k_y & 0 \end{pmatrix}$$

with the spectrum $E = \pm ck_y$. The slope c of the spectrum is obtained from the matrix elements of the normalized eigenfunctions

$$c = \frac{\int_{-\infty}^{\infty} dx 1}{\int_{-\infty}^{\infty} dx \exp[2\int_0^x A(x')dx']} = \frac{d}{\int_0^d e^{2\int_0^x A(x')dx'}}. \tag{6.28}$$

For $A(x) = \beta\cos(x)$ we thus get $c = 1/I_0(2\beta)$, where $I_0(x)$ is the zeroth Bessell function of the first kind. When $c \ll 1$, requiring $\beta \gg 1$, the result is an approximate flat band.

Alternatively, we may consider the case of a periodic line dislocation. There, the vector potential is proportional to the strain field, $A(x) = \alpha_1 u_{xx}(x) + \alpha_2 u_{yy}(x)$, where α_1 and α_2 are coupling constants and

$$u_{xx}(x) = \frac{bz}{2\pi(1-\nu)} \frac{3x^2+z^2}{(x^2+z^2)^2}$$
$$u_{yy}(x) = \frac{bz\nu}{\pi(1-\nu)} \frac{1}{x^2+z^2},$$

where b is the size of the Burgers vector of the dislocation, z is the distance from the dislocation plane, and ν is the Poisson ratio. We also assume that such dislocations repeat after each d. In this case we may estimate the slope c for $d \gg z$ by

$$c \approx \exp\left[-2\int_0^\infty A(x)\right] = \exp\left[-\frac{b(\alpha_1+\nu\alpha_2)}{1-\nu}\right].$$

The flat band dispersion where $c \ll 1$ thus requires either $\nu \approx 1$ or coupling constants $\alpha_i \gg 1/b$. Note that this result show that the estimates done in [39] are overoptimistic, as there $\alpha b \approx 1$.

6.5 Superconductivity in Graphene or Graphite?

As discussed in Sect. 6.3, bulk neutral graphite and graphene are typically considered to have a very low density of states. This is why the occurrence of superconductivity in these bulk systems would require a strong doping, shifting the Fermi energy to a finite value and thereby increasing the density of states. Let us consider the example case of a 2D Fermi line with the superconducting coupling g, but with a shifted Fermi level by a value μ. In this case (6.2) yields for $\mu = 0$ [41]

$$\Delta = max\,[0,\ (a\varepsilon_{uv} - 1/a)/2], \tag{6.29}$$

where $a = g/(\pi\hbar^2 v_F^2)$. This is non-zero only for a large coupling strength $a > 1/\varepsilon_{uv}$. For weak coupling $|a| < 1/\xi_c$, superconductivity is enhanced by doping, because for non-zero μ the solution is $\Delta = 2|\mu|\exp(-\frac{1/a-\xi_c}{|\mu|} - 1)$.

This strategy has been followed by some graphite experimentalists. For example [42] demonstrates bulk superconductivity of two graphite intercalation compounds C_6Yb and C_6Ca with critical temperatures of 6.5 and 11.5 K, respectively. There one of the effects from the intercalant layers is the charge transfer, i.e., doping the graphite.

The situation is opposite in flat band systems: doping does not aid superconductivity, but rather decreases the critical temperature. With a non-zero chemical potential μ, the gap becomes

$$\Delta = \sqrt{\Delta_{\rm FB}^2 - \mu^2}, \tag{6.30}$$

where $\Delta_{\rm FB}$ is the gap obtained for $\mu = 0$, as in (6.7).

There are experimental indications for the presence of superconductivity at graphite interfaces [36]. In this case, the interfaces form between differently oriented regions of Bernal graphite, so that the graphite c-axis (p_z in our work here) runs perpendicular to these surfaces. These observations hence cannot be explained by the flat bands at the lateral interfaces (along p_x or p_y) as one would expect in Bernal graphite. There are also no direct indications of the presence of rhombohedral stacking in these systems, but the resolution of the imaging does not allow ruling out some rhombohedral regions close to the interfaces exhibiting superconducting properties. Note that rhombohedral stacking has been found in highly oriented pyrolytic graphite, see for example [43, 44], and recently in graphene multilayers [33]. The remaining scenarios are based on the formation of an array of dislocations (Sect. 6.4) at these surfaces as the surface layers try to adapt to the neighbouring graphite planes, or the interaction-induced flat bands at Van Hove singularities occurring at saddle points of twisted graphene layers [45].

The discussion in Sect. 6.1 concerns only the relation of the mean field order parameter with normal-state electronic spectrum. The details of the flat band superconducting state, such as the quasiparticle spectrum, supercurrent and collective modes, depend on the way the flat band is formed. The case of rhombohedral graphite has been worked out in [46–48] and summarized in [49]. The density of states in the superconducting state was computed in [50]. In that case the superconducting spectrum is not flat, but rather has an inverse parabolic shape and exhibits a minigap whose value is inversely proportional to the distance between adjacent surfaces. The supercurrent is characterized by a large critical current that is linearly proportional to Δ. However, in this model the supercurrent does not only flow along the surfaces, but also between them. Even a flat superconducting dispersion (and hence a vanishing group velocity for the quasiparticles) may lead to a nonvanishing supercurrent as was pointed out in [51].

In this chapter we have concentrated on illustrating the results for mean-field models of superconductivity on flat bands. As discussed in [49], fluctuation effects are much more important in flat band superconductors than in ordinary BCS superconductors. The nature of the fluctuation response depends on the mechanism of the flat band formation, and the ensuing superconducting spectrum. For example, in the case of surface flat bands of topological semimetals, the fluctuations may overwhelm the mean field contribution to the thermodynamic response, indicating that the attractive interaction leads to a strongly correlated state of electrons [52].

As we have discussed in this chapter, there are many ways of realizing (approximate) flat bands. Some of these realizations may be relevant in interfaces of graphite, where indications of superconductivity with a very high critical temperature have been observed. It remains to be demonstrated whether these properties can be explained within the flat band scenario of superconductivity.

Acknowledgments We acknowledge Pablo Esquinazi, Ville Kauppila and Timo Hyart for discussions. This work was supported by the Academy of Finland through its Center of Excellence program, and by the European Research Council (Grant No. 240362-Heattronics).

References

1. Y. Kopaev, Superconductivity of alloyed semimetals. JETP **31**, 544 (1970)
2. Y. Kopaev, A. Rusinov, Enhancement of superconducting critical temperature due to metal-semiconductor transition. Phys. Lett. A **121**, 300 (1987)
3. V.A. Khodel, V.R. Shaginyan, Superfluidity in system with fermion condensate. JETP Lett. **51**, 553 (1990)
4. G.E. Volovik, A new class of normal Fermi liquids. JETP Lett. **53**, 222 (1991)
5. P. Nozieres, Properties of Fermi liquids with a finite range interaction. J. Phys. (Fr.) **2**, 443–458 (1992)
6. A.A. Shashkin, V.T. Dolgopolov, J.W. Clark, V.R. Shaginyan, M.V. Zverev, V.A. Khodel, Merging of Landau levels in a strongly-interacting two-dimensional electron system in silicon. Phys. Rev. Lett. **112**, 186402 (2014)
7. G.E. Volovik, On Fermi condensate: near the saddle point and within the vortex core. JETP Lett. **59**, 830–835 (1994)
8. D. Yudin, D. Hirschmeier, H. Hafermann, O. Eriksson, A.I. Lichtenstein, M.I. Katsnelson, Fermi condensation near Van Hove singularities within the Hubbard model on the triangular lattice. Phys. Rev. Lett. **112**, 070403 (2014)
9. L. Landau, Paramagnetism of metals. Z. Phys. **64**, 629–637 (1930)
10. S. Ryu, Y. Hatsugai, Topological origin of zero-energy edge states in particle-hole symmetric systems. Phys. Rev. Lett. **89**, 077002 (2002)
11. T.T. Heikkilä, N.B. Kopnin, G.E. Volovik, Flat bands in topological media. JETP Lett. **94**, 233–239 (2011). arXiv:1012.0905
12. A.P. Schnyder, S. Ryu, Topological phases and flat surface bands in superconductors without inversion symmetry. Phys. Rev. B **84**, 060504(R) (2011)
13. G.E. Volovik, Quantum phase transitions from topology in momentum space. Lect. Notes Phys. **718**, 31–73 (2007)
14. R.S.K. Mong, V. Shivamoggi, Edge states and the bulk-boundary correspondence in Dirac Hamiltonians. Phys. Rev. B **83**, 125109 (2011)
15. A.M. Essin, V. Gurarie, Bulk-boundary correspondence of topological insulators from their respective Green's functions. Phys. Rev. B **84**, 125132 (2011)
16. G.M. Graf, M. Porta, Bulk-edge correspondence for two-dimensional topological insulators. Commun. Math. Phys. **324**, 851 (2013)
17. G.E. Volovik, *The Universe in a Helium Droplet* (Oxford University Press, Oxford, 2003)
18. A.A. Burkov, L. Balents, Weyl semimetal in a topological insulator multilayer, Phys. Rev. Lett. **107**, 127205 (2011); A.A. Burkov, M.D. Hook, L. Balents, Topological nodal semimetals
19. M.A. Silaev, G.E. Volovik, Andreev-Majorana bound states in superfluids. JETP **119**, 1042–1057 (2014)
20. T.T. Heikkilä, G.E. Volovik, Dimensional crossover in topological matter: evolution of the multiple Dirac point in the layered system to the flat band on the surface. JETP Lett. **93**, 59–65 (2011)
21. H. Weng, Y. Liang, Q. Xu, Yu Rui, Z. Fang, Xi Dai, Y. Kawazoe, Topological Node-Line Semimetal in Three Dimensional Graphene Networks. Phys. Rev. B. **92**, 045108 (2015)
22. Y. Kim, B.J. Wieder, C.L. Kane, A.M. Rappe, Dirac line nodes in inversion symmetric crystals. Phys. Rev. Lett. **115**, 036806 (2015)
23. K. Mullen, B. Uchoa, D.T. Glatzhofer, Line of Dirac nodes in hyper-honeycomb lattices. Phys. Rev. Lett. **115**, 026403 (2015)
24. T.T. Heikkilä, *The Physics of Nanoelectronics* (Oxford University Press, Oxford, 2013)
25. M.I. Katsnelson, *Graphene - Carbon in Two Dimensions* (Cambridge University Press, Cambridge, 2012)
26. P. Delplace, D. Ullmo, G. Montambaux, Zak phase and the existence of edge states in graphene. Phys. Rev. B **84**, 195452 (2011)
27. J.W. McClure, Band structure of graphite and de Haas-van Alphen effect. Phys. Rev. **108**, 612–618 (1957)

28. G.P. Mikitik, YuV Sharlai, Band-contact lines in the electron energy spectrum of graphite. Phys. Rev. B **73**, 235112 (2006)
29. G.P. Mikitik, YuV Sharlai, The Berry phase in graphene and graphite multilayers. Low Temp. Phys. **34**, 794 (2008)
30. T.T. Heikkilä, G.E. Volovik, Nexus and Dirac lines in topological materials. arXiv:1505.03277
31. T. Hyart, T.T. Heikkilä, Momentum-space structure of surface states in a topological semimetal with a nexus point of Dirac lines. Phys. Rev. B. (in press). arXiv:1604.06357
32. A.A. Zyuzin, V.A. Zyuzin, Anisotropic flat bands on the surface of multilayer graphenelike lattice, Pis'ma ZhETF **102** (2015)
33. D. Pierucci et al., Evidence for flat bands near the Fermi level in epitaxial rhombohedral multilayer graphene. ACS Nano **9**, 5432 (2015)
34. P. Esquinazi, T.T. Heikkilä, Y.V. Lysogorskiy, D.A. Tayurskii, G.E. Volovik, On the superconductivity of graphite interfaces. Pis'ma ZhETF **100**, 374–378 (2014). arXiv:1407.2060
35. N.Ya. Fogel, E.I. Buchstab, Yu V. Bomze, O.I. Yuzephovich, A.Yu. Sipatov, E.A. Pashitskii, A. Danilov, V. Langer, R.I. Shekhter, M. Jonson, Interfacial superconductivity in semiconducting monochalcogenide superlattices. Phys. Rev. B **66**, 174513 (2002)
36. P. Esquinazi, Graphite and its hidden superconductivity, Papers in Physics 5, 050007 (2013); A. Ballestar, J. Barzola-Quiquia, T. Scheike, P. Esquinazi, Josephson-coupled superconducting regions embedded at the interfaces of highly oriented pyrolytic graphite, New J. Phys. **15**, 023024 (2013); A. Ballestar, T.T. Heikkilä, P. Esquinazi, Interface size dependence of the Josephson critical behaviour in pyrolytic graphite, Supercond. Sci. Technol. **27**, 115014 (2014)
37. G.E. Volovik, M.A. Zubkov, Emergent geometry experienced by fermions in graphene in the presence of dislocations. arXiv:1412.2683
38. V. Kauppila, F. Aikebaier, T.T. Heikkilä, Flat band superconductivity in strained Dirac materials. Phys. Rev. B. **93**, 214505 (2016)
39. E. Tang, L. Fu, Strain-induced partially flat band, helical snake states, and interface superconductivity in topological crystalline insulators. Nature Phys. **10**, 964–969 (2014). arXiv:1403.7523
40. F. Guinea, M. Katsnelson, M.A.H. Vozmediano, Midgap states and charge inhomogeneities in corrugated graphene. Phys. Rev. B **77**, 075422 (2008)
41. N.B. Kopnin, E.B. Sonin, BCS superconductivity of Dirac electrons in graphene layers. Phys. Rev. Lett. **100**, 246808 (2008)
42. T.E. Weller, M. Ellerby, S.S. Saxena, R.P. Smith, N.T. Skipper, Superconductivity in the intercalated graphite compounds C_6Yb and C_6Ca. Nature Phys. **1**, 39 (2005)
43. Q. Lin, T. Li, Z. Liu, Y. Song, L. He, Z. Hu, Q. Guo, H. Ye, High-resolution TEM observations of isolated rhombohedral crystallites in graphite blocks. Carbon **50**, 2369 (2012)
44. S. Hattendorf, A. Georgi, M. Liebmann, M. Morgenstern, Networks of ABA and ABC stacked graphene on mica observed by scanning tunneling microscopy. Surf. Sci. **610**, 53 (2013)
45. I. Brihuega et al., Unraveling the intrinsic and robust nature of Van Hove singularities in twisted bilayer graphene by scanning tunneling microscopy and theoretical analysis. Phys. Rev. Lett. **109**, 196802 (2012)
46. N.B. Kopnin, T.T. Heikkilä, G.E. Volovik, High-temperature surface superconductivity in topological flat-band systems. Phys. Rev. B **83**, 220503(R) (2011)
47. N.B. Kopnin, Surface superconductivity in multilayered rhombohedral graphene: supercurrent. JETP Lett. **94**, 81 (2011)
48. N.B. Kopnin, M. Ijäs, A. Harju, T.T. Heikkilä, High-temperature surface superconductivity in rhombohedral graphite. Phys. Rev. B **87**, 140503(R) (2013)
49. N.B. Kopnin, T.T. Heikkilä, Surface superconductivity in rhombohedral graphite, Chap. 9, in *Carbon-based superconductors*, ed. by J. Haruyama (Pan Standford 2014). arXiv:1210.7075
50. W.A. Muñoz, L. Covaci, F.M. Peeters, Tight-binding description of intrinsic superconducting correlations in multilayer graphene, Phys. Rev. B **87**, 134509 (2013)
51. S. Peotta, P. Törmä, Superfluidity in topologically nontrivial flat bands. arXiv:1506.02815
52. V.J. Kauppila, T. Hyart, T.T. Heikkilä, Collective amplitude mode fluctuations in a flat band superconductor. arXiv:1505.02670

Chapter 7
Experimental Evidence for the Existence of Interfaces in Graphite and Their Relation to the Observed Metallic and Superconducting Behavior

Pablo D. Esquinazi and Yury V. Lysogorskiy

Abstract This chapter reviews the experimental evidence obtained for the existence of embedded interfaces between crystalline regions with Bernal and/or rhombohedral stacking order in usual graphite samples, and their relationship with the observed metallic and superconducting behavior.

7.1 Interfaces in Graphite Samples

Within the graphite literature there have been several publications on the lattice defects found in graphite structures, like point defects (vacancies and interstitials and their clusters), dislocations, twin boundaries, etc., see e.g. Chap. 3 in [1] and Refs. therein. For radiation defects the readers should refer to a recently published work [2]. The interfaces we are interested in this chapter are boundaries between either: (a) two slightly rotated crystalline regions around the *c*-axis, both with Bernal stacking order. It means the *c*-axes of the two regions are the same but their *a*-axes have a twist angle respect to each other, and (b) the boundaries between Bernal and rhombohedral stacking order regions. Both boundaries have been recognized time ago [3], but only recently their extraordinary properties have been partially studied, theoretically and experimentally.

P.D. Esquinazi (✉)
Division of Superconductivity and Magnetism, Institute for Experimental Physics II, University of Leipzig, Linnéstrasse 5, 04103 Leipzig, Germany
e-mail: esquin@physik.uni-leipzig.de

Y.V. Lysogorskiy
Institute of Physics, Kazan Federal University, Kremlevskaya St. 18, 420008 Kazan, Russia
e-mail: yura.lysogorskii@gmail.com

P.D. Esquinazi (ed.), *Basic Physics of Functionalized Graphite*,
Springer Series in Materials Science 244, DOI 10.1007/978-3-319-39355-1_7

7.1.1 Experimental Evidence Through Transmission and Scanning Electron Microscopy

Kish graphite samples are obtained from iron and purified later with halogen gas at high temperatures. According to literature these kind of graphite samples show one of the largest resistivity ratio ($R(300)/R(4.2)$) of nearly 50 [3] indicating a high degree of crystallinity. In p. 32 of the book of Inagaki [3] one finds an interesting double photo of the edges of a kish graphite sample, see Fig. 7.1 (left). As pointed out in that book, in those pictures one can see a regular stacking of layers at the edges of a Kish graphite sample. The difference in color are related to slightly different orientation, i.e. very probably rotations along a well aligned c-axis. The interfaces we are interested are those regions separating the single crystalline regions, each one characterized by a homogeneous gray color in Fig. 7.1 (left). The electrical transport "quality" of the Kish graphite samples can be derived from their large resistivity ratio, a ratio that depends very much on sample [3]. According to recent studies [4] the metalliclike behavior of graphite is not intrinsic but it comes from the interfaces properties, as will become clear in the next sections.

Regions with interfaces can be observed in nearly any well ordered graphite sample. Even in micrometer large graphite grains of ultrapure graphite powder, see

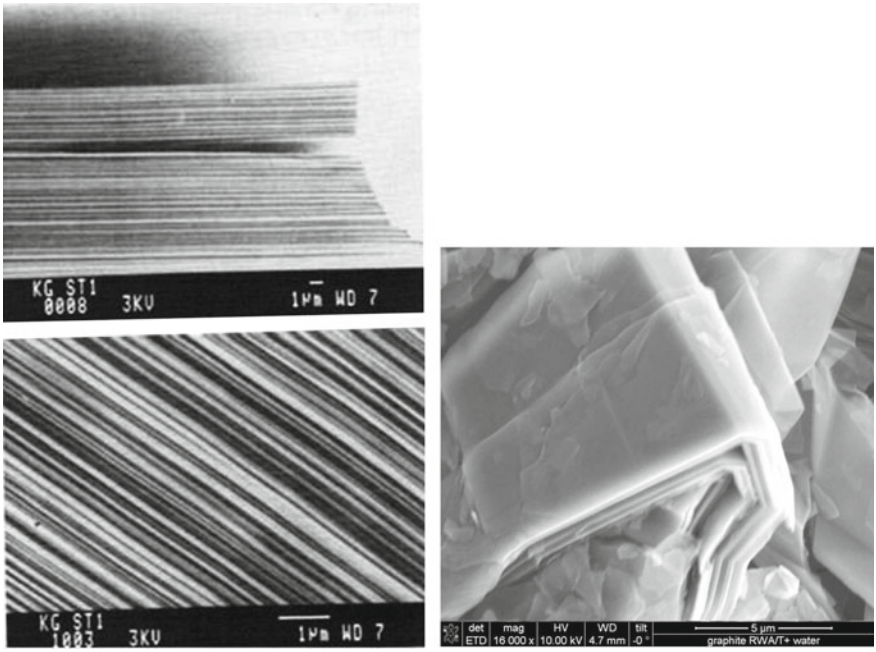

Fig. 7.1 *Left* pictures are taken for a kish graphite sample from [3]. *Right* scanning electron microscope (SEM) picture is taken from [5] (see Supporting information in [5])

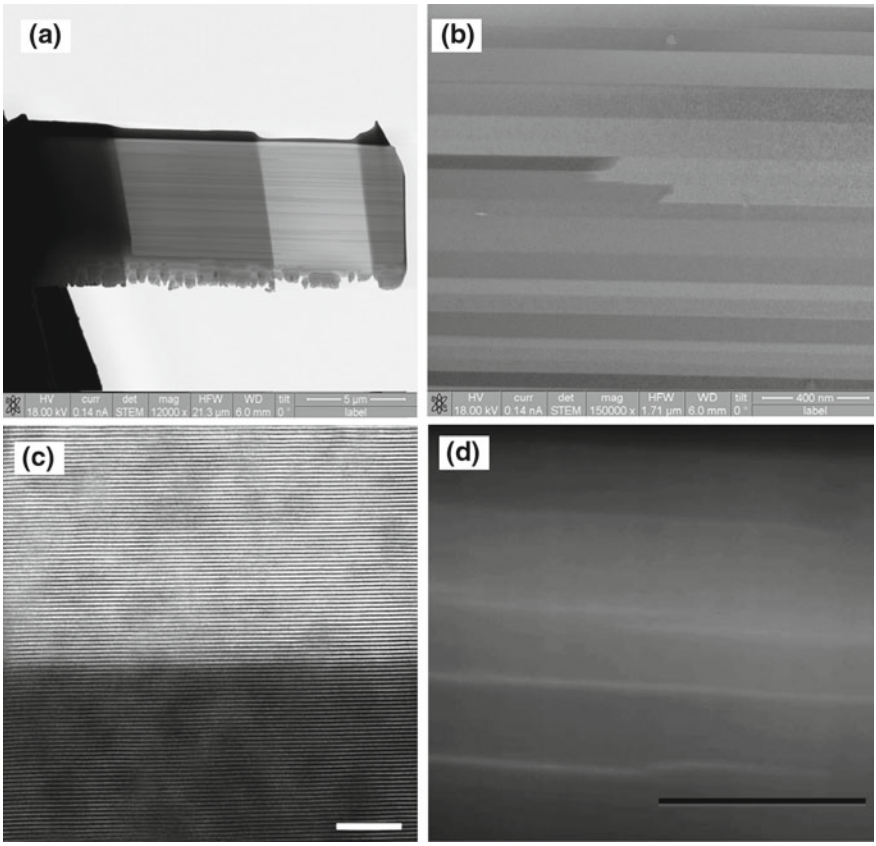

Fig. 7.2 **a** SEM picture taken from a lamella of a HOPG sample after cutting, before leaving it on a substrate. The scale bar corresponds to 5 μm. **b** Transmission electron microscope (TEM) picture of a HOPG ZYA sample, taken from [4]. The scale bar corresponds to 0.4 μm. **c** TEM picture of a similar sample, taken from [6]. The scale bar corresponds to 5 nm. **d** TEM picture of a HOPG sample grade B, taken from [7]. The scale bar corresponds to 1 μm

Fig. 7.1 (right), those interfaces are evident [5]. If these interfaces have different electronic properties than the graphene layers of the single crystalline regions, several experimental methods like transport and magnetization may provide the response of those interfaces in parallel to the one from the graphene layers. If one does not take this possibility into account the interpretation of the experimental results can be misleading.

A much clearer picture of some details of the internal structure of graphite samples can be obtained using transmission electron microscopy (TEM) lamellae. In this case one takes TEM pictures with the electron beam pointing roughly parallel to the graphene planes and at relatively low energies (e.g. ∼15 keV). Figure 7.2a shows one SEM picture of a cut lamella (using a dual beam microscope) from a HOPG

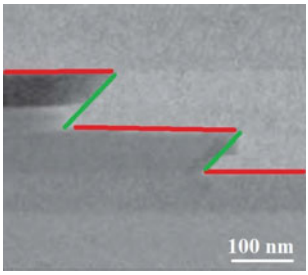

Fig. 7.3 Transmission electron microscopy (TEM) picture of a highly oriented pyrolytic graphite (HOPG) ZYA sample taken parallel to graphene layers of the HOPG lamella. *Red lines* indicate the interfaces between twisted graphene blocks. *Green lines* shows the tilt grain boundaries. The scale bar indicates 100 nm. Image adapted from [4] (color figure online)

sample and fixed to a manipulator tip. In that picture and in spite of the relatively low resolution one can roughly observe single crystalline regions of graphite. These regions are more clearly observed using TEM, see Figs. 7.2b–d. Note the difference in the sharpness and the length of the interface regions between HOPG samples of grade A (b, c) and B (d). This difference plays an important role in the behavior of the magnetotransport and the size of the possible superconducting regions localized at the interfaces.

7.1.2 Twisted Layers: Moiré Patterns and Dislocation Lines

7.1.2.1 The Concept

One can divide the possible types of boundaries in graphite sample onto several groups: (a) two dimensional (2D) interfaces between twisted layers of graphene, which could be characterized by rotation angle θ and lateral translation δ. This type of interfaces produces the so-called moiré patterns [8, 9]; (b) 2D interfaces between regions with Bernal (ABA) and rhombohedral (ABCA) stacking and (c) one dimensional (1D) dislocation lines or topological line defects [10]. The location of some 2D and 1D boundaries are schematically shown in Fig. 7.3. However, the possible lattice defects in the graphite structure are much more plentiful. As example we refer to the exhaustive review of defects in graphite obtained after irradiation given in [2].

7.1.2.2 Moiré Patterns and Van Hove Singularities in Twisted Graphene Layers

In the work of Kuwabara and coauthors [8] the superperiodicity in scanning tunneling microscopy images of highly oriented pyrolytic graphite (HOPG) sample

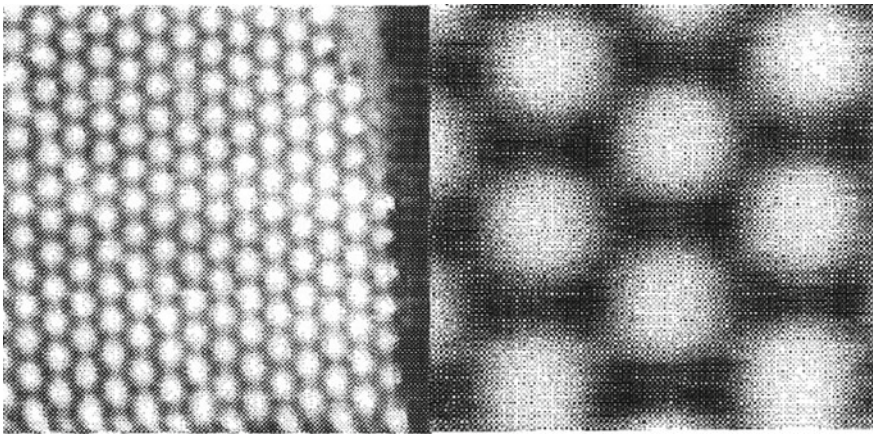

Fig. 7.4 High-resolution scanning tunneling microscope (STM) at constant current images of a superperiodicity on a graphite (001) surface. Superperiodicity was associated with a moiré pattern, resulting from the overlap between a misoriented layer of graphite and the underlying graphite single crystal. The shown images are of size 100 nm × 100 nm (*left*) and 22.5 nm × 25.0 nm (*right*). The graphene lattice period itself is 0.246 nm and is hardly visible on the given images. Adapted from [8]

was observed (see Fig. 7.4). This superperiodicity was associated with a moiré pattern (MP), resulting from the overlap between a misoriented layer of graphite and the underlying graphite single crystal. Moiré patterns on graphite consist of huge hexagonal lattices made of bright spots on STM images. It was proposed for the first time that in addition to the periodicity of the graphite lattice, the presence of a misoriented substrate a number of atomic spacings below the surface might be expected to introduce spatially periodic perturbations in the surface local density of states [8, 11].

In [12] the exhaustive analysis of different moiré patterns on graphene was done. Generally, one can classify the areas in misoriented graphene bilayer into three types: (a) normal, Bernal AB-stacking, (b) SlipAB-stacking and (c) AA-stacked graphene. In AA regions all carbon atoms of one layer are stacked over the carbon atoms of the other layer, whereas in AB regions only half of the atoms (Bernal stacking). SlipAB-stacking is obtained after a little shift of one layer in the AB-stacked structure.

DFT calculations of the density of states (DOS) at the Fermi level lead to the conclusion that only AB-stacked graphite regions are invisible, whereas AA-stacked graphite regions are the most visible, represented by bright spots. SlipAB-stacked graphite regions show an intermediate brightness in the STM images [12]. However, not all misorientation rotation angles between two adjacent layers will lead to a moiré pattern, but only under relative rotation angles between 0° and 15°, otherwise the regions with AA-stacking, which give the bright spots on STM images, disappear [12].

Further moiré patterns induced by rotations of surface and subsurface layers of graphite *bulk* samples were reported in [9, 13] (see Fig. 7.5). This evidence

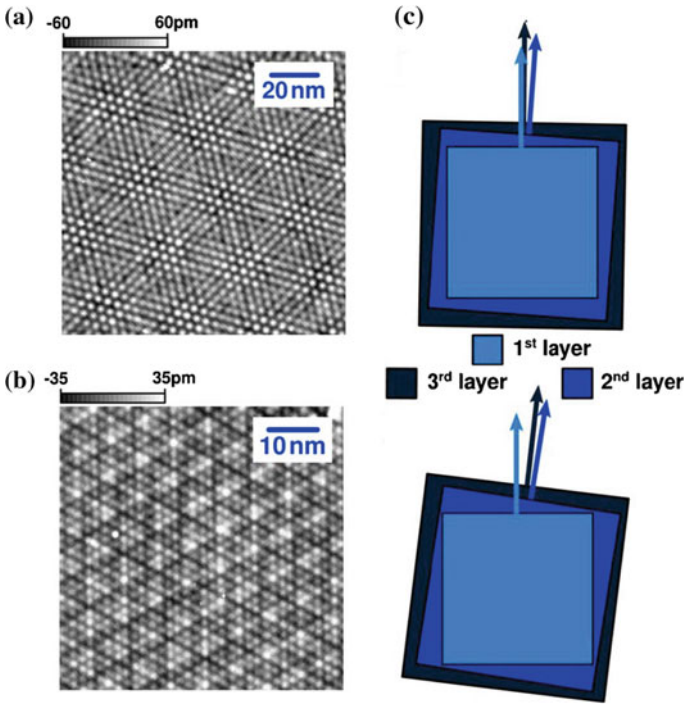

Fig. 7.5 Scanning tunneling microscopy images of twisted graphene layers (**a**, **b**) along with its schematic of layer orientation (**c**). Moiré patterns could be formed by a misorientation of several graphene layers. Adapted from [13]

indicates that by the measurement of a transport property like the electrical resistivity or Hall effect one cannot be sure, which region of the sample provides the measured voltage signal. If the input current mainly flows through the interface regions where due to the rotation of the graphene blocks, a larger density of electrons than in ideal Bernal stacking order exists, then we will measure a voltage that can be due to the contribution of, at least, two resistances in parallel, as example see the discussion in Sect. 7.2.1. Although the anomalies in the DOS at the surface of usual graphite samples were reported already in 1990 [8], apparently their influence on the transport was not taken into account till 2008, where the authors observed that the absolute resistivity of graphite samples of different thickness, increased the smaller the thickness of the sample (see also a similar experiment in [14]) and that the metalliclike temperature dependence of bulk graphite turns to a semiconductinglike the thinner the graphite sample [4]. We note also that the authors in [15] after scanning the surface of a HOPG sample of high quality using Kelvin force microscopy (KFM) concluded on the coexistence of regions with "metalliclike" and "insulatinglike" behaviors showing large potential fluctuations of the order of 0.25 V. This micrometer large inhomogeneous domain distribution was not observed in disordered HOPG samples. Taking into account several reports on twisted graphene layers found on the

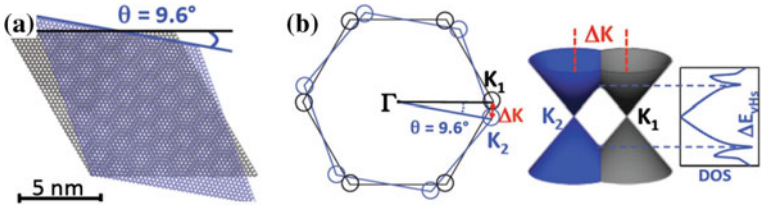

Fig. 7.6 Illustration of a moiré pattern arising from the rotation of one graphene sheet relative to another by the twist angle $\theta = 9.6°$ (**a**) and mechanisms of emergence of Van Hove singularities as a consequence of this rotation (**b**). Dirac cones of each layer merge into two saddle points at energies $\pm E_{\mathrm{vHs}}$. Adapted from [16]

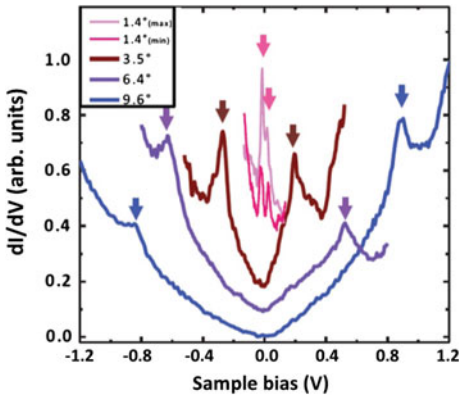

Fig. 7.7 Scanning tunneling spectroscopy (dI/dV) of the twisted graphene layers with different rotation angles θ. Its intensity is proportional to local density of state of the sample, whereas the sample bias corresponds to shift with respect to the Fermi level. The energy difference between the Van Hove singularities (which are indicated by *arrows*) decreases with decreasing angle. Adapted from [16]

top surface of high quality graphite samples [8, 9, 13], it appears plausible that the results obtained using KFM [15] are related with the change in the electronic properties due to a inhomogeneous twist angle distribution of the top graphene planes in the samples.

In-depth systematic studies of moiré patterns and induced Van Hove singularities (vHs) in twisted graphene layers (TGL) was reported, for example, in [16] by means of scanning tunneling spectroscopy (STS) and ab initio simulations. The mechanism of increasing the local density of states is briefly described in Fig. 7.6. The rotation of graphene layers results in the equal rotation of its Brillouin zones by the same angle θ. Thus, the Dirac cones of each layer are now centered in different points of the reciprocal space K_1 and K_2. The cones merge into two saddle points at energies $\pm E_{\mathrm{vHs}}$ from the Dirac point, leading to vHs which generate peaks in the DOS [16]. The experimental evidence of this hypothesis is given in Fig. 7.7.

In addition, TGL under the interlayer bias could demonstrate very intriguing peculiarities such as the helical networks—the topologically protected electronic

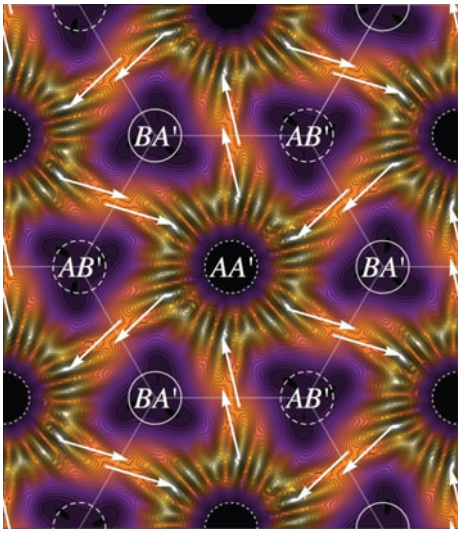

Fig. 7.8 Enhanced electron probability density (*bright areas*) between the regions with AA′, AB′ and BA′ typical stacking of twisted bilayer graphene. In AA′ regions all carbon atoms of one layer are stacked over the carbon atoms of the other layer, whereas in AB′ or BA′ regions—only the half of the atoms (Bernal stacking). A fully developed helical network state is formed. *White arrows* show the direction of the valley current. Adapted from [17]

states [17]. The emergence of this phenomenon could be explained in following manner: TGL forms moiré pattern which smoothly alternates between the three minimal types AA′ (bright region on the STM image, see Fig. 7.4), AB′ and BA′ (dark region on the STM image). In AA′ regions all carbon atoms of one layer are stacked over the carbon atoms of the other layer, whereas in AB′ or BA′ regions—only the half of the atoms (Bernal stacking). For any reasonable interlayer bias AA′ bilayer is a good metal, whereas a band gap opens around each valley of TGL of Bernal-type stacking (AB′ or BA′). Change of the topology of a tuned gap can be induced with a uniform bias U by smoothly transitioning from AB′ to BA′ stackings, which are related by mirror symmetry. Performing such an inversion between two adjacent regions in space gives rise to two topologically protected helical (TPH) modes per valley and spin. These modes could flow without resistance along the interface between the two regions [17]. On Fig. 7.8 a fully developed helical network state is shown. One can see the enhanced electron probability density between the regions with AA′, AB′ and BA′ typical stacking. Electrons propagate without any dissipation along the links of the network. However, special types of defects, that could produce the valley scattering, can shut off the transmission through these links. The hydrogen adsorbates or vacancies were proposed as such defects [17]. Moreover, we note that the influence of H^+ in between two graphene planes, on the dispersion relation of the carriers as well as on the DOS, is not thoroughly studied.

Besides the scanning tunneling spectroscopy, DOS of carbon structures could be also studied by means of resonance Raman spectroscopy. The Raman signal intensity increases significantly when both the incident and scattered photons are in resonance with transitions between vHs in the valence and conduction bands. In [18] the exhaustive study of the intensity of the G band peak in Raman spectra depending on the twist angle θ in a range between 0° and 30° was performed (see Fig. 7.9).

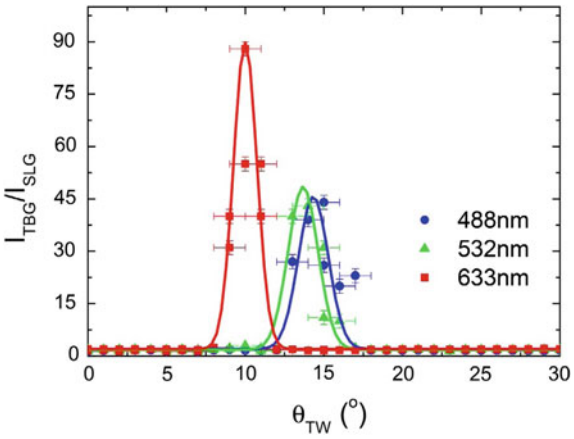

Fig. 7.9 The ratio of Raman G peak intensity of twisted bilayer graphene to the intensity of single layer graphene (I_{TBG}/I_{SLG}) for different samples with different twist angles θ_{TW} between 0° and 30°. The Raman signal intensity increases significantly when both, the incident and scattered photons are in resonance with transitions between Van Hove singularities in the valence and conduction bands. *Blue*, *green*, and *red dots* are data taken at photon wavelengths equal to 488, 532 and 633 nm. Adapted from [18]

Among the TGL samples, only samples with twist angle from 9° to 17° demonstrate a strong increasing of the Raman intensity, whereas no enhancement was observed for TGL samples with low and high twist angles. So the experimental measurements as well as results of calculations by tight-binding method indicate that the vHs become more singular and intense for the case of the quasi-periodic moiré unit cell size of TGL since there are more k states at the flat region of the energy dispersion [18]. This fact may provide an answer to the observed interface size dependence of the Josephson critical behaviour [19], see Sect. 7.3.2.

One-dimensional topological defects in graphene embedded in a perfect graphene sheet are theoretically predicted and experimentally confirmed to have an almost flat band near Fermi energy and can act as a quasi-one-dimensional metallic wire [10, 20]. The results of STM/STS measurements of typical 1D topological defect on the surface of HOPG are shown in Fig. 7.10. As one can see, there are Van Hove-like singularities at Fermi level at the points along the 1D defect, whereas the singularity disappears far away from this defect [10]. Similar features were reported in [21]. Theoretical calculations by means of density functional theory (DFT) on the model system with periodic 1D defect line on graphene give similar results, i.e. presence of flat bands in band structure as well as vHs at the Fermi level (see Fig. 7.11). The flat band arise from the sp^2 dangling bonds of undercoordinated carbon atoms at the edges of defects [10, 20].

As one can see, the flat bands in multilayer graphene structures could arise from moiré patterns as well as from 1D topological line defects. A discussion of the possible influence of vHs on the transport properties is given in Sect. 7.2.

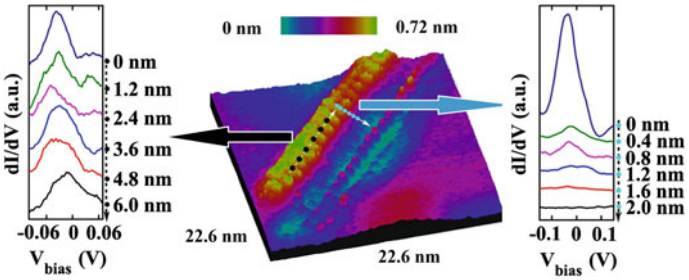

Fig. 7.10 The 22.6 nm × 22.6 nm scanning tunneling microscopy image of an area with 1D defect on a HOPG surface (in the *center*) as well as the set of dI/dV spectra measured at different positions (*black* and *cyan dots* on the *left* and *right*). dI/dV is proportional to the local DOS of the sample, whereas the sample bias V_{bias} corresponds to shift with respect to Fermi level. Van Hove singularities at Fermi level are presented along the 1D defect, whereas the singularity disappears far away from this defect. Adapted from [10]

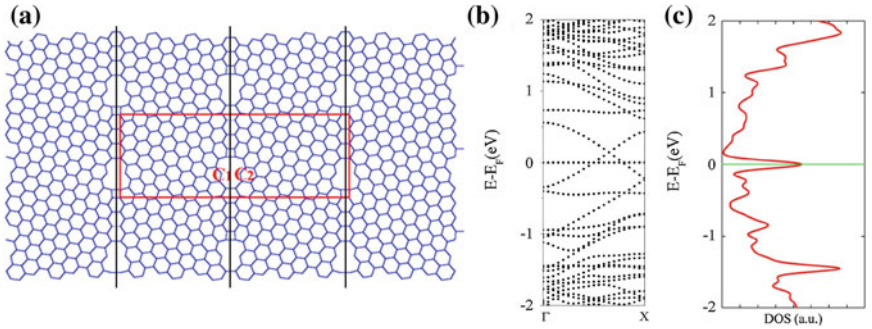

Fig. 7.11 **a** The structure of particular 1D defect lines (*black line*) on a graphene sheet simulated by means of density functional theory, **b** its electronic band structure along the defect line and **c** the corresponding DOS. One can see the flat band in the band structure of given system as well as the Van Hove singularity at the Fermi level. Adapted from [10]

7.1.3 Recent Evidence for the Existence of Rhombohedral Stacking Order in Graphite

Because rhombohedral graphite (stacking order ABCA...) is expected to show flat bands at its surface, or at the interfaces with Bernal stacking order [22, 23], it is of interest to check whether this stacking order has been observed in graphite or multilayer graphene samples. The existence of this stacking order has been already pointed out in several publications in the past, see [24] and Refs. therein. Upon graphite sample, a concentration of up to 30% of this stacking order respect to the Bernal order appears possible, especially in natural graphite samples. According to [25], a certain amount of isolated rhombohedral crystallites has been detected in bulk samples without suffering severe shear deformation. In particular, it is interesting to

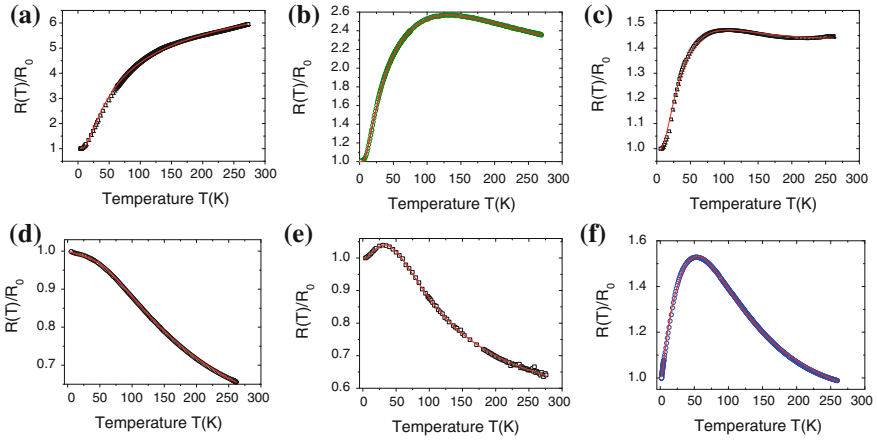

Fig. 7.12 Normalized resistance R/R_0 versus temperature for six HOPG samples with thickness, length (between voltage electrodes), width and R_0: **a** $\simeq$20 μm, 2 mm, 1 mm, 0.003 Ω; **b** $\simeq$10 μm, 1 mm, 1 mm, 0.013 Ω; **c** $\simeq$50 nm, ∼3 μm, ∼3 μm, 15 Ω. **d** $\simeq$13 nm, 14 μm, 10 μm, 490 Ω; **e** $\simeq$20 nm, 5 μm, 10 μm, 32 Ω; **f** $\simeq$37 nm, 27 μm, 6 μm, 69 Ω. The (*red*) lines through the experimental data are obtained from a parallel resistors model, see (7.1) and [30]. For similar experimental results and fits using both stacking orders, see [29]. Adapted from [30] (color figure online)

note the localization of an isolated rhombohedral graphite grain with thickness ∼80 and 550 nm length along the [0001] and [1100] directions. In another experimental work [26] the authors prepared multilayer graphene samples on freshly cleaved mica by exfoliation and studied them by scanning tunneling spectroscopy. The authors observed that multilayer graphene can exhibit a regular pattern of alternating ABA and ABC stacking with stacking areas as small as $(200\,\text{nm})^2$.

Evidence for the existence of flat bands near the Fermi level at the surface of epitaxially grown rhombohedral multilayer graphene has been recently reported [27]. The rhombohedral multilayers (sequences of about five layers and covering ∼70% of the sample total surface) were obtained by epitaxial growth on a 12 μm thick 3C-SiC(111) film on a 2° off-axis 6H-SiC(0001). The existence of a flat band at the Fermi level has been concluded by scanning tunneling spectroscopy and angle-resolved photoemission spectroscopy. Further evidence for extended flat bands and gapped subbands for rhombohedral stacking was obtained by Raman spectroscopy in multilayers flake [28].

X-rays diffraction (XRD) can be used to check for the existence of the rhombohedral stacking in a graphite sample, if the amount of this phase and the side or thickness of these regions are large enough. We note, however, that there are several Bragg peaks in XRD, which are not suitable for distinguishing both stacking modifications of graphite. Both the $(00l)$ and $(hh0)$ peaks of the Bernal and rhombohedral stacking are superposed, for example. The easiest way to determine and approximately quantify the rhombohedral phase in a graphite sample is to restrict the 2Θ range between 40° and 47°. In this range one has two Bernal peaks at 42.22°

(100) and 44.39° (101) and two peaks at 43.45° (101) and 46.33° (012) due to the rhombohedral stacking. Direct transport measurements from only the rhombohedral phase were not yet reported. However, recent transport studies in bulk and mesoscopic graphite samples with both stacking orders, indicate that the rhombohedral phase would behave semiconducting with an energy gap of the order of 100 meV and its interfaces with the Bernal phase metalliclike [29].

7.2 Experimental Evidence of the Contributions of Interfaces to the Transport Properties of Graphite Samples

7.2.1 On the Intrinsic Temperature Dependence and Absolute Value of the Resistivity of Graphite

Basically, the observed temperature dependence of the total resistance $R(T)$ for all graphite samples shown in Fig. 7.12 and in the literature can be understood assuming the contribution of the graphene layers $R_s(T)$ in parallel to that of interfaces $R_i(T)$:

$$R(T) = [R_s(T)^{-1} + R_i(T)^{-1}]^{-1}. \tag{7.1}$$

The fit curves in Fig. 7.12 were obtained assuming a semiconductinglike behavior for $R_s(T)$ with a gap of the order of 30 meV, independently of the thickness of the sample, and an exponential thermally activated increase with activation energy of the order of ~50 K [30]. The fits indicate that the graphene layers inside graphite behave semiconducting and that there is an extra metalliclike contribution which shows, however, an exponential increase with temperature, similar to that observed in granular superconductors [31]. The influence of this granular superconductivity in some internal interfaces of graphite samples is very probable the reason for the anomalous behavior of early high resolution magnetoresistance results of graphite flakes in [32]. We note that in case regions with rhombohedral stacking order embedded in the Bernal stacking order matrix would exist, it might be necessary to include a further resistance in parallel in (7.1), as has been done recently [29]. The parallel contribution of the rhombohedral stacking in the electrical resistance of a given graphite sample as well as a temperature dependent mobility appear to be necessary to include especially in samples that show minimum and maximum as a function of temperature, like in Fig. 7.12c. A systematic study of the temperature and thickness dependence of the resistance of more than 10 graphite samples with both stacking orders has been done recently [29]. This rhombohedral contribution, however, will be sample depend because the amount of this stacking relative to the Bernal stacking order depends on the graphite sample.

Note that the usual top contact electrodes configuration, or even a mixture of edge and upper graphene layer electrodes contacts in bulk samples involve always the

contribution of the c-axis resistivity. A contribution that in the simplest case and for fields normal to the graphene layers and interfaces, it does not change with applied field. However, the absolute value of this contribution is unpredictable because it depends on each sample. At least one of the free parameters used to fit the temperature dependent of the measured resistance, see Fig. 7.12, may depend on the c-axis resistance.

Because the contribution of the interfaces, internal as well as the two surfaces of a given graphite sample, cannot be easily subtracted from the measured total resistance, the absolute value of the resistivity in the a, b plane of the Bernal graphite structure remain unknown to some extent. If one plots the resistivity of graphite samples obtained from samples of the same batch but with different thicknesses, i.e. with similar density of interfaces as done in [4], this resistivity increases to values $\rho_{a,b}(4\,\mathrm{K}) \gtrsim 200\,\mu\Omega\mathrm{cm}$ for samples with the smallest interface contribution [29].

One may argue that the semiconductinglike dependence of the resistance for graphite samples with small enough thickness, see Fig. 7.12d, does not necessarily represent the intrinsic dependence because: (a) Either the lattice disorder in the thin graphite flakes is too large, or (b) ballistic and not diffusive transport may play a role. The hypothesis (a) can be easily ruled out through systematic Raman spectroscopy characterisation of the samples, see Sect. 7.2.2 for further references and details. Regarding the ballistic transport in graphite, indeed, a study of the mean free path with a parameter-free constriction method on bulk graphite HOPG samples indicates that the mean free path of the carriers in graphite is very large, i.e. several micrometers at low temperatures [33]. To check that the semiconductinglike behavior is intrinsic and not due to a hidden, non-diffusive carrier transport, we discuss here the results obtained using a relatively long graphite flake with low contribution of interfaces [34].

Figure 7.13 shows an optical microscope picture of a graphite sample of 20 nm thickness with 14 electrodes at different positions distributed through the whole 30 μm sample length. The results of the resistance at different length of the same sample, see Fig. 7.13c, indicate that the absolute shift in resistance with length does not follow rigourously the Ohm law prediction due to an extra ballistic contribution. The data can be used to obtain the carrier mean free path versus temperature using Sharvin–Knudsen formula and Ohm's law [34]. Especially the finite resistance one extrapolates at $L \rightarrow 0$ from the experimental data of $R(T, L)$ versus L, where L is the length between the voltages electrodes, can be used to obtain without free parameters the mean free path, see Fig. 7.13d. One main conclusion obtained in [34] is that the contribution of ballistic transport is relatively small for a sample with a length several times larger than the mean free path. Furthermore, the semiconductinglike behavior with a saturation at low temperatures is observed at all distances between the voltage electrodes indicating that this dependence is intrinsic and not related to the sample size. With the same parallel resistance model and the exponential temperature dependence appropriate for semiconductors, see Fig. 7.12, the obtained energy gap $E_g \simeq \mathrm{k_B}\ 350\,\mathrm{K}$ is independent of the distance between electrodes.

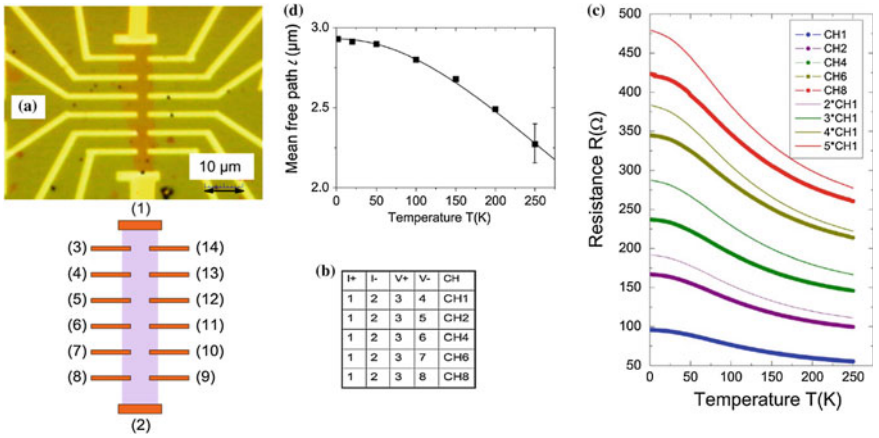

I+	I-	V+	V-	CH
1	2	3	4	CH1
1	2	3	5	CH2
1	2	3	6	CH4
1	2	3	7	CH6
1	2	3	8	CH8

Fig. 7.13 **a** Optical microscope photo of the measured graphite flake $\simeq 30\,\mu$m long, $(5 \ldots 8.5) \pm 0.3\,\mu$m wide and (20 ± 2) nm thick with its 14 electrodes. **b** The *left sketch* shows the current and voltage electrodes configuration for the different channels. The *right picture* shows a table where the channels with the corresponding configuration for current and voltage electrodes are defined. **c** Temperature dependence of the resistance of the graphite flake at five different channels defined in (**b**). The *continuous lines* represent the expected resistance if it would be just only proportional to the length between electrodes according to the Ohm law. **d** Temperature dependence of the carriers mean free path obtained from an equation assuming that the measured resistance has a ballistic, sample-length independent contribution and a Ohmic contribution, see (1–4) in [34]. The *continuous line* follows the equation $\ell(T) = ((2.93)^{-1} + ((6.4 \times 10^5)/T^2)^{-1})^{-1}$ (T in K and ℓ in μm). After [34]

7.2.2 *How Large Is the Carrier Density and Carrier Mobility in Ideal Graphite? Quantum Oscillations in the Transport Properties Revised*

Figure 7.14 shows the field dependence of the Hall coefficient for graphite flakes of different thickness obtained from kish graphite samples [35, 36]. In those results there are several interesting details we would like to emphasize:

(A) The amplitude of the Shubnikov-de Haas (SdH) oscillations tends to decrease the smaller the thickness of the sample. This tendency appears more systematic in Fig. 7.14b. If the crystalline quality between the samples remains similar, this result points out that these oscillations are not intrinsic. A graphite sample with a thickness of 18 nm (and several tens of square microns area) can certainly be considered as bulk, if homogeneous.

One may argue that the reason for the decrease of the amplitude of the SdH oscillations is the decrease in the amount of perfect graphene layers, in other words the increase in the lattice disorder existing in the sample. Within this hypothesis small patches of ideal graphene layers coexist with disordered graphene layers and the SdH occur only in the ideal graphene layers. However, the experimental evidence obtained

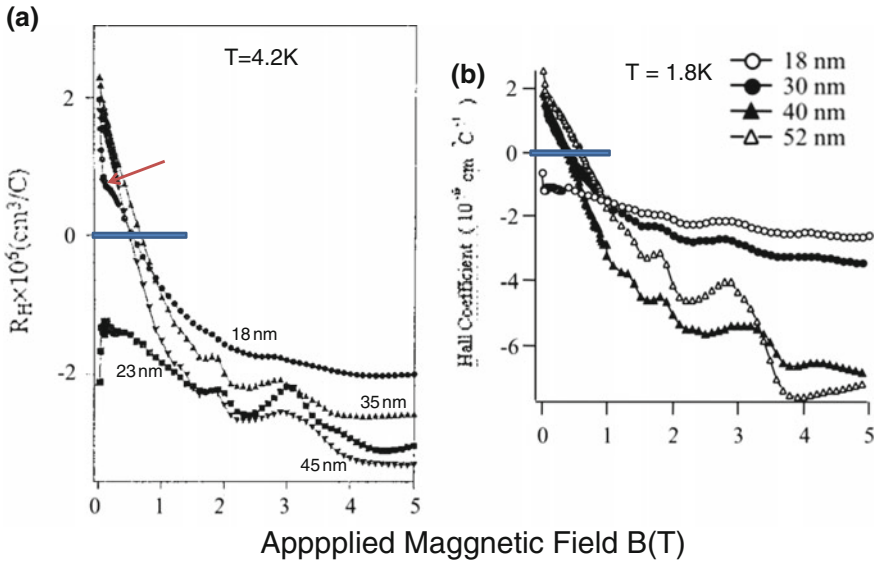

Fig. 7.14 **a** Hall coefficient as a function of applied field normal to the graphene planes of graphite flakes of different thickness taken from a kish graphite sample. The *red arrow* points to the field region where a clear kink shows in the field dependence of the 18 nm thick sample. Adapted from [35]. **b** Similar but from other kish sample. Adapted from [36]. The *blue horizontal bars* shows the zero coefficient value. With exception of the 23 nm thick sample in (**a**) and the 18 nm in (**b**), all other samples show a clear change in sign of the Hall coefficient from positive to negative increasing field. This sign change occurs at a sample-dependent field (color figure online)

by different studies the last years indicates that this hypothesis is not always correct. For example: (a) There is no evidence from Raman that the thinner the sample the larger the disorder, see e.g. [4, 29, 37], as example. (b) The amplitude of the SdH oscillations depends on the region one measures within the same sample, as Fig. 7.15 shows [38]. This result indicates that there is a non-homogeneous distribution of patches where the density of carriers is large enough to provide SdH oscillations with a similar period (in $1/B$) to that observed for bulk graphite samples. The question is then whether those regions, where SdH oscillations occur, are perfect graphene layers or the opposite, regions where the lattice disorder or the interface regions with their higher DOS (see Sect. 7.1.2), are those with enough carrier density.

A partial answer to this question was given by the authors in [38] after irradiating with Ga^+ ions only a part of the graphite flake, see Fig. 7.15. The irradiated fluence introduced an average defects (e.g. vacancies) concentration of $\sim 10^{12}$ cm^{-2}. We see that after irradiation the amplitude of the SdH oscillations, measured only in that part of the sample, increased drastically and started to be measurable at lower magnetic fields, see Fig. 7.15a. From the period in $1/B$ one can estimate a carrier concentration per graphene layer $n \sim 3 \times 10^{11}$ cm^{-2} similar to that found in bulk HOPG samples in literature [24, 39]. Note that the SdH oscillations in the small graphite flake as

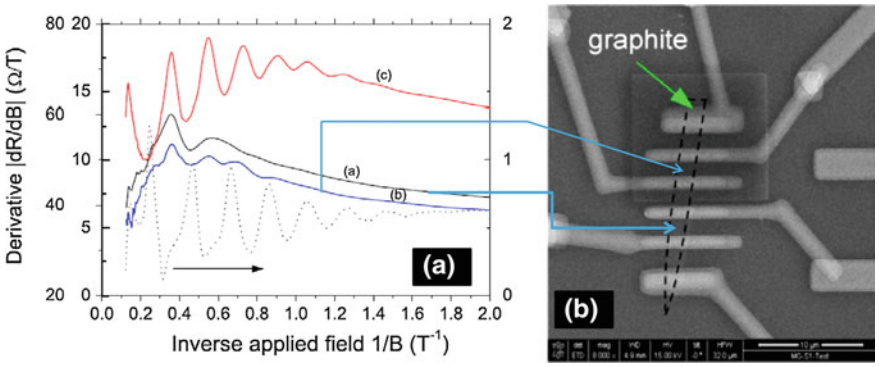

Fig. 7.15 **a** First derivative of the magnetoresistance at $T = 4\,\mathrm{K}$ of different graphite samples. Curves (a) and (b) ($0 - 20\ \Omega/\mathrm{T}$ range) represents the results obtained from two different parts (follow *blue arrows*) of the same graphite flake shown in the picture in (**b**). The curve (c) ($20 - 80\ \Omega/\mathrm{T}$ range) represents the results obtained from the same part (**a**) of that flake but after irradiation with Ga^+ ions with a fluence of $5 \times 10^{11}\ Ga^+/cm^2$. The *dashed line* (right *y*-axis) was obtained for the bulk HOPG sample of size $2 \times 1 \times 0.2\,mm^3$. Adapted from [41]. **b** Scanning electron microscope image of a 15 nm thick graphite flake (*dashed line* denotes its borders) with six Au/Pt electrodes (scale bar denotes 10 μm). One recognizes the region with 300 nm thick negative electron beam resist used to protect part of the graphite flake from the Ga^+ irradiation. Adapted from [38] (color figure online)

well as after Ga^+ irradiation are shifted respect to that obtained for the bulk HOPG samples, see Fig. 7.15a. From this result we would conclude that the origin for the SdH oscillations in graphite is not related to perfect, defect-free graphene layers but the opposite.

It is interesting to note that after a similar second Ga^+ irradiation on the same part of the graphite sample shown in Fig. 7.15, the absolute value of the magnetoresistance (MR) and the resistance itself changed as expected, i.e. the resistance increased and the MR decreased [38]. Nevertheless, the SdH oscillations did not change qualitatively, i.e. these start to be measurable at a similar low field and with a similar oscillation period (in $1/B$). This result indicates that no further increase in the carrier density has been achieved when the distance between the produced defects (e.g. vacancies) on each graphene layer is below 2 nm. Apparently, this result is related to the ∼3 nm range where a modification of the electronic structure due to a single vacancy has been measured [40].

A possible reason for the observation of the SdH oscillations in the virgin thin sample at high fields only, can be as follows [41]: For the measured sample area that gives curve (a) in Fig. 7.15 there are no SdH oscillations up to a field $B \simeq 1.8\,\mathrm{T}$ in clear contrast to the irradiated sample. This fact can be understood assuming that in most of this sample part $n_0 \lesssim 10^9 cm^2$. Then, the corresponding Fermi wavelength $\lambda_F \gtrsim 0.8\,\mu\mathrm{m}$ is of the order of the sample size and larger than the cyclotron radius $r_c = m^\star v_F/eB$ for $B > 0.07\,\mathrm{T}$ assuming $m^\star = 0.01m$ (m is the free electron mass). In this case we do not expect to observe any SdH oscillations. However, for $B \simeq 1.8$

and 2.8 T two maxima are observed. From the measured "period" in $1/B$ as well as from the first field at which the first maximum appears we estimate the existence of domains of size $<2r_c \lesssim 100$ nm at which $\lambda_F \lesssim 50$ nm, i.e. domains with $n_0 \gtrsim 10^{11}$ cm^{-2} within a matrix of much lower carrier concentration. This indicates that the description of the SdH oscillations in real graphite samples can be achieved only within the framework of inhomogeneous 2D systems [42, 43]. At the end of this section we discuss experimental studies that provide carrier concentrations $n_0 \lesssim 10^9$ cm^{-2} for ideal graphene layers inside graphite, supporting the hypothesis that the usually measured SdH and de Haas-van Alphen (dHvH) oscillations in bulk graphite samples in literature, from where carrier densities $n \gtrsim 10^{11}$ cm^{-2} are extracted, do not represent ideal graphite.

(B) From the SdH oscillations period the authors in [35, 36] obtained that the cross section of the Fermi surface in the thin graphite flakes appears to be half of the one for bulk graphite samples, implying that the flakes should have a smaller carrier density by the same amount. Taking into account the large density of interfaces in kish graphite samples, see Fig. 7.1, one can speculate that the reduction of the SdH oscillations is related to a smaller amount of interfaces in thinner samples, assuming that the interfaces have a larger density of carriers than the graphene planes.

(C) For most of the samples shown in Fig. 7.14 there is a clear change of sign of the Hall coefficient, from positive to negative, increasing magnetic field. In particular in the 18 nm flake in Fig. 7.14a we see a clear kink in the field dependence. The field at which there is a crossover from positive to negative, depends on the sample, suggesting a non-intrinsic nature. A recent study of the Hall coefficient measured in different graphite samples since 1955 and in graphite flakes without interfaces, indicates that the negative sign is not intrinsic of the ideal graphite [44], as we discuss below in Sect. 7.2.3.

Finally, the reported values for the Hall coefficient in Fig. 7.14 [35, 36] are five orders of magnitude smaller than the one reported in the literature [44] (see Sect. 7.2.3); this large discrepancy might be due to an error in the units or a missing factor in the calculation of the Hall coefficient in [35, 36].

7.2.2.1 An Experimental Approach to Obtain the Intrinsic Carrier Density and Mobility

The measurement of the carrier mean-free path ℓ is not straightforward and, in general, the value obtained depends on several other not well-known parameters within the selected transport model, usually based on a Drude–Boltzmann approach. However, in case of ballistic conduction, there are at least two more transparent methods to obtain $\ell(T)$ without adjustable parameters. One method is to measure the resistance as a function of the sample length as has been done in [34] and the results shown in Fig. 7.13c can be used to obtain $\ell(T)$, as shown in Fig. 7.13d. The other method is based on the measurement of the longitudinal resistance as a function of the constriction width W, a constriction located between the voltage electrodes, see Fig. 7.16a, b. The resistance can be quantitatively understood taking into account

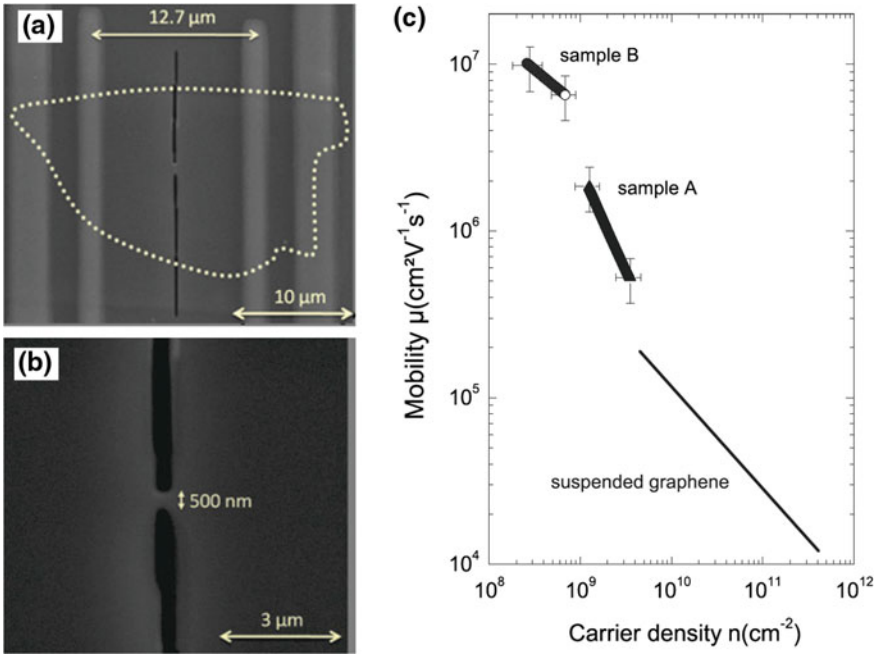

Fig. 7.16 **a** Graphite flake (sample A of 15 nm thickness, the *point line* denotes the edge of the sample) with four electrodes and a constriction in the *middle*. **b** Blow out of a constriction of 500 nm size in sample A. **c** Mobility versus carrier density obtained from the measurements of the resistance at different constrictions widths and at different temperatures. The points are obtained between 300 and 10 K for sample B of 40 nm thickness (60 K for sample A). The *line* corresponds to the data of a suspended graphene sample at 20 K from [45]. Taken from [46]

three contributions, the ballistic one given by the Knudsen–Sharvin resistance [33]; a logarithmic term due to the ohmic, spreading resistance in two dimensions, and a third term due to the ohmic resistance of the constriction itself [46]. The resistance is expected to show an oscillatory behavior as a function of W or the Fermi wavelength λ_F [47, 48], as observed experimentally in bismuth (Bi) nanowires [49] as well as in GaAs devices [50, 51]. Although the experiments were done changing only five times the constriction width of the sample, the behavior obtained appears compatible with the one observed previously allowing to calculate the mean free path $\ell(T)$, the Fermi wavelength $\lambda_F(T)$ and the mobility $\mu(T) = (e/h)\ell(T)\lambda_F(T)$. The carrier density per graphene layer can be calculated from $n = 2\pi/\lambda_F^2$.

The results for the mobility versus carrier density per graphene layer of the measured samples are shown in Fig. 7.16c and indicate that the intrinsic carrier density (without the contribution of the interfaces) is three orders of magnitude smaller than the one obtained in literature for bulk graphite samples with interfaces, i.e. $n(T < 10\text{K}) \lesssim 10^9\ \text{cm}^{-2}$ per graphene layer [33, 46]. From the results in bulk HOPG and thin flakes one obtains that the mean free path $\ell(T) \propto T^{-2}$ reaching values of

microns at room temperature [33, 34, 46]. Such large mean free path and small carrier density (large Fermi wavelength) indicate that the carrier mobility should be large. Indeed the obtained carrier mobility is two orders of magnitude larger than the one found in literature obtained from graphite samples with interfaces.

There is further experimental evidence that indicates that the carriers mean free path is extraordinarily large. The reported clear increase of the (basal) magnetoresistance (for magnetic fields normal to the graphene planes) with sample size in, for example, bulk graphite samples (see Fig. 2 in [52]), graphite thin flakes (see Fig. 10 in [4]) and graphite thin flakes with constrictions (see Fig. 6 in [46]) demonstrates that the carrier mean free path is several micrometers long. The decrease of the mean free path with temperature, see e.g. Fig. 7.13d, is the main reason for the *increase* of the magnetoresistance with temperature observed in relatively small graphite samples, see Fig. 6 in [4], or graphite samples with constrictions, see Fig. 11 in [4]. The magnetoresistance of small graphite samples can increase or decrease with temperature upon the relative size of the carriers mean free path to the effective (lateral) sample size.

We note that several interpretations of the experimental transport data of real graphite samples relied on the assumption that these were intrinsic properties. As an example, the carrier (electron plus hole) densities obtained from the SdH oscillations, see above in this section, are several orders of magnitude larger than the one the graphene planes have in graphite, see e.g. Fig. 7.16. For example, at low temperatures, the carrier density per graphene layer in graphite assumed in the literature is $n_0 > 10^{10}\,\mathrm{cm}^{-2}$, as one can read in the standard book of Kelly [24], or the old publication from [53], or from recently published work [54] ($n_0 \simeq 10^{12}\,\mathrm{cm}^{-2}$) or [55] ($n_0 \simeq 2.4 \times 10^{11}\,\mathrm{cm}^{-2}$).

Therefore, it is interesting to reconsider the development of the electronic band structure of graphite, which came out based on experimental parameters of the last, say, 80 years. As pointed out in previous publications [41, 56] we would like here to note the following development:

- Hund and Mrowka from Leipzig published one of the first calculations of the energy band structure of simple atom lattice structures, in particular of diamond [57], also published by Kimball in the same year [58]. The first attempt to calculate the dispersion relation of the graphite structure was also published by Hund and Mrowka from Leipzig in the same year [59]. In this last publication, the authors analyzed the energy states of the graphene structure and wrote explicitly the dispersion relation for this structure assuming s-wave functions, a dispersion relation that partially resembles the one we use for graphene within the tight binding approximation.
- Two-dimensional calculations assuming a coupling γ_0 between nearest in-plane neighbors C-atoms on the graphene plane of zero-gap semiconducting graphite gave a carrier density (free electrons and positive holes per C-atom) $n(T) \simeq 0.3(k_B T/\gamma_0)^2$ [60]. If one assumes $\gamma_0 \simeq 3\,\mathrm{eV}$ the effective carrier density per C-atom at 300 K would be $n(300) \simeq 2 \times 10^{-5}$. This is equivalent to $7.64 \times 10^{10}\,\mathrm{cm}^{-2}$ total carrier density at 300 K using the areal density of carbon atom per

graphene layer ($=3.82 \times 10^{15}\,\mathrm{cm}^{-2}$). A similar value for the total carrier density was obtained for bulk HOPG samples at similar temperatures using the constriction method [33]. Moreover, the obtained temperature dependence carrier density can be fitted up to ~200 K by $n[\mathrm{cm}^{-2}] \simeq n_0 + 10^5 T^2 + 7.5 \times 10^3 T^3$ with T in [K] and $n_0 \simeq 2 \times 10^8\,\mathrm{cm}^{-2}$. We note, however, that the same data can be also well explained by a semiconducting-like exponential function $\exp(-E_g/2T)$ with an energy gap $E_g \sim 50\,\mathrm{meV}$.

- Because several experimental values obtained from bulk graphite samples with interfaces indicated a finite $n(T \to 0) = n_0 > 0$ then more free parameters in the tight-binding electronic band structure calculations were included in order to provide a finite carrier density at zero temperature. For example, with a new coupling γ_1 between C-atoms of type α in adjacent planes one obtains $n(T) = a(\gamma_1/\gamma_0^2)T + b(T/\gamma_0)^2 + c(T^3/\gamma_0^2\gamma_1) + \ldots$ ($a, b, c, \ldots$ are numerical constants), where the "accepted" value for $\gamma_1 \sim 0.3\,\mathrm{eV}$. Also in this case $n(T \to 0) \to 0$. To fit experimental data and obtain a finite Fermi energy E_F—in the simplest case $E_F \sim \gamma_2$ [24, 61]—up to seven free parameters were and still are introduced, even for carrier density as small as $n \simeq |-8 \times 10^9|\,\mathrm{cm}^{-2}$ ($E_F \simeq -29\,\mathrm{meV}$) [62].

Taking into account the exhaustive experience accumulated in gapless or narrow gap semiconductors [63] we should actually expect that at least part of the measured carrier density at low temperatures is not intrinsic of the graphite structure but it is influenced by interfaces, impurities and/or defects in the graphite/graphene lattice. We note that a carrier density of the order of $10^8\,\mathrm{cm}^{-2}$ means one carrier in $1\,\mu\mathrm{m}^2$ graphene area, which could be produced actually by having a single vacancy or impurity in the same graphene area, in case one carrier is generated by one of these defects [41, 64]. Therefore, we should cast doubts on the relevance of related electronic band structure parameters obtained in the past.

7.2.3 *On the Intrinsic Low-Field Hall Coefficient of Graphite*

Recently reported study of the low-field Hall coefficient of thin graphite flakes and a overall comparison with literature arrived to the conclusion that its negative sign is not intrinsic but it is due to the contribution of the internal interfaces. The temperature dependence of low-field R_H shown in Fig. 7.17 for three different graphite flakes obtained from a HOPG sample and its behavior at higher fields (sample S3 in the figure) suggests that the change of sign is not intrinsic but it is due to the contribution of interfaces [44]. From the temperature dependence of the resistance one can roughly guess how important is the contribution of the interfaces for the transport properties of given sample. The samples in Fig. 7.17 showed different interface contributions, being the sample S1 with smaller contribution that in samples S2 and S3 [44].

The available data would indicate also that the reported behavior, specially the change in sign of the Hall coefficient as a function of field in Fig. 7.14 [35, 36], is not intrinsic but due the contribution of interfaces. If these interfaces would have

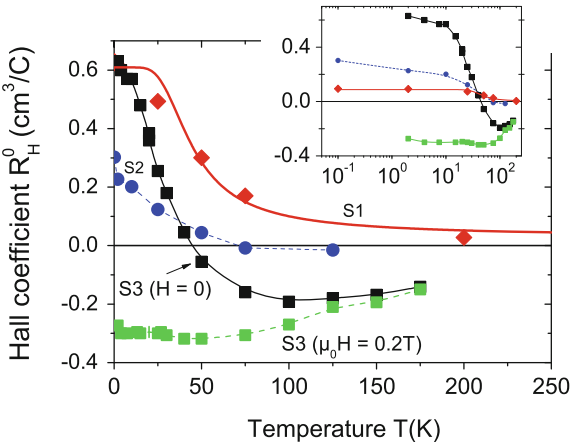

Fig. 7.17 Temperature dependence of the low-field Hall coefficient for the three studied samples. For sample S3 (*black squares*) we show also the Hall coefficient (*green squares*) obtained at a field $\mu_0 H = 0.2\,\mathrm{T}$ applied normal to the interfaces. The data from sample S1 in the main panel of the figure were multiplied by a constant factor of 6.7. The *inset* shows the same data but in a logarithmic temperature scale. The line through the S1 data points follows the function $R_H^0 = (11^{-1} + (4 \times 10^{-3} \exp(300/(2T)))^{-1})^{-1}$. All other lines are only a guide to the eye. Taken from [44]

superconducting properties we expect a finite, negative contribution at high enough temperatures, as can be seen for samples S2 and S3 in Fig. 7.17, similarly at high enough applied fields [44], see also Fig. 7.14. At low temperatures and at low enough applied fields, we expect that the contribution of the interfaces, if they exist in a given sample, to the Hall signal will be minimum. From old and new available Hall data [44] we can conclude that the intrinsic, low magnetic field Hall coefficient of graphite appears to be positive with a low-temperature value around 0.1 cm^3/C and a temperature dependence that follows closely that of a semiconductor with an energy gap of the order of 300 . . . 400 K, in agreement with the fits of the longitudinal resistance of different samples, see Fig. 7.12 [30].

7.2.4 Trying to Get the Response of a Single Interface

It is clear that one cannot obtain the transport behavior of an interface of a graphite sample directly, because one cannot introduce simply electrical contacts inside the sample without destroying it. The use of electrical contacts at the edges of the interfaces will be described in the next section. Therefore, a simple way to obtain a rough signal of a single interface is to localize voltage electrodes at two sides of a step of a graphite flake, see the left picture in Fig. 7.18. The graphite flake measured in [65] was heterogeneously thick and several micrometers long, allowing to find regions to locate voltage electrodes that may pick up more clearly the response of a single interface.

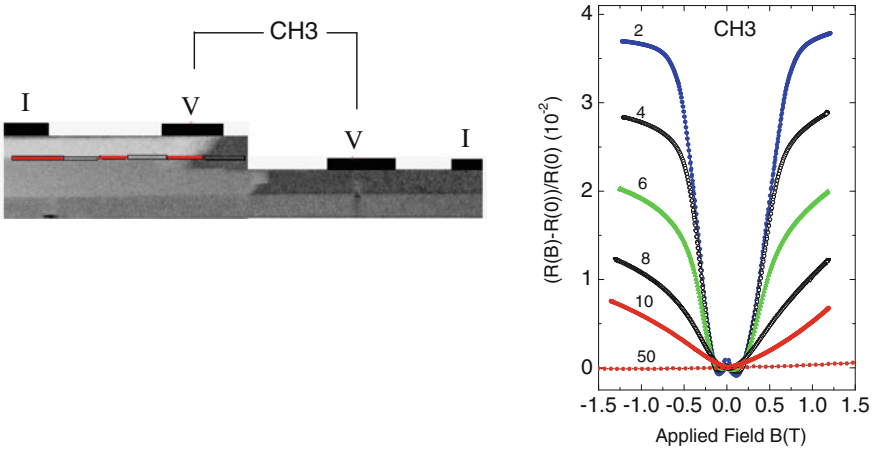

Fig. 7.18 The *left picture* shows an electron transmission microscope picture of a 200 nm thick lamella with the *c*-axis of the graphite structure running normal to the interfaces between the crystalline graphite structure. The thickness of the single crystalline regions (defined by the homogeneous *gray color* regions) is ∼70 nm. At the top of the TEM picture the positions of the electrodes of channel 3 (CH3) and current (I) electrodes are schematically drawn. In case superconducting regions exist between the CH3 electrodes we expect to see some evidence in the voltage drop. The *right figure* shows the magnetoresistance measured at CH3 versus magnetic field applied parallel to the graphene planes within ±3° at different temperatures. Adapted from [65] (color figure online)

The magnetoresistance of a region of the selected sample with voltage electrodes at the up and low sides of a 120 nm large step height is shown in the right picture of Fig. 7.18. The magnetoresistance measured at this location of the sample shows an unique behavior that suggests the existence of inhomogeneous or granular superconductivity in that sample region. At low T the magnetoresistance increases abruptly at $B \gtrsim 0.25$ T and saturates at $B \gtrsim 0.75$ T, see Fig. 7.18. We note that in order to decrease substantially the large background of the intrinsic magnetoresistance of graphite observed for fields parallel to the *c*-axis, the magnetic field in that experiment [65] was applied nearly parallel to the graphene planes and interfaces, reducing in this case the field component normal to the graphene layers [66]. The small negative magnetoresistance obtained at low fields is probably related to the magnetic order due to defects (DIM, see Chaps. 1–3) that exists in parts of the selected sample, as shown in more detail in [65].

7.3 Experiments with TEM Lamellae

A direct measurement of the transport properties of the interfaces is not a simple task. Even if one would prepare a graphene bilayer with a selected twist angle between the two graphene planes, locating the contact at the top of the graphene plane does not

provide the response of an internal interface. The idea used in recent publications [7, 19, 56, 67] was to prepare TEM lamellae from the bulk graphite sample in question and deposit electric contacts at the edges of the lamella. In this case one gets a better chance to measure the direct voltage response of several interfaces in parallel when an electrical current is passing through. If some of those interfaces show superconducting properties, then it is clear that a negligible voltage should be measured. A graphite TEM lamella is in general prepared using the in-situ lift out method of a dual beam microscope (FIB/SEM). The TEM lamellae are cut perpendicular to the graphene layers and to the embedded interfaces using the Ga^+ ion source. Before cutting it, a thin film is deposited using electron beam induced deposition (EBID) in order to protect the internal structure of the sample from the Ga^+ ions used to cut the lamella. Nevertheless, a region $\sim$20 nm thick at each of the edges of the lamellae is contaminated with Ga. This region remains highly disordered and high electrical resistance [38]. The usual four contacts method used to measure the voltage response of the lamella prevents therefore the contribution of this $\sim$20 nm thick disordered layer in the measurement [68]. The total procedure to obtain a thin TEM lamella with low Ga contamination and well polished edges (like the several steps milling of the main surface done at progressively high to low currents) requires however large experience with several non-simple preparation details and the use of the technical capabilities of the dual beam microscope [68]. Lamellae with different thickness $100\,\text{nm} \lesssim d \lesssim 1\,\mu\text{m}$ were prepared and contacted, see Fig. 7.19. The electron transmission diffraction pattern obtained with the beam parallel to the graphene layers provides information on the crystalline regions and their defective parts parallel to the graphene layers, as shown in Figs. 7.2 and 7.19.

In this introductory section we show experimental results of different graphite lamellae published recently and discuss several open issues on these results. We divide the presentation into three parts, namely, (A) the temperature dependence of the voltage (or resistance) at different constant currents, (B) Voltage-Current ($I-V$) characteristics at different temperatures and (C) field dependence. The other two subsections handle on the size dependence of the critical behavior (Sect. 7.3.2) and the results obtained from a graphite sample of lower grade (Sect. 7.3.1).

(A) Temperature Dependence at Constant Currents

Figure 7.20 shows the results from three different lamellae, two of them (a, b) with the usual contacts configuration in series (like in Fig. 7.19) and one (c) with a Van der Pauw configuration, i.e. the contacts were positioned at the edges of the lamella [67, 68]. The measured resistance is in all cases non-ohmic, i.e. its absolute value and behavior with temperature depends on the input current. We note that the absolute value of the resistance can be relatively large, up to $10^6\ \Omega$, at high enough temperature, where the input current does not influence notably. In case of the lamella in Fig. 7.20a the obvious transition shifts to lower temperatures or vanishes increasing the input current. Something similar is observed in the lamella in (b) below 20 K for input currents $I \leq 10$ nA. The noise level observed in that measurement ($\sim$300 nV) is related to the intrinsic properties of the sample and not to the electronic equipment. It was interpreted as due to the contribution of different Josephson coupled

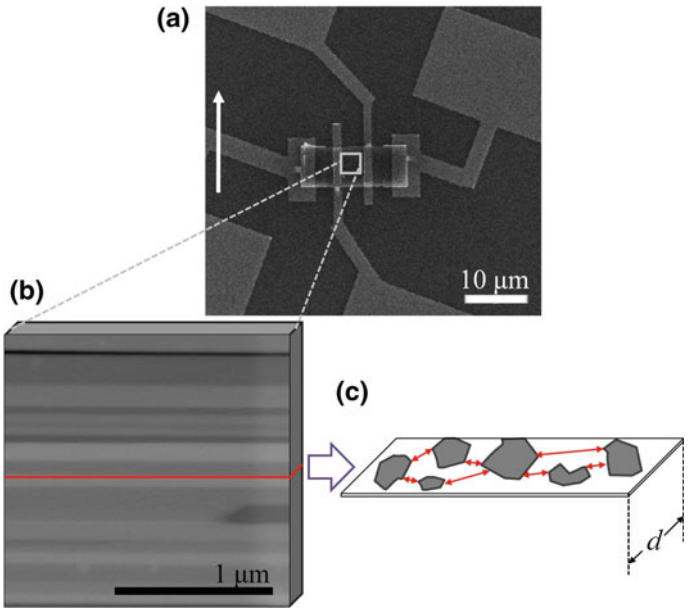

Fig. 7.19 **a** Scanning electron microscope picture of a lamella on a Sin/Si substrate with its four in series contact arrangement. **b** Transmission electron microscope picture of the internal microstructure of a lamella from the same batch. The *red line* is a guide to indicate the possible existence of an interface between two crystalline regions with a given twisted angle around the *c*-axis. **c** The model behinds the observations is that localized regions exists within certain interfaces in which superconducting patches exist (*grey regions* in the sketch) Josephson coupled (*red lines* connecting them). The size of the interface in depth, i.e. its width (equivalent to the thickness of the lamella) is *d*. Taken from [19] (color figure online)

regions within the current path in the sample [67]. In all samples, where this noise was observed, it vanishes after applying a magnetic field of ∼1 kOe, a field that apparently influences the Josephson coupling between the superconducting regions. One expects interfaces where superconducting regions of different sizes exist at different positions within the interface. They can be Josephson coupled, in particular if the distance between those regions is small enough. We note further that Cooper pairs in a graphene layer have a large diffusion length of several hundreds of nm [69]. Therefore, it does seem possible to have Josephson coupled superconducting patches within the same interface.

The results of the lamella (c) with the Van der Pauw configuration of the electrodes shows a "negative" resistance at low temperature. This "negative" resistance is obtained from the negative voltage one measures in this Wheatstone-like bridge configuration, when one of the resistances tends to zero as described in detail in [67]. It is clear that an increase of the input current of two orders of magnitude changes qualitatively the temperature dependence of the evaluated resistance, see Fig. 7.20c. From this last result we may expect to have superconducting regions with critical

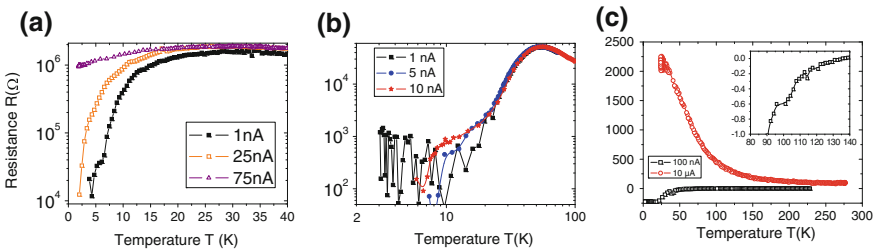

Fig. 7.20 Resistance versus temperature at different input DC currents of three TEM lamellae with different sizes and different contact configurations. The resistance was calculated dividing the measured voltage (at the voltage electrodes) by the input current. The lamellae were prepared from HOPG samples of grade A. **a**, **b** Electrodes in linear configuration like the ones shown in Fig. 7.19; **c** electrodes in Van der Pauw configuration. The negative values of the resistance are due to this Van de Pauw configuration that provides negative voltages when one of the resistance in a Wheatstone-like bridge configuration tends to zero [67]. Adapted from [67, 68]

temperatures above 100 K, as the $I-V$ characteristic curves suggest, see section (B) below.

The last point we would like to stress from the results shown in Fig. 7.20 is that the resistance does not go to zero at the lowest temperatures and lowest currents used in those measurements. There can be different reasons for this fact, like sensitivity of the instrument, noise level (whatever its origin) or a finite, non-superconducting resistance in the current path of the samples. A constant ohmic resistance in series would produce a finite slope in a $I-V$ curve and its contribution might be easily subtracted. On the other hand we should note that a finite resistance, even below a critical Josephson current I_c, can appear due to thermally activated phase processes [70]. This thermally activation has to be taken into account to understand quantitatively the $I-V$ measured curves.

(B) Current-Voltage Characteristics

Figure 7.21 shows the $I-V$ curves obtained at different temperatures for two lamellae [67] at no applied magnetic field. In the lamella with the Van der Pauw configuration, Fig. 7.21a, the curves show a non simple behavior upon temperature. With the assumption that the voltage measured can be understood in first approximation with a Wheatstone-like bridge configuration and that two of the resistors of the bridge have the influence of Josephson coupled superconducting regions, the curves can be well understood using the Josephson-coupling model with thermal activation [70]. Each of those resistors have a different effective Josephson critical current $I_c(T)$, the only free parameter in the model [67]. For the lamella with the contacts in series configuration, Fig. 7.21b, the curves can be also well fitted assuming only one effective Josephson critical current. We note that due to the thermally activation and upon the value of the Josephson critical current, the resistance does not strictly vanish at finite currents, even at 2 K. From the fits to those experimental curves, the temperature dependence of the Josephson critical current has been obtained for several lamellae

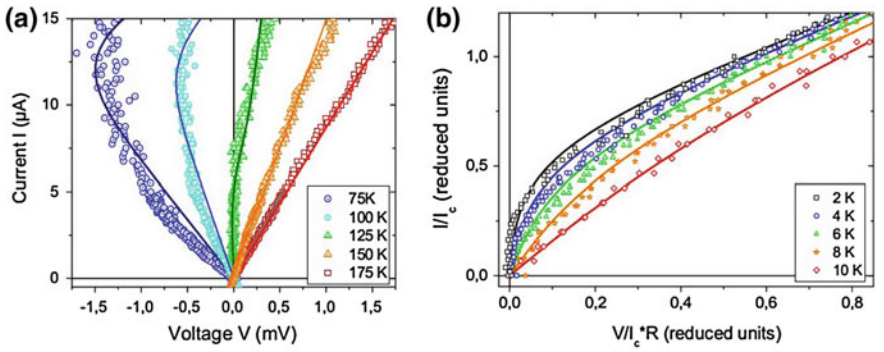

Fig. 7.21 Current-voltage characteristic curves at different temperatures of two lamellae. **a** Lamella with a Van der Pauw contact configurations. The lines were calculated taking into account the Josephson-coupling model with thermal activation presented in [70] with two different Josephson critical currents $I_c(T)$ from two resistors within a Wheatstone-like bridge configuration [67]. **b** Similar to (**a**) but in reduced units for a lamella with in series electrode configuration; R is the resistance at the critical temperature that is taken at high enough temperatures. The lines were calculated with the same model as in (**a**), but with only one Josephson critical current as free parameter; R is the resistance of the junction at the critical temperature, i.e. in the normal state, which in the case of the lamellae, it is usually taken directly from the measurement at a temperature where the apparent granular superconductivity behavior vanish. Adapted from [19, 68]

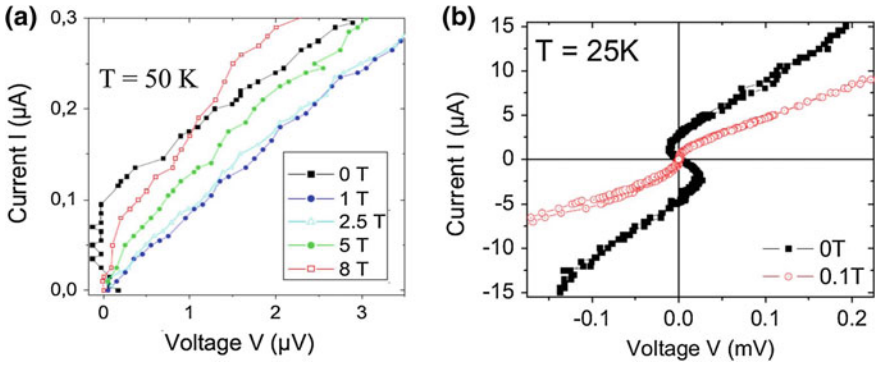

Fig. 7.22 Current-voltage characteristic curves at different applied fields normal to the interfaces for two lamellae. **a** Lamella with usual contact configuration at a fixed temperature of 50 K and at different applied fields, adapted from [67]. **b** Characteristic curves obtained at 25 K for a lamella with Van der Pauw configuration at zero and 0.1 T applied fields. Adapted from [56]

[67] and it follows reasonably well the predictions for short junction length where the normal state barrier between the superconducting regions is a graphene layer [71].

(C) Magnetic Field Dependence

The effect of an applied magnetic field to the transport behavior measured in the lamellae remains a puzzle and more experimental studies should be done in the near future. Figure 7.22 shows two results obtained in two lamellae of very different sizes

and with different contacts configurations. Figure 7.22a shows the $I-V$ curves at 50 K of a rather thick (∼800 nm) lamella. At zero field the $I-V$ curve resembles the one of a Josephson junction. At a field of 1 T applied normal to the interfaces (and graphene layers) the resistance is finite at all measured currents and at larger field it starts to show a kind of reentrance at low enough currents. A field applied parallel to the interfaces does not affect the $I-V$ curves within experimental error [67]. We note that a reentrance to a metallic-like state at low temperatures was observed in the longitudinal resistance of ordinary graphite bulk samples at high magnetic fields above that of the metal-insulator transition [72]. This kind of reentrance might be related to the one we observe in Fig. 7.22a. A kind of reentrance with magnetic field was also observed recently in an electric field-induced superconducting-like transition [73]. Its origin remains in all these cases unknown. Figure 7.22b shows the $I-V$ curves of a lamella with contacts in the Van der Pauw configuration at a fixed temperature of 25 K and at zero and 0.1 T applied field. The s-like $I-V$ curve can be quantitatively explained using a Wheatstone-bridge model and assuming that two resistors of the bridge follow the $I-V$ Josephson characteristic with different critical Josephson currents, see also Fig. 7.21. A field of 0.1 T is enough to strongly affect the Josephson behavior especially in one of the resistors in the circuit.

An applied magnetic field is expected to be detrimental to the superconducting state. In the case of the granular superconductivity expected to occur within the interfaces and due to the Josephson like behavior, the magnetic field should affect also the Josephson coupling between the superconducting regions. Due to the expected Josephson array distribution within the interfaces and the unknown characteristics of the junctions it is not possible to predict a general behavior as a function of magnetic field. In fact, in some lamellae the applied field did not affect the characteristic curves within experimental error [67]. These results suggest that the effect of a magnetic field on the transport response of the interfaces might be size dependent, whereas the size can refer to the junction or to the superconducting regions.

At this stage we would like to note that superconductivity in single- as well as multiwall carbon nanotubes (CNT), was reported in more than 12 publications in the last 14 years [74–84]. The experimental data indicate that even individual double-wall CNT show superconductivity with critical temperatures from a few Kelvin to ∼20 K [82]. Superconductivity in 4 Å CNT is observed not in single but aligned and embedded in specially prepared matrices [80, 83]. Their behavior depends apparently on the coupling between each other along their length and through the matrix. The origin for the superconductivity in CNT in general is still a matter of discussion. If superconductivity exists in such a small pure carbon structure, we may speculate that a similar phenomenon should exist in certain regions of graphite. The observed field independence of the resistance in certain lamellae [67] resembles a similar field independence of the superconducting transition observed in CNT [80, 83] and interpreted as a sign of quasi 1D superconductivity, with thermally activated phase slips according to the Langer–Ambegaokar–McCumber–Halperin (LAMH) theory [85, 86]. This similarity suggests that upon the properties of the superconducting regions at certain interfaces in graphite samples, we may expect quasi 1D superconductivity, i.e. magnetic field independent broad resistivity transitions.

On the other hand the effects of a magnetic field on the superconducting state of 2D superconductors or in case the coupling does not correspond to a singlet state are not yet completely clarified. For example, superconductivity can be even enhanced by a parallel magnetic field to the interface where superconductivity is localized [87]. If the pairing is p-type [88] the influence of a magnetic field is expected to be qualitatively different from the conventional behavior [89, 90] with even an enhancement of the superconducting state at intermediate fields, in case the orbital diamagnetism can be neglected or for parallel field configuration. Further experimental studies are necessary to clarify the effect of a magnetic field to the state at the interfaces of lamellae of graphite samples of high grade.

7.3.1 Response of Lower Grade Samples

The response of lamellae obtained from HOPG samples of lower grade (i.e. larger rocking curve width) has been recently reported [7]. A TEM picture of the inner structure of this sample is shown in Fig. 7.2d. In that TEM picture it is clearly seen that the interfaces, i.e. the regions between different grey colors, are not as well defined as in the case of higher grade sample, i.e. compare it with the TEM picture of Fig. 7.2b. Therefore, if the interfaces are the reason for the behavior observed in the others lamella, we expect to measure clear differences in the electric response. Indeed, clear differences are observed in the temperature, current and field dependence. At high enough input currents ($I \gtrsim 200\,\mathrm{nA}$) the electrical resistance of a lamella of this lower grade sample (SPI-II), increases decreasing temperature and tends to saturate at low temperatures [7]. A clear non-ohmic behavior is observed, namely the resistance decreases the larger the input current. In the low input current region ($I < 200\,\mathrm{nA}$) the resistance starts to show a maximum at $T \sim 3.5\,\mathrm{K}$, see Fig. 7.23a. With applied magnetic field this maximum vanishes. The curves shown in Fig. 7.23a follows qualitatively a similar MIT than the ones measure in usual bulk HOPG and kish graphite samples. A rough but similar scaling can be obtained from those curves that resembles the one obtained for higher grade HOPG samples [91]. There is, however, a difference that is worth to mention, namely the "critical" field H_c, necessary to trigger the transition from a metallic to an insulating state, is, roughly speaking, ten times larger in the lower grade sample than the H_c obtained in higher grade samples, i.e. $\mu_0 H_c \sim 1\,\mathrm{T}$ instead of $\sim 0.1\,\mathrm{T}$ [72, 92], see Fig. 7.23a. It is therefore tempting to relate this change to some specific characteristic of the internal interfaces. Assuming that the internal interfaces in both kind of samples have a similar range of twist angle and any possible doping within the interfaces is also similar, the main difference according to the TEM pictures would be related to the effective smaller size of well-defined 2D interface in the lower grade graphite samples, a conclusion compatible with the study done in [19] and discussed in Sect. 7.3.2.

The results shown in Fig. 7.23b, c, i.e. the non-linear $I - V$ curves and the differential conductance $G = \mathrm{d}I/\mathrm{d}V$ obtained from those curves, support further the existence of granular superconductivity in this kind of HOPG sample. Note that in

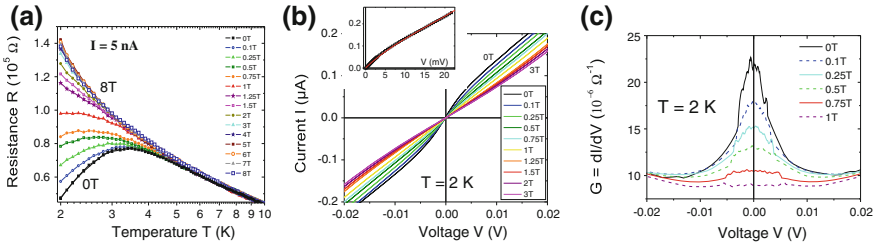

Fig. 7.23 Results obtained of a lamella cut from a HOPG bulk sample grade B (SPI-II). **a** Resistance measured at a current of 5 nA versus temperature at different applied magnetic fields. **b** $I-V$ curves at 2 K at different applied magnetic fields. The *inset* shows the result at zero field with the fit curve following [70] with a critical current of 82 nA. **c** Differential conductance calculated from the $I-V$ curves at 2 K and at different applied fields. Adapted from [7]

the measured temperature range the resistance of the lamella does not reach a zero value at the used currents. The temperature dependence of the conductivity peak at zero voltage, (the curves are similar to those in Fig. 7.23c but at zero field at different fixed temperatures) follows an exponential temperature dependence [7], as observed in granular superconductors [31]. Extrapolating the conductance to zero temperature one concludes that most of the finite value at 2 K is due to thermal fluctuations [7]. In this case the $I-V$ curves should follow a similar Josephson like dependence as observed in the other lamellae, see Fig. 7.21. The inset in Fig. 7.23b shows the $I-V$ curve at 2 K at zero applied field and the fit following the equation derived in [70], calculated with an effective critical Josephson current of 82 nA [7].

7.3.2 Size Dependence

Most if not all the experimental facts indicate that the internal interfaces are the reason for the decrease of the resistance of graphite samples decreasing temperature. Several facts speak for the existence of granular superconductivity embedded in some of the interfaces. The questions arises regarding the dependence of the temperature at which the Josephson coupling between the expected superconducting regions starts to influence the measured voltage (or resistance). Comparing different graphite samples with interfaces, it appears that this "critical" temperature T_c depends much on the sample, whether it is a lamella or a bulk graphite or a graphite flake. However and in general, we observe that bulk samples of high order and with interfaces start to show this decrease in resistance at higher temperatures. This difference in T_c might be related to the size of the interface area, i.e. the smaller the area the lower is the temperature where the Josephson coupling starts to be effectively active. Certainly, this hypothesis is highly speculative because one does not know anything about the differences between intrinsic characteristics of the interfaces of different samples, like doping, twist angles, etc. Fig. 7.24 shows the temperature at which a maximum

is measured in the voltage-temperature curve of lamellae of different thickness d, this last defined in Fig. 7.19 [19]. The upper point represents the temperature of the maximum in the resistance for the bulk HOPG sample, from where the other lamellae were cut. The arrow indicates the expected range ($1\,\mu\text{m} \lesssim d \lesssim 10\,\mu\text{m}$) for the size of the interfaces in the bulk sample, taking into account TEM [67] as well as EBSD [52] measurements.

The results in Fig. 7.24 suggest an apparent size dependence of this kind of "critical" temperature. That the real critical temperature T_c for superconductivity depends on the size of a sample, it is not completely unusual, although its origin is still under discussion and may depend on each case [93–95]. Taking into account that the observed behavior can be related to the existence of superconducting and normal conducting regions, one is allowed to compare those results with the the linear decrease of the superconducting critical temperature decreasing the *whole thickness* of an ensemble of superconducting/metal multilayers (leaving constant the thickness of each of the layers), see [93] and Refs. therein. The dashed-dotted straight line in Fig. 7.24 is the experimental line obtained for Nb/Al multilayers [93] multiplying by 10 both axes. We note that the obtained $T_c(d)$ dependence of the lamellae has a nearly identical slope as that obtained for Nb/Al multilayers.

The origin for the change of T_c in conventional superconducting multilayers and thin wires has been tentatively given in [93, 94] based on weak localization (WL) corrections to T_c for 2D superconductors [95]. In both, the presence of disorder affects the screening of the Coulomb interaction resulting into an exponential suppression of T_c. As pointed out in [19], the parameter dependence of this exponential is different in the theory of [94] than the one used to fit the experimental results of Nb/Al multilayers in [93]. The continuous (green) line in Fig. 7.24 follows

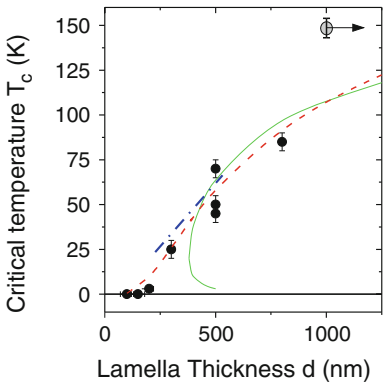

Fig. 7.24 Critical temperature T_c versus thickness of the lamella. The critical temperature was taken at the maximum of the voltage versus temperature curve measured at 1 nA current, i.e. it is the temperature at which the Josephson coupling starts to affect the measured voltage. The thickness d of the lamella is defined in Fig. 7.19. For the meaning of the different curves see main text. Taken from [19]

$$T_c(d) = T_\infty e^{-\ell_{\rm th}(T_c)/d}\,, \tag{7.2}$$

where T_∞ is the critical temperature for infinitely large samples, $\ell_{\rm th}(T) = (\hbar D/k_B T)^{1/2}$ is the thermal length at temperature T, $D = v_F \ell/2$ the 2D diffusion constant, with $v_F \approx 10^6$ m/s the Fermi velocity and ℓ the mean free path. Independent measurements done in graphite flakes without (or with much less influence of) interfaces provide $\ell \sim 3\,\mu$m at $T < 100\,$K [34] and therefore $D \sim 1.5 \times 10^4$ cm^2/s, a value four orders of magnitude larger than the one used in [93], meaning that the effect is relevant in far thicker samples or at much higher temperatures than in Nb/Al multilayers with $T_c \lesssim 10$ K. With this diffusion constant and $T_\infty = 150\,$K the obtained numerical solution of (7.2) is the continuous green line in Fig. 7.24. The semiquantitative agreement is remarkable as well as the estimated cut-off $d_{\rm min} = \ell_{\rm th}(T_c)/2.7 \approx 0.38\,\mu$m, below which (7.2) has no solution.

Following [19], the important aspect of the disorder correction in [94] is screening and the parameter controlling the correction is $t = (e^2/(2\pi^2\hbar))R_\square$, where $R_\square$ is the sheet resistance [94]. In the limit $t \ll \gamma^2$, where γ is the dimensionless bare BCS coupling parameter, the effective critical temperature is

$$T_c(d) = T_\infty \exp^{-t(d)/(6\gamma^3)} = T_\infty \exp^{-\alpha/d}\,, \tag{7.3}$$

where $\alpha = t(d)/(6\gamma^3)$. The dashed line in Fig. 7.24 shows a fit of this type of behavior to the data of [19]. A discussion of the validity range of the approach in [94] and of the parameters obtained from the fits can be read in [19].

7.4 Conclusion

There are clear experimental and theoretical evidence on the existence of specific electronic properties, such as the enhanced density of states in multilayer graphene, twisted graphene as well as at the grain boundaries of graphene or graphite. These electronic peculiarities coming from these defects or interfaces will undoubtedly affect the electronic transport properties measured in graphite and determine the metallic and/or superconducting behavior of whole samples. The existence of rhombohedral stacking order regions embedded in an overall Bernal stacking order matrix and/or twisted Bernal ordered regions may provide a key contribution to understand several details of the transport properties of graphite samples. Taking these peculiarities into account, it is not necessary to speculate too much to arrive to the conclusion that transport and magnetization measurements may change upon microstructure of the graphite sample in question. These differences between samples or changes after certain treatment of a given sample remain difficult to predict and understand if we do not know the internal interface structure and further characteristics. For example, in [96] evidence has been obtained for the change in the structure of AB and BA domains in bilayer graphene after annealing at 1,000 to 1,200 °C.

The interfaces observed in bulk graphite exist also in graphite powders before as well as after certain treatments and may well be the reason for the superconducting-like response measured in magnetization and transport measurements [5, 7, 67, 97]. It should be also clear that if the interfaces play a main role in the measured properties, then time dependence, instabilities or even the apparent irreproducibility of some of the obtained results can be expected, unless one is able to fix the properties and density of the interfaces in a given sample. The existence of high-temperature superconductivity in (non-intercalated) graphite, even with critical temperatures above room-temperature, has been claimed in different publications of the last 40 years [98–104]. These independent reports show some striking peculiarities: The superconducting signal shows low reproducibility, some signals are not stable in time, the amount of superconducting mass (if at all) is small and there is no clear idea on the superconducting phase(s). These peculiarities and the general (over)skepticism in the community on the reported evidence are the reasons, why there was so little interest in this kind of phenomenon. If we assume that interfaces are the reason for all these signals, the interest of the community on these tantalizing phenomena should improve in the future.

We gratefully acknowledge Tero Heikkilä and Grigori Volovik for the fruitful discussions. Y.V.L. aknowledges the support given by the Russian Government Program of Competitive Growth of Kazan Federal University.

References

1. M.S. Dresselhaus, G. Dresselhaus, K. Sugihara, I.L. Spain, H.A. Goldberg, *Graphite Fibers and Filaments* (Springer, Berlin, 1988)
2. R.H. Telling, M.I. Heggie, Philos. Mag. **87**, 4797 (2007)
3. M. Inagaki, *New Carbons: Control of Structure and Functions* (Elsevier, New York, 2000)
4. J. Barzola-Quiquia, J.L. Yao, P. Rödiger, K. Schindler, P. Esquinazi, Phys. Status Solidi (a) **205**, 2924 (2008)
5. T. Scheike, W. Böhlmann, P. Esquinazi, J. Barzola-Quiquia, A. Ballestar, A. Setzer, Adv. Mater. **24**, 5826 (2012)
6. P. Esquinazi, T.T. Heikkilä, Y.V. Lysogoskiy, D.A. Tayurskii, G.E. Volovik, JETP Lett. **100**, 336 (2014). arXiv:1407.1060
7. A. Ballestar, P. Esquinazi, W. Böhlmann, Phys. Rev. B **91**, 014502 (2015)
8. M. Kuwabara, D.R. Clarke, A.A. Smith, Appl. Phys. Lett. **56**, 2396 (1990)
9. M. Flores, E. Cisternas, J. Correa, P. Vargas, Chem. Phys. **423**, 49 (2013)
10. L. Feng, X. Lin, L. Meng, J.C. Nie, J. Ni, L. He, Appl. Phys. Lett. **101**, 113113 (2012)
11. D. Tománek, S.G. Louie, Phys. Rev. B **37**, 8327 (1988)
12. J.M. Campanera, G. Savini, I. Suarez-Martinez, M.I. Heggie, Phys. Rev. B **75**, 235449 (2007)
13. D.L. Miller, K.D. Kubista, G.M. Rutter, M. Ruan, W.A. de Heer, P.N. First, J.A. Stroscio, Phys. Rev. B **81**, 125427 (2010)
14. Y. Zhang, J.P. Small, W.V. Pontius, P. Kim, Appl. Phys. Lett. **86**, 073104 (2005)
15. Y. Lu, M. Muñoz, C.S. Steplecaru, C. Hao, M. Bai, N. García, K. Schindler, P. Esquinazi, Phys. Rev. Lett. **97**, 076805 (2006). See also the comment by S. Sadewasser, Th. Glatzel, Phys. Rev. Lett. **98**, 269701 (2007) and the reply by Lu et al., idem **98**, 269702 (2007) and also R. Proksch. Appl. Phys. Lett. **89**, 113121 (2006)

16. I. Brihuega, P. Mallet, H. González-Herrero, G.T. de Laissardière, M.M. Ugeda, L. Magaud, J.M. Gómez-Rodríguez, F. Ynduráin, J.Y. Veuillen, Phys. Rev. Lett. **109**, 196802 (2012)
17. P. San-Jose, E. Prada, Phys. Rev. B **88**, 121408(R) (2013)
18. H. Ribeiro, K. Sato, G. Eliel, E. de Souza, C.C. Lu, P.W. Chiu, R. Saito, M. Pimenta, Carbon **90**, 138 (2015)
19. A. Ballestar, T.T. Heikkilä, P. Esquinazi, Superc. Sci. Technol. **27**, 115014 (2014)
20. J. Lahiri, Y. Lin, P. Bozkurt, I. Oleynik, M. Batzill, Nat. Nanotechnol. **5**, 326 (2010)
21. P. Esquinazi, A. Setzer, R. Höhne, C. Semmelhack, Y. Kopelevich, D. Spemann, T. Butz, B. Kohlstrunk, M. Lösche, Phys. Rev. B **66**, 024429 (2002)
22. N.B. Kopnin, M. Ijäs, A. Harju, T.T. Heikkilä, Phys. Rev. B **87**, 140503 (2013)
23. W.A. Muñoz, L. Covaci, F. Peeters, Phys. Rev. B **87**, 134509 (2013)
24. B.T. Kelly, *Physics of Graphite* (Applied Science Publishers, London, 1981)
25. Q. Lin, T. Li, Z. Liu, Y. Song, L. He, Z. Hu, Q. Guo, H. Ye, Carbon **50**, 2369 (2012)
26. S. Hattendorf, A. Georgi, M. Liebmann, M. Morgenstern, Surf. Sci. **610**, 53 (2013)
27. D. Pierucci, H. Sediri, M. Hajlaoui, J.C. Girard, T. Brumme, M. Calandra, E. Velez-Fort, G. Patriarche, M.G. Silly, G. Ferro, V. Soulire, M. Marangolo, F. Sirotti, F. Mauri, A. Ouerghi, ACS Nano **9**, 5432 (2015)
28. Y. Henni, H.P. Ojeda Collado, K. Nogajewski, M.R. Molas, G. Usaj, C.A. Balseiro, M. Orlita, M. Potemski, C. Faugeras, arXiv:1603.03611
29. M. Zoraghi, J. Barzola-Quiquia, M. Stiller, A. Setzer, P. Esquinazi, G.H. Kloeß, T. Muenster, T. Lühmann, I. Estrela-Lopis, arXiv:1603.06365
30. N. García, P. Esquinazi, J. Barzola-Quiquia, S. Dusari, New J. Phys. **14**(5), 053015 (2012)
31. Y. Shapira, G. Deutscher, Phys. Rev. B **27**, 4463 (1983)
32. P. Esquinazi, N. García, J. Barzola-Quiquia, P. Rödiger, K. Schindler, J.L. Yao, M. Ziese, Phys. Rev. B **78**, 134516 (2008)
33. N. García, P. Esquinazi, J. Barzola-Quiquia, B. Ming, D. Spoddig, Phys. Rev. B **78**, 035413 (2008)
34. P. Esquinazi, J. Barzola-Quiquia, S. Dusari, N. García, J. Appl. Phys. **111**, 033709 (2012)
35. Y. Ohashi, T. Hironaka, T. Kubo, K. Shiiki, TANSO **195**, 410 (2000)
36. Y. Ohashi, K. Yamamoto, T. Kubo, Carbon'01, An International Conference on Carbon, Lexington, KY, United States, 14–19 July. (The American Carbon Society, 2001), pp. 568–570. www.acs.omnibooksonline.com
37. K. Thiyagarajan, B. Saravanakumar, R. Mohan, S.J. Kim, Sci. Adv. Mater. **5**, 542 (2013)
38. J. Barzola-Quiquia, S. Dusari, G. Bridoux, F. Bern, A. Molle, P. Esquinazi, Nanotechnology **21**, 145306 (2010)
39. I.A. Luk'yanchuk, Y. Kopelevich, Phys. Rev. Lett. **93**, 166402 (2004)
40. R. Ruffieux, O. Gröning, P. Schwaller, L. Schlapbach, P. Gröning, Phys. Rev. Lett. **84**, 4910 (2000)
41. A. Arndt, D. Spoddig, P. Esquinazi, J. Barzola-Quiquia, S. Dusari, T. Butz, Phys. Rev. B **80**, 195402 (2009)
42. V.T. Dolgopolov, A.A. Shashkin, G.V. Kravchenko, I.M. Mukhametzhanov, M. Wendel, J.P. Kotthaus, L.W. Molenkamp, C.T. Foxon, JETP Lett. **63**, 63 (1996)
43. N. Harrison, J. Singleton, J. Phys.: Condens. Matter **13**, L463 (2001)
44. P. Esquinazi, J. Krüger, J. Barzola-Quiquia, R. Schönemann, T. Hermannsdörfer, N. García, AIP Adv. **4**, 117121 (2014)
45. X. Du, I. Skachko, A. Barker, E.Y. Andrei, Nat. Nanotechnol. **3**, 491 (2008)
46. S. Dusari, J. Barzola-Quiquia, P. Esquinazi, N. García, Phys. Rev. B **83**, 125402 (2011)
47. N. García, L. Escapa, Appl. Phys. Lett. **54**, 1418 (1989)
48. I. Snyman, J. Tworzydło, C.W.J. Beenakker, Phys. Rev. B **78**, 045118 (2008)
49. J.L. Costa-Krämer, N. García, H. Olin, Phys. Rev. Lett. **78**, 4990 (1997)
50. B.J. van Wees, H. van Houten, C.W.J. Beenakker, J.G. Williamson, L.P. Kouwenhoven, D. van der Marel, C.T. Foxon, Phys. Rev. Lett. **60**, 848 (1988)
51. D.A. Wharam, T.J. Thornton, R. Newbury, M. Pepper, H. Ahmed, J.E.F. Frost, D.G. Hasko, D.C. Peacockt, D.A. Ritchie, G.A.C. Jones, J. Phys. C: Solid State Phys. **21**, L209 (1988)

52. J.C. González, M. Muñoz, N. García, J. Barzola-Quiquia, D. Spoddig, K. Schindler, P. Esquinazi, Phys. Rev. Lett. **99**, 216601 (2007)
53. J.W. McClure, IBM J. Res. Dev. **8**, 255 (1964)
54. A. Grüneis, C. Attaccalite, T. Pichler, V. Zabolotnyy, H. Shiozawa, S.L. Molodtsov, D. Inosov, A. Koitzsch, M. Knupfer, J. Schiessling, R. Follath, R. Weber, P. Rudolf, R. Wirtz, A. Rubio, Phys. Rev. Lett. **100**, 037601 (2008)
55. A. Kumar, J.M. Poumirol, W. Escoffier, M. Goiran, B. Raquet, J.C. Pivin, J. Phys.: Condens. Matter **22**, 436004 (2010)
56. J. Barzola-Quiquia, A. Ballestar, S. Dusari, P. Esquinazi, *Experimental Study of the Intrinsic and Extrinsic Transport Properties of Graphite and Multigraphene Samples* (Intech, Open Access Publisher, Jian Ru Gong (ed.), 2011), chap. 8. ISBN 978-953-307-292-0
57. F. Hund, B. Mrowka, Sächs. Akad. Wiss., Leipzig **87**, 185 (1935)
58. G.E. Kimball, J. Chem. Phys. **3**, 560 (1935)
59. F. Hund, B. Mrowka, Sächs. Akad. Wiss., Leipzig **87**, 325 (1935)
60. P.R. Wallace, Phys. Rev. **71**, 622 (1947)
61. R.O. Dillon, I.L. Spain, J.W. McClure, J. Phys. Chem. Solids **38**, 635 (1977)
62. J.M. Schneider, M. Orlita, M. Potemski, D.K. Maude, Phys. Rev. Lett. **102**, 166403 (2009). see also the comment by I.A. Luk'yanchuk, Y. Kopelevich, idem **104**, 119701 (2010)
63. I.M. Tsidilkovski, *Electron Spectrum of Gapless Semiconductors*, vol. 116, Springer Series in Solid-State Sciences (Springer, New York, 1997)
64. T. Stauber, N.M.R. Peres, F. Guinea, Phys. Rev. B **76**, 205423 (2007)
65. J. Barzola-Quiquia, P. Esquinazi, J. Supercond. Nov. Magn. **23**, 451 (2010)
66. H. Kempa, H.C. Semmelhack, P. Esquinazi, Y. Kopelevich, Solid State Commun. **125**, 1 (2003)
67. A. Ballestar, J. Barzola-Quiquia, T. Scheike, P. Esquinazi, New J. Phys. **15**, 023024 (2013)
68. Ana Ballestar, Ph.D. thesis entitled "Superconductivity at graphite interfaces", University of Leipzig (2014), unpublished
69. H.B. Heersche, P. Jarillo-Herrero, J.B. Oostinga, L.M.K. Vandersypen, A.F. Morpurgo, Nature **446**, 56 (2007)
70. V. Ambegaokar, B.I. Halperin, Phys. Rev. Lett. **22**, 1364 (1969)
71. I. Hagymási, A. Kormányos, J. Cserti, Phys. Rev. B **82**, 134516 (2010)
72. Y. Kopelevich, J.H.S. Torres, R.R. da Silva, F. Mrowka, H. Kempa, P. Esquinazi, Phys. Rev. Lett. **90**, 156402 (2003)
73. A. Ballestar, P. Esquinazi, J. Barzola-Quiquia, S. Dusari, F. Bern, R. da Silva, Y. Kopelevich, Carbon **72**, 312 (2014)
74. Z.K. Tang, L. Zhang, N. Wang, X.X. Zhang, G.H. Wen, G.D. Li, J.N. Wang, C.T. Chan, P. Sheng, Science **292**, 2462 (2001)
75. M. Kociak, A.Y. Kasumov, S. Guéron, B. Reulet, I.I. Khodos, Y.B. Gorbatov, V.T. Volkov, L. Vaccarini, H. Bouchiat, Phys. Rev. Lett. **86**, 2416 (2001)
76. M. Ferrier, F. Ladieu, M. Ocio, B. Sacépé, T. Vaugien, V. Pichot, P. Launois, H. Bouchiat, Phys. Rev. B **73**, 094520 (2006)
77. I. Takesue, J. Haruyama, N. Kobayashi, S. Chiashi, S. Maruyama, T. Sugai, H. Shinohara, Phys. Rev. Lett. **96**, 057001 (2006)
78. N. Murata, J. Haruyama, Y. Ueda, M. Matsudaira, H. Karino, Y. Yagi, E. Einarsson, S. Chiashi, S. Maruyama, T. Sugai, N. Kishi, H. Shinohara, Phys. Rev. B **76**, 245424 (2007)
79. T. Tsuneta, L. Lechner, P.J. Hakonen, Phys. Rev. Lett. **98**, 087002 (2007)
80. R. Lortz, Q. Zhang, W. Shi, J.T. Ye, C. Qiu, Z. Wang, H. He, P. Sheng, T. Qian, Z. Tang, N. Wang, X. Zhang, J. Wang, C.T. Chan, Proc. Natl. Acad. Sci. **106**(18), 7299 (2009)
81. Z. Wang, W. Shi, H. Xie, T. Zhang, N. Wang, Z. Tang, X. Zhang, R. Lortz, P. Sheng, I. Sheikin, A. Demuer, Phys. Rev. B **81**, 174530 (2010)
82. W. Shi, Z. Wang, Q. Zhang, Y. Zheng, C. Ieong, M. He, R. Lortz, Y. Cai, N. Wang, T. Zhang, H. Zhang, Z. Tang, P. Sheng, H. Muramatsu, Y.A. Kim, M. Endo, P.T. Araujo, M.S. Dresselhaus, Sci. Rep. **2**, 625 (2012)
83. Z. Wang, W. Shi, R. Lortz, P. Sheng, Nanoscale **4**, 21 (2012)

84. J. Barzola-Quiquia, P. Esquinazi, M. Lindel, D. Spemann, M. Muallem, G. Nessim, Carbon **88**, 16 (2015)
85. J.S. Langer, V. Ambegaokar, Phys. Rev. **164**, 498 (1967)
86. D.E. McCumber, B.I. Halperin, Phys. Rev. B **1**, 1054 (1970)
87. H.J. Gardner, A. Kumar, L. Yu, P. Xiong, M.P. Warusawithana, L. Wang, O. Vafek, D.G. Schlom, Nat. Phys. **7**, 895 (2011)
88. J. González, F. Guinea, M.A.H. Vozmediano, Phys. Rev. B **63**, 134421 (2001)
89. K. Scharnberg, R.A. Klemm, Phys. Rev. B **22**, 5233 (1980)
90. A. Knigavko, B. Rosenstein, Phys. Rev. B **58**, 9354 (1998)
91. Y. Kopelevich, P. Esquinazi, J.H.S. Torres, R.R. da Silva, H. Kempa, Graphite as a highly correlated electron liquid, in *Advances in Solid State Physics*, vol. 43, ed. by B. Kramer (Springer, Berlin, 2003), pp. 207–222
92. H. Kempa, Y. Kopelevich, F. Mrowka, A. Setzer, J.H.S. Torres, R. Höhne, P. Esquinazi, Solid State Commun. **115**, 539 (2000)
93. J. Guimpel, M.E. de la Cruz, F. de la Cruz, H.J. Fink, O. Laborde, J.C. Villegier, J. Low Temp. Phys. **63**, 151 (1986)
94. Y. Oreg, A. Finkel'stein, Phys. Rev. Lett. **83**, 191 (1999)
95. H. Fukuyama, Physica **126B**, 306 (1984). See also H. Ebisawa, H. Fukuyama, S. Maekawa, J. Phys. Soc. Jpn. **54**, 2257 (1985)
96. J.S. Alden, A.W. Tsen, P.Y. Huang, R. Hovden, L. Brown, J. Park, D.A. Muller, P.L. McEuen, Proc. Natl. Acad. Sci. **110**, 11256 (2013)
97. T. Scheike, P. Esquinazi, A. Setzer, W. Böhlmann, Carbon **59**, 140 (2013)
98. K. Antonowicz, Nature **247**, 358 (1974)
99. R.R. da Silva, J.H.S. Torres, Y. Kopelevich, Phys. Rev. Lett. **87**, 147001 (2001)
100. H.P. Yang, H.H. Wen, Z.W. Zhao, S.L. Li, Chin. Phys. Lett. **18**, 1648 (2001)
101. S. Moehlecke, P.C. Ho, M.B. Maple, Philos. Mag. B **82**, 1335 (2002)
102. I. Felner, Y. Kopelevich, Phys. Rev. B **79**, 233409 (2009)
103. S.W. Han, J.D. Lee, J.P. Noh, D.W. Jung, J. Low Temp. Phys. **160**, 41 (2010)
104. Y. Kawashima, AIP Adv. **3**, 052132 (2013)

Index

P.D. Esquinazi (ed.), *Basic Physics of Functionalized Graphite*,
Springer Series in Materials Science 244, DOI 10.1007/978-3-319-39355-1